1-1-1999

Selected studies on the thermal and mechanical responses of amorphous glassy polymers at different length scales.

Emmett D. Crawford
University of Massachusetts Amherst

SELECTED STUDIES ON THE THERMAL AND MECHANICAL RESPONSES OF AMORPHOUS GLASSY POLYMERS AT DIFFERENT LENGTH SCALES

A Dissertation Presented

By

EMMETT D. CRAWFORD

Submitted to the Graduate School of the
University of Massachusetts Amherst in partial fulfillment
of the requirements for the degree of

DOCTOR OF PHILOSOPHY

May 1999

Polymer Science and Engineering

SELECTED STUDIES ON THE THERMAL AND MECHANICAL RESPONSES OF AMORPHOUS GLASSY POLYMERS AT DIFFERENT LENGTH SCALES

A Dissertation Presented

By

EMMETT D. CRAWFORD

Approved as to style and content by:

Alan J. Lesser, Chair

David A. Hoagland, Member

Thomas J. Lardner, ~~Member~~

Richard J. Farris, Department Head
Polymer Science and Engineering

ACKNOWLEDGMENTS

The author would like to thank Professor Alan J. Lesser for providing guidance and support during the author's graduate studies. Professor Lesser was a great mentor and a friend. The author would also like to thank his committee members Professor David A. Hoagland and Professor Thomas J. Lardner. Professor Hoagland listened and encouraged the author. Professor Lardner provided the author with a fundamental knowledge of solid mechanics and inspired the author by his level of teaching excellence.

The author would like to thank all his coworkers and friends. Their support and input made this possible. The author would like to thank his family for providing continual support through out the years. Finally, the author would like to thank Alicia King for her help and patience.

ABSTRACT

SELECTED STUDIES ON THE THERMAL AND MECHANICAL RESPONSES

OF AMORPHOUS GLASSY POLYMERS

AT DIFFERENT LENGTH SCALES

MAY 1999

EMMETT D. CRAWFORD, B.S., NORTH CAROLINA STATE UNIVERISTY

PH.D., UNIVERSITY OF MASSACHUSETTS AMHERST

Directed by: Professor Alan J. Lesser

This thesis describes investigations into the mechanical and thermal characteristics of amorphous polymeric materials by structural changes on the molecular and the microscopic scale. On the molecular scale, the structure of a cross-linked polymeric material is controlled by changes in the molecular weight between cross-links, cross-link functionality, and chain stiffness. With control of the network structure, an expansive range of mechanical and thermal characteristics is possible. These properties range from intrinsic properties, such as the glass transition temperature, to performance properties, such as impact behavior. Relationships between the network structure and measured properties are established by the use of a variety of theories from rubber elasticity to free volume. Relationships are also established between the various measured properties through solid and fracture mechanics.

The introduction of soft rubbery particles on the microscopic scale into a glassy polymeric matrix is commonly employed to create a tougher material. Despite the prevalent use, the mechanisms and sequence of mechanisms of toughening are poorly understood. The mechanisms and sequence of mechanisms are elucidated in this

investigation through the use of unique mechanical tests and materials with favorable properties. The unique mechanical tests in this investigation include tensile dilatometry and a multi-axial stress state test. The multi-axial stress state test, which allows independent control of the dilational and deviatoric stresses of a material between uniaxial compression and equal biaxial tension, consists of a uniaxially loaded and pressurized thin walled hollow cylinder. The materials include liquid rubber modified epoxies, voided epoxies, and core-shell rubber modified polyvinylchloride. The voided epoxy material separates the matrix contributions from those of the rubbery phase, while the core-shell rubber modified polyvinylchloride provides optical verification of rubber particle cavitation. By combined use of these materials and the unique mechanical tests, the mechanics of rubber toughening are evaluated.

TABLE OF CONTENTS

LIST OF TABLES

LIST OF FIGURES

CHAPTER 1

INTRODUCTION

The mechanical and physical characteristics of amorphous polymeric materials can be controlled by structural changes on the molecular scale, described in Chapter 2, and by structural changes on the microscopic scale, described in Chapter 3. On the molecular scale, the structure of a cross-linked polymeric network is controlled by three variables: the molecular weight between cross-links (M_c), cross-link functionality (f_c), and chain stiffness. Figure 1.1 shows a schematic of the molecular structural variables in a cross-linked polymeric material. The majority of studies to date have investigated the effect of M_c on a single property or a small range of properties.[1-4] Theoretical studies have addressed the role of cross-link functionality, yet experimental studies addressing mechanical properties have not been conducted in thermosetting systems.[5-7] Given the multitude of chemical structures and the nature of thermosetting processes a clear investigation into cross-link functionality is necessary. In addition to addressing this issue, a wide range of mechanical and thermal characteristics are determined. The characteristics of interest range from intrinsic type properties, such as the glass transition temperature to performance type properties, such as instrumented impact behavior. The characteristics examined in this investigation include: rubbery modulus, glassy modulus, dynamic mechanical spectroscopy, glass transition temperature, yield behavior, fracture toughness, impact behavior, and indentation behavior. The objective is to address how changes in molecular structure affect these intrinsic and performance properties.

On the microscopic scale, the addition of soft rubbery inclusions into a glassy matrix is an effective technique for improving the material's toughness. Despite the

frequent use, the mechanisms and sequence of mechanisms are poorly understood. The popular belief is that rubber particle cavitation is required first to alleviate the hydrostatic stress, resulting in stress state more favorable to yielding.[8,9] Figure 1.2 shows a schematic of rubber toughening and associated mechanisms. The objective of this investigation is to develop tests and materials that can elucidate the mechanics associated with rubber toughening. In the microscopic scale investigation, described in Chapter 3, tensile dilatometry and multi-axial stress state testing is performed on rubber modified systems. The rubber modified systems of this investigation include: liquid rubber modified epoxies, core-shell modified polyvinylchloride, and voided epoxy material. Through the combinations of these tests and materials, the mechanisms and sequence of mechanisms present in rubber toughening are evaluated.

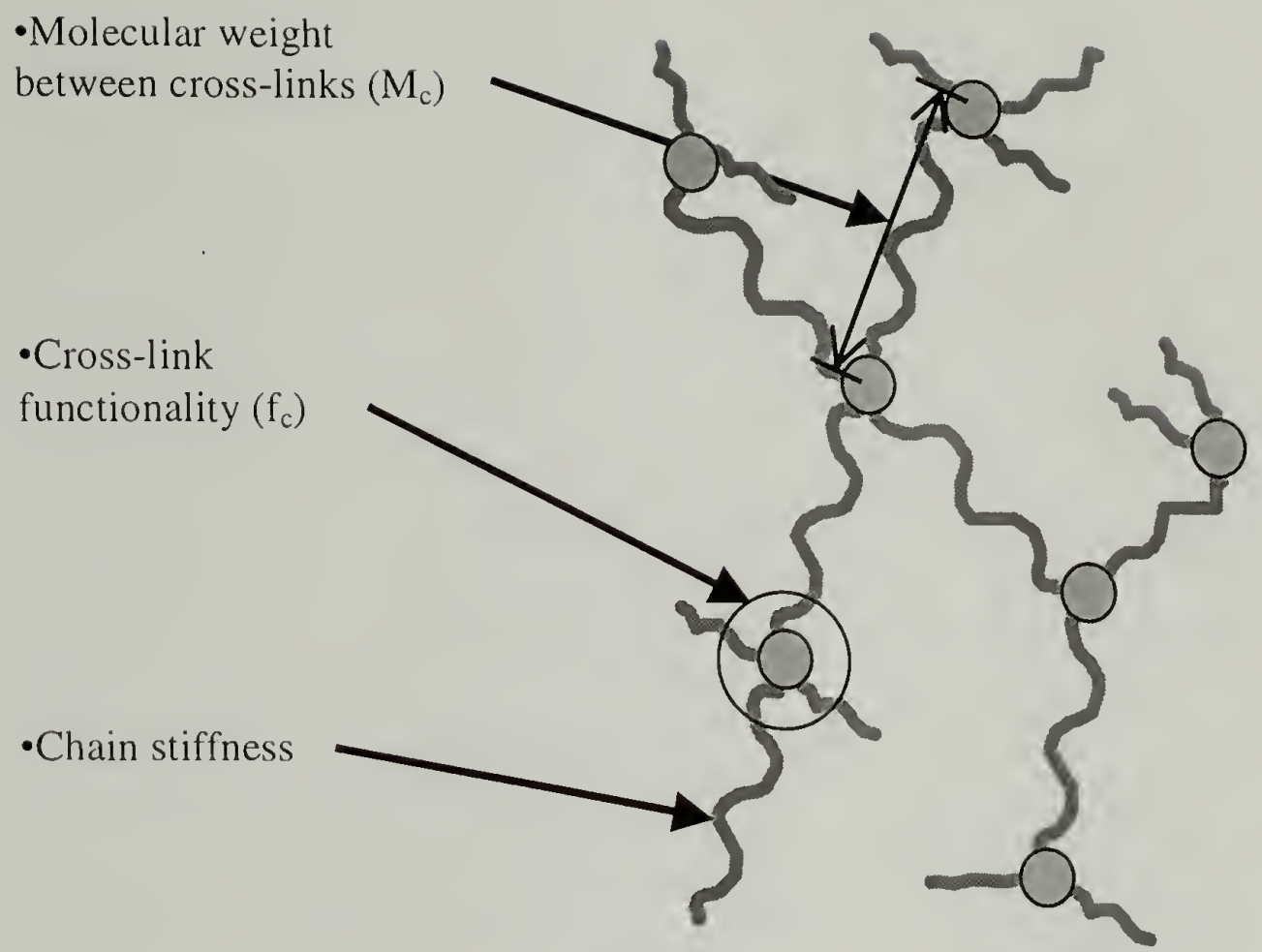

Figure 1.1: Molecular structural variables in molecular scale investigation.

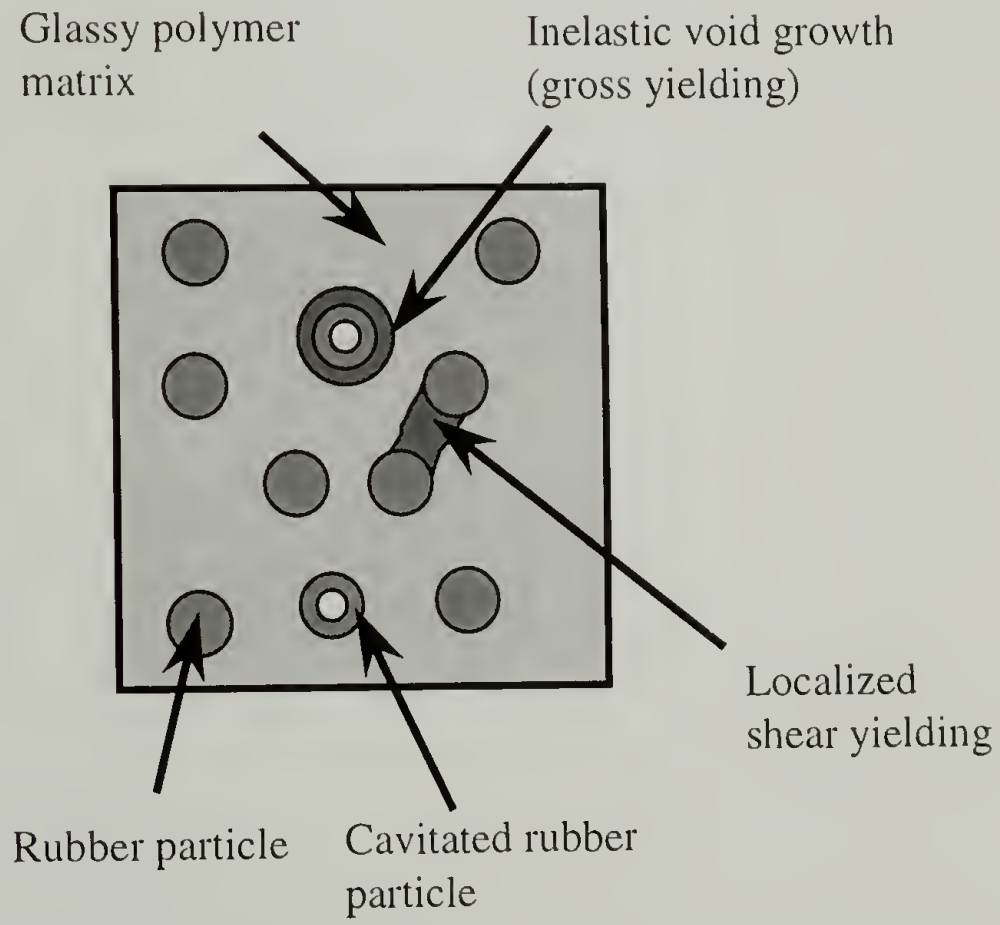

Figure 1.2: Mechanisms of rubber toughening evaluated in microscopic scale investigation.

CHAPTER 2

MOLECULAR SCALE INVESTIGATION

2.1 Introduction

The mechanical and physical characteristics of amorphous polymeric materials are influenced by structural changes on the molecular scale. The molecular structure of a cross-linked polymeric material is described by three variables: the molecular weight between cross-links (M_c), cross-link functionality (f_c), and chain stiffness. To date, the majority of studies have investigated the effect of M_c on the mechanical and thermal properties in thermosetting polymers.[1-4] In epoxy thermosetting systems alone there are at least 400 different curing agents and resins available.[10] Given the multitude of chemical structures and the nature of thermosetting processes, a clear investigation into cross-link functionality and chain stiffness is necessary.

In this investigation, epoxy networks are constructed in which M_c, f_c, and chain stiffness are systematically controlled. Changing the chemical nature of the amines from an aromatic structure to an aliphatic structure alters chain stiffness. By reacting difunctional, trifunctional, and tetrafunctional amines of similar chemical structure in stoichiometry with a difunctional epoxy resin permits control of M_c and f_c. The measured mechanical and physical characteristics of these controlled network materials range from intrinsic properties, such as the glass transition (T_g), to performance properties, such as instrumented impact energy. This study determines the role network architecture plays on a variety of thermal and mechanical characteristics, such that these systems can be optimized and tailored for specific applications.

2.2 Materials

Shell Chemical Company supplied diglycidyl ether of bisphenol A based difunctional epoxy resins, Epon 825 and Epon 828. The chemical structures of these resins and their epoxide equivalent weight (M_e) are shown in Figure 2.1. The aromatic amine curing system consists of 1,3-phenylenediamine, N-methyl-1,2-phenylenediamine, and aniline. The chemical structures of these amines are shown in Figure 2.2. These molecules have respective reactive functionalities of 4, 3, and 2. The aliphatic amine curing system consists of ethylenediamine, N-methylethylenediamine, and N,N'-dimethylethylenediamine. These molecules have respective reactive functionalities of 4, 3, and 2. The chemical structures of these amines are shown in Figure 2.3. In addition to the aromatic and aliphatic amine curing systems, a variety of other amine curing agents were employed to address certain structure-property relationships in an economical manner. The structures of these amines are shown in Figure 2.4. All amines were purchased from Aldrich Chemical Company and used without purification.

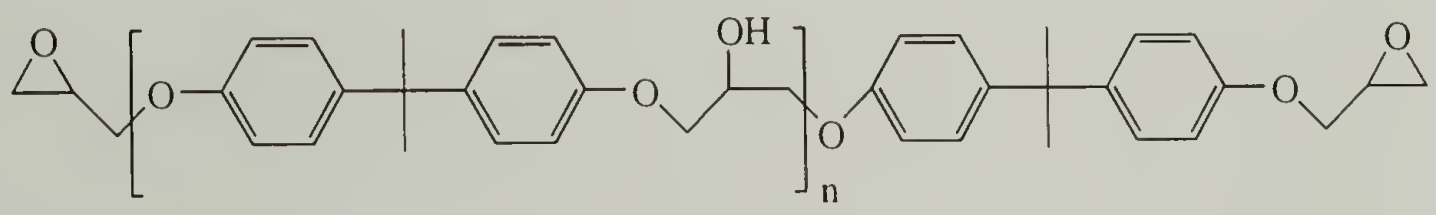

Figure 2.1: Chemical structures of Epon 825 (n=0.04, M_e=175 g/mol) and Epon 828 (n=0.15, M_e=188 g/mol).

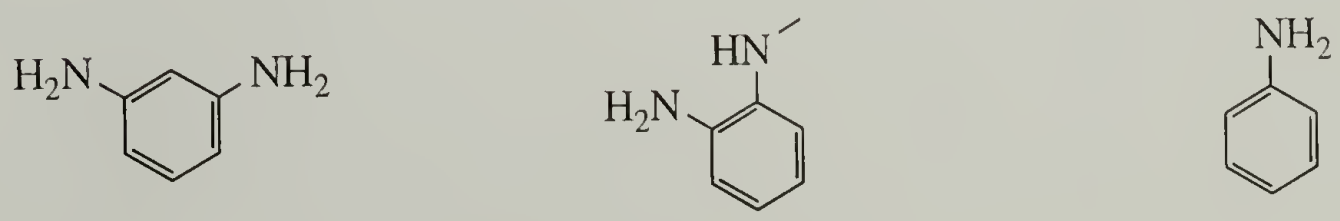

Figure 2.2: Chemical structures of aromatic amine curing system. 1,3-phenylenediamine (left), N-methyl-1,2-phenylenediamine (center), aniline (right).

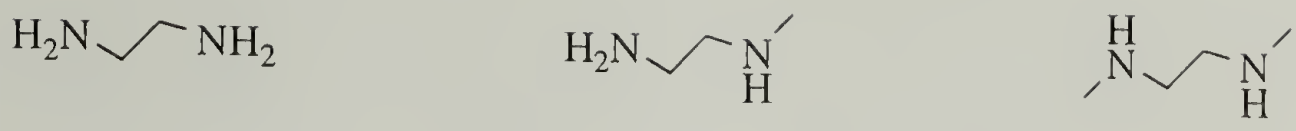

Figure 2.3: Chemical structures of aliphatic amine curing system. Ethylenediamine (left), N-methylethylenediamine (center), N,N'-dimethylethylenediamine (right).

Figure 2.4: Chemical structures of amines. 3-methoxypropylamine (left), N-aminoethylpiperazine (AEP, right).

2.3 Network Fabrication

The epoxy resins were dried under vacuum at 80°C for 10 hours prior to use. The resin was weighed out and placed in an oven at 50°C. Once the resin had equilibrated, the amines were then blended with the resin. All the amines were at room temperature with exception to 1,3-phenylenediamine, which was melted at 80°C before blending. After mixing the amines vigorously with the epoxy resin for 3 minutes, the samples were placed back into a 50°C oven for 5 minutes to allow air bubbles to escape. The mixture was then poured into treated 11.5 mm diameter glass test tubes and between two treated glass plates that were separated by a teflon spacer and clamped with several c-clamps. The glass was pretreated with SurfaSil (Pierce Chemical Company), a silating agent that prevents the adhesion between the resulting network and the glass. Once the resin was poured, the mold and test tubes were placed back into the oven at 50°C for 3 to 12 hours in order for gelation to occur. The length of cure depended on the nature of the amine, with longer cure times for the aromatic amines. The molds and test tubes were then

placed in an oven and post-cured for 3 hours at a temperature 20 °C above the maximum glass transition temperature possible for each network. After post-cure, the plaques and test tubes were allowed to slowly cool to room temperature and then separated from the glass.

2.4 Calculation of Network Parameters

2.4.1 Differential Scanning Calorimetry (DSC)

Differential scanning calorimetry was performed with a DuPont Thermal Analyzer 2000 on 5-10 mg samples taken from the plaques. The glass transition temperature of each network was measured at a heating rate of 10 °C/min using the inflection point as the T_g of the network.

2.4.2 Calculation Basis

All network parameters are based on the assumption that reactions occur solely between epoxide groups and primary and secondary amines and that full conversion is achieved. Reactions of epoxide groups with primary and secondary amines are more favored than the base-catalyzed epoxide etherfication reaction, which does not occur until reaction temperatures are much greater than 150 °C.[11-13] Infrared (IR) analysis performed on epoxy-amine systems, similar to the systems used in this study, show conversions of 95%, with the reactions between the epoxide groups and the primary and secondary amines the dominant mechanisms.[4] However, use of IR to measure conversion during the later stages of the cure of an epoxy resin becomes inaccurate because of difficulty in determining the concentration of epoxide groups.[14] Gillham and Wisanrakkit[15] showed that the T_g of an epoxy network could be used to measure conversion in the later stages of cure, since it is sensitive to the structural changes occurring in the network. In this

analysis, full conversion is achieved when the glass transition temperature does not increase with an increase in cure temperature and cure time. The cure of the networks in this study is considered complete since the networks' glass transition temperatures reached a maximum (T_{gx}) with respect to cure time and cure temperature, thereby fulfilling the above requirements.

Horie et al.[16] argue that an increase in the number of methylene units in aliphatic diamines of the structure $H_2N\text{-}(CH_2)_n\text{-}NH_2$ results in an increase in the final conversion when reacted with diepoxy resins, with near 100% conversion being achieved by diamines of 6 or more methylene units. The lack of high conversions in shorter amines was attributed to the restriction of segmental mobility due to high levels of cross-linking. The work in this study does not support this finding. Figure 2.5 is a plot of T_{gx} versus the number of methylene units for networks constructed with Epon 825 and a homologous series of aliphatic diamines of the structure $H_2N\text{-}(CH_2)_n\text{-}NH_2$. Horie et al.[16] findings would suggest a plateau in T_{gx} as the number of methylene units approaches 3 to 4. Such a trend is not apparent in Figure 2.5. Consequently, high degrees of conversion do not seem to be limited in networks constructed with ethylenediamine.

With full conversion, f_c and M_c can be calculated from stoichiometry by equations 2.1 and 2.2.

$$M_c = \frac{2\left(M_e + \sum_{f=2}^{\infty} \frac{M_f}{f}\Phi_f\right)}{\sum_{f=3}^{\infty}\Phi_f} \qquad (2.1)$$

$$f_c = \frac{\sum_{f=3}^{\infty}\Phi_f}{\sum_{f=3}^{\infty}\left(\frac{\Phi_f}{f}\right)} \qquad (2.2)$$

where: M_e epoxide equivalent weight of the resin
f reactive functionality of amine
M_f molecular weight of the f^{th} functional amine
Φ_f mole fraction of amine hydrogen atoms provided by the f^{th} functional amine.

In the analysis of cross-linked materials, the molar cross-link density (X_m) is sometimes employed in structure-property relations. The molar cross-link density can be calculated by equation 2.3.

$$X_m = \frac{\sum_{f=3}^{\infty} \frac{\Phi_f}{f}}{\left(\frac{1}{2} + \sum_{f=2}^{\infty} \frac{\Phi_f}{f}\right)} \qquad (2.3)$$

In equations 2.1-2.3, the mechanical cross-link functionality in an elastic network is assumed to equal the chemical functionality. For the aromatic cross-linking reagents, there are no rotatable bonds between the two nitrogen atoms. Since the end to end distance of this short chain does not change, the aromatic cross-linking agents cannot contribute to conformational elasticity. Therefore in the case of the aromatic curing agents, the assumption of the mechanical functionality equaling the chemical functionality seems valid. The case for the aliphatic reagents is not as clear. However, the literature lends some support to modeling ethylenediamine as a tetrafunctional cross-link. Charlesworth[17] thoroughly investigated the low temperature γ relaxation for diepoxides cured with diamines of the structure $H_2N\text{-}(CH_2)_n\text{-}NH_2$. Charlesworth[17] showed that the γ relaxation does not occur when the number of methylene units is less than four. This data supports the view of little to no motion of the small chain between the two nitrogen atoms present in ethylenediamine. Orientational elasticity due to the

presence of short rigid chains has also been shown to be negligible.[18] Taking this into account, ethylenediamine is modeled as a tetrafunctional cross-link.

A final comment should be made with respect to the relationships between mechanical functionality and chemical functionality. In the calculations of f_c and M_c, ethylenediamine and 1,3-phenylenediamine are assumed to act as a single tetrafunctional cross-link. However, ethylenediamine and 1,3-phenylenediamine can be treated as two trifunctional mechanical cross-links. In the latter case, the effect of cross-link functionality is removed and the values of M_c change. This latter approach also collapses the data. Both approaches are mathematically equivalent, but conceptually distinct, with the tetrafunctional cross-link opinion being presented in light of the arguments voiced in the previous paragraph.

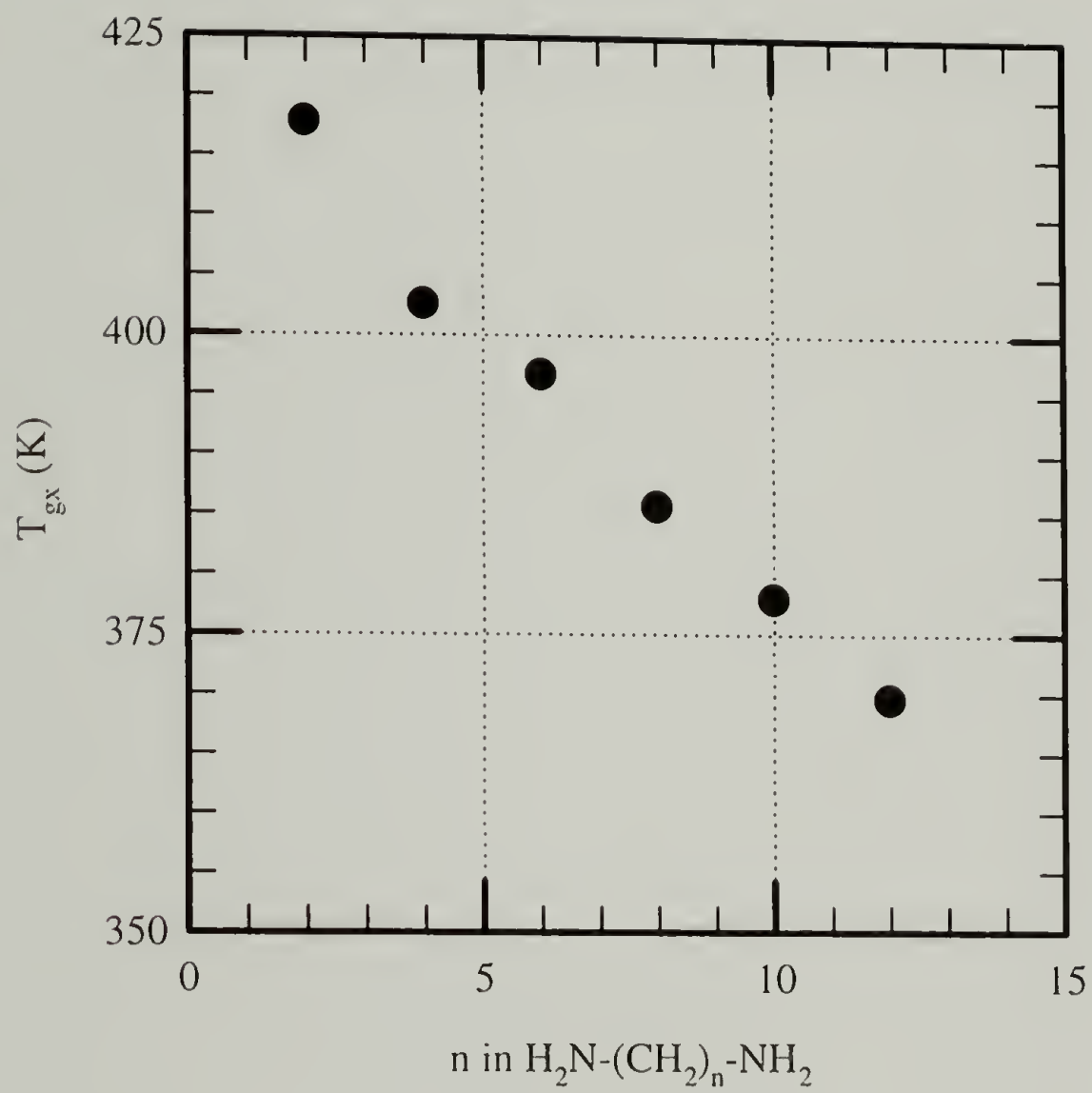

Figure 2.5: Maximum glass transition temperatures for networks created with Epon 825 and a homologous series of amines.

2.5 Density and Thermal Expansion Coefficients

2.5.1 Measurement Techniques

Density measurements were obtained by Archimedes' principle. The materials were weighed in air and silicon oil (ρ=0.963) at room temperature with an analytical balance. The density (ρ_o) was calculated by equation 2.4.

$$\rho_o = \frac{0.963\,\Delta W}{W_a} \qquad (2.4)$$

where: W_a weight of material in air
ΔW weight difference of material in air and in silicon oil.

The changes in specific volume of the materials with temperature were made with a Gnomix PVT apparatus at a heating rate of 2 °C/min and a pressure of 10 MPa. Linear regressions were performed to obtain the linear thermal expansion coefficient (α) in the glassy state (α_g) and in the rubbery state (α_r) as defined by equation 2.5.

$$\alpha = \rho_o \left(\frac{\partial \hat{V}}{\partial T} \right)_P \qquad (2.5)$$

2.5.2 Effect of Molecular Weight Between Cross-links

The bulk densities of the networks constructed with Epon 825, ethylenediamine, and 3-methoxypropylamine are shown in Table 2.1. The density of the networks decreases as M_c increases. This trend is consistent with reports by Nielsen[19], which show density increasing with the extent of cross-linking. The observed behavior in these networks can also be explained by room temperature bulk density differences between ethylenediamine (ρ=0.899), 3-methoxypropylamine (ρ=0.874), and Epon 825 (ρ=1.155).

As M_c increases the ratio of amines to epoxy increases resulting in a decrease in density assuming ideal mixing.

The thermal expansion coefficients are also reported in Table 2.1. The thermal expansion coefficients of the networks in the rubbery state are greater than the expansion coefficients in the glassy state. There appears to be no trend between the expansion coefficients and M_c. This behavior is in partial agreement with reports by Vakil and Martin[4], who indicate the rubbery expansion coefficient increases slightly with M_c while the glassy expansion coefficient is unaffected by M_c.

Table 2.1: Effect of M_c on density and thermal expansion coefficients for networks constructed with Epon 825, ethylenediamine, and 3-methoxypropylamine.

M_c (kg/mol)	f_c	ρ_o (g/cm^3)	α_g (10^{-4} K^{-1})	α_r (10^{-4} K^{-1})
0.38	4	1.18	1.3	5.2
0.49	4	1.17	1.9	6.1
0.67	4	1.17	1.9	4.3
1.04	4	1.16	1.7	5.5
2.14	4	1.16	2.3	6.0

2.6 Rubbery Modulus Behavior

2.6.1 Measurement Techniques

Epoxy cylinders, from the test tube molds, were cut with a diamond saw to form 23 mm long compression samples. Compression tests were performed above the network's maximum T_g, determined by DSC, at a crosshead speed of 0.5 mm/min with a Model 1123 Instron. Each network was compressed to 75% of its original length and decompressed.

2.6.2 Rubber Elasticity Theory

Static compression tests performed on the networks above T_{gx} allow for an interpretation of the network structure. In all static compression tests, little to no mechanical hysterisis occurred between compressing and decompressing the samples allowing application of rubber elasticity theory. The theory of rubber elasticity provides the following relationship for an elastomeric network in uniaxial compression.

$$\frac{\sigma_c}{-(\lambda - 1/\lambda^2)} = G_r \propto g\frac{\rho RT}{M_c} \qquad (2.6)$$

where: G_r rubbery modulus
σ_c nominal compressive stress
R gas constant
T temperature
ρ polymer density
λ compressive ratio
g factor which depends on cross-link mobility.[6]

Exact numerical agreement with rubber elasticity theory is not expected in epoxy networks due to non-Gaussian chain behavior, steric interactions at cross-links, network imperfections, trapped or physical entanglements, network compressibility, and internal energy contributions to the deformation.[20-23] Despite all these imperfections, hence the proportionality symbol, equation 2.6 still predicts the trends in the rubbery modulus behavior of cross-linked epoxies above the glass transition. For instance, Figure 2.6 is a plot of σ_c versus $-(\lambda-1/\lambda^2)$ at three different temperatures (T_{gx}+20K, +35 K, +50 K) for a network constructed with Epon 825, ethylenediamine, and 3-methoxypropylamine (M_c=0.49 kg/mol). In accordance with equation 2.6, at a given level of deformation the compressive stress increases with an increase in temperature.

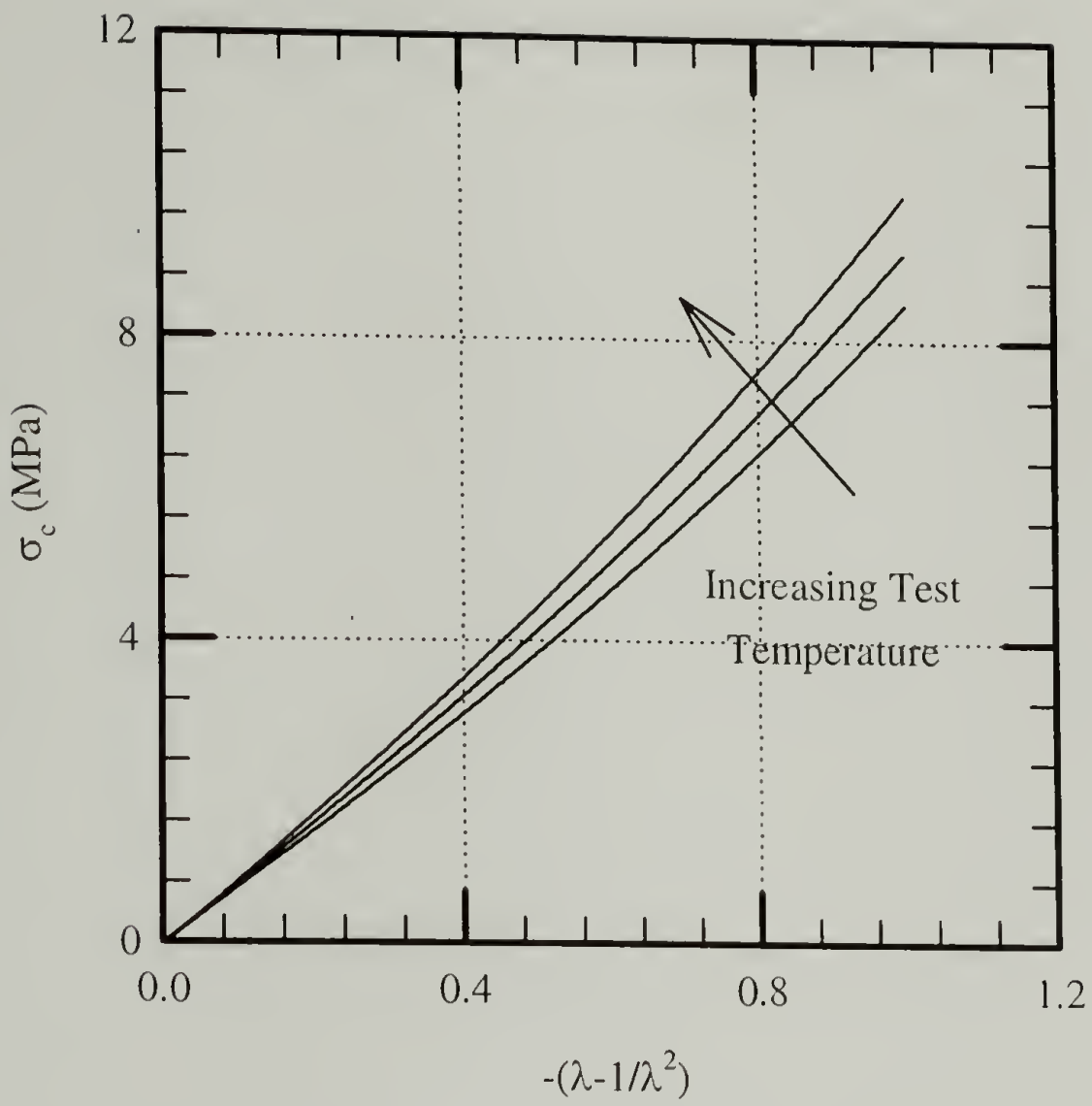

Figure 2.6: Compressive stress versus rubber elasticity strain at T_{gx}+20 K, +35 K, +50 K for network constructed with Epon 825, ethylenediamine, and 3-methoxypropylamine (M_c=0.49 kg/mol).

2.6.3 Effect of Molecular Weight Between Cross-links

Data analogous to the data displayed in Figure 2.6 was obtained for networks with different molecular weights between cross-links constructed with Epon 825, ethylenediamine, and 3-methoxypropylamine. The lower cross-linked materials display linearity of the rubbery moduli responses over the range of deformation interrogated. Non-linearity in the higher cross-linked materials, with shorter network chains, arises from non-Gaussian chain behavior and steric interactions at cross-links. The rubbery moduli (G_r) of these networks were determined at various test temperatures and are

presented in Table 2.2. By rearranging equation 2.6 and dropping g since cross-link functionality is constant in these networks (f_c=4) results in equation 2.7.

$$\frac{G_r}{\rho T} \propto \frac{1}{M_c} \qquad (2.7)$$

The density was estimated with the measured density at room temperature and the thermal expansion coefficients. Figure 2.7 is a plot of the left hand side of equation 2.7 versus $1/M_c$ calculated from reaction stoichiometry. Equation 2.7 predicts the trends of the response. As M_c decreases the rubbery modulus increases. Although these tests cannot provide exact numerical agreement with the theories due to reasons previously stated, measuring the sensitive response of an epoxy network in the rubbery state is useful from the viewpoint of structure-property relationships.

Table 2.2: Rubber modulus values at different temperatures for networks formed with Epon 825, ethylenediamine, and 3-methoxypropylamine.

M_c (kg/mol)	f_c	T_{gx} (K) DSC	G_r (MPa) @T_{gx}+ 20 K	G_r (MPa) @T_{gx}+ 35 K	G_r (MPa) @T_{gx}+ 50 K
0.38	4	418	19.40	20.67	21.57
0.49	4	386	8.46	9.15	9.89
0.67	4	363	5.45	6.03	6.07
1.04	4	345	3.52	3.65	3.88
2.14	4	335	2.32	2.42	2.53

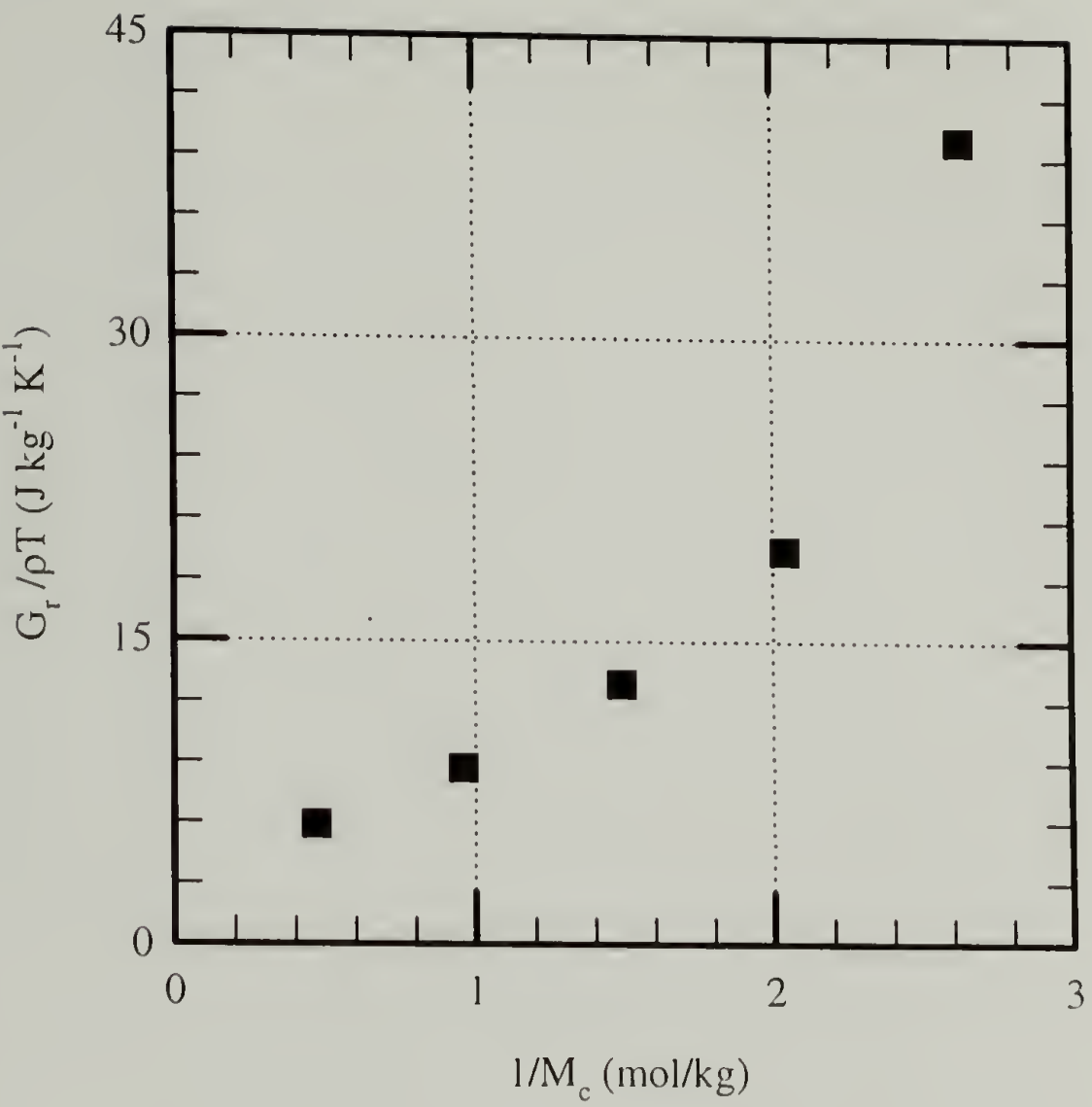

Figure 2.7: Measured rubbery modulus normalized by test temperature and density versus $1/M_c$ for networks constructed with Epon 825, ethylenediamine, and 3-methoxypropylamine.

2.6.4 Effect of Cross-link Functionality

The effect of cross-link functionality on the rubbery modulus is addressed through the front factor (g) in equation 2.6. For mobile cross-links, $g=(f_c-2)/f_c$, while immobile cross-links are represented by $g=1$.[2,5,7] The effect of cross-link functionality is investigated with Epon 825 cross-linked with the aliphatic amine curing system and the aromatic amine curing system. Each network was tested 20 K above its' respective T_{gx}. Figures 2.8 and 2.9 are plots of σ_c/T versus $-(\lambda-1/\lambda^2)$ for the aliphatic tetrafunctional cross-linked networks and the aliphatic trifunctional cross-linked networks, respectively. Figures 2.10 and 2.11 are plots of σ_c/T versus $-(\lambda-1/\lambda^2)$ for the aromatic tetrafunctional

cross-linked networks and the aromatic trifunctional cross-linked networks, respectively. For a given compression ratio, the compressive stress increases with a decrease in M_c as described in the previous section. Non-linearity between the compressive stress and rubber elasticity strain is evident in the higher cross-linked materials over the range of deformation.

It is apparent from Figures 2.8-2.11 that cross-link functionality affects the rubbery modulus. This effect is even made more apparent with networks in which the average cross-link functionality is altered while maintaining a constant M_c. Figure 2.12 is a plot of σ_c/T versus $-(\lambda-1/\lambda^2)$ for the aromatic networks in which f_c was varied at constant M_c. Linear regressions were performed on all curves shown in Figures 2.8-2.12 to obtain values for the temperature normalized rubbery modulus.

Figure 2.13 presents the temperature normalized rubbery moduli data of the aliphatic networks with g=1, while Figure 2.14 presents the same data with $g=(f_c-2)/f_c$. Because the densities of the materials are similar in the rubbery state, the collapse of the data in Figure 2.14 suggests cross-link mobility. Cross-link mobility represents the ability of the chains to feel each other through the cross-link sites. Figure 2.15 presents the temperature normalized rubbery moduli data of the aromatic networks with g=1, while Figure 2.16 presents the same data with $g=(f_c-2)/f_c$. Because the density of the materials are similar in the rubbery state, the collapse of the data in Figure 2.16 suggests the ability of the chains to feel each other through the cross-link sites. Banks and Ellis[3] have also suggested cross-link mobility in epoxy resins from broad line proton NMR studies.

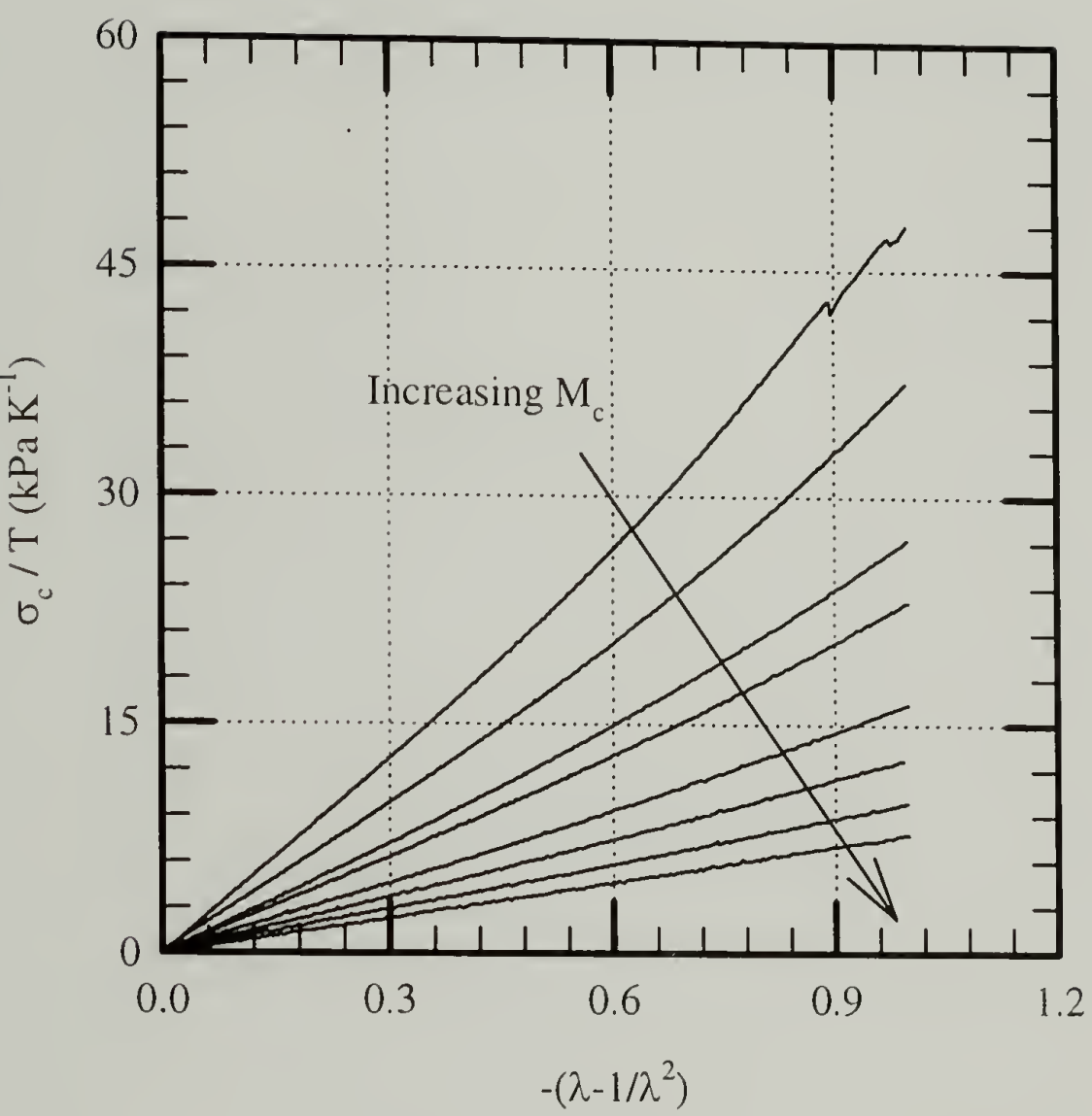

Figure 2.8: Compressive stress versus rubber elasticity strain at T_{gx}+20 K for tetrafunctional cross-linked networks with different M_c s constructed with Epon 825 and the aliphatic amine curing system.

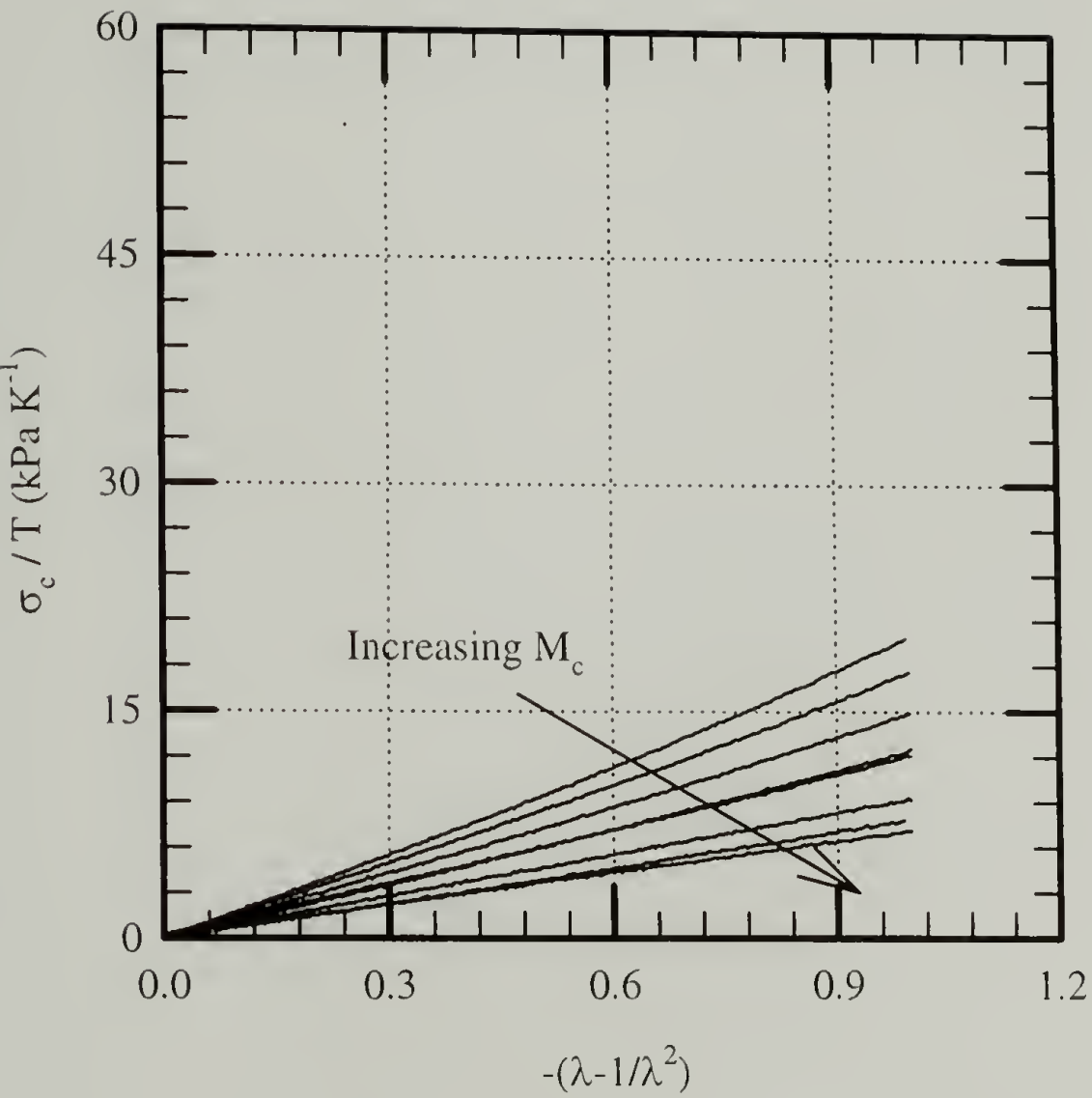

Figure 2.9: Compressive stress versus rubber elasticity strain at T_{gx}+20 K for trifunctional cross-linked networks with different M_c s constructed with Epon 825 and the aliphatic amine curing system.

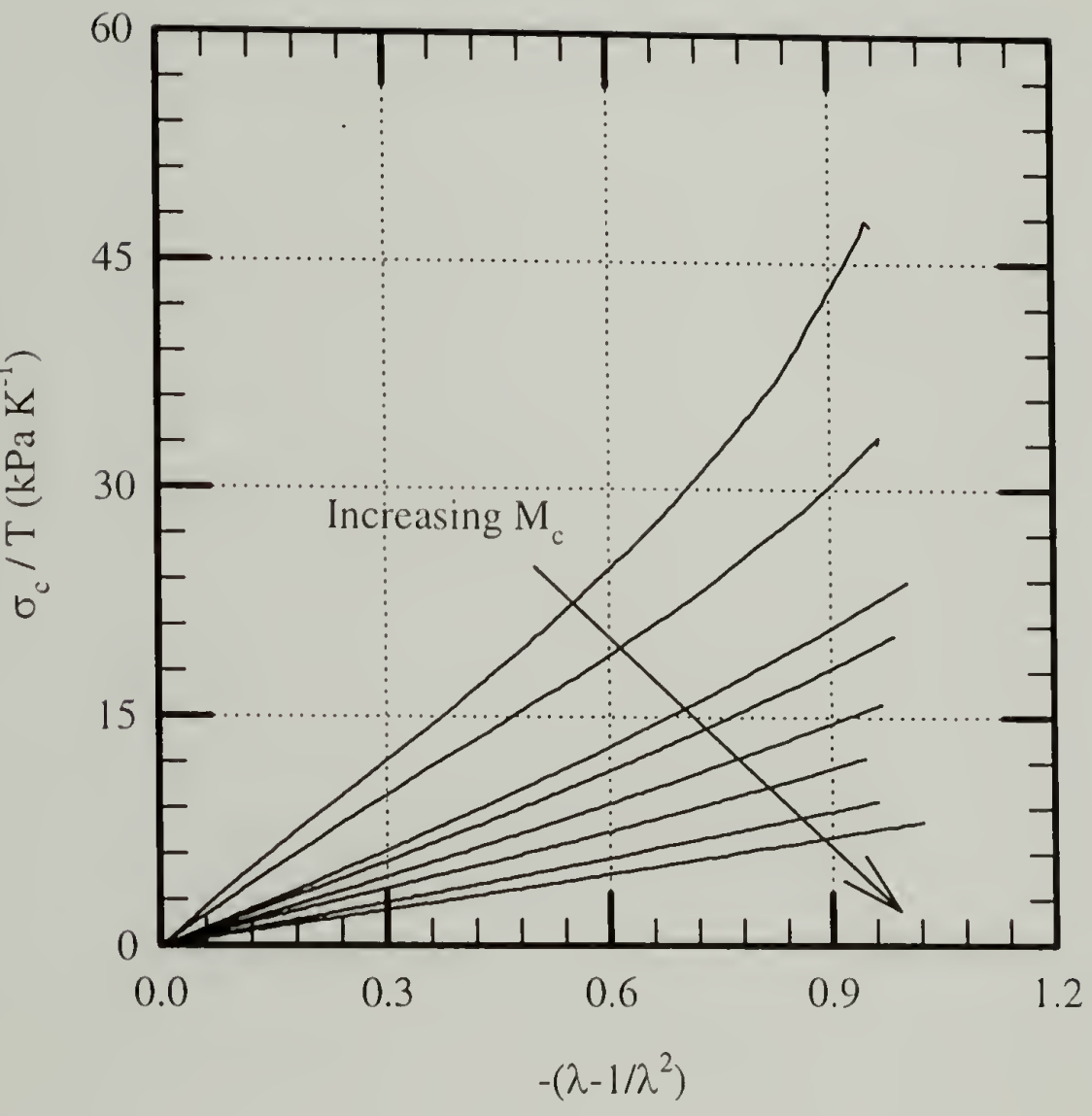

Figure 2.10: Compressive stress versus rubber elasticity strain at T_{gx}+20 K for tetrafunctional cross-linked networks with different M_c s constructed with Epon 825 and the aromatic amine curing system.

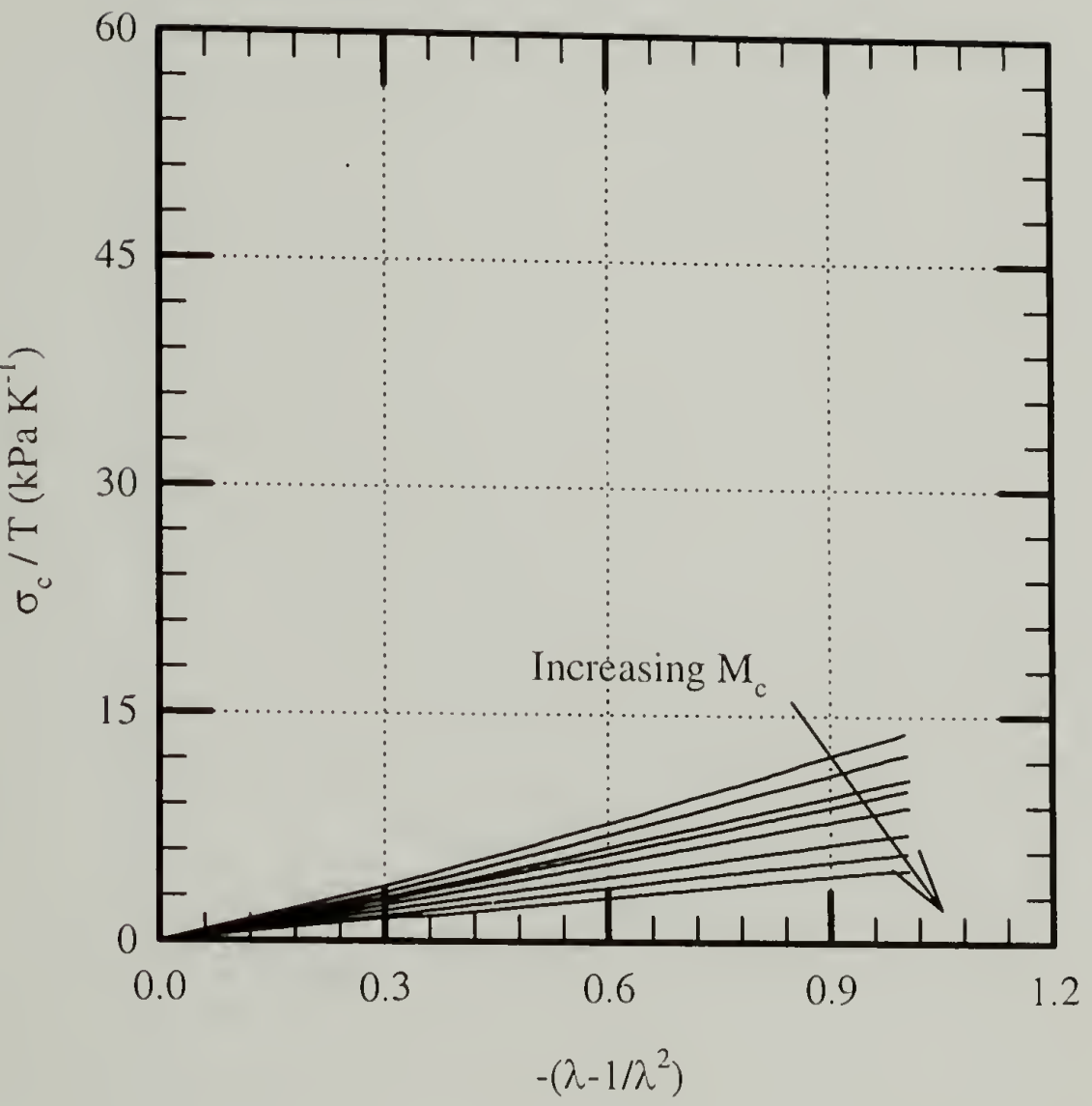

Figure 2.11: Compressive stress versus rubber elasticity strain at T_{gx}+20 K for trifunctional cross-linked networks with different M_c s constructed with Epon 825 and the aromatic amine curing system.

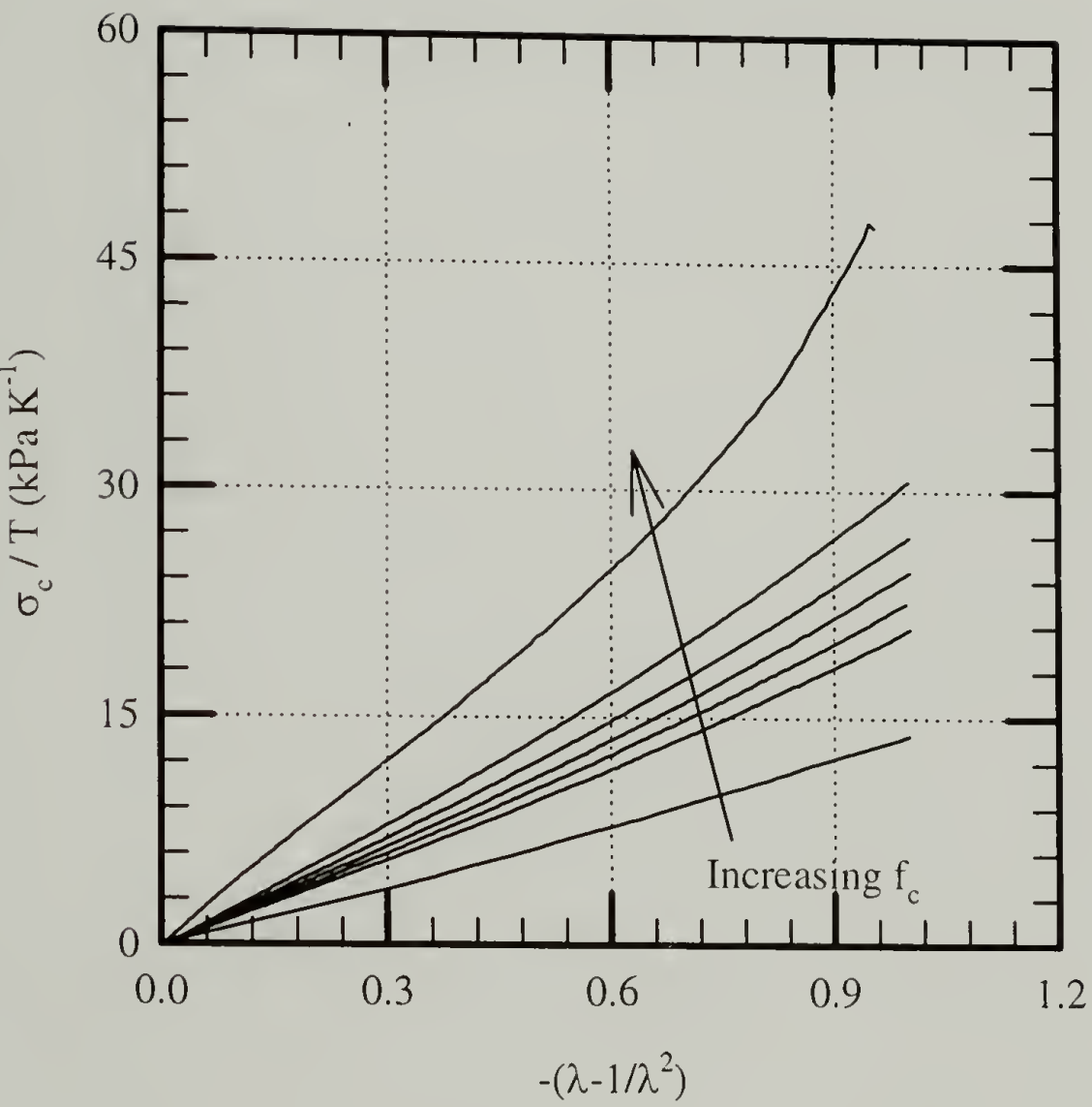

Figure 2.12: Compressive stress versus rubber elasticity strain at T_{gx}+20 K for trifunctional/tetrafunctional cross-linked networks with different f_c s and constant M_c constructed with Epon 825 and the aromatic amine curing system.

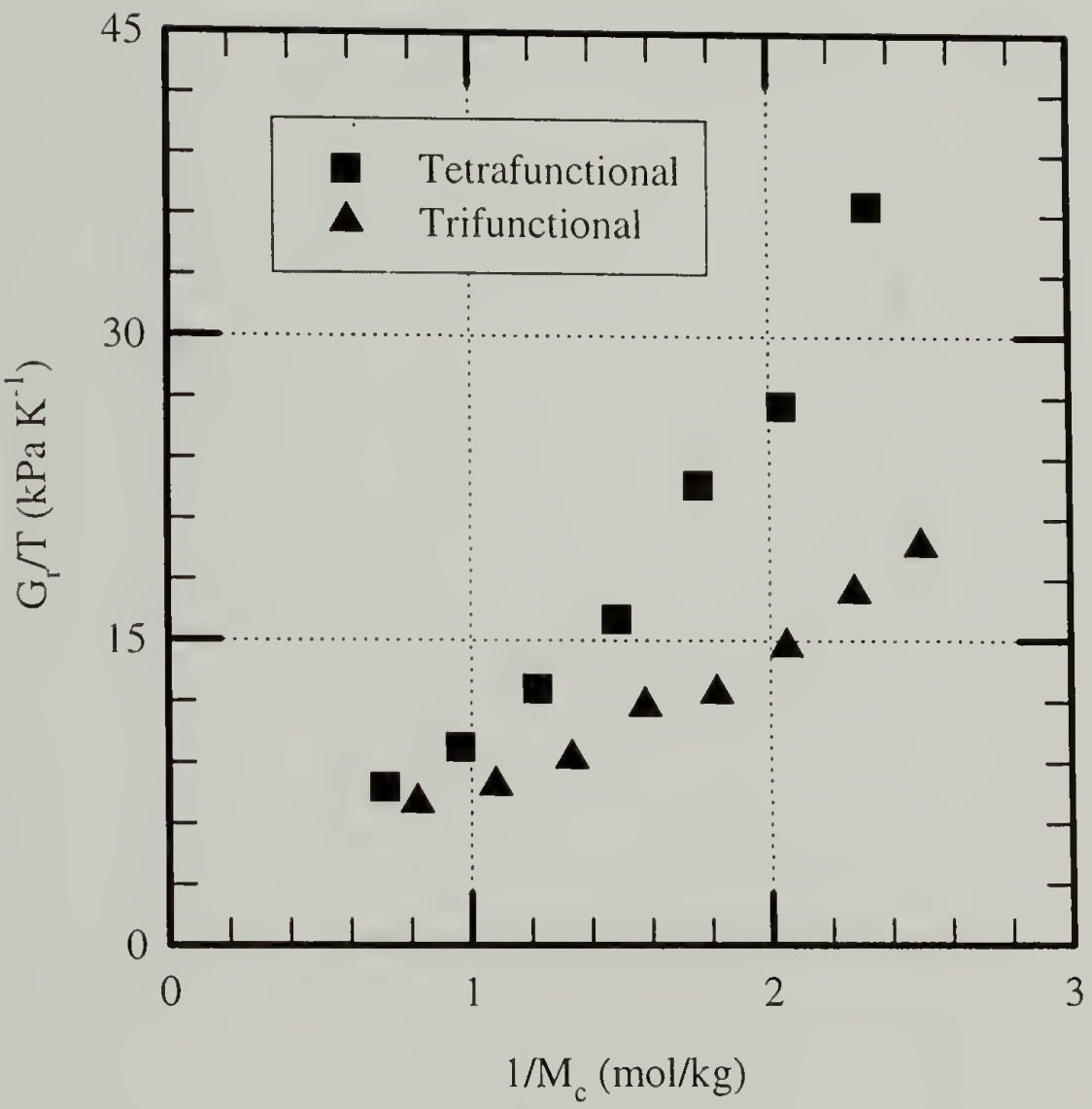

Figure 2.13: Temperature normalized rubbery modulus versus $1/M_c$ for networks constructed with Epon 825 and the aliphatic amine curing system.

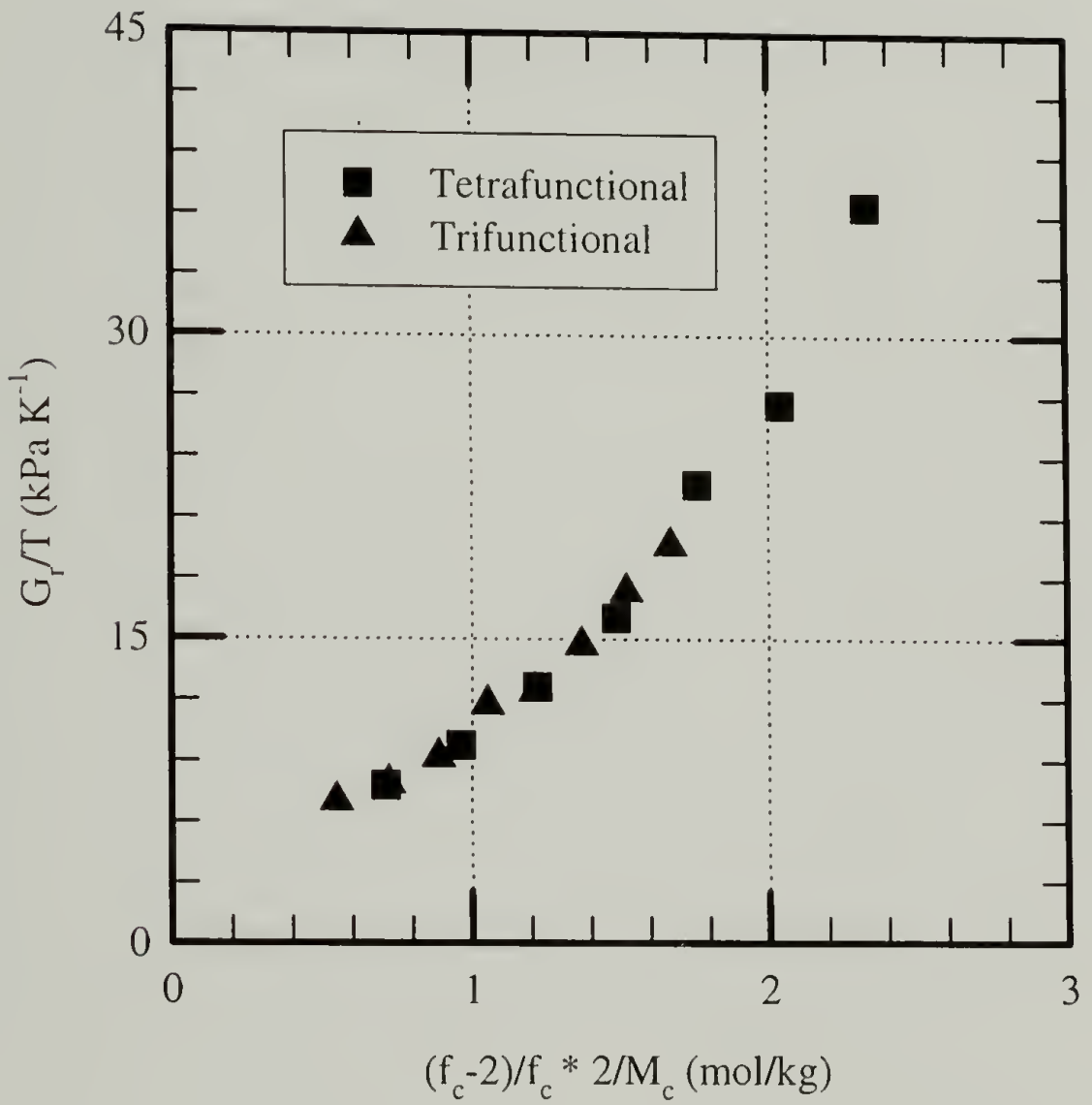

Figure 2.14: Temperature normalized rubbery modulus versus $(f_c-2)/f_c*2/M_c$ for networks constructed with Epon 825 and the aliphatic amine curing system.

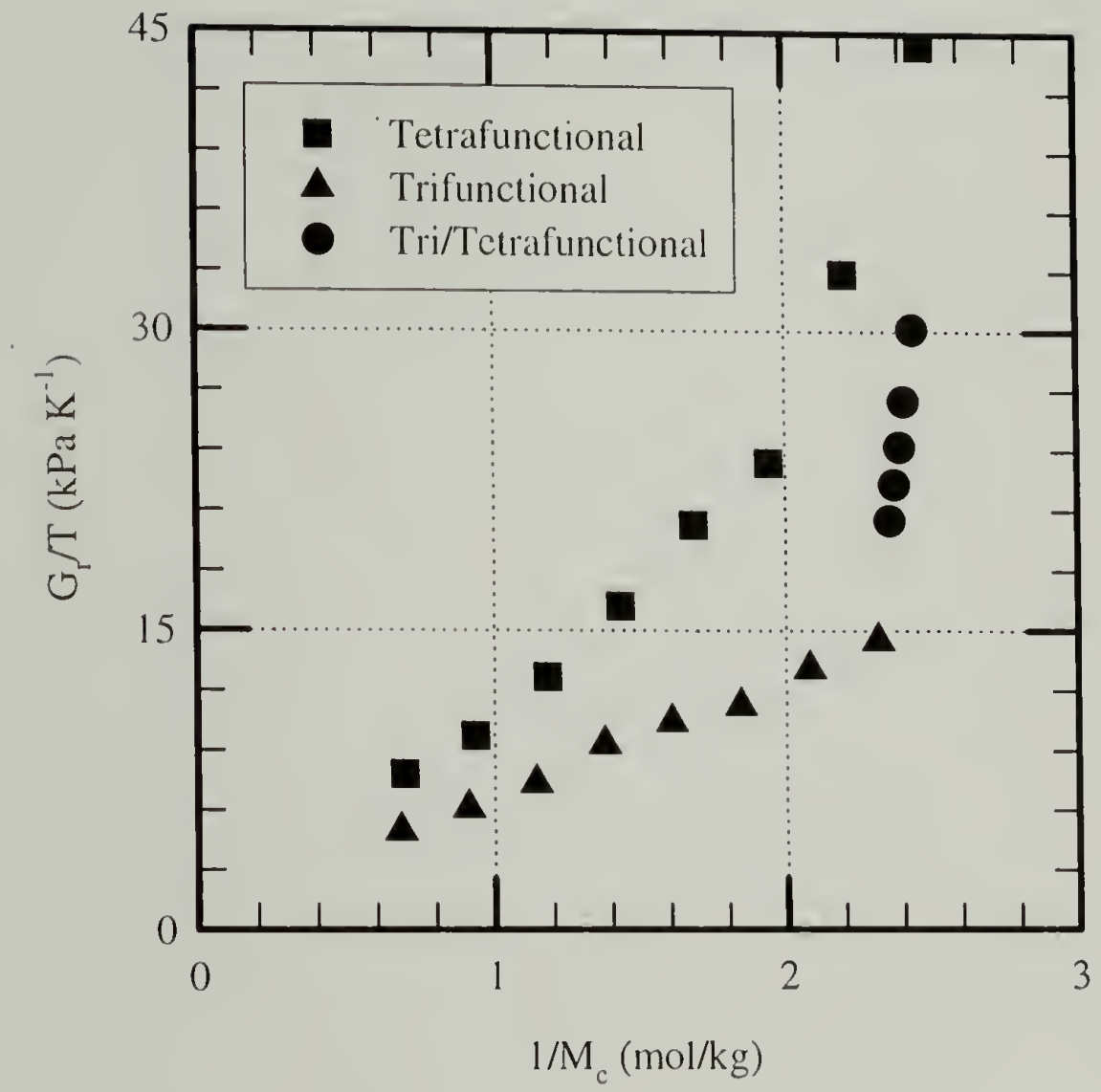

Figure 2.15: Temperature normalized rubbery modulus versus $1/M_c$ for networks constructed with Epon 825 and the aromatic amine curing system.

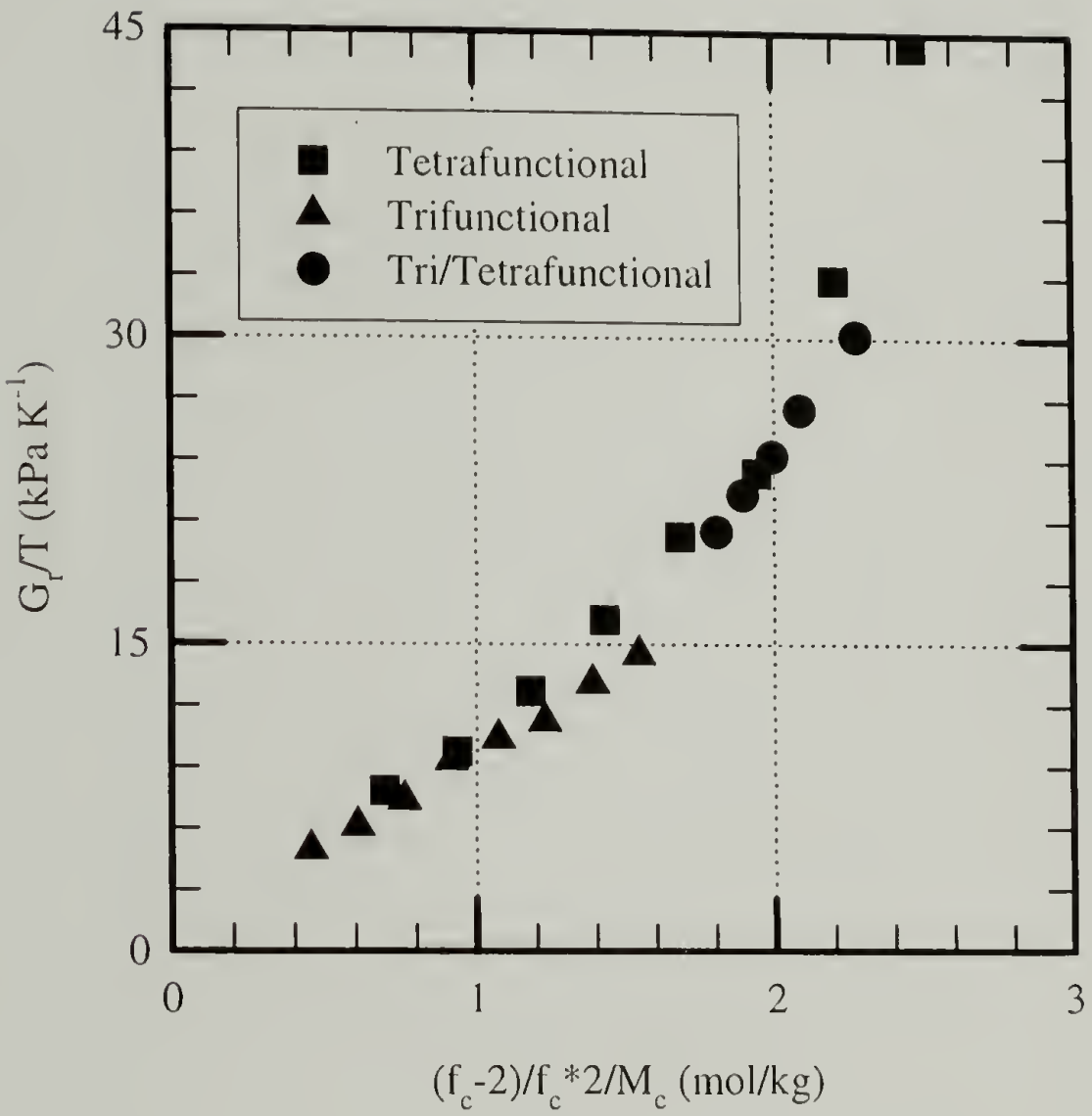

Figure 2.16: Temperature normalized rubbery modulus versus $(f_c-2)/f_c*2/M_c$ for networks constructed with Epon 825 and the aromatic amine curing system.

2.6.5 Effeet of Chain Stiffness

In Figure 2.17, the values of G_r for the aliphatie and aromatie networks versus $(f_c\text{-}2)/f_c*2/M_c$ are plotted. Figure 2.17 shows that chemieal nature of the curing agent system has little effeet on the rubbery moduli of the networks. This finding is eonsistent with rubber elastieity theory, which does not address the ehemieal nature of an elastomer except through f_c and M_c.

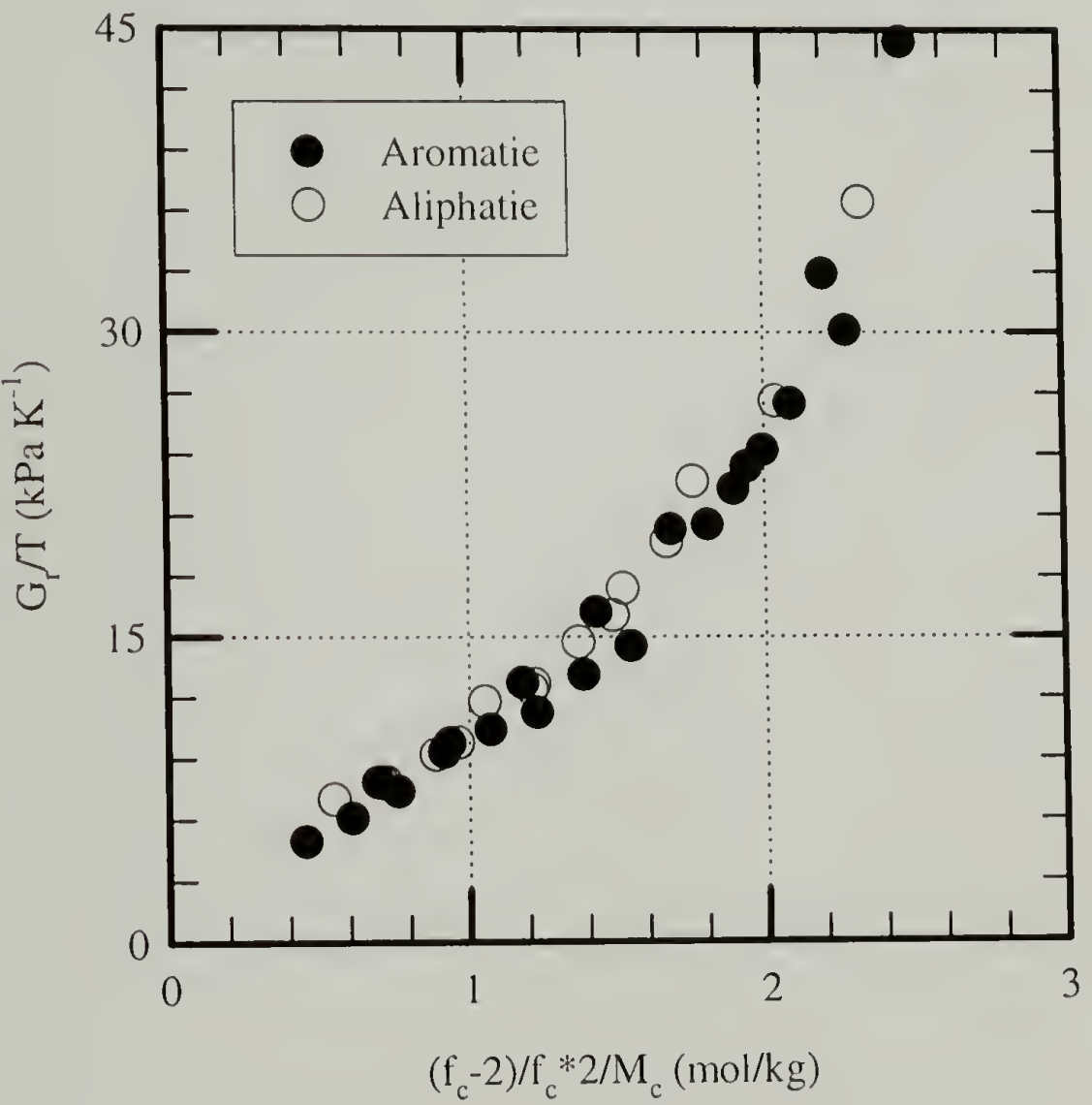

Figure 2.17: Effect of chain stiffness, curing agent system, on the rubbery modulus behavior of networks.

2.7 Glass Transition Temperature of Networks

2.7.1 Measurement Techniques

2.7.1.1 Differential Scanning Calorimetry (DSC)

Samples (5-10 mg) were taken from the plaques and analyzed by a DuPont Thermal Analyzer 2000. The glass transition temperature of each synthesized network was measured at a heating rate of 10 °C/min using the inflection point as the T_{gx} of the network.

2.7.1.2 Dynamic Mechanical Thermal Analysis (DMTA)

Rectangular bars, machined from 1.59 mm thick plaques using a specially designed router, were analyzed by a Polymer Laboratories' MK1 DMTA in the single cantilever beam mode at 1 hz and a heating rate of 2 °C/min. The temperature was scanned from -100 °C to 20 °C past the glass transition temperature of each network. The glass transition temperature was taken as the α peak in the tan δ response.

2.7.1.3 Thermal Expansion Measurements (PVT)

The changes in specific volume of the materials with temperature were made with a Gnomix PVT apparatus at a heating rate of 2 °C/min and a pressure of 10 MPa. The glass transition temperature was taken as the intersection of tangent linear regression fits of the glassy volumetric expansion and the rubbery volumetric expansion.

2.7.2 Effect of Molecular Weight Between Cross-links

The maximum glass transition temperatures (T_{gx}), obtained by 3 different measurement techniques, for networks constructed with Epon 825, ethylenediamine, and 3-methoxypropylamine are reported in Table 2.3. Differences between the glass

transition temperatures for a given network, measured by the three analytical methods, are the result of differences in the definitions of the glass transition temperature and measurement methods. In Figure 2.18, the glass transition temperatures of these networks determined by DSC are plotted against $1/M_c$. Fox and Loshaek[24] were the first to describe the linear behavior between T_{gx} and $1/M_c$. More recently, Banks and Ellis[3] proposed a linear relationship based on the addition and redistribution of network free volume. In this model, T_{gx} is described by equation 2.8.

$$T_{gx} = T_{g\infty} + \frac{\zeta}{M_c} \qquad (2.8)$$

where: $T_{g\infty}$ glass transition temperature of the linear polymer backbone at infinite molecular weight

ζ free volume constant.

The first term in equation 2.8 represents the effect of chain stiffness and intermolecular forces on T_g, while the second term represents the entropic penalty for the addition of cross-links. Linear regressions of the data, determined by the three analytical methods, are reported in Table 2.3. ζ is in agreement with the often cited value by Nielsen[19] of 39 kg K/mol. Although 3-methoxypropylamine is not an ideal difunctional equivalent to ethylenediamine, the trend described by equation 2.8 is obeyed. This obediance is a result of the entropic penalty for the addition of cross-links exceeding the copolymer effect.

An alternative route to controlling M_c is through the use of higher molecular weight analogs of Epon 825, such as Epon 828. Figure 2.19 shows the glass transition temperatures of networks formed with Epon 825, Epon 828, and the aromatic amine curing system. Higher molecular weight analogs cured with 1,3-phenylenediamine, reported by Vakil and Martin,[4] are also displayed in Figure 2.19.

The similar T_g s and T_g behavior between this study and the study by Vakil and Martin[4] shows the consistency of fabricating epoxy networks by independent researchers. One limitation to the use of these higher molecular weight analogs is their high viscosity.

Table 2.3: Glass transition temperatures, determined by different measurement techniques, for networks constructed with Epon 825, ethylenediamine, and 3-methoxypropylamine.

M_c (kg/mol)	T_{gx}DSC (K)	T_{gx} PVT (K)	T_{gx} DMTA (K)
0.38	418	400	419
0.49	386	368	391
0.67	363	353	370
1.04	345	328	348
2.14	335	316	339
	DSC	PVT	DMTA
$T_{g\infty}$ (K)	311	294	316
ζ (kg K/mol)	39	39	38

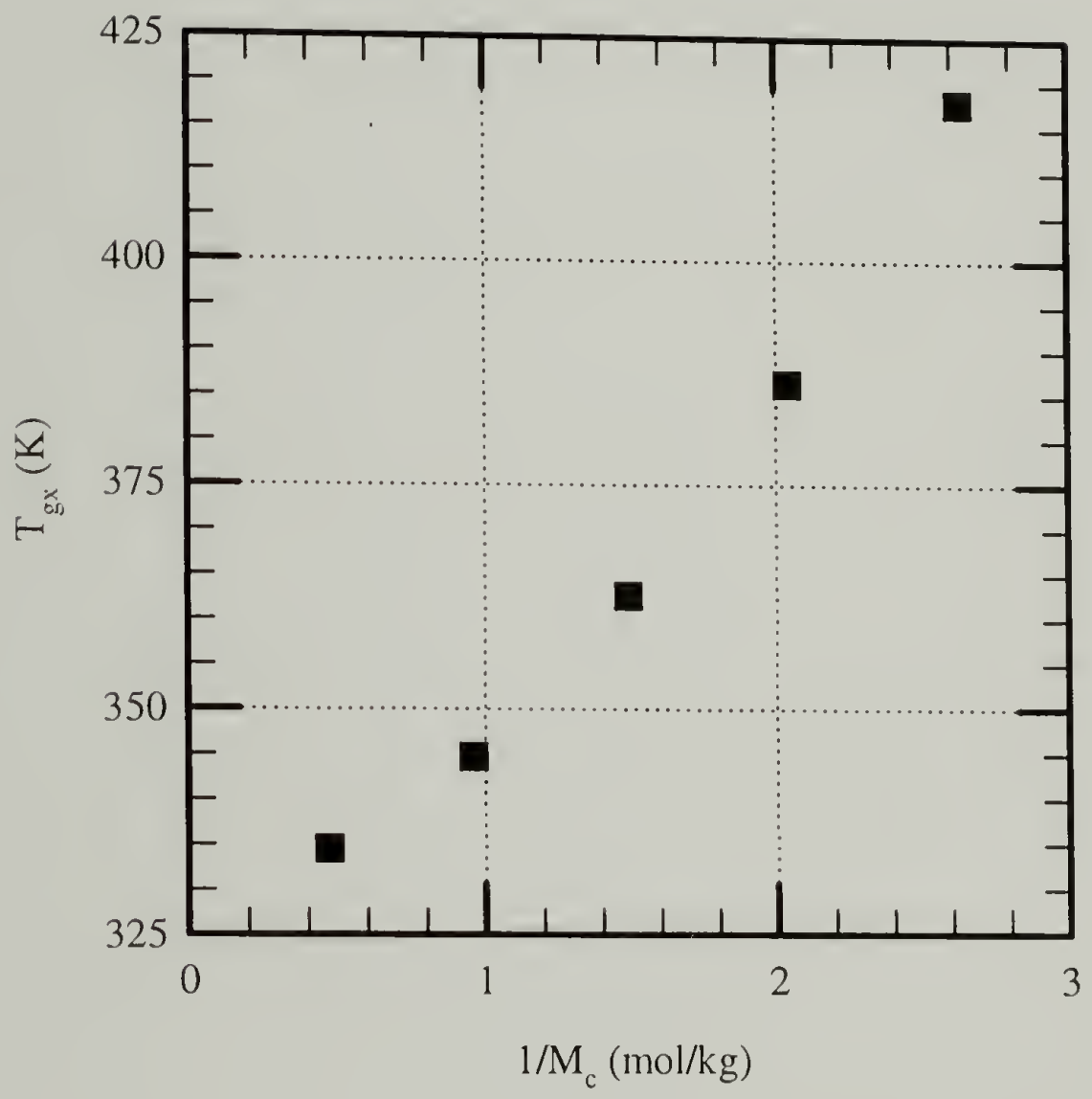

Figure 2.18: Maximum glass transition temperature versus $1/M_c$ for networks constructed with Epon 825, ethylenediamine, and 3-methoxypropylamine.

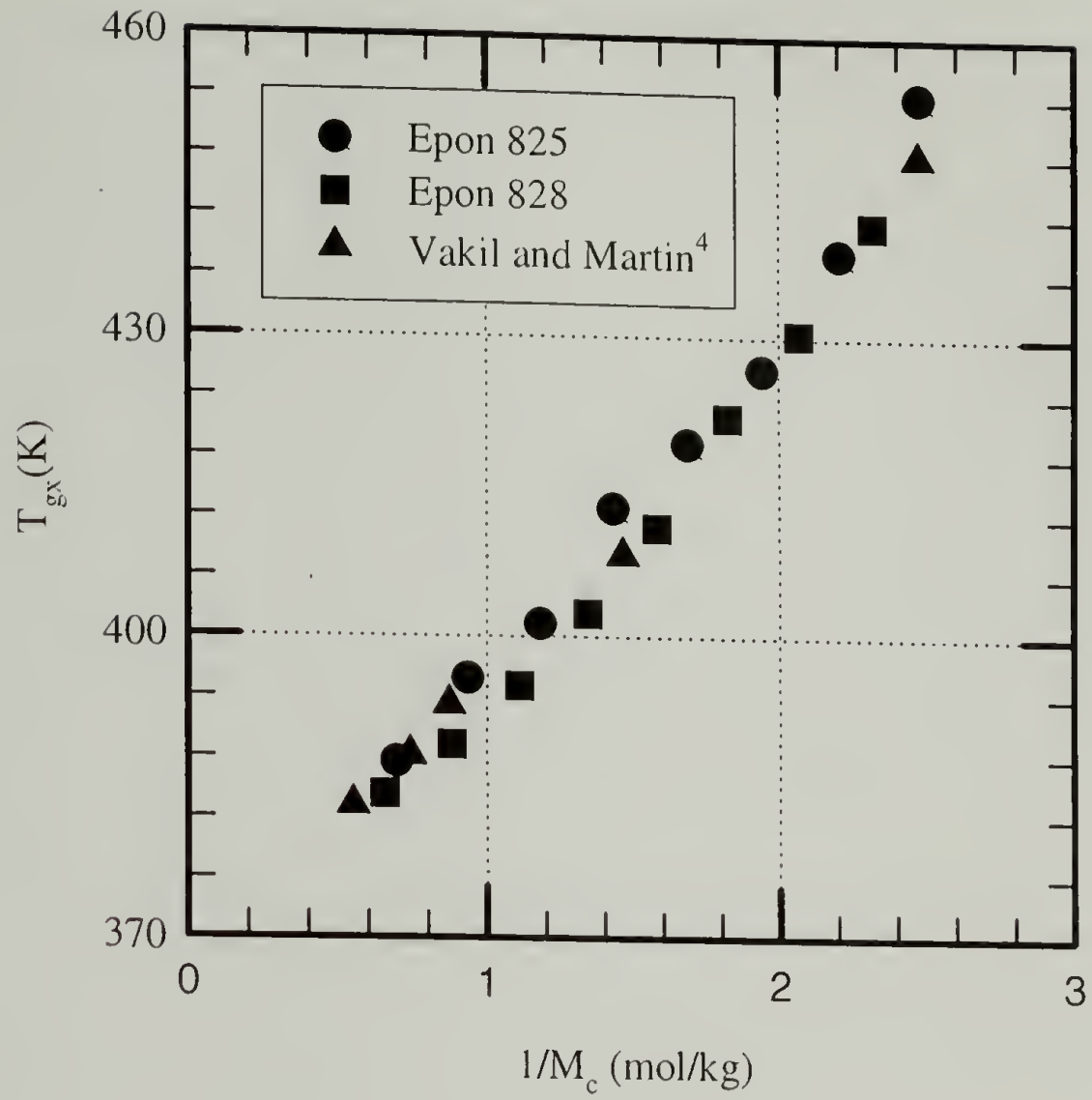

Figure 2.19: Glass transition temperature behavior of networks formed with Epon 825, Epon 828, and the aromatic amine curing system along with other higher molecular weight analogs cured with 1,3-phenylenediamine.

2.7.3 Effect of Cross-link Functionality

In Figure 2.20, T_{gx} is plotted against $1/M_c$ for networks constructed with Epon 825 and the aliphatic amine curing system. Both tetrafunctional and trifunctional cross-linked networks show an increase in T_{gx} as M_c decreases. However, the rate of increase is greater for tetrafunctional cross-linked networks than trifunctional cross-linked networks. Linear regression of the data in Figure 2.20 results in ζ=24 kg K/mol for trifunctional cross-linked networks and ζ=40 kg K/mol for tetrafunctional cross-linked networks. In terms of the free volume theory, tetrafunctional cross-links would have less incremental

free volume than trifunctional cross-links. The value of ζ obtained for the tetrafunctional networks is close to the cited value of 39 kg K/mol. Figure 2.21 shows the T_{gx} of networks constructed with Epon 825 and the aromatic curing agent system. The effect of cross-link functionality is clearly evident by the networks in which f_c is varied while maintaining a constant M_c. Although the network free volume theory is effective in analyzing the data, it contains many parameters that cannot be evaluated experimentally.

DiBenedetto[25] proposed a non-linear model based on the principle of corresponding states. In this theory, T_{gx} is described by equation 2.9.

$$\frac{T_{gx} - T_{g\infty}}{T_{g\infty}} = k \frac{X_m}{1 - X_m} \qquad (2.9)$$

where: k universal constant
X_m molar cross-link density.

The glass transition behavior described by equation 2.9 for the aliphatic networks is shown in Figure 2.22. Linear regression of the data in Figure 2.22 results in k =0.23 for trifunctional cross-linked networks and k=0.57 for tetrafunctional cross-linked networks The k value for the tetrafunctional cross-linked networks seems reasonable when compared with the data of Stutz et al.[26], who report k ranging from 0.636 to 0.925 for a variety of network polymers from cross-linked epoxies to natural rubber. However, the value of k for the trifunctional cross-linked networks falls below this range.

Neither theory seems to have the ability to directly account for the effect of cross-link functionality on T_{gx}. The first attempt to accommodate cross-link functionality was made by Stutz et al..[26] Implicit in this approach is that T_{gx} is affected by cross-link functionality in the same manner as described by the theory of rubber elasticity with

cross-link mobility. However, Stutz et al.[26] could not test their networks in the rubbery regime to validate their model since the networks were only partially reacted. Another limitation to studying partially reacted networks is that a distribution of cross-link functionality has to be assumed. The networks in this study clearly prescribe cross-link functionality.

The experimental evidence suggests factors that control rubber elasticity also control T_{gx}. An empirical modification is supported by the entropic theory of the glass transition, which states T_g is controlled by many of the same factors that control rubber elasticity.[27] Consequently, the two theories describing the effect of M_c on T_{gx} can be modified by the front factor from rubber elasticity to account for cross-link functionality. Using a tetrafunctional cross-linked network as the basis, the theory based on network free volume can be expressed by equation 2.10.

$$T_{gx} = T_{g\infty} + \frac{2(f_c - 2)}{f_c}\frac{\zeta}{M_c} \qquad (2.10)$$

The physical interpretation of ζ in equation 2.10 has been altered from equation 2.08 with the free volume contribution of cross-link functionality now being directly addressed. Figures 2.23 and 2.24 show the result of applying equation 2.10 to the aliphatic and aromatic networks respectively. Linear regression of the data results in ζ = 39 kg K/mol and $T_{g\infty}$ = 311 K for the aliphatic networks and ζ = 34 kg K/mol and $T_{g\infty}$= 360 K for the aromatic networks. In a similar fashion X_m, in the theory based on the principle of corresponding states can be normalized to take into account cross-link functionality (X_{mf}). Again, using a tetrafunctional cross-link as the basis, X_{mf} is expressed by equation 2.11.

$$X_{mf} = \left(\frac{f_c}{2} - 1\right) X_m \qquad (2.11)$$

Figure 2.25 shows the results of using X_{mf} to interpret the data for the aliphatic networks. Linear regression results in k = 0.58 and $T_{g\infty}$ = 328 K. Figures 2.23-2.25 show how the front factor collapses the tetrafunctional and trifunctional cross-linked network data onto a single curve with reasonable values of ζ and k for the two T_g models when compared with the literature.

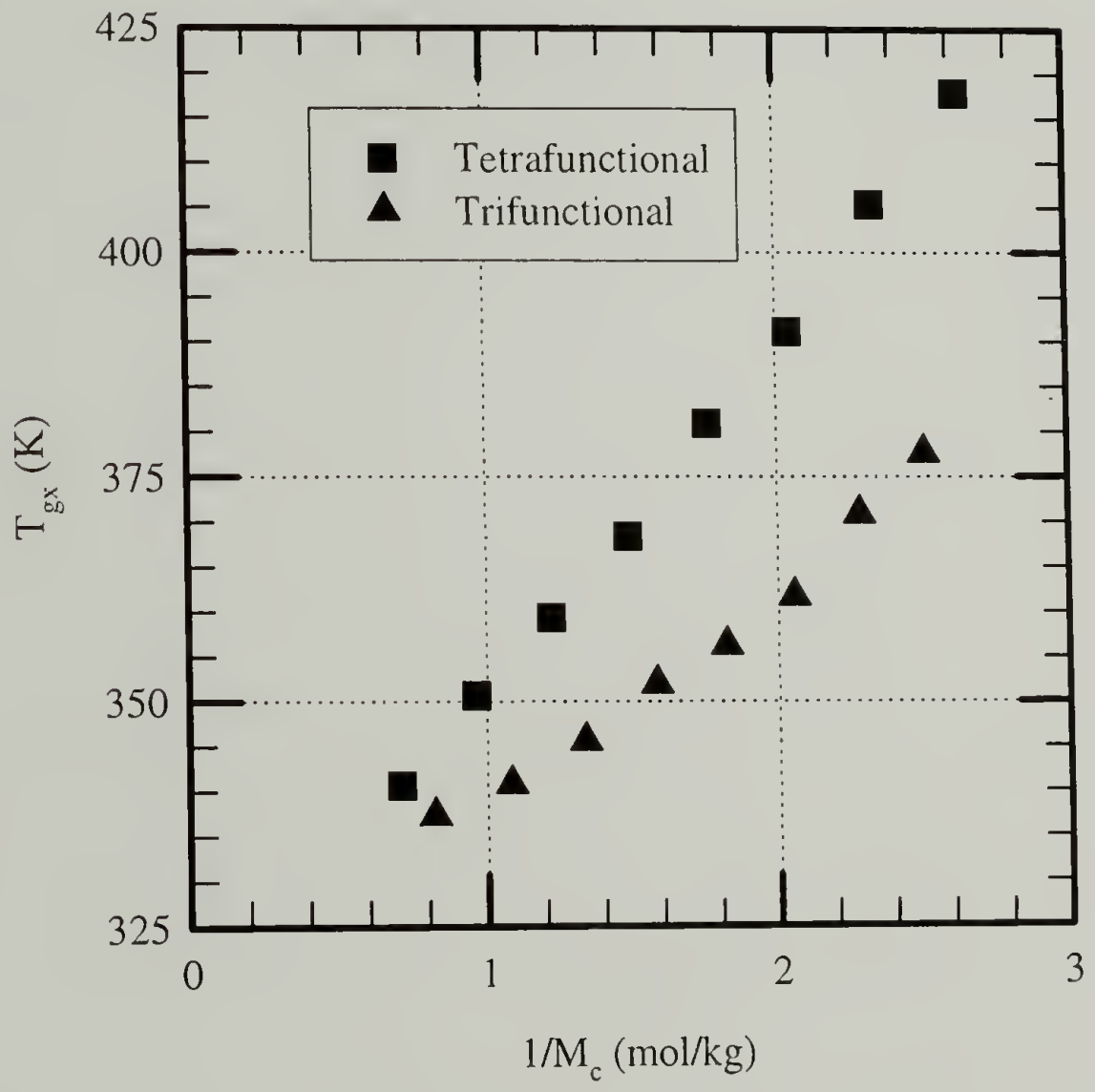

Figure 2.20: Glass transition temperature behavior of networks constructed with Epon 825 and the aliphatic amine curing system analyzed by free volume theory.

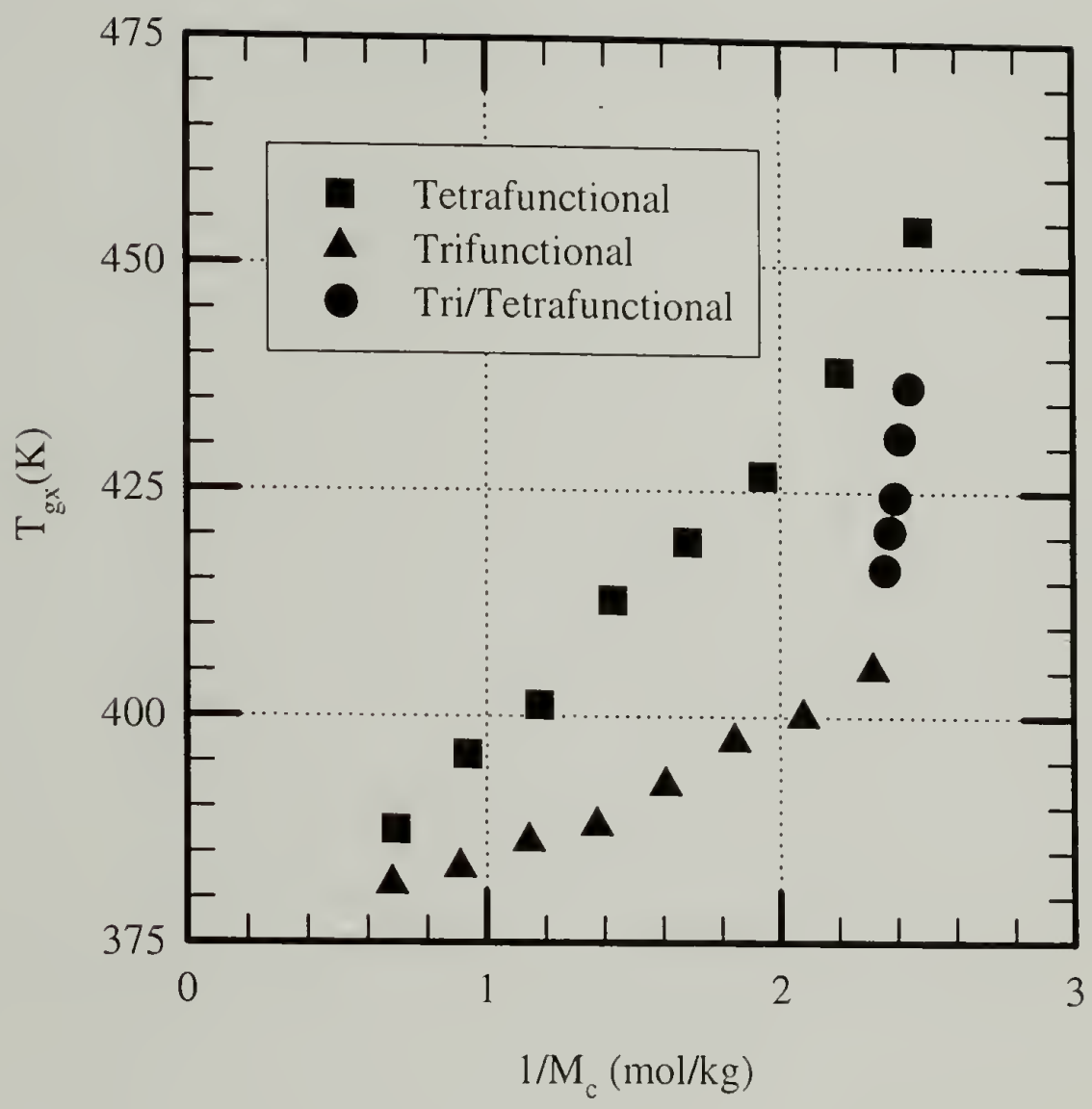

Figure 2.21: Glass transition temperature behavior of networks constructed with Epon 825 and the aromatic amine curing system analyzed by free volume theory.

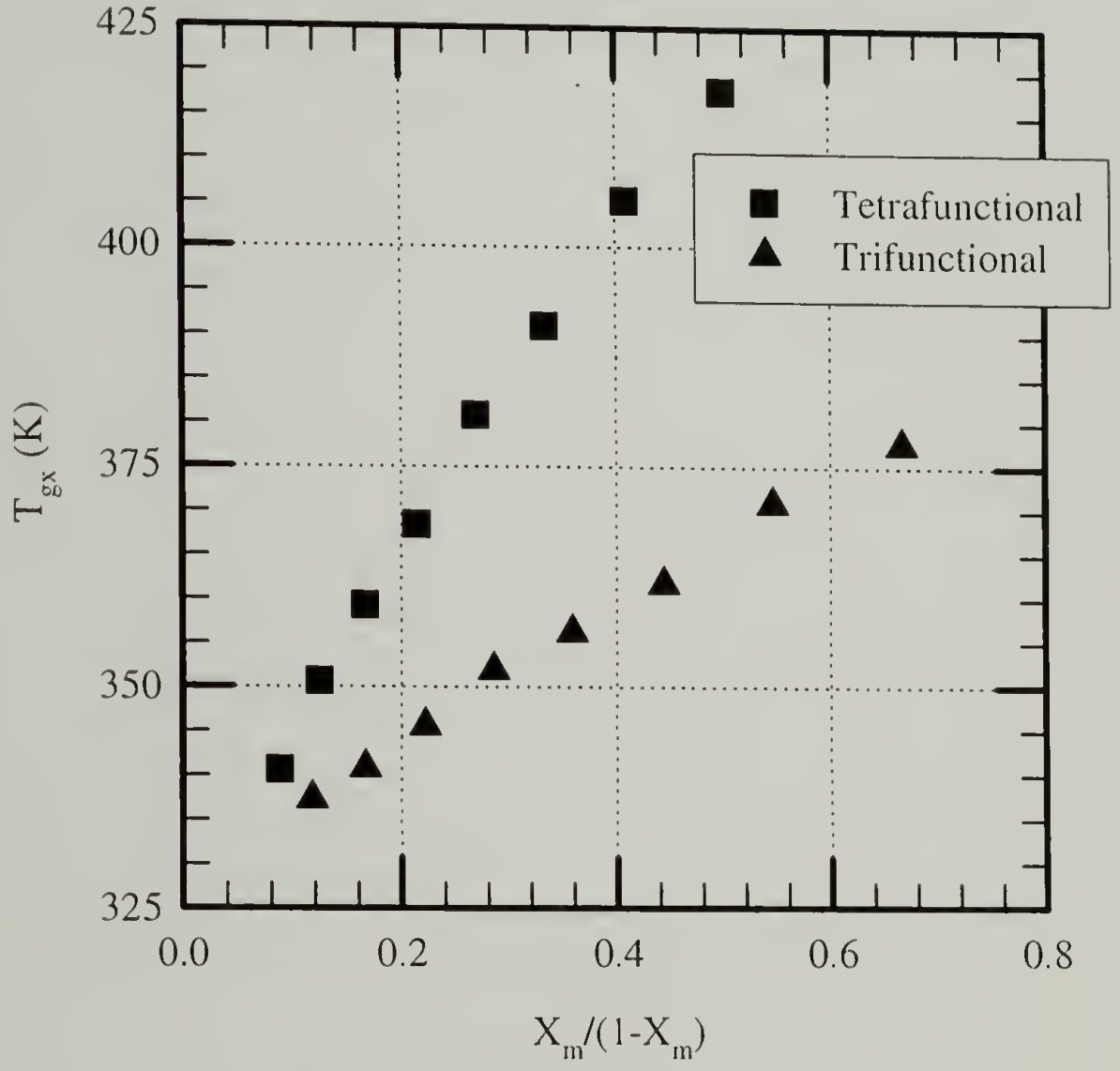

Figure 2.22: Glass transition temperature behavior of networks constructed with Epon 825 and the aliphatic amine curing system analyzed by corresponding state theory.

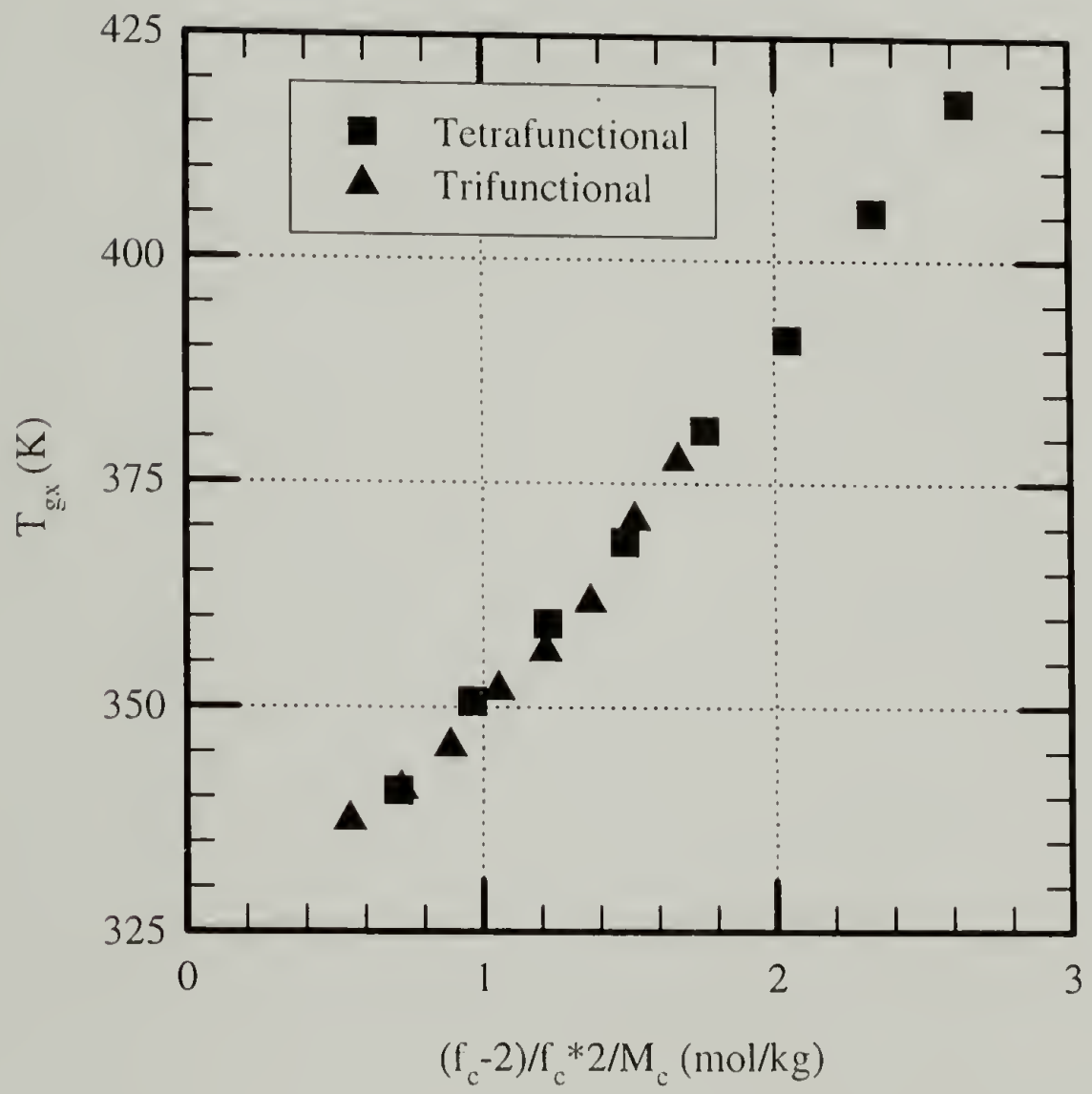

Figure 2.23: Glass transition temperature behavior of networks constructed with Epon 825 and the aliphatic amine curing system analyzed by free volume theory taking into account cross-link functionality by the front factor from rubber elasticity.

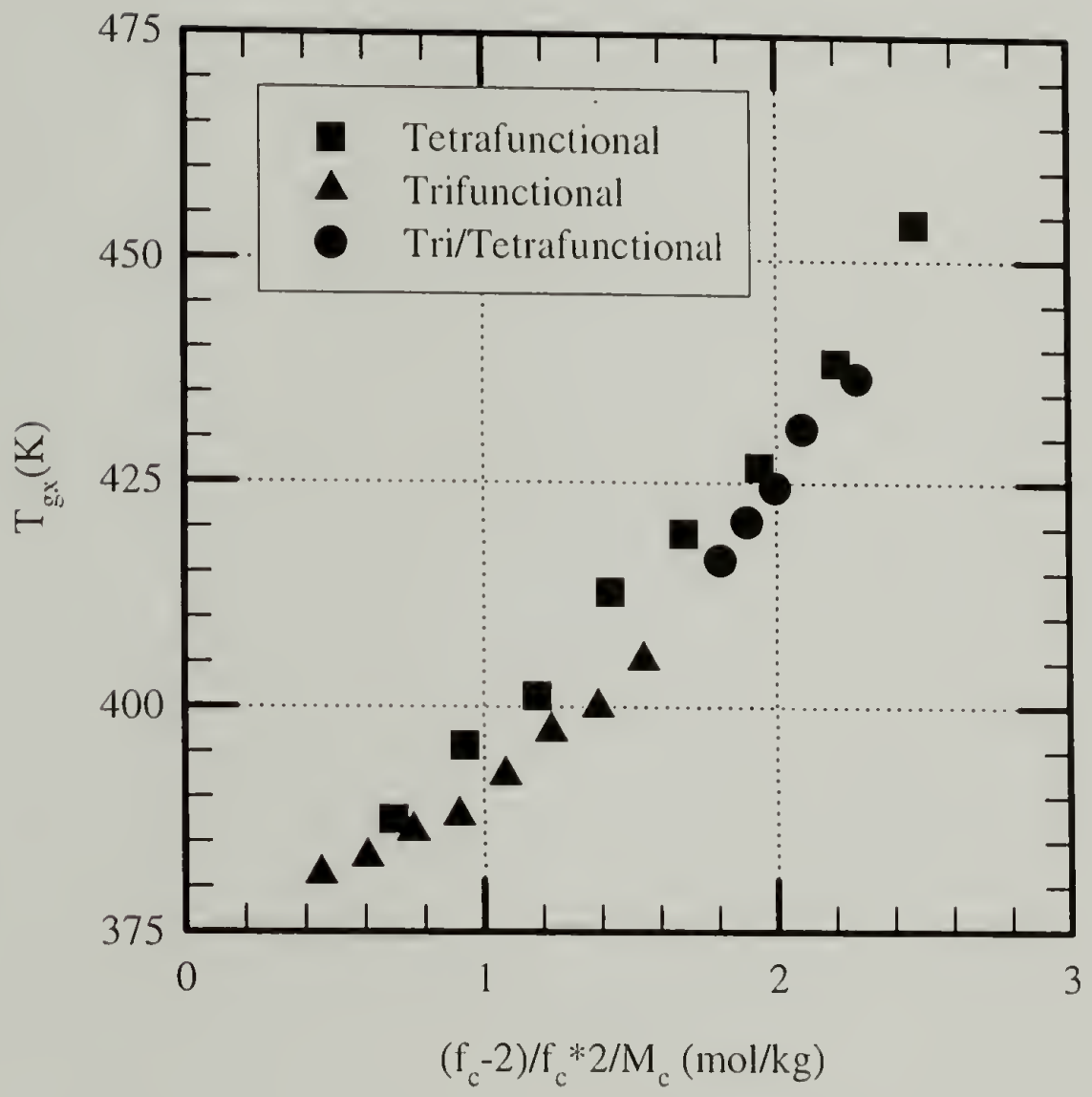

Figure 2.24: Glass transition temperature behavior of networks constructed with Epon 825 and the aromatic amine curing system analyzed by free volume theory taking into account cross-link functionality by the rubber elasticity theory front factor.

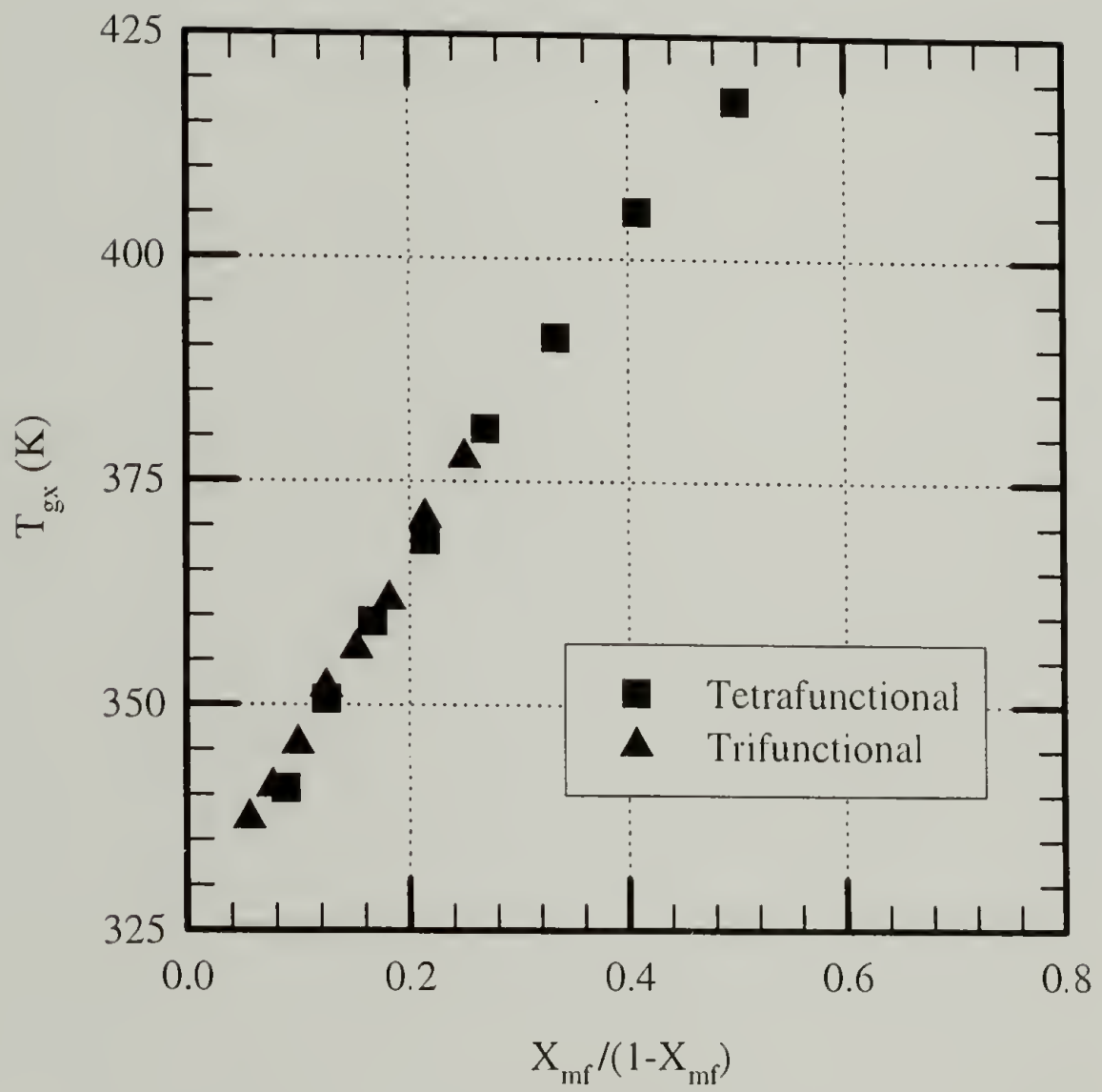

Figure 2.25: Glass transition temperature behavior of networks constructed with Epon 825 and the aliphatic amine curing system analyzed by corresponding state theory taking into account cross-link functionality by the rubber elasticity theory front factor.

2.7.4 Effect of Chain Stiffness

The effect of chain stiffness, which is controlled by curing agent system, is shown in Figure 2.26. As mentioned in the previous paragraph, linear regression analysis results in $\zeta = 34$ kg K/mol and $T_{g\infty} = 360$ K for the aromatic networks and in $\zeta = 39$ kg K/mol and $T_{g\infty} = 311$ K for the aliphatic networks. The curing agent system changes the linear polymer backbone stiffness, hence $T_{g\infty}$. However, the curing agent system has little effect on ζ which represents the entropic penalty for the addition of cross-links.

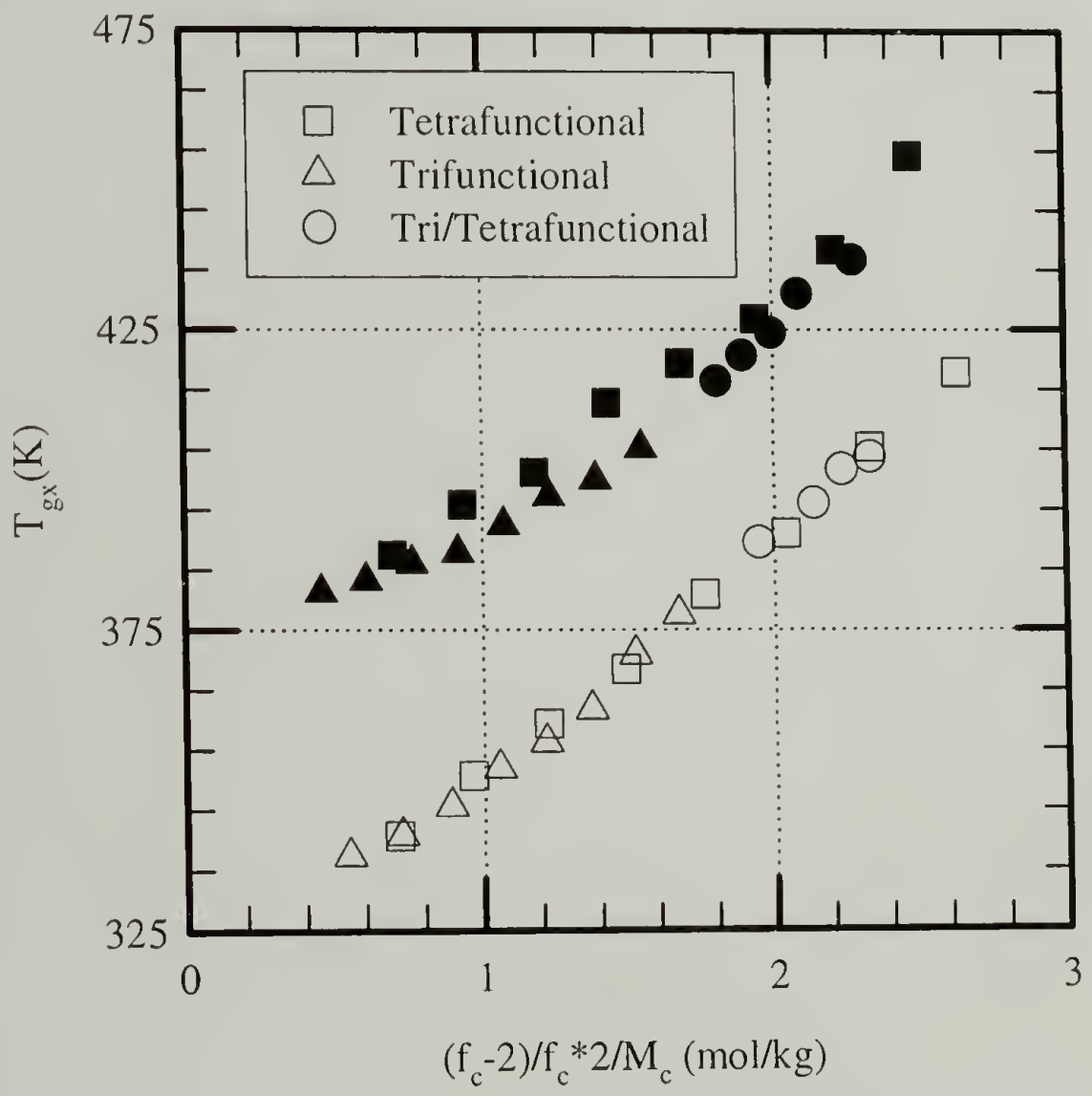

Figure 2.26: The effect of chain stiffness on the glass transition behavior of cross-linked materials (aromatic-solid, aliphatic-hollow).

2.8 Dynamic Mechanical Thermal Analysis

2.8.1 Measurement Techniques

Rectangular bars, machined from 1.59 mm thick plaques using a specially designed router, were analyzed by a Polymer Laboratories' MK1 DMTA in the single cantilever beam mode at 1 hz and a heating rate of 2 °C/min. The temperature was scanned from -100 °C to 20°C past the glass transition temperature for each network.

2.8.2 Effect of Molecular Weight Between Cross-links

Dynamic mechanical thermal analysis of networks constructed with Epon 825, ethylenediamine, and 3-methoxypropylamine are shown in Figure 2.27 and Figure 2.28. Figure 2.27 shows that M_c does not significantly affect the glassy moduli, while M_c affects the glass transition and rubbery moduli. The T_g behavior and rubbery modulus behavior have been discussed previously. Using DMTA to analyze accurately the rubbery modulus is limited due to issues associated with gripping and rate of testing. Figure 2.28 shows that the α relaxation, which is associated with the glass transition, is dependent on M_c. Figure 2.28 and Table 2.4 show the secondary (β) relaxation, which is identified with the localized motions of chain segments or side chains, is slightly affected by M_c. The β relaxation in epoxy resins has been reported to be a result of two motions, one associated with the diphenylenepropane group[28,29], and the other associated with hydroxy ether group.[30,31] Shi et al.[32] showed that the low temperature side of the β relaxation arises from the diphenylenepropane group, while the high temperature side of the β relaxation arises from motion of the hydroxy ether groups. As M_c increases the concentration of hydroxy ether groups decreases and the beta relaxation temperature

decreases for the networks in this study. This trend is consistent with reacting epoxy-amine systems. As curing reactions proceed in epoxy-amine systems, the concentration of hydroxy ether groups increases and T_β increases.[29,33] In addition, the local environment of the hydroxy ether groups changes in networks constructed with Epon 825, ethylenediamine, and 3-methoxypropylamine. As M_c increases in these networks, more 3-methoxypropylamine is used, leading to the possibility of interactions between the hydroxy ether group and the ether linkage in 3-methoxypropylamine.

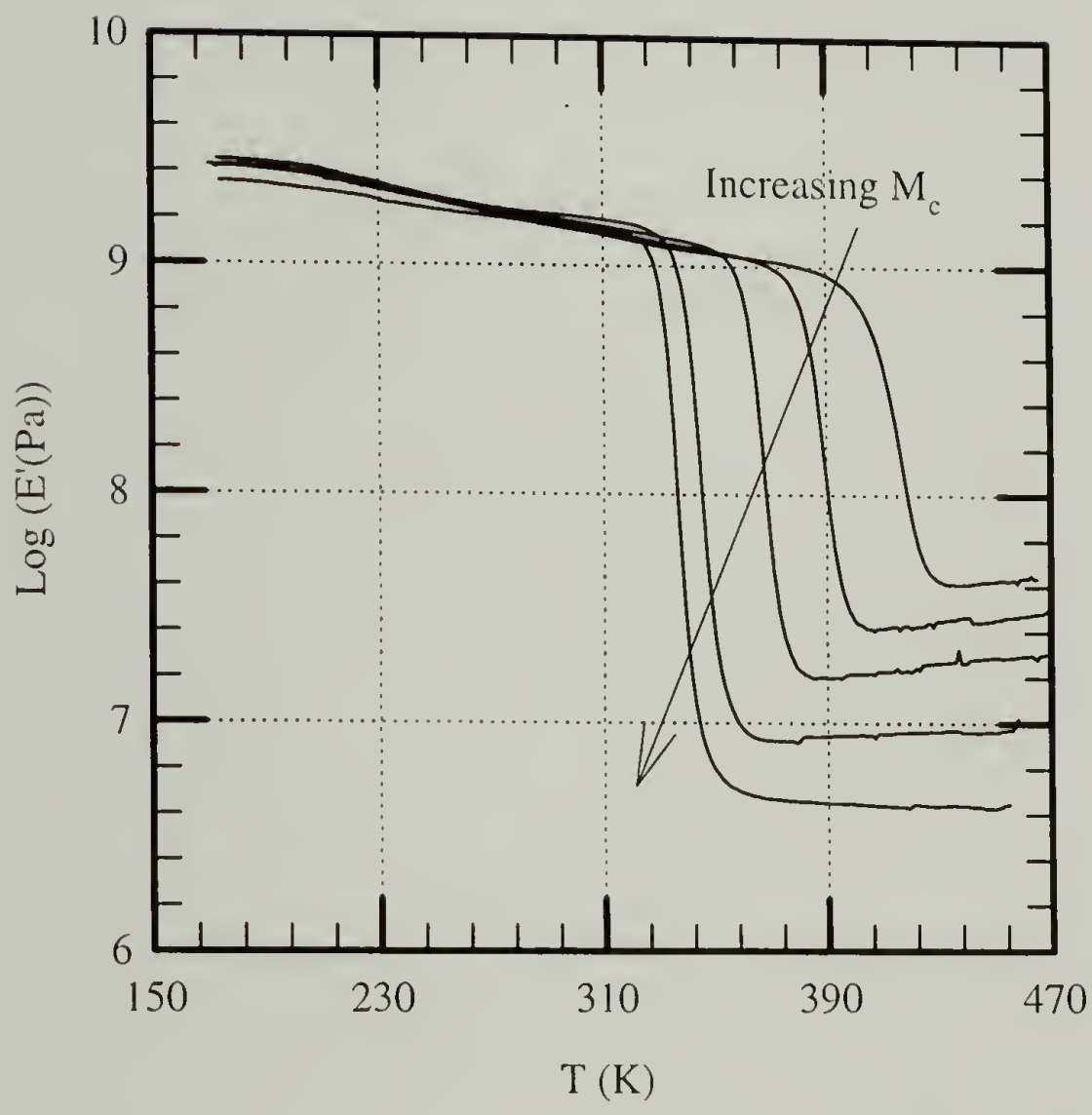

Figure 2.27: Storage modulus response for networks constructed with Epon 825, ethylenediamine, and 3-methoxypropylamine showing the effect of M_c.

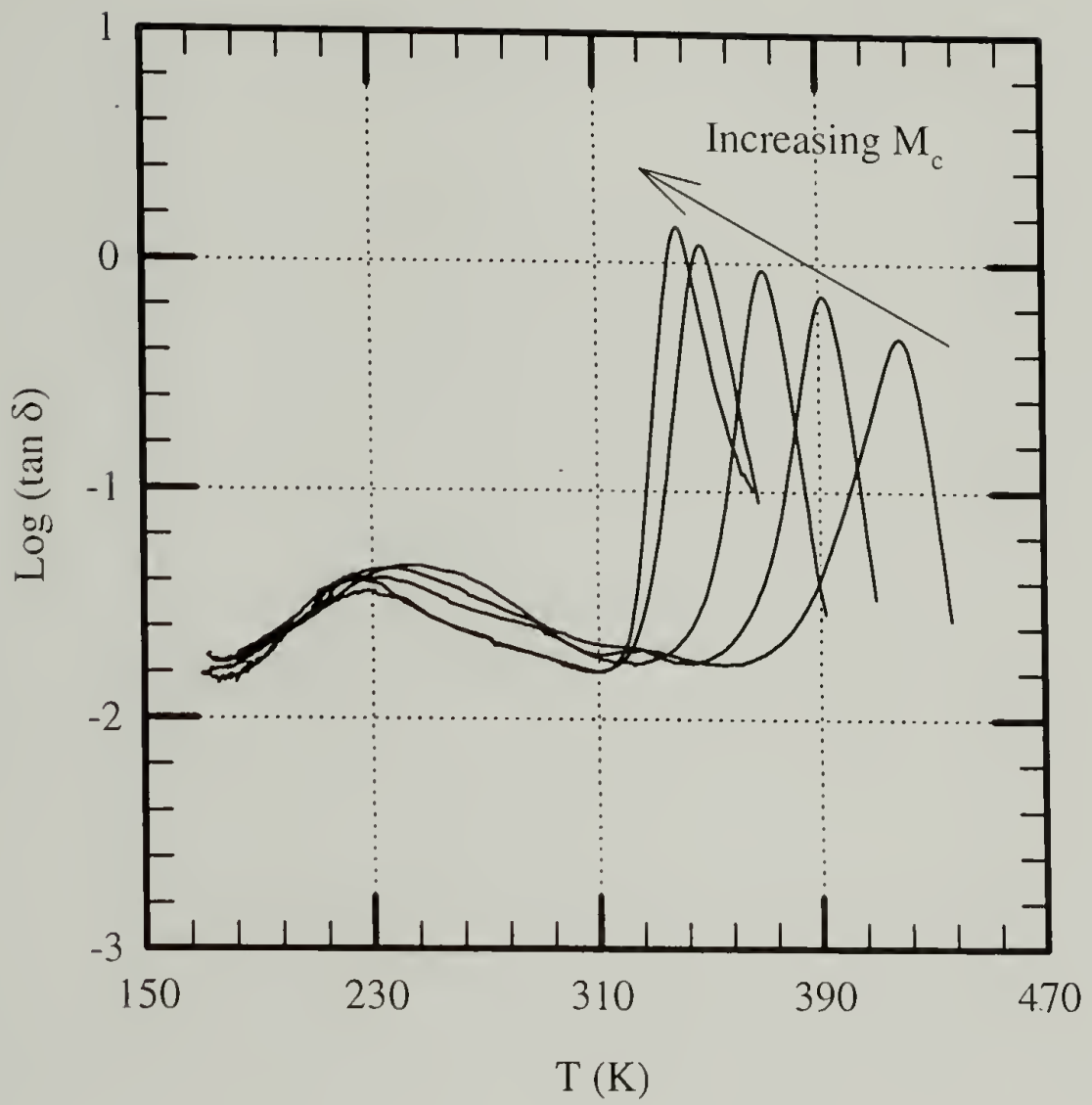

Figure 2.28: Relaxation spectra of networks constructed with Epon 825, ethylenediamine, and 3-methoxypropylamine showing the effect of M_c.

Table 2.4: The effect of M_c on the β relaxation temperature of networks constructed with Epon 825, ethylenediamine, and 3-methoxypropylamine.

M_c (kg/mol)	T_β DMTA (K)
0.38	244
0.49	236
0.67	234
1.04	224
2.14	228

2.8.3 Effect of Cross-link Functionality and Chain Stiffness

Dynamic mechanical thermal analysis of networks constructed with Epon 825 and the aliphatic curing system and the aromatic curing system are shown in Figures 2.29-2.36. This data shows that f_c does not significantly affect the glassy moduli, while f_c affects the glass transition temperatures. The effect of f_c on the β relaxation is not significant. In addition, the data in Figures 2.29-2.36 support the behavior describing the effect of M_c. Chain stiffness or curing agent system, affects T_g but displays no influence on the glassy moduli or the glassy state secondary relaxations.

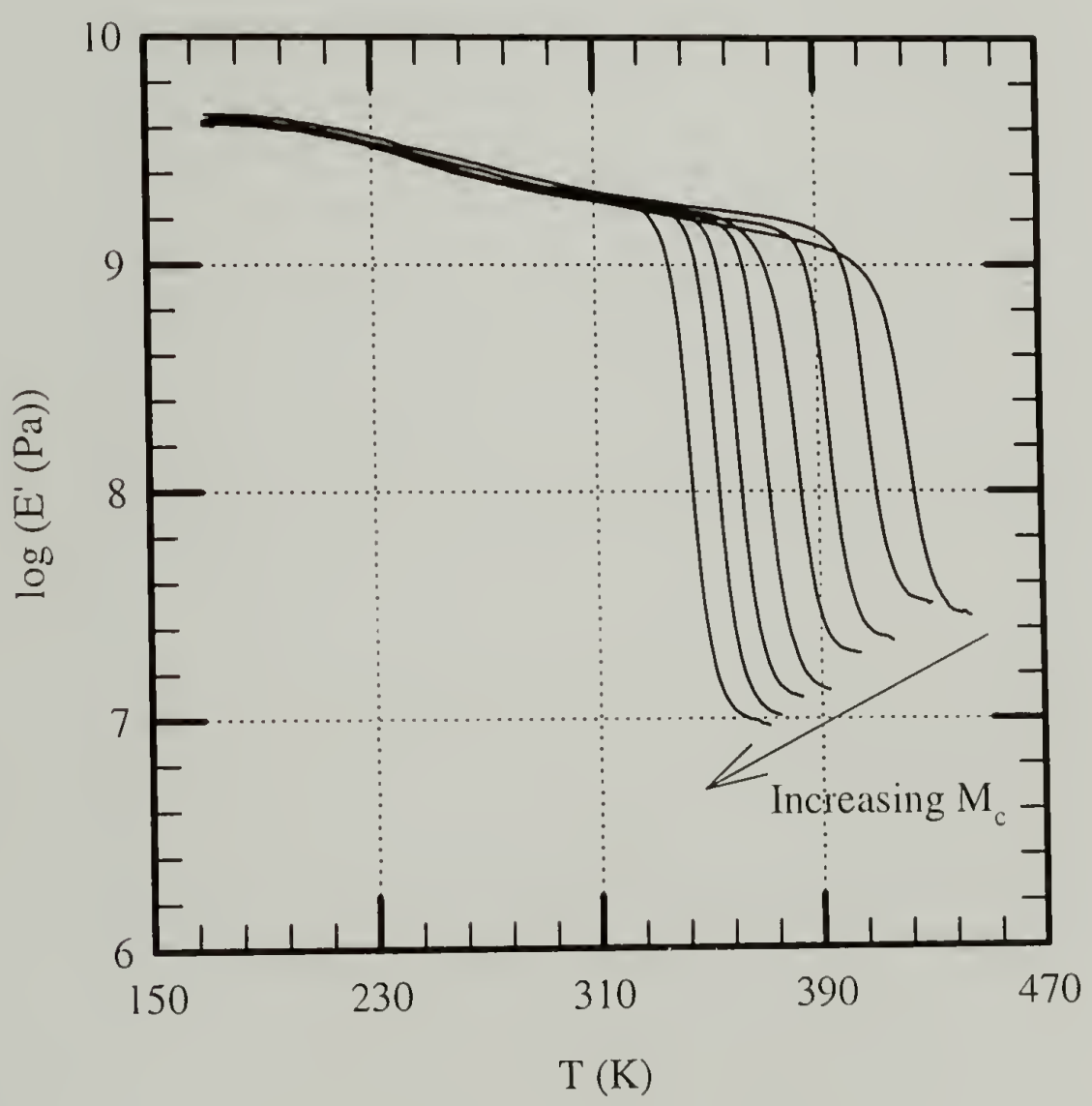

Figure 2.29: Storage modulus response of networks constructed with Epon 825 and the aliphatic amine curing system with tetrafunctional cross-links.

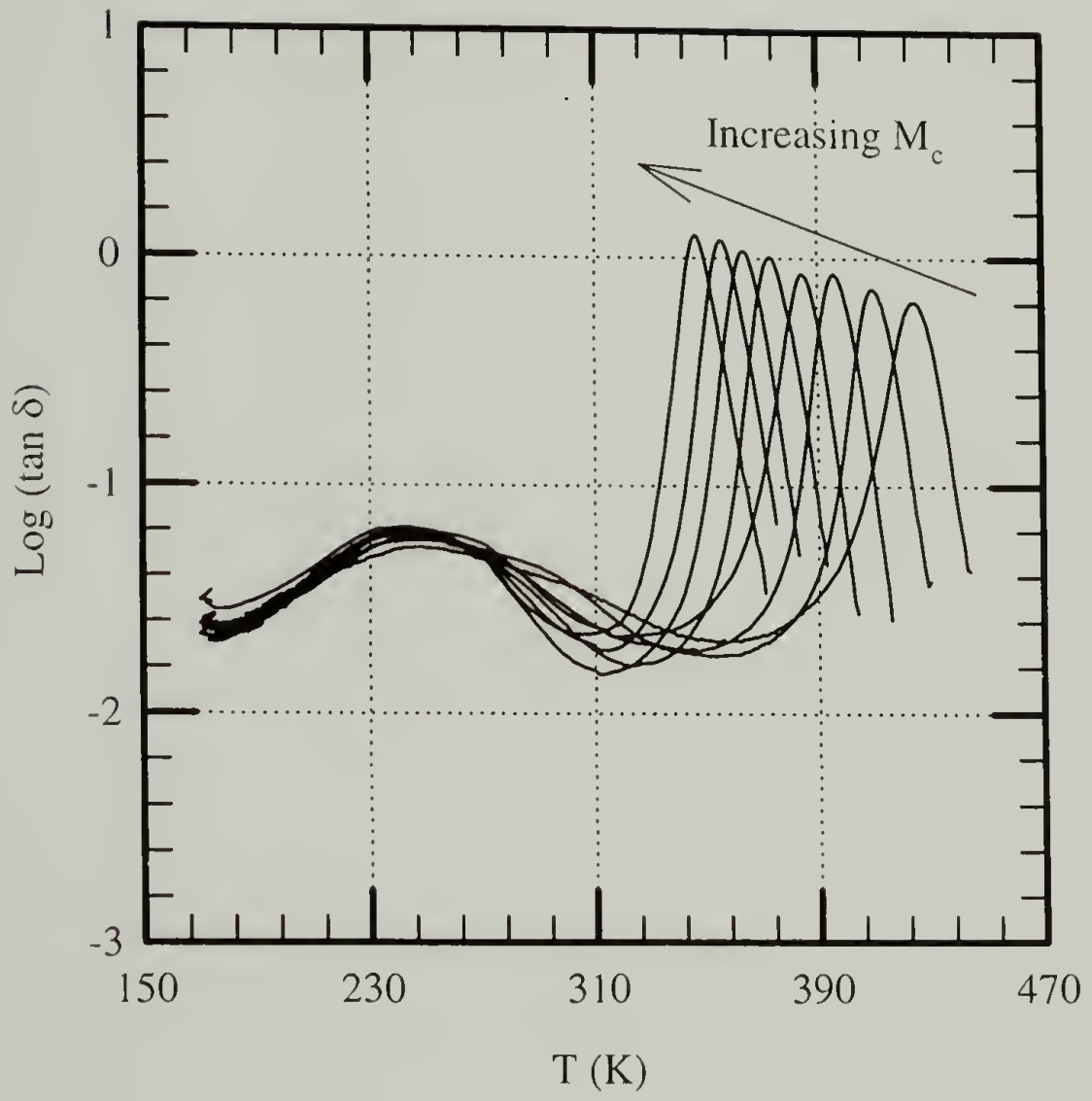

Figure 2.30: Relaxation spectra of networks constructed with Epon 825 and the aliphatic amine curing system with tetrafunctional cross-links.

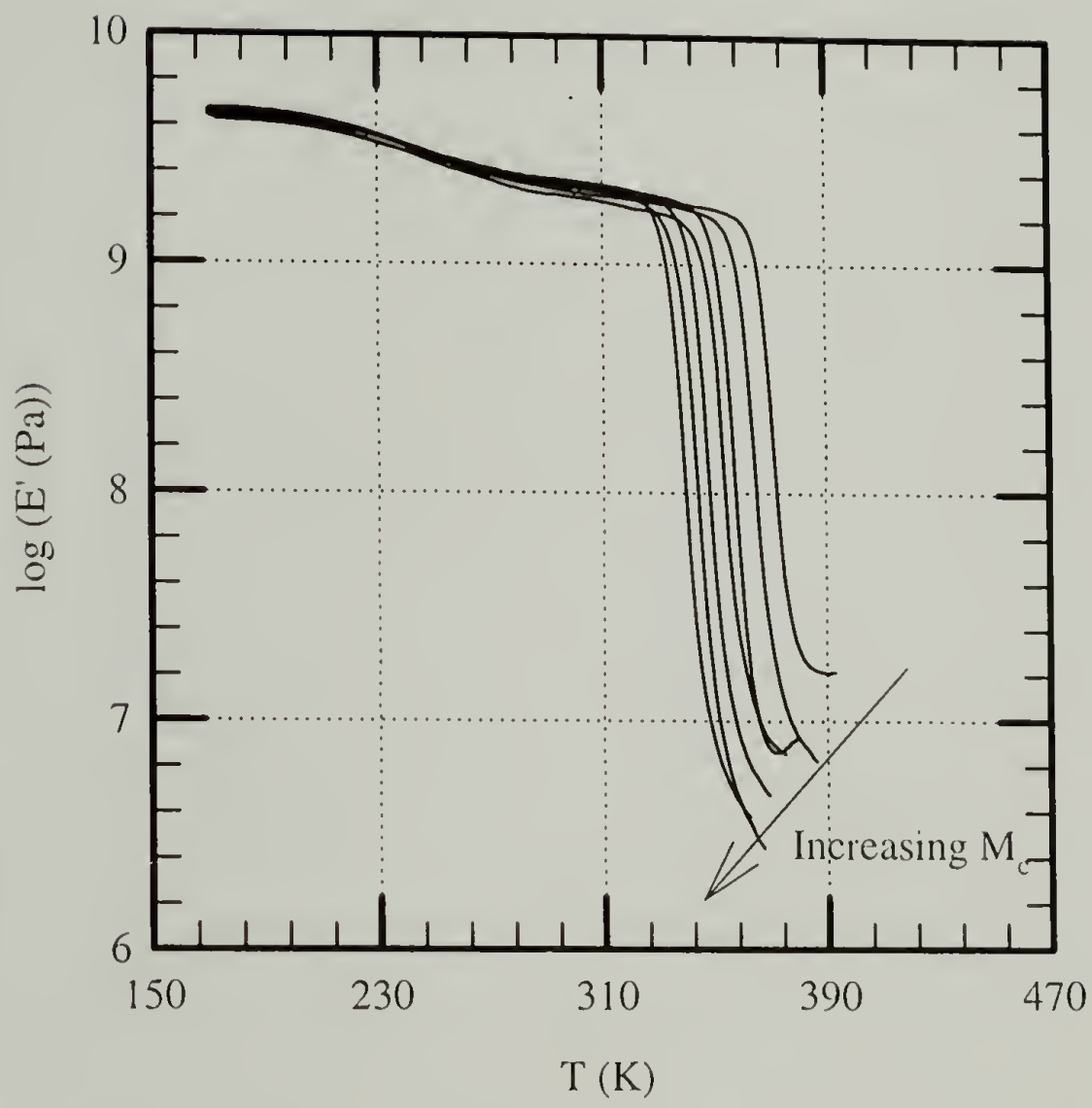

Figure 2.31: Storage modulus response of networks constructed with Epon 825 and the aliphatic amine curing system with trifunctional cross-links.

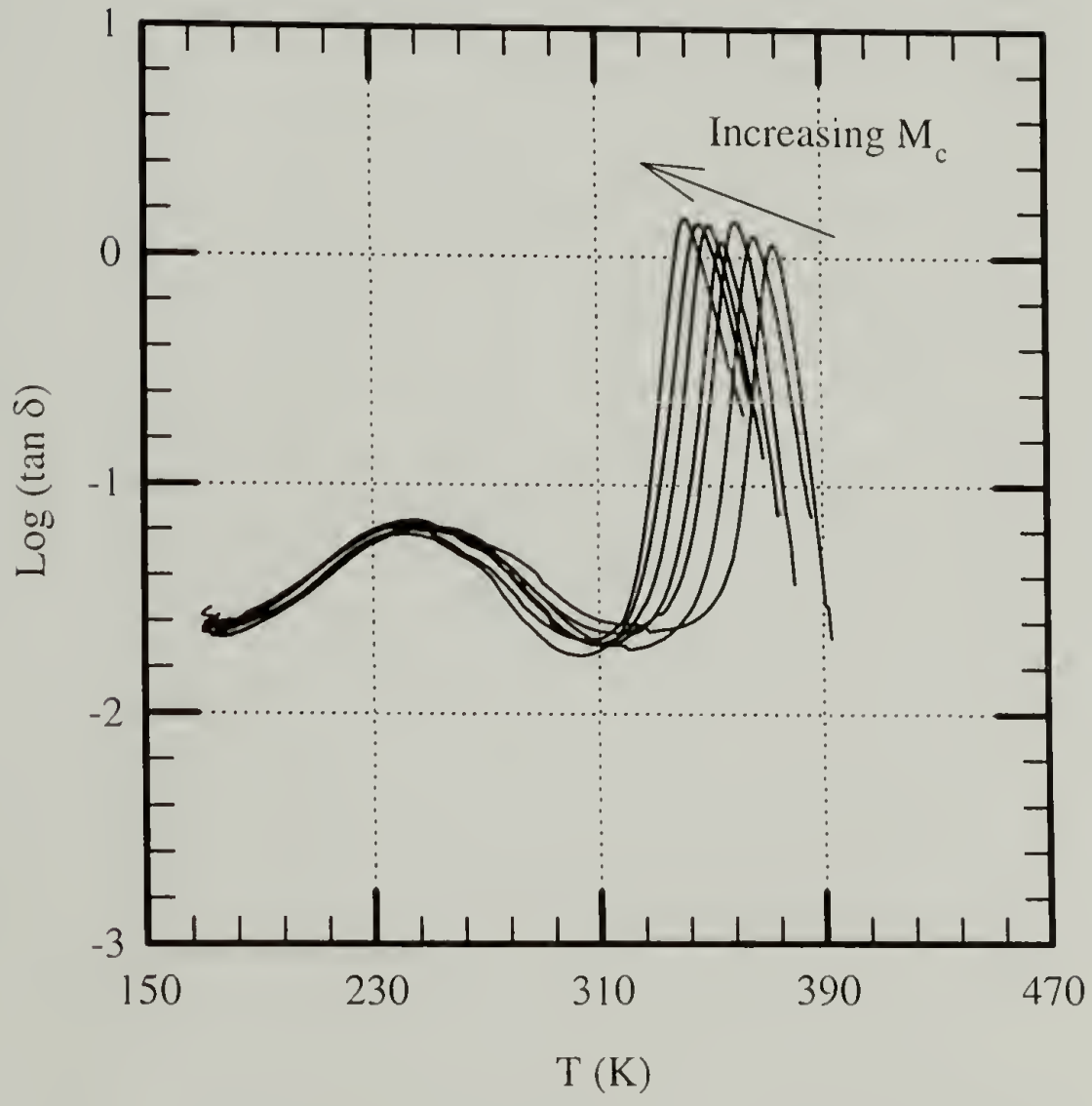

Figure 2.32: Relaxation spectra of networks constructed with Epon 825 and the aliphatic amine curing system with trifunctional cross-links.

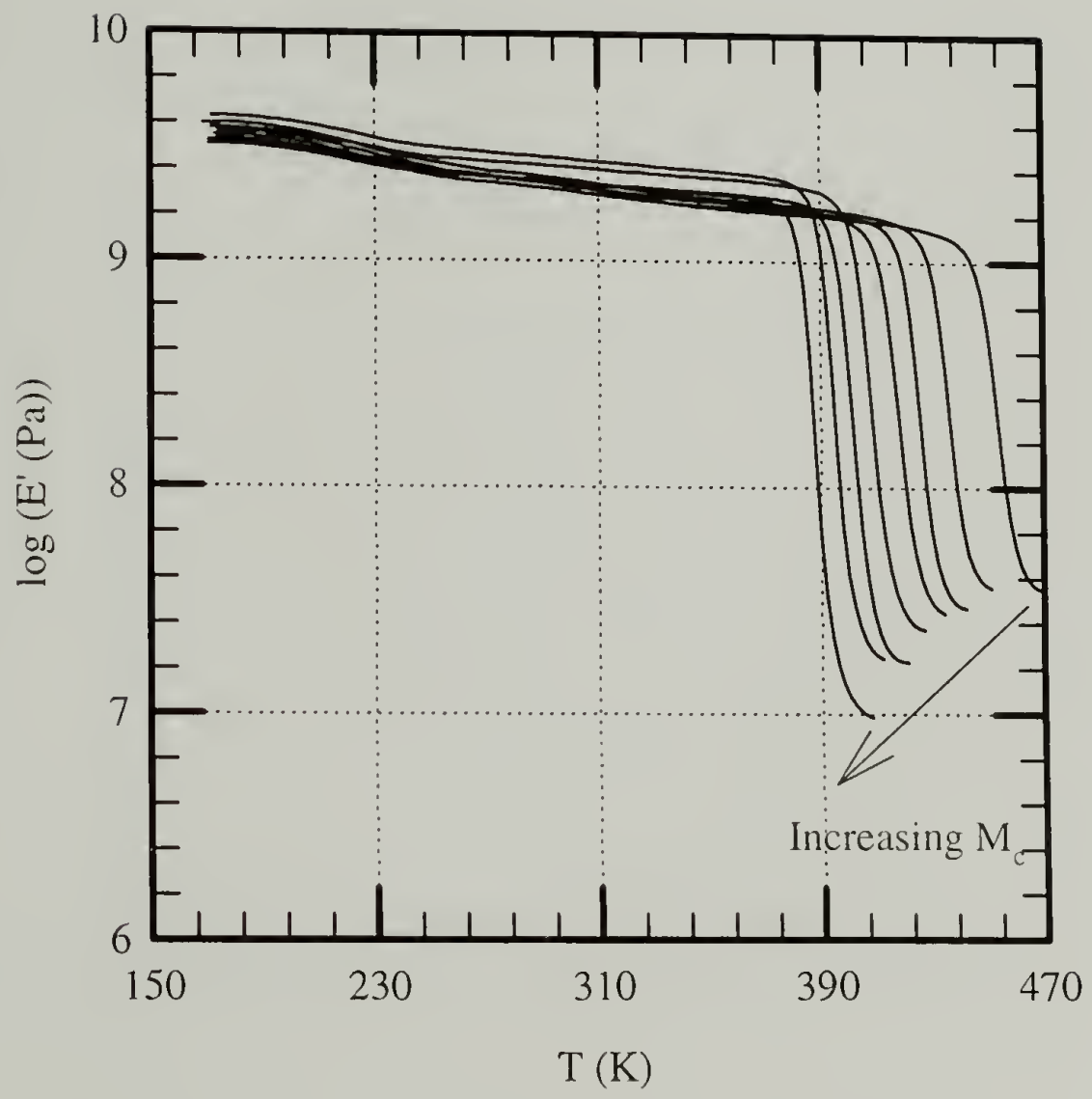

Figure 2.33: Storage modulus response of networks constructed with Epon 825 and the aromatic amine curing system with tetrafunctional cross-links.

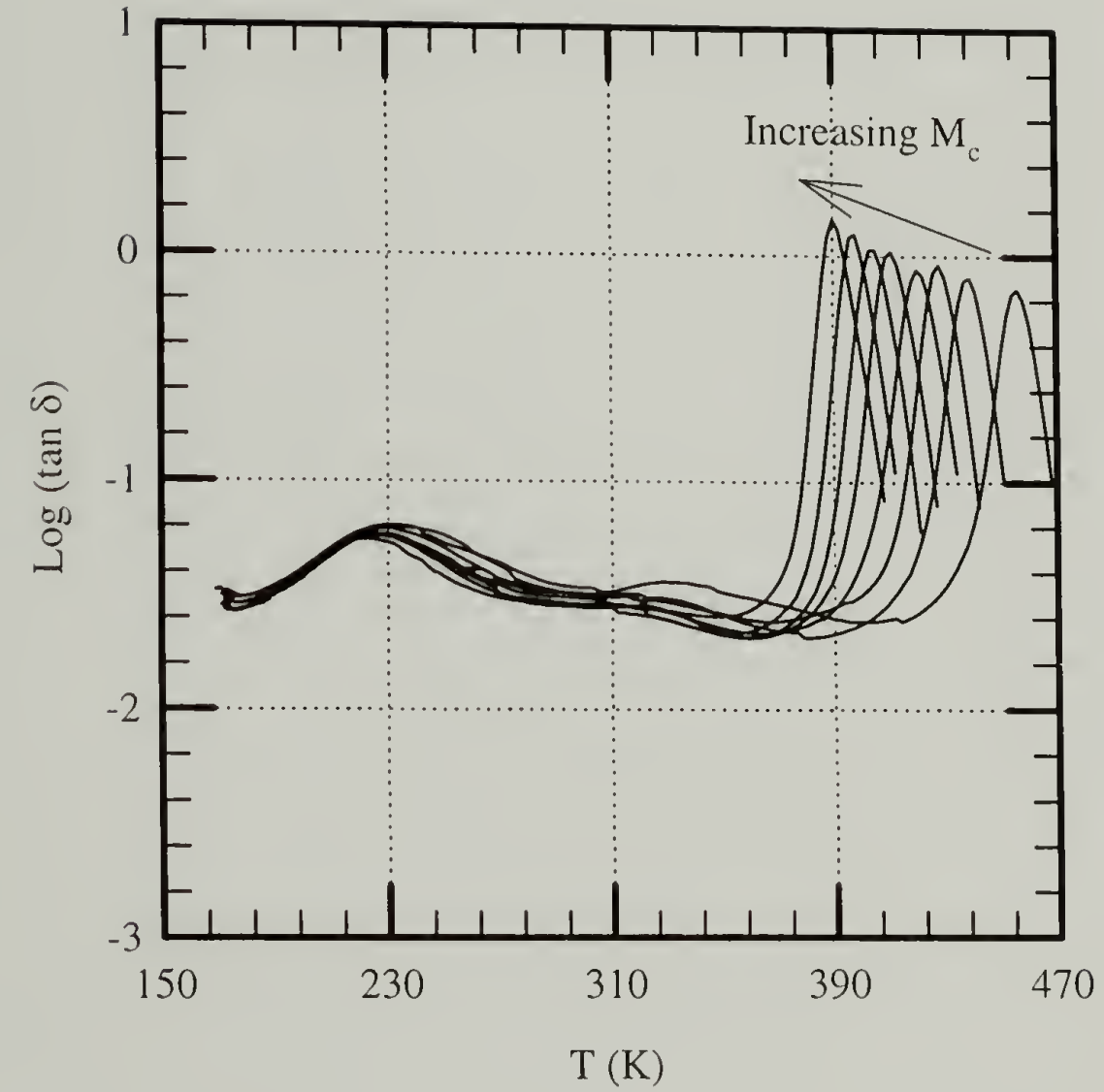

Figure 2.34: Relaxation spectra of networks constructed with Epon 825 and the aromatic amine system with tetrafunctional cross-links.

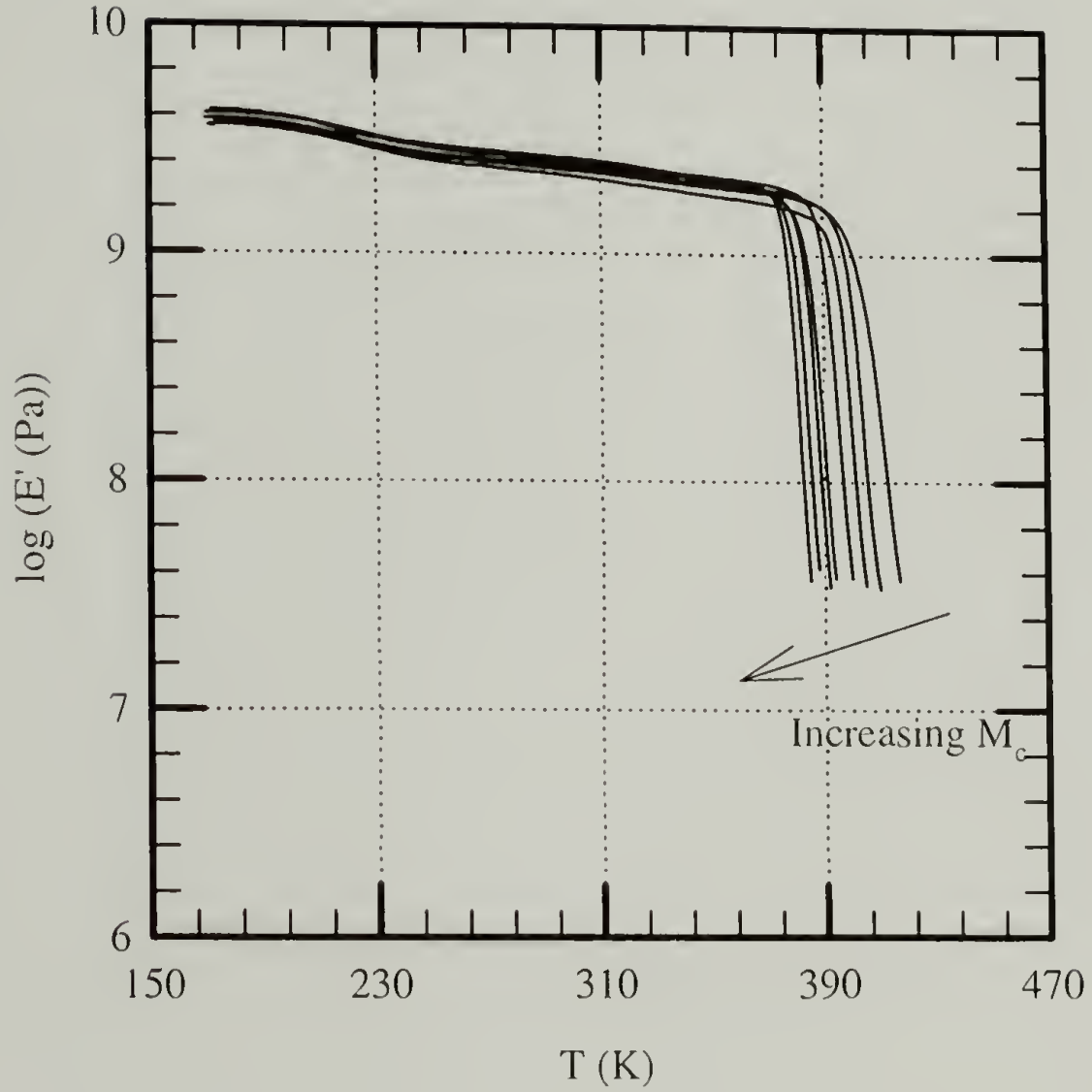

Figure 2.35: Storage modulus response of networks constructed with Epon 825 and the aromatic amine curing system with trifunctional cross-links.

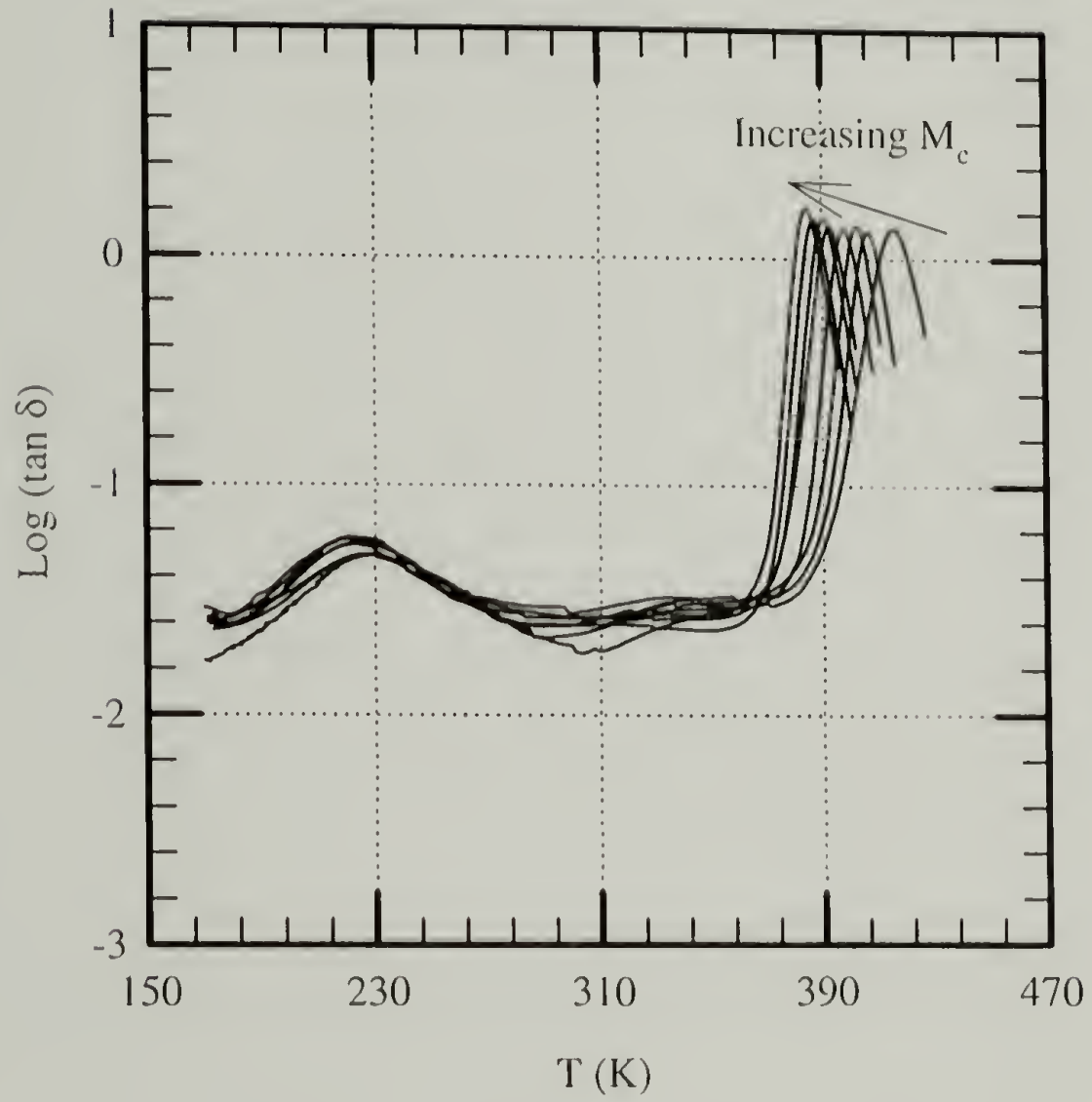

Figure 2.36: Relaxation spectra of networks constructed with Epon 825 and the aromatic curing system with trifunctional cross-links.

2.9 Glassy State Elastic Behavior

2.9.1 Measurement Techniques

Tensile bars (ASTM D638 Type I) were machined from plaques with a specially designed router. The tensile bars were tested at room temperature and a crosshead speed of 5 mm/min with a Model 1123 Instron equipped with an axial strain gauge to measure the axial extension upon loading and a transverse strain gauge to measure the lateral contraction. Linear regressions were performed on the responses from 0 to 30% of the maximum load to obtain Young's modulus and Poisson's ratio.

2.9.2 Elastic Properties

The dynamic mechanical thermal analysis indicated that the glassy modulus was unaffected by structural parameters such as M_c and f_c. Tensile tests, which provide a more accurate modulus measurement, reveal that M_c does not affect the elastic properties. Table 2.5 shows the elastic properties of networks constructed with Epon 825, ethylenediamine, and 3-methoxypropylamine. The average Young's modulus and Poisson's ratio of these networks at room temperature are 2.7 GPa and 0.37 respectively. This trend is in agreement with literature[4,28,34,35] and is expected since all the networks are glassy at room temperature and not affected by large length scale parameters such as M_c. Chain stiffness, or curing agent system, slightly influences the elastic properties. Networks constructed with Epon 825 and the aromatic amine curing system have an average Young's modulus of 3.2 GPa compared with the networks constructed with Epon 825 and the aliphatic amine curing system, which have an average Young's modulus of 2.7 GPa at room temperature. Chain packing and intermolecular forces, which represent smaller length scale parameters than M_c and f_c, govern the glassy state elastic properties.

Table 2.5: Elastic properties of networks constructed with Epon 825, ethylenediamine, and 3-methoxypropylamine.

M_c (kg/mol)	E (GPa)	ν
0.38	2.7	0.37
0.49	2.5	0.38
0.67	2.7	0.37
1.04	2.8	0.35
2.14	2.8	0.36

2.10 Yield Behavior of Networks

2.10.1 Measurement Techniques

Compression tests were performed at various strain rates and temperatures with a Model 1123 Instron on casted epoxy cylinders (11.5 mm diameter x 23 mm long). From these tests, the compressive yield strength (σ_{yc}) of each network was taken as the maximum in the nominal stress versus nominal strain curve. Tensile tests were performed at various strain rates and temperatures with a Model 1123 Instron. From these tests, the tensile yield strength (σ_{yt}) of each material was taken as the maximum in the nominal stress versus nominal strain curve.

2.10.2 Modeling of Yield Behavior

A thermally activated modified von Mises yield model can describe the yield behavior of epoxy resins.[36-38] This model is described in equations 2.12 and 2.13.

$$\tau_y^{oct} = \tau_{yo}{}^{oct} - \mu \sigma_m \qquad (2.12)$$

$$\tau_y^{oct} = \frac{\Delta E}{v^*} + \frac{RT_g}{v^*} \ln\left(\frac{\dot{\gamma}^{oct}}{\Gamma}\right) + \left(T - T_g\right)\ln\left(\frac{\dot{\gamma}^{oct}}{\Gamma}\right) - \mu \sigma_m \qquad (2.13)$$

where: τ_y^{oct} shear yield strength on the ocatahedral plane
τ_{yo}^{oct} shear yield strength on the octahedral plane in pure shear
ΔE activation energy
v^* activation volume
R gas constant
T_g glass transition temperature of the network
$\dot{\gamma}^{oct}$ octahedral shear strain rate
T temperature
Γ proportionality constant
μ coefficient of internal friction
σ_m mean stress.

The first three terms on the right hand side of equation 2.13 describe how the octahedral shear strength in pure shear changes as the rate of deformation, temperature, and glass transition temperature are changed. The fourth term takes into account the state of stress, since the yield strength of polymeric materials is pressure dependent. For the case of uniaxial compression, equation 2.14 is used to calculate the octahedral shear yield strength.

$$\tau_y^{oct} = \frac{\sigma_{cy}}{3}\left(\sqrt{2} - \mu\right) \quad (2.14)$$

It can be shown from equations 2.13 and 2.14 that the compressive yield strength should scale linearly with T_g at a given test temperature and strain rate if the fitting parameters (ΔE, v^*,μ) are not significantly affected by network structure. Bradley et al.[1] reported the compressive yield strength collapses as a function of $T-T_g$ for different cross-linked epoxies. The compressive yield strength at room temperature should be proportional to the molecular variables as shown in equation 2.15.

$$\sigma_{cy} \propto T_g \propto \frac{(f_c - 2)}{f_c}\frac{\zeta}{M_c} \quad (2.15)$$

Figure 2.37 presents the compressive yield strengths (T=294 K, uniaxial strain rate of 0.1 min^{-1}) of networks constructed with Epon 825 and the aliphatic amine curing system and the aromatic amine curing system. Figure 2.37 demonstrates the ability of the front factor of $(f_c-2)/f_c$ to account for cross-link functionality. The effect of chain stiffness, curing agent system, influences the yield strength. This influence is shown in Figure 2.38, which is a plot of the compressive yield strength versus $T-T_g$. Figure 2.38 shows that the simple relationship between the compressive yield strength and $T-T_g$ is more complicated and influenced by other structural variables. Figure 2.39 shows the tensile yield strength as a function of temperature at a constant uniaxial strain rate (0.1 min^{-1}) for two networks with basically equivalent T_gs, yet different network fabrication. Again, the process seems to be influenced by other variables than simply T and T_g.

Correlation between μ and the chemical details of epoxy networks are scarce, since μ can only be determined by changing the state of stress. If the strain rate and temperature are held constant the coefficient of internal friction can be determined by equation 2.16.

$$\mu = \sqrt{2}\frac{\left(\sigma_{yc} - \sigma_{yt}\right)}{\left(\sigma_{yc} + \sigma_{yt}\right)} \qquad (2.16)$$

Table 2.6 shows the effect of M_c on the coefficient of internal friction for networks constructed with Epon 825, ethylenediamine, and 3-methoxypropylamine. The calculation of μ for the highest cross-linked material is prevented by brittle behavior. Other experimental techniques must be employed such as a multi-axial stress state test, as described by Kody and Lesser[39], which allows for the fine control of the state of stress ranging from uniaxial compression to equal biaxial tension, in order to evaluate μ for

relatively brittle materials. The data presented in Table 2.5 is consistent with the findings of Kody and Lesser[39] that the coefficient of internal friction is unaffected by M_c.

The activation volume of epoxy networks are relatively unaffected by changes in the chemical structure such as cross-link density, chain flexibility, and even rubber modification (2 nm^3/molecule).[2,28,36] However, Sindt et al.[34] reported that the activation volume is a function of T/T_g with a plateau activation volume of 2 nm^3/molecule when T/T_g is small. The activation energy (ΔE) is also relatively unaffected by changes in the chemical structure. Several studies report an activation energy between 300 kJ/mol – 500 kJ/mol.[36,39] Figures 2.40 and 2.41 show the strain rate and temperature behavior of networks formed with Epon 825 and AEP (T_{gx}=126 °C) in compression and tension respectively. Fitting the data results in an activation volume of 2.6 nm^3/molecule and an activation of 420 kJ/mol. By holding the strain rate constant, the effect of temperature on μ can be evaluated by equation 2.16 and is shown in Figure 2.42. It is interesting to note from linear regression that μ is zero at $T=T_{gx}$.

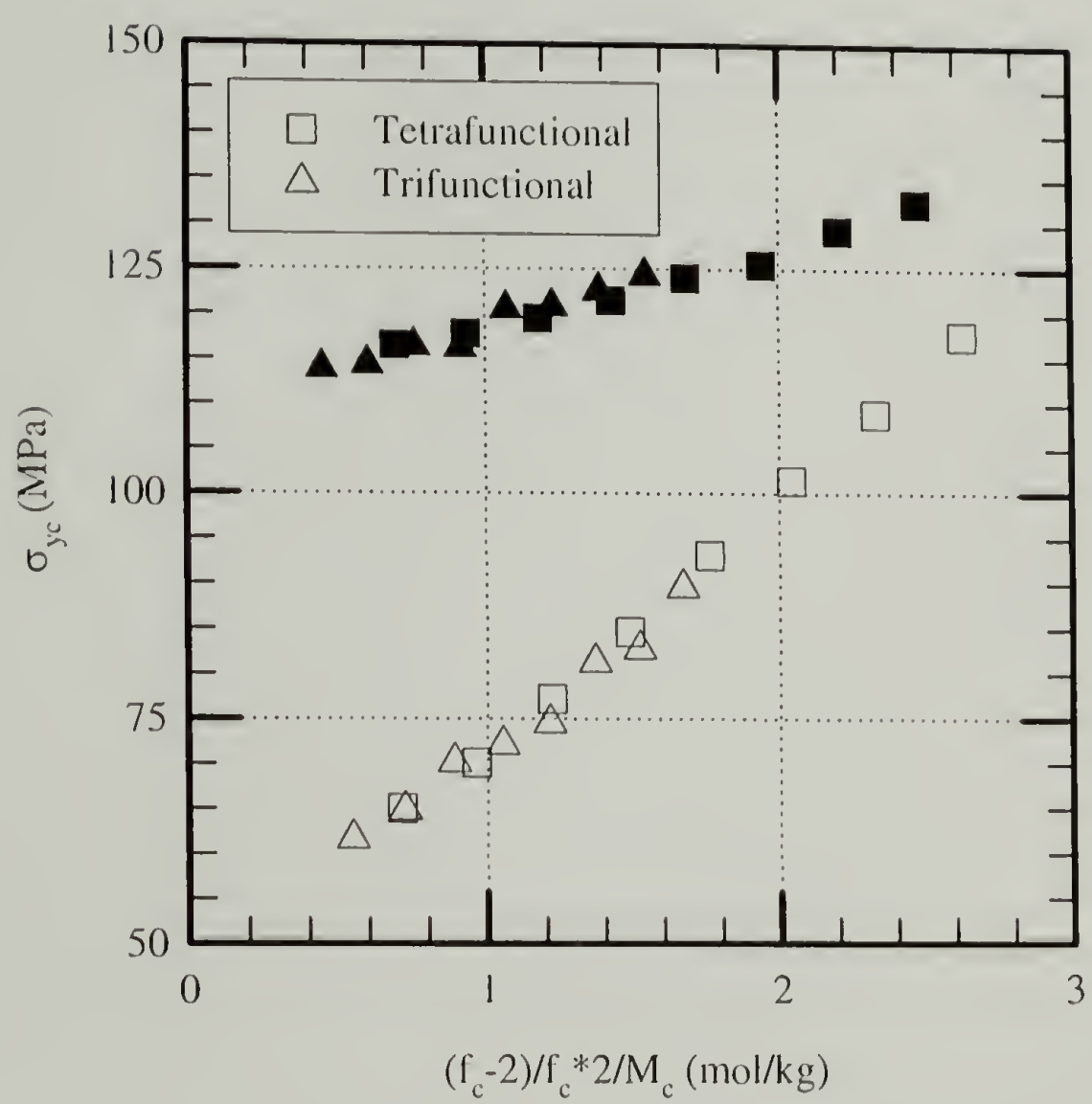

Figure 2.37: The compressive yield strength behavior of networks constructed with Epon 825 and the aliphatic amine curing system (hollow) and aromatic amine curing system (solid).

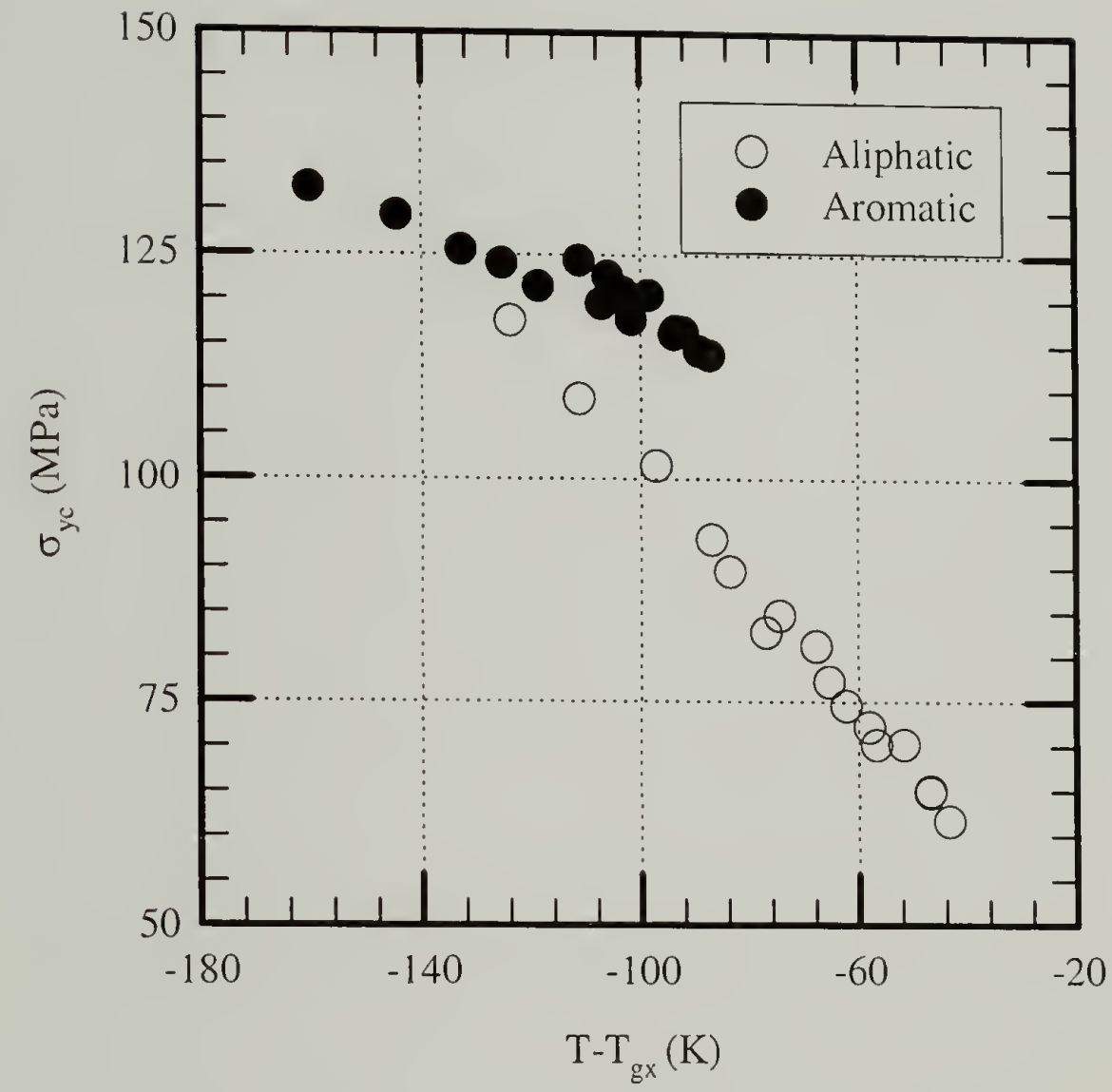

Figure 2.38: The compressive yield strength versus T-T_g of networks constructed with Epon 825 and the aliphatic amine curing system and the aromatic amine curing system.

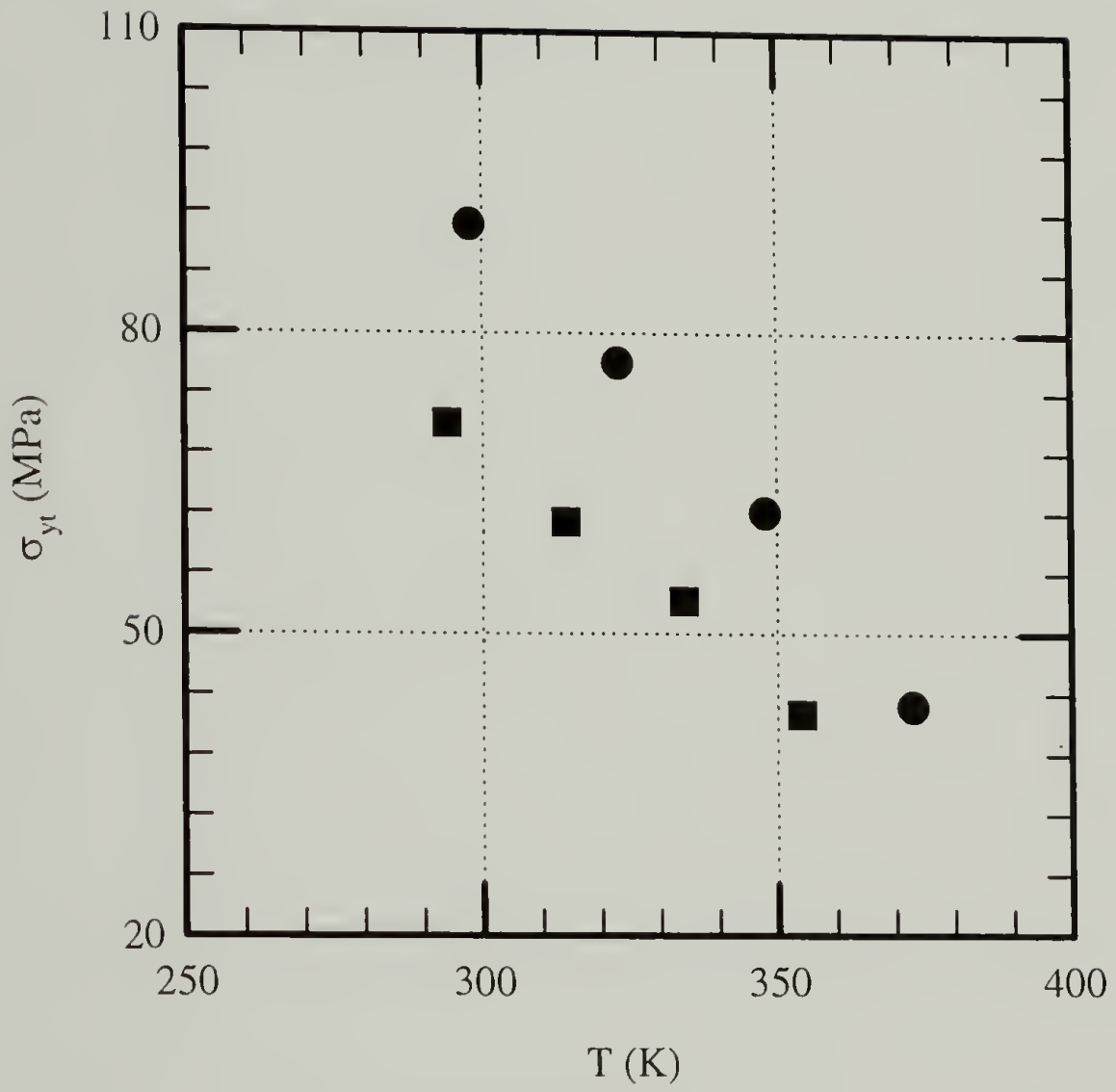

Figure 2.39: Yield strength as a function of temperature for networks with similar T_g yet different network construction (circle-Epon 828/Aromatic curing system with M_c=0.9 and T_{gx}=122 °C, square-Epon 825/AEP with T_{gx}=126 °C).

Table 2.6: Effect of M_c on μ for the networks constructed with Epon 825, ethylenediamine, and 3-methoxypropylamine.

M_c (kg/mol)	σ_{yc} (MPa)	σ_{yt} (MPa)	μ
0.38	117	92	0.17
0.49	99	74	0.20
0.67	93	70	0.20
1.04	83	66	0.16
2.14	75	62	0.13

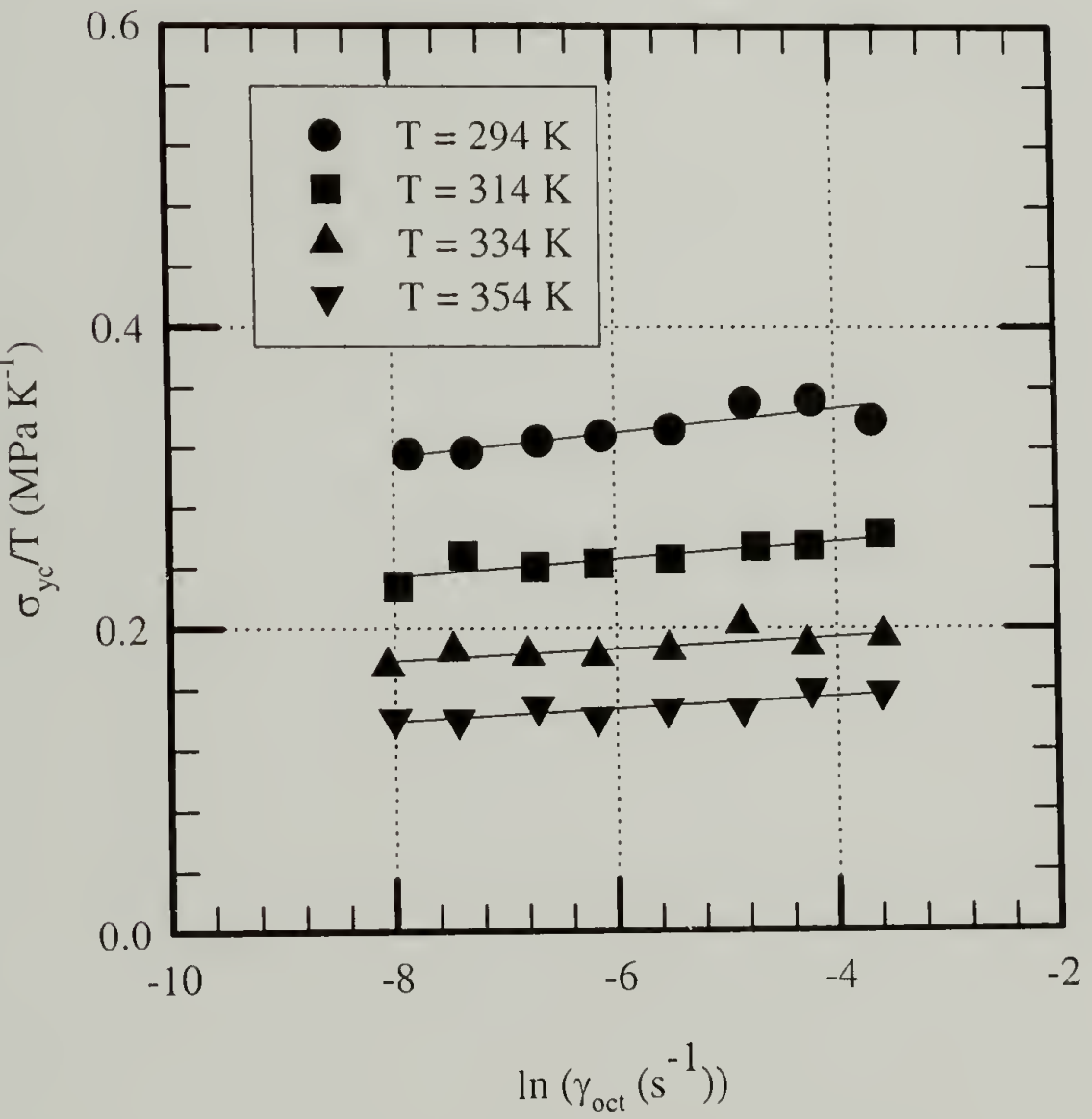

Figure 2.40: Compressive yield behavior of Epon 825 cured with AEP as a function of strain rate and temperature.

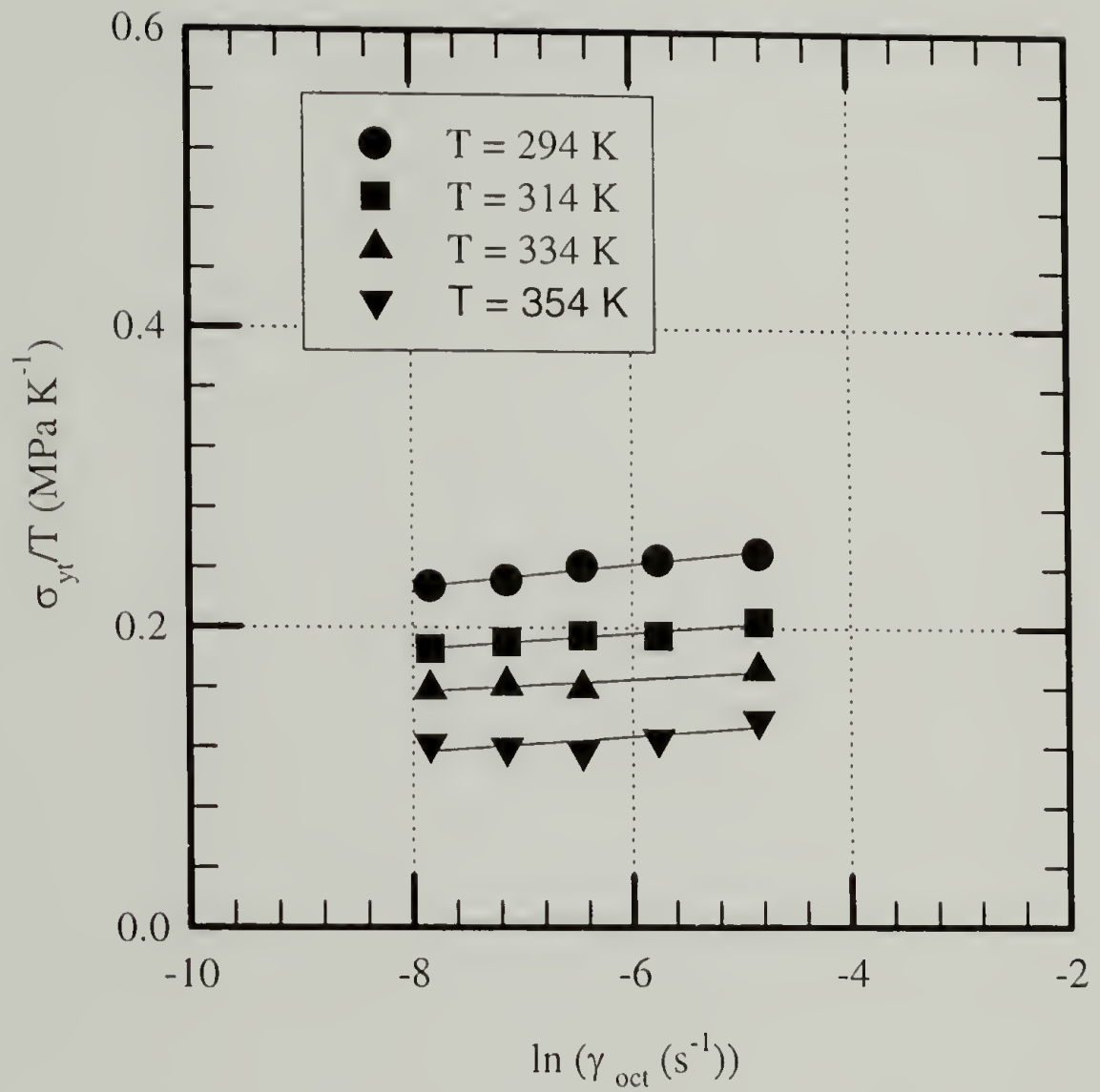

Figure 2.41: Tensile yield behavior of Epon 825 cured with AEP as a function of strain rate and temperature.

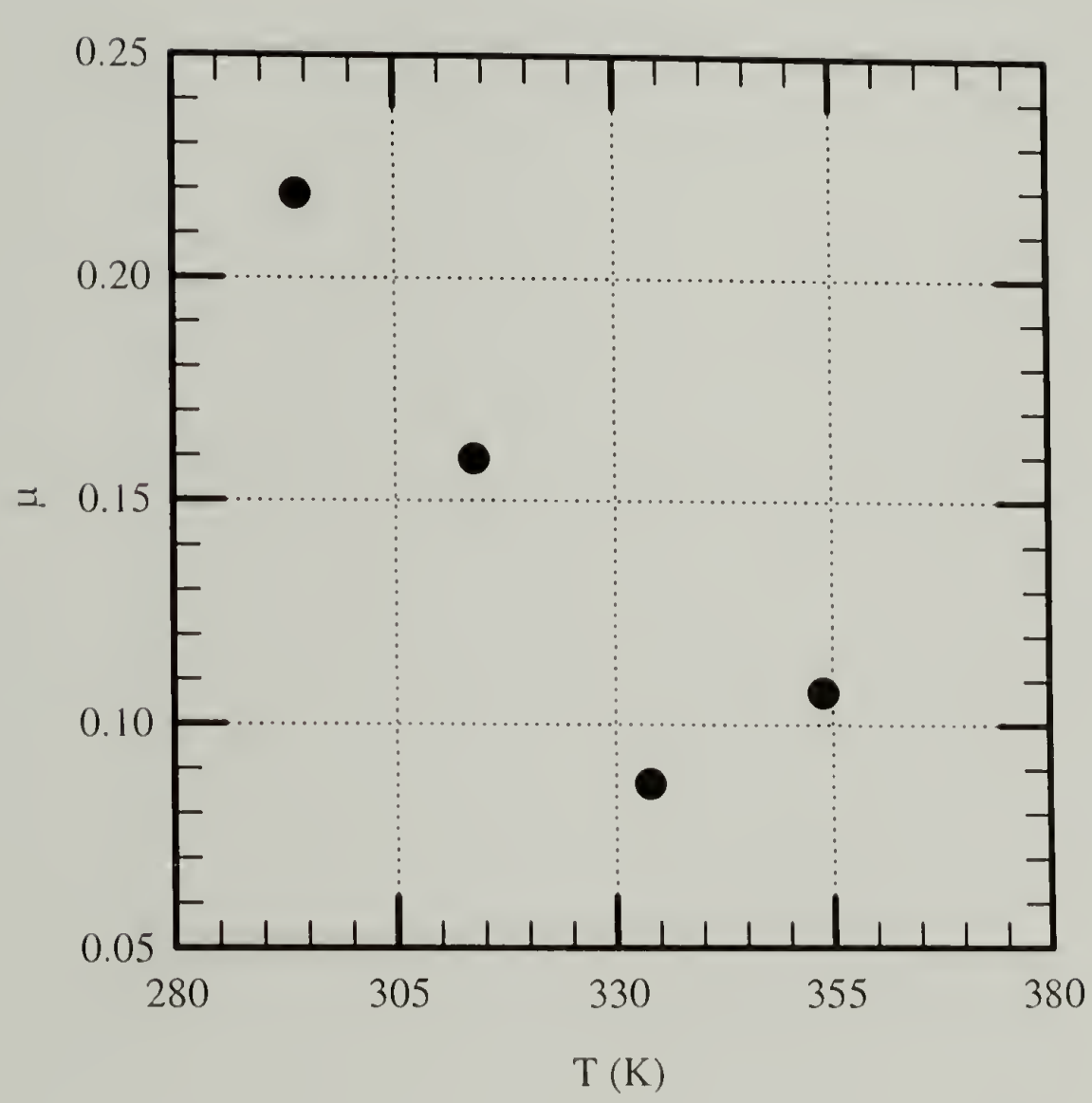

Figure 2.42: Coefficient of internal friction as a function of temperature for Epon 825 cured with AEP.

2.11 Fracture Toughness

2.11.1 Introduction

In both industry and academia the fracture toughness of materials are often measured over a range of temperatures, strain rates, additive concentrations, and other environmental variables. Quite often, the fracture behavior itself changes as the investigator measures the fracture response over the range of interest. Brittle fracture is evidenced by a linear load deflection curve until the clear onset of crack propagation. Evaluation of the energy requirements for crack propagation in brittle processes (G_q) is usually described by linear elastic fracture mechanics (LEFM).[40] If G_q satisfies the small scale yielding requirements set forth in ASTM E399[41] and ASTM D5045[42] standards, then G_q is equated to the linear elastic plane strain fracture energy (G_{Ic}). In contrast, a non-linear load deflection curve and an ambiguous onset of crack propagation characterize a ductile fracture. The evaluation of the energy requirements for crack propagation in ductile processes (J_q) is usually described by non-linear elastic fracture mechanics, commonly referred to as elastic-plastic fracture mechanics (EPFM).[40] If J_q satisfies the small scale yielding requirements set forth in ASTM E813 standard[43], then J_q is equated to the non-linear elastic plane strain fracture energy (J_{Ic}). Evaluation of fracture energies requires that different tests and different analyses be performed depending on the response of the material: brittle or ductile.

One of the critical performance properties of epoxy materials is fracture toughness. The general fracture energy of a constant thickness epoxy material as a function of yield strength is shown in Figure 2.43.[44,45] At high yield strengths, the fracture energies are relatively low. High yield strengths can typically be achieved by

low temperature testing, high strain rate testing, and low modifier content. At low yield strengths, the fracture energy increases rapidly with further decreases in yield strength. In addition, the mode of failure changes as the fracture energy begins to rise rapidly[44,45] from a brittle fracture to a ductile fracture.

In this section, fracture tests are performed on controlled epoxy networks[21,35,46] with different molecular weights between cross-links. The purpose of this mapping is to determine how M_c and temperature affect the fracture energy. In the process of mapping, the fracture behavior or mode changed from a brittle process to a ductile process. As a consequence of this mode change, the tests and analyses used to estimate the fracture energy changed. With suitable estimates of fracture energies, two popular models[45,47] are used to describe the fracture toughness over the brittle-to-ductile range.

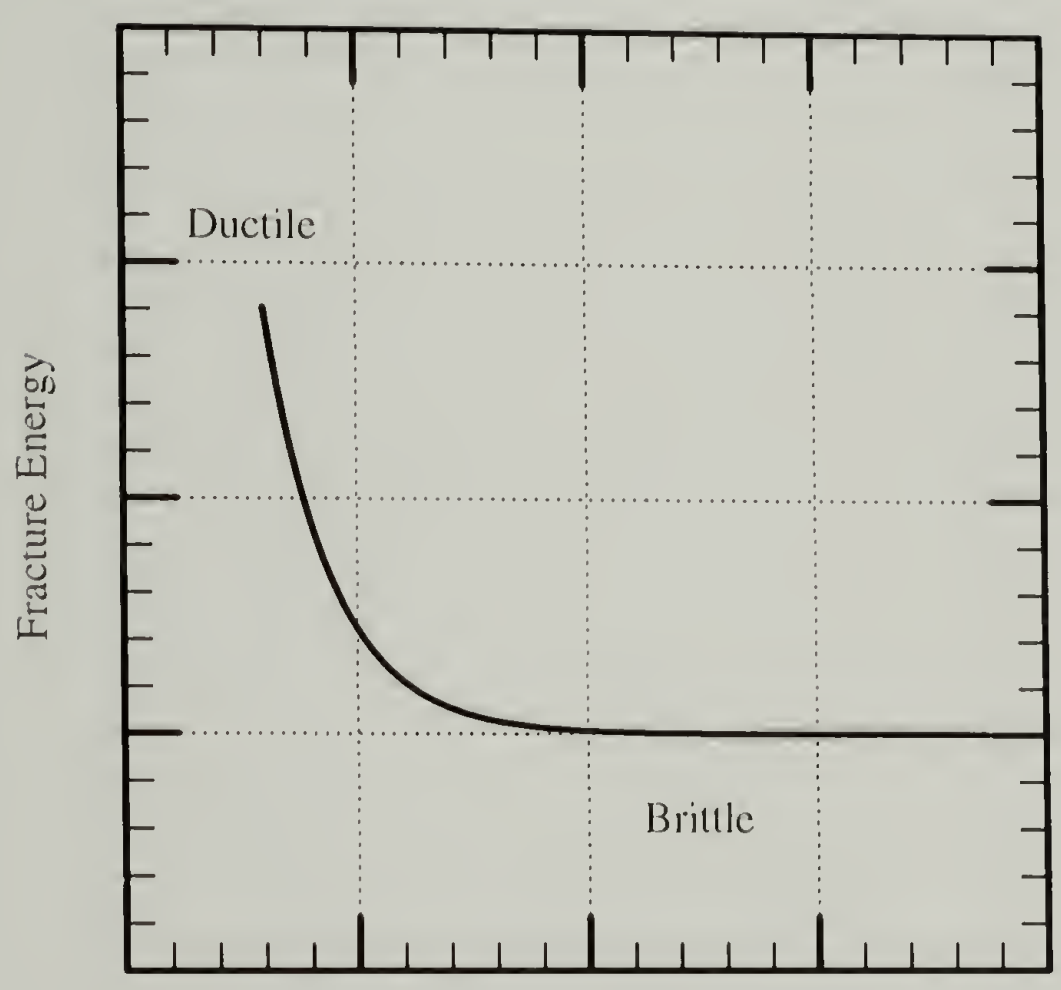

Figure 2.43: Fracture toughness versus yield strength holding specimen thickness constant.

2.11.2 MeasurementTechniques

Single notched three point bend fracture toughness bars (100 mm x 19.1 mm) were machined from 3.18 mm thick plaques. Small notches were made by a diamond saw from which precracks were introduced by tapping a fresh razor blade into the material. Tests were performed at room temperature with a Model 1123 Instron at a crosshead speed of 2 mm/min. The span-to-width ratio was set at 4. Prior to each test, the crack length was measured with an eyepiece.

2.11.2.1 Linear Elastic Fracture

The fracture behavior was analyzed by linear elastic fracture mechanics if the load deflection curve was linear until a critical load was reached at which point crack propagation occurred. The fracture energy for a linear elastic material, G_q, was then calculated by equation 2.17.[48]

$$G_q = \frac{P_q^2}{2B}\left(\frac{\partial C}{\partial a}\right)_{P_q} \qquad (2.17)$$

where: B specimen thickness
P_q critical load or failure load
C specimen compliance
a crack length.

Four specimens were tested for each network that behaved in a brittle fashion.

2.11.2.2 Elastic Plastic Fracture

The fracture behavior was analyzed by elastic plastic fracture mechanics if the load deflection curve was non-linear and the onset of crack propagation ambiguous. Non-linearity and crack propagation onset ambiguity adds complexity to the test, analysis, and theory used to evaluate the fracture energy. However, it was not the

purpose of this study to examine the theoretical details of EPFM. The following procedure, based on ASTM E813[43] with some modifications, was used to analyze the fracture energy.

First the sample was loaded until the load deflection curve became non-linear at which point the sample was unloaded and the amount of crack extension ($\Delta a_i = a_i - a_o$) recorded. The area under the load deflection curve at the point of unloading (A_{ti}) was recorded along with the area between the loading and unloading curves (A_{pi}). The non-linear elastic energy, J, was then calculated by equation 2.18.[40]

$$J_i = \frac{2A_i}{BL} \qquad (2.18)$$

where: A_i area under the load deflection curve for a given crack extension
B specimen thickness
L ligament width ($W - a_o$).

Equation 2.18 models the ligament as a plastic hinge and the material behaving in a non-linear elastic manner. For the first loading and unloading, $A_i = A_{ti}$. The sample was then loaded and unloaded again (i=2) and the amount of crack extension ($a_2 - a_o$) recorded. The energy required for crack extension in this case (J_2) and all further loading and unloading cycles (J_i) was calculated by using equation 2.19 to evaluate the area (A_i) required to extend the crack Δa_i.

$$A_i = A_{ti} + \sum_{n=1}^{i-1} A_{pi} \qquad (2.19)$$

This procedure was performed for 5 loading and unloading cycles on 4 specimens for the cross-linked materials in which the response was ductile. The non-linear elastic energy values, J_i, were then plotted against the corresponding crack extensions (Δa_i) for a given

material. Linear regression was performed on the resulting plot from which the fracture energy for a non-linear elastic material (J_q) was evaluated from the intercept.

$$J_q = \lim_{\Delta a_i \to 0} J_i(\Delta a_i) \qquad (2.20)$$

2.11.3 Fracture Toughness and Fracture Behavior

2.11.3.1 Linear Elastic Fracture (Brittle)

All of the networks constructed with Epon 825 and the aromatic amine curing system failed in a brittle manner. The three highest cross-linked materials constructed with Epon 825, ethylenediamine, and 3-methoxypropylamine also failed in a brittle manner. As a result of the brittle response, LEFM was used to estimate the fracture energy. In evaluation of G_q, the compliance versus crack length polynomial fit was determined by all of the samples constructed with Epon 825, ethylenediamine, and 3-methoxypropylamine that behaved in a brittle manner. This assumption is validated by two facts. First, the tensile data shows that the elastic modulus is not dependent on M_c. In other words, the stiffness of the materials without a gross crack is the same. Secondly, the systems behaved in a brittle manner during fracture testing. The brittle behavior indicates that the plastic zone size is small and therefore cannot play a significant role in the stiffness of the overall specimen. Figure 2.44 is a plot of the compliance as a function of crack length fit with a second order polynomial. The derivative of this fit was evaluated for a given crack length and combined with corresponding critical load values to calculate G_q for the networks by equation 2.17. The fracture energies, G_q, of the three networks are shown in Table 2.7. Other methods are available for determining G_q, namely the geometric stress intensity method.[48] This method is described by equation 2.21.

$$K_q = \sqrt{a}\left(\frac{6P_q}{BW}\right) f\left(a/W\right) \quad (2.21)$$

where: K_q critical stress intensity factor
W specimen width
f form factor.[49]

The critical stress intensity factors for the three networks constructed with Epon 825, ethylenediamine, and 3-methoxypropylamine are reported in Table 2.7. The geometric stress intensity factor method was used to determine the critical stress intensity factor for the networks constructed with Epon 825 and the aromatic curing agent system. The critical stress intensity factors of these materials are presented in Table 2.8. Equation 2.22 or 2.23, depending on the degree of constraint, can be used to calculate the fracture energy from the stress intensity factors.

$$G_q = \frac{K_q^2}{E} \quad \text{plane stress (2.22)}$$

$$G_{Ic} = \frac{K_{Ic}^2(1-\nu^2)}{E} \quad \text{plane strain (2.23)}$$

The compliance method for determining G_q has an advantage over the geometric stress intensity factor method since the degree of constraint does not have to be specified. To determine the degree of constraint based on K_q values, the ASTM E399[41] and D5045[42] standards requires that the crack length, specimen width, and specimen thickness satisfy values based on estimates of the plastic zone size. The thickness requirement, expressed by equation 2.24, is usually the most difficult requirement to satisfy.

$$B > 2.5\left(\frac{K_q}{\sigma_y}\right)^2 \quad (2.24)$$

The yield strength (σ_y) in equation 2.24 is defined as the tensile yield strength in the ASTM standards. The tensile yield strengths used in the specimen requirement calculations ($\sigma_y = \sigma_{yt}$) were calculated from the compressive yield strength and a coefficient of internal friction of 0.18. The specimens constructed with Epon 825, ethylenediamine, 3-methoxypropylamine, and the aromatic amine curing system satisfied the dimensional requirements. As a result, the K_q values were ascribed to K_{Ic} and the G_q values were ascribed to G_{Ic}. It should be noted that the yield strength of polymers are dependent on the state of stress and leads one to question whether the tensile yield strength is the best yield strength to evaluate specimen requirements.

2.11.3.2 Elastic Plastic Fracture (Ductile)

The two least cross-linked networks constructed with Epon 825, ethylenediamine, and 3-methoxypropylamine (M_c = 1.04, 2.14 kg/mol) behaved in a ductile manner during fracture. As a result of the ductile response, EPFM was used to estimate the fracture energy. Figure 2.45 is a plot of the non-linear elastic energy as a function of crack extension (Δa). The intercepts of this plot represent the fracture energies of the two networks (J_q) and are reported in Table 2.7. The ASTM E813[43] standard, from which the testing procedure in this study was based, advocates the use of a blunting line to evaluate J_q. Objections have been made against the use of a blunting line in theory[40] and in practice with polymeric systems.[50,51] The optically measured crack extension method without a blunting line has been shown to be effective in obtaining J_q values for polymeric materials. The ASTM E813[43] standard also makes requirements on specimen dimensions before J_q can be ascribed to J_{Ic}. The thickness requirement, expressed by equation 2.25, is usually the most difficult requirement to satisfy.

$$B > 25\left(\frac{J_q}{\sigma_y}\right) \qquad (2.25)$$

The two ductile networks' specimens satisfied the dimensional requirements and as a result the J_q values were ascribed to J_{Ic}. The thickness requirements for ASTM E813[43] are more relaxed than the thickness requirements of ASTM E399.[41] Other investigators have advocated the use of stricter specimen thickness requirements with a prefactor of 200 instead of 25.[52]

Stable ductile crack growth occurred for the two less cross-linked materials due in part to R curve behavior. An increasing fracture resistance with crack extension characterizes R curve behavior.[40] An increasing J with crack extension is shown graphically in Figure 2.45. The increasing fracture resistance of a material is often characterized by the tearing modulus (T).[53]

$$T = \left(\frac{dJ}{da}\right)\frac{E}{\sigma_{yt}^2} \qquad (2.26)$$

The tearing modulus of the two networks, M_c = 1.04 kg/mol and M_c = 2.14 kg/mol, are 1.7 and 8.9, respectively. The tearing modulus has been shown not to be a material parameter because dJ/da is dependent on specimen geometry and loading conditions.[40,50] Therefore, studies on ductile polymers ascribe J_{Ic} to the essential fracture work, while dJ/da is ascribed to the nonessential fracture work in the essential work of fracture approach.[50,54,55] In addition to the quantitative data showing the increasing toughness, visual inspection of the samples revealed lateral contraction and the formation of shear lips, which have been seen in other ductile polymeric systems.[47] Figure 2.46 shows the two ductile fracture specimens viewed under cross-polars indicating the residual strain field due to the plastic zone created in the fracture testing.

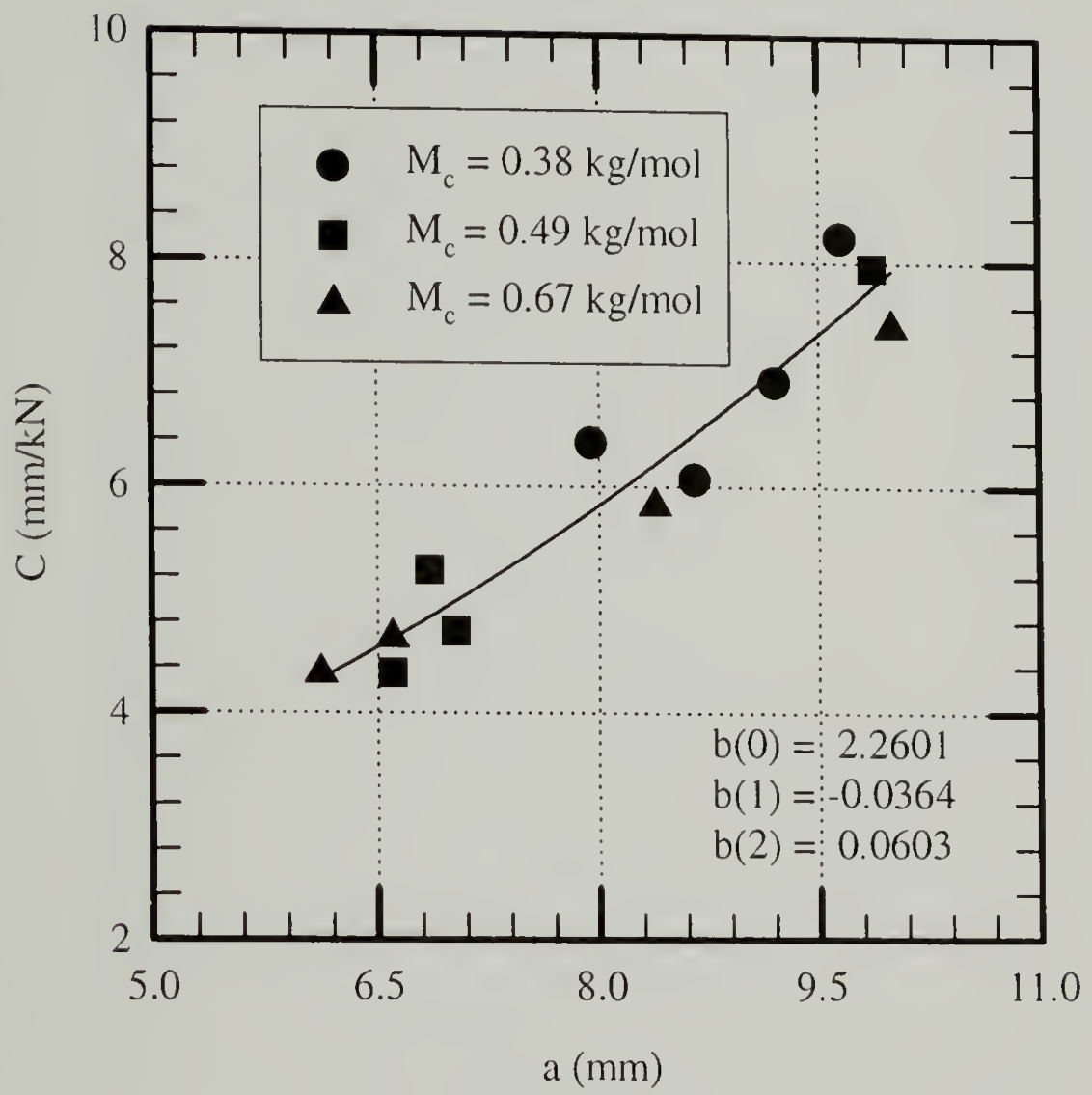

Figure 2.44: Compliance as a function of crack length for 3 highest cross-linked networks formed with Epon 825, ethylenediamine, and 3-methoxypropylamine.

Table 2.7: Fracture energy and critical stress intensity factors for networks constructed with Epon 825, ethylenediamine, and 3-methoxypropylamine.

M_c (kg/mol)	$G_q=G_{Ic}=R_{Ic}$ (kJ/m^2)	$K_q=K_{Ic}$ ($MPa\text{-}m^{1/2}$)	$J_q=J_{Ic}=R_{Ic}$ (kJ/m^2)
0.38	0.19	0.73	-
0.49	0.47	1.03	-
0.67	1.17	1.65	-
1.04	-	-	3.0
2.14	-	-	6.6

Table 2.8: Critical stress intensity factors of networks constructed with Epon 825 and the aromatic curing agent system.

M_c (kg/mol)	f_c	$K_q=K_{Ic}$ ($MPa\text{-}m^{1/2}$)
0.40	4	0.70
0.85	4	0.80
0.55	4	0.69
1.73	4	0.97
0.43	3	0.82
0.87	3	0.84

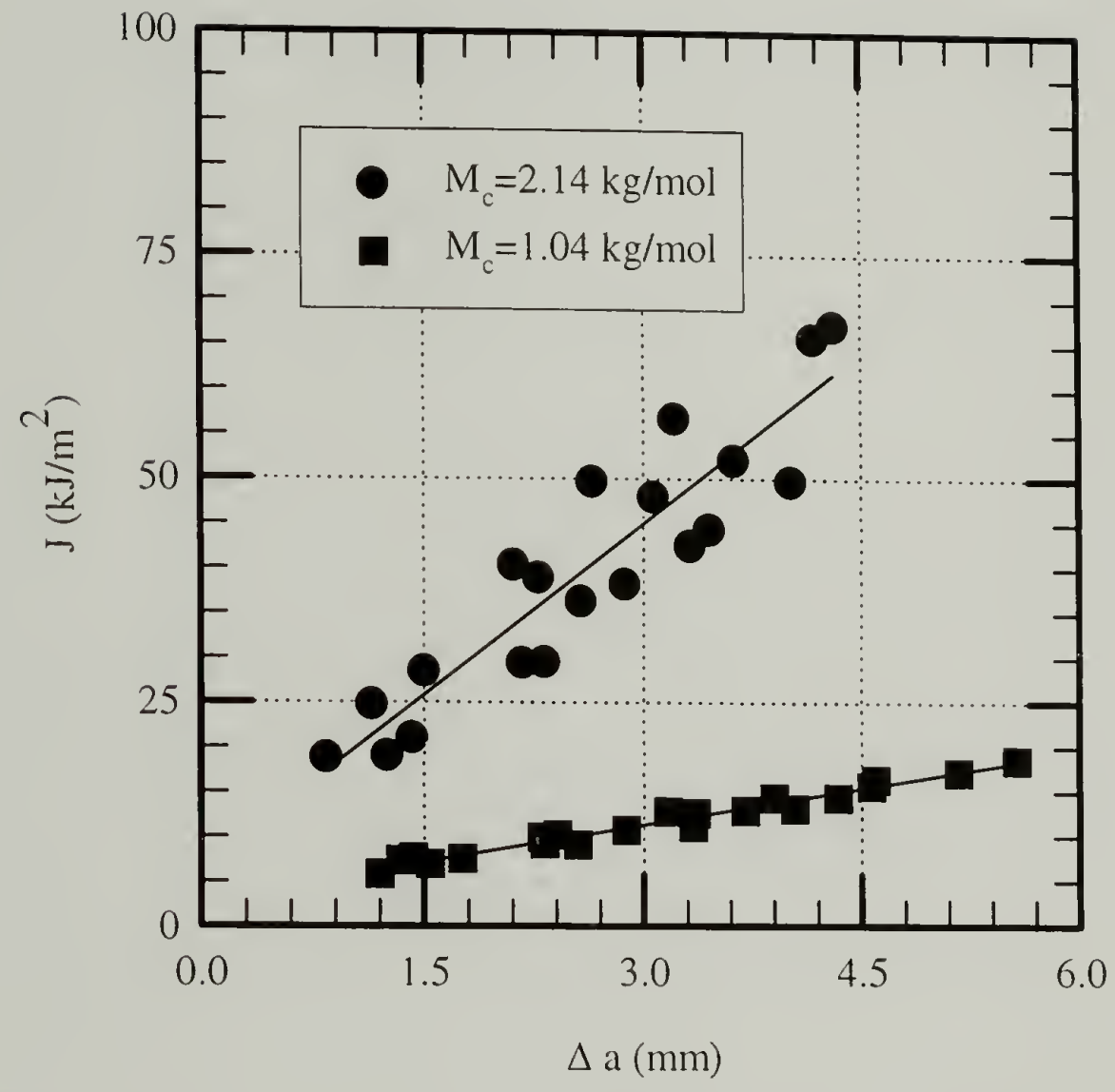

Figure 2.45: Non-linear elastic energy (J) versus crack extension for networks constructed with Epon 825, ethylenediamine, and 3-methoxypropylamine.

M_c=1.04 kg/ mol

Crack Growth Direction

M_c=2.14 kg/ mol

Figure 2.46: Side view of J Integral fracture specimens after testing under cross-polars for networks constructed with Epon 825, ethylenediamine, and 3-methoxypropylamine.

2.11.4 Fracture Toughness Models

Figure 2.47 is a plot of the fracture energy R_{Ic} (J_{Ic} or G_{Ic}) versus the tensile yield strength as a result of changes in M_c for networks created with Epon 825, ethylenediamine, and 3-methoxypropylamine. As the yield strength decreases, the energy required for crack propagation increases. Yielding in front of the crack tip is effectively blunting the stress intensification, increasing energy for crack propagation. The increasing scatter in the fracture energy data with decreasing yield strength is the result of the fracture process being dominated by the yielded zone ahead of the crack tip.[56] Figure 2.48 is a plot of the fracture energy of a network constructed with Epon 828 and the aromatic curing agent system as a function of temperature. The trend similarity in Figures 2.47 and 2.48 demonstrate how temperature and T_g, which control the yielding behavior (see equation 2.13) influence the measured fracture toughness. The crack tip blunting model[45] and the bimodal fracture model[47] can be used to describe the fracture toughness-yield strength relationship.

The crack tip blunting model is based on the idea that yielding in front of the crack tip can be modeled by a change in the radius of curvature of the crack.[45] From the stress equations describing the stress field ahead of a notch (blunt crack) with length (a) and radius of curvature (ρ), Kinloch and Williams[45] showed that the increasing fracture toughness can be expressed by equation 2.27.

$$\frac{K_{IB}}{K_{Ics}} = \frac{(1+\rho/2c)^{3/2}}{1+\rho/c} \qquad (2.27)$$

where: K_{IB} stress intensity factor for blunt crack
K_{Ics} stress intensity factor for a sharp crack
c critical distance ahead of the blunt crack..

Making use of equation 2.23, which holds for J_{Ic} as well, equation 2.27 can be written in terms of fracture energies, where the blunted crack fracture energy is taken as the measured fracture energy.

$$\frac{R_{Ic}}{G_{Ics}} = \frac{(1+\rho/2c)^3}{(1+\rho/c)^2} \qquad (2.28)$$

In terms of the crack tip blunting model, G_{Ics} can be expressed by equation 2.29.

$$G_{Ics} = \frac{\sigma_{tc}^2 2\pi c(1-\nu^2)}{E} \qquad (2.29)$$

where σ_{tc} is the critical stress at c.

The radius of curvature of a blunted crack can be approximated by equating ρ with the crack tip opening displacement expressed by equation 2.30.[36,57,58]

$$\rho \approx \delta_{tc} = \frac{R_{Ic}}{\sigma_{yt}} \qquad (2.30)$$

In Figure 2.49, the critical crack tip opening displacement for Epon 825/aromatic networks is plotted against the $f_c/(f_c-2)*M_c/2$, which is inversely proportional to the yield strength of the materials by equation 2.15. Figure 2.49 shows a linear relationship between δ_{tc} and the inverse of the material's ability to yield. Fischer[2] has also reported a linear relationship between the critical crack tip opening displacement and the molecular weight between cross-links with a similar range of critical crack opening displacements.

Substituting equation 2.30 into equation 2.28 results in equation 2.31.

$$\frac{R_{Ic}}{G_{Ics}} = \frac{\left(1+\frac{R_{Ic}}{2\sigma_{yt}c}\right)^3}{\left(1+\frac{R_{Ic}}{\sigma_{yt}c}\right)^2} \qquad (2.31)$$

Non-linear fitting to equation 2.31, for the data shown in Figure 2.47 results in the best c value of 0.64 μm and best G_{Ics} value of 0.28 kJ/m^2 (σ_{tc} = 340 MPa). Figure 2.47 shows a graphic representation of this fit. The c and σ_{tc} values are in agreement with the range of values, 0.1-1.0 μm and 220-500 MPa respectively, for various epoxy materials as reported by Kinloch and Williams.[45] In one study by Kinloch[36], the yield strength and hence fracture energy was controlled by changing the test temperature of an epoxy resin cured with piperidine. Since the yield strengths of various cross-linked samples can be collapsed as function of $T-T_g$[1,38], changing the T_g by altering the network structure at a given test temperature is basically equivalent to changing the test temperature of a cured resin system with a constant T_g. This collapsing yield behavior explains the similar c value between this study and the study by Kinloch.[36] Although the crack tip blunting model is effective in predicting the response, the physical significance of the parameters, c and σ_{tc}, still remain unclear. However, Kinloch[57] suggests that σ_{tc} can be viewed as a constrained yield strength.

The bimodal fracture model[47], which has been used to explain the increase in fracture energy with decreasing specimen thickness, is based on the idea that a material has two fracture toughness values. K_1 and R_1 represent the material's toughness in a highly constrained plane strain stress system in which there is a minimal amount of plastic deformation. K_2 and R_2 represent the material's toughness in a plane stress system in which there is no lateral constraint and hence more plastic deformation. In a fracture toughness specimen the amount of constraint varies through the thickness. The outer surfaces of the sample are in plane stress while the interior of the sample is in plane

strain. The depth of the plane stress layer can be approximated by the radius of the plastic zone (r_p) and correlates with the depth of the shear lips.[59]

$$r_p = \frac{1}{2\pi}\left(\frac{ER_{Ic}}{\sigma_{yt}^2}\right) \qquad (2.32)$$

Figure 2.50 shows top views of fracture specimens after testing at various temperatures for an Epon 828/aromatic network. The process zone increases in size with increasing temperature. The measured process zone shows a strong correlation with the predicted process zone (equation 2.32) as shown in Figure 2.51. The measured response, R_{Ic}, is a averaged value of R_1 and R_2 depending on the process zone size.

$$BR_{Ic} = (B - 2r_p)R_1 + 2r_pR_2 \qquad (2.33)$$

The original model suggests that the measured response should be a thickness averaged value of the stress intensity parameters, K_1 and K_2.[47] Subsequent models and experiments suggest that the measured response with a thickness averaged energy is more appropriate.[59] Since the definitions R_1 and G_{Ics} are basically the same, substituting equation 2.32 into equation 2.33 and replacing R_1 with G_{Ics} results in equation 2.34.

$$R_{Ic} = G_{Ics} + \left(\frac{ER_{Ic}}{B\sigma_{yt}^2}\right)\frac{1}{\pi}\left(R_2 - G_{Ics}\right) = G_{Ics} + \frac{\beta}{\pi}(R_2 - G_{Ics}) \qquad (2.34)$$

The β parameter in equation 2.34, first shown by Irwin[60,61], controls the brittle to ductile transition. For β values less than π, materials have lower fracture toughness values and a smaller percentage of shear lips. For β values greater than π, materials have higher fracture toughness values and a greater percentage of shear lips. Fitting the data shown in Figure 2.47 to equation 2.34, results in G_{Ics}=0.31 kJ/m^2 and R_2=10.98 kJ/m^2.

Both models are effective in describing the behavior, as shown in Figure 2.47, with basically identical values of G_{Ics}. In addition, the bimodal fracture model can predict a material's measured fracture toughness as a function of specimen thickness. However, the crack tip blunting model makes no direct statement with regards to specimen thickness. By comparing the two models, the parameters in the crack tip blunting model can be related to specimen thickness. For large values of $R_{Ic}/(2c\sigma_{yt})$, equation 2.31 can be simplified to equation 2.35.

$$\frac{R_{Ic}}{G_{Ics}} \approx \frac{R_{Ic}}{8\sigma_{yt}c} \qquad (2.35)$$

Large values of $R_{Ic}/(2c\sigma_{yt})$ correspond to large values of β. Since R_2 is much greater than G_{Ics}, equation 2.34 can be simplified to equation 2.36 for large values of β.

$$R_{Ic} \approx \left(\frac{ER_{Ic}}{\pi\sigma_{yt}^2 B}\right)R_2 \qquad (2.36)$$

Substituting equation 2.35 into equation 2.36 and solving for c results in equation 2.37.

$$c \approx \left(\frac{G_{Ics}\pi e_{yt}}{8R_2}\right)B \qquad (2.37)$$

where: e_{yt} yield strain.

The c parameter in the crack tip blunting model should be linearly proportional to specimen thickness. G_{Ics} is a constant and not affected by changes in either yield strength and or specimen thickness. Substituting equation 2.29, neglecting the Poisson's ratio effect, into equation 2.37 and solving for σ_{tc} results in equation 2.38.

$$\sigma_{tc} \approx \left(\frac{4R_2E}{\pi^2 e_{yt}}\right)^{1/2}\left(\frac{1}{B}\right)^{1/2} \qquad (2.38)$$

σ_{tc} should be inversely proportional to the square root of specimen thickness. With equations 2.37 and 2.38, the crack tip blunting model can now be used to predict specimen thickness effects.

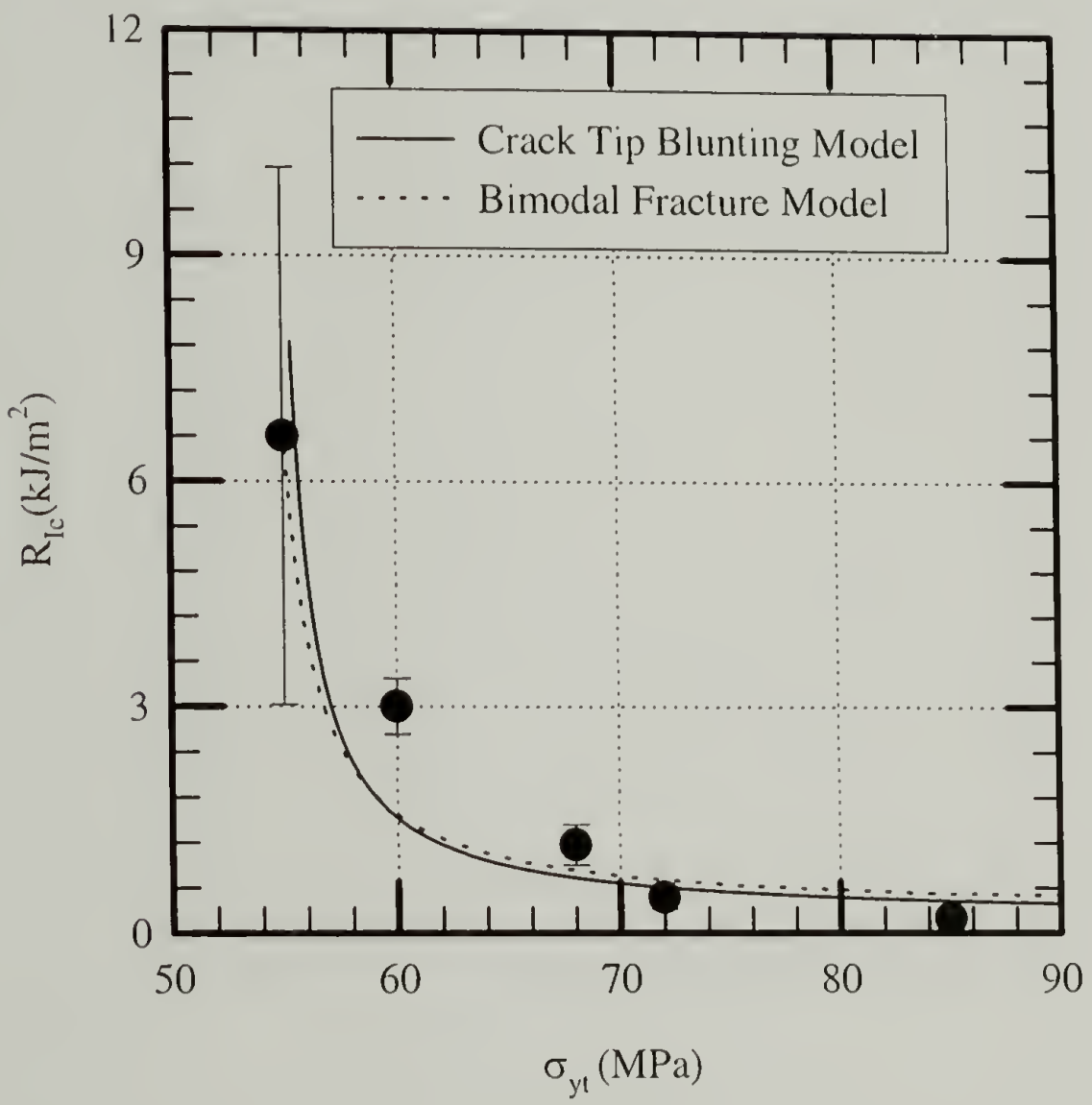

Figure 2.47: Fracture energy versus tensile yield strength for networks constructed with Epon 825, ethylenediamine, and 3-methoxypropylamine.

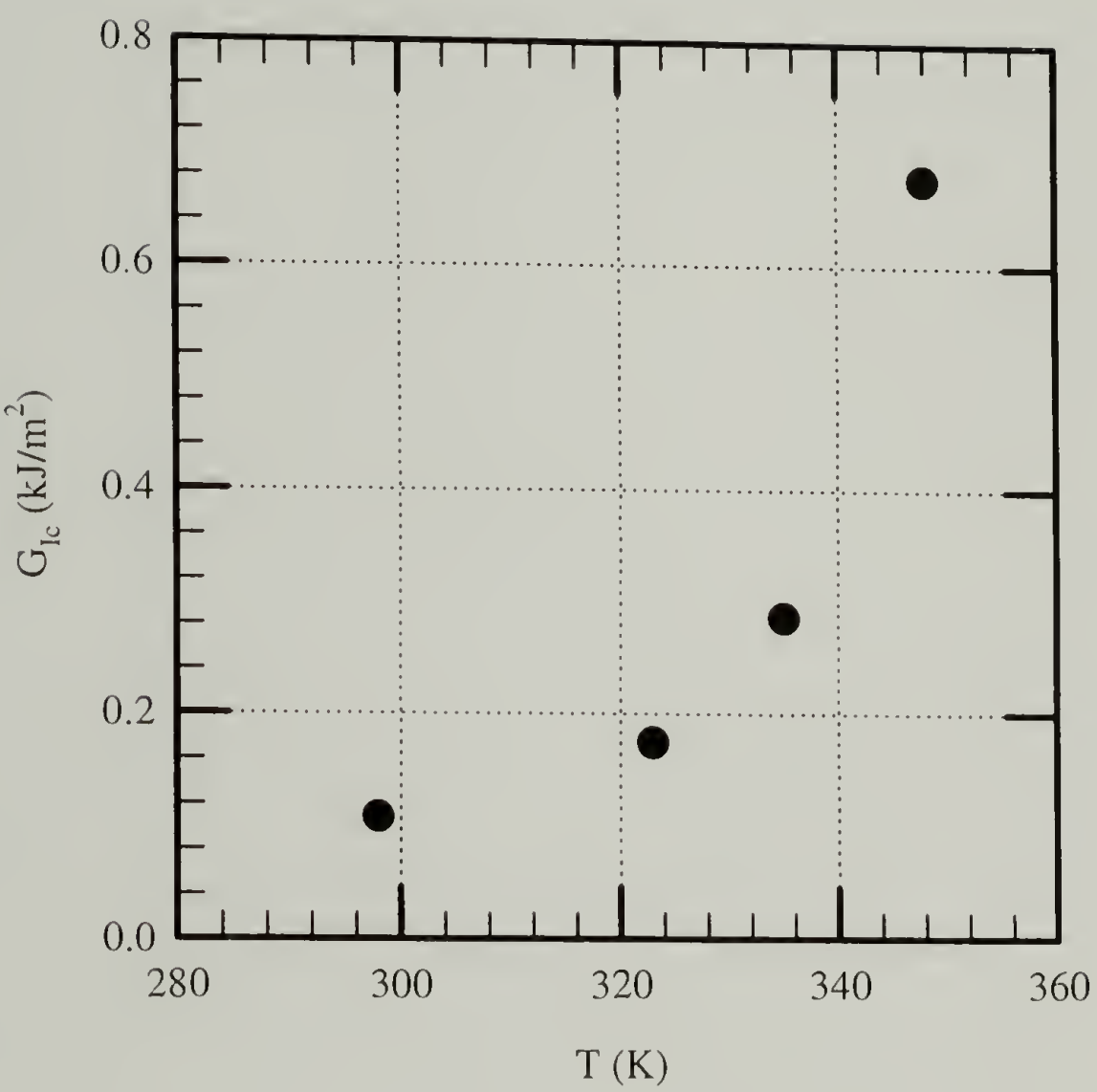

Figure 2.48: Fracture energy as a function of test temperature for an epoxy network formed with Epon 828 and the aromatic curing agent system (M_c=0.9 kg/mol).

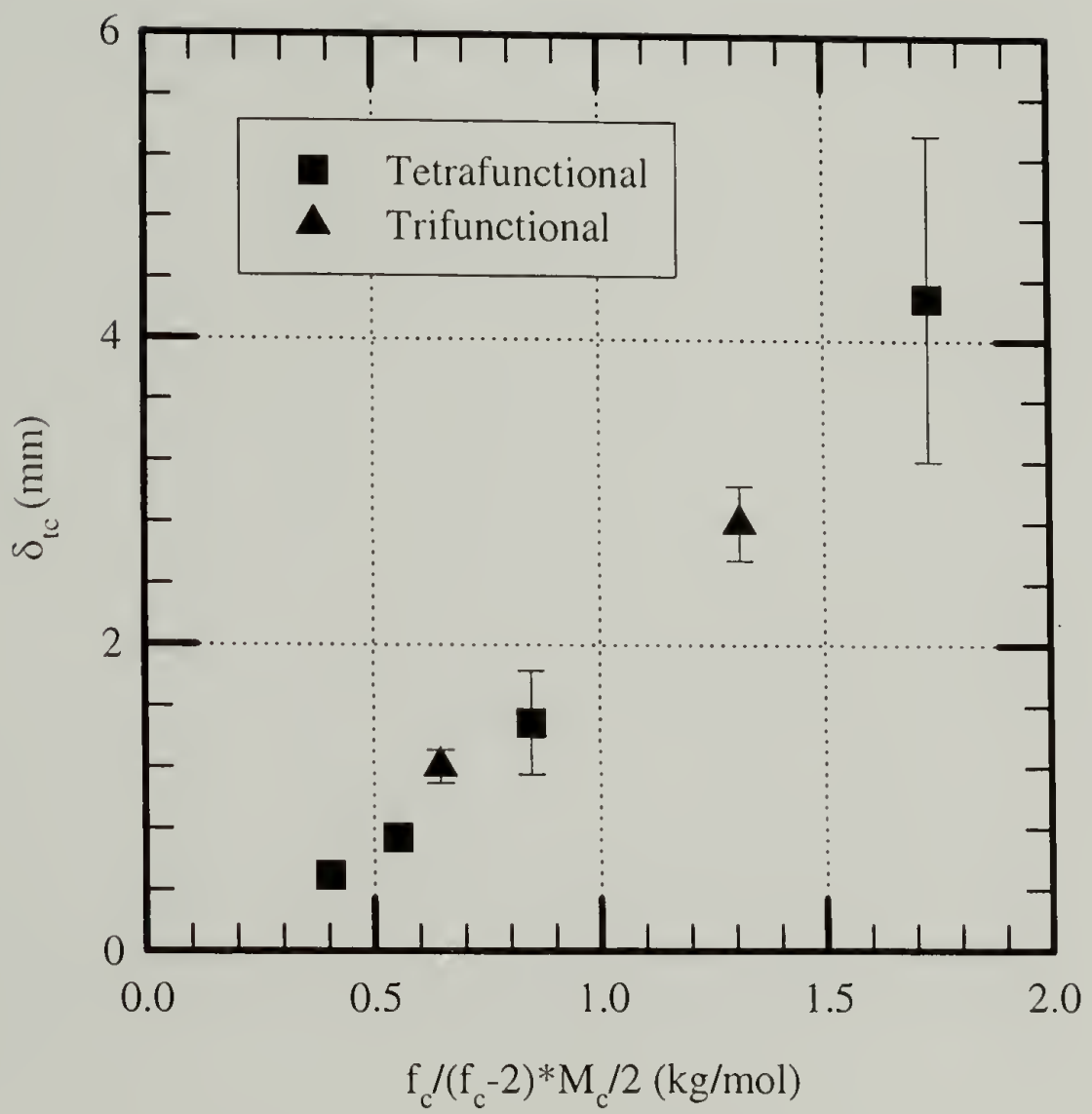

Figure 2.49: Crack tip opening displacement as a function of the inverse of the ability to yield.

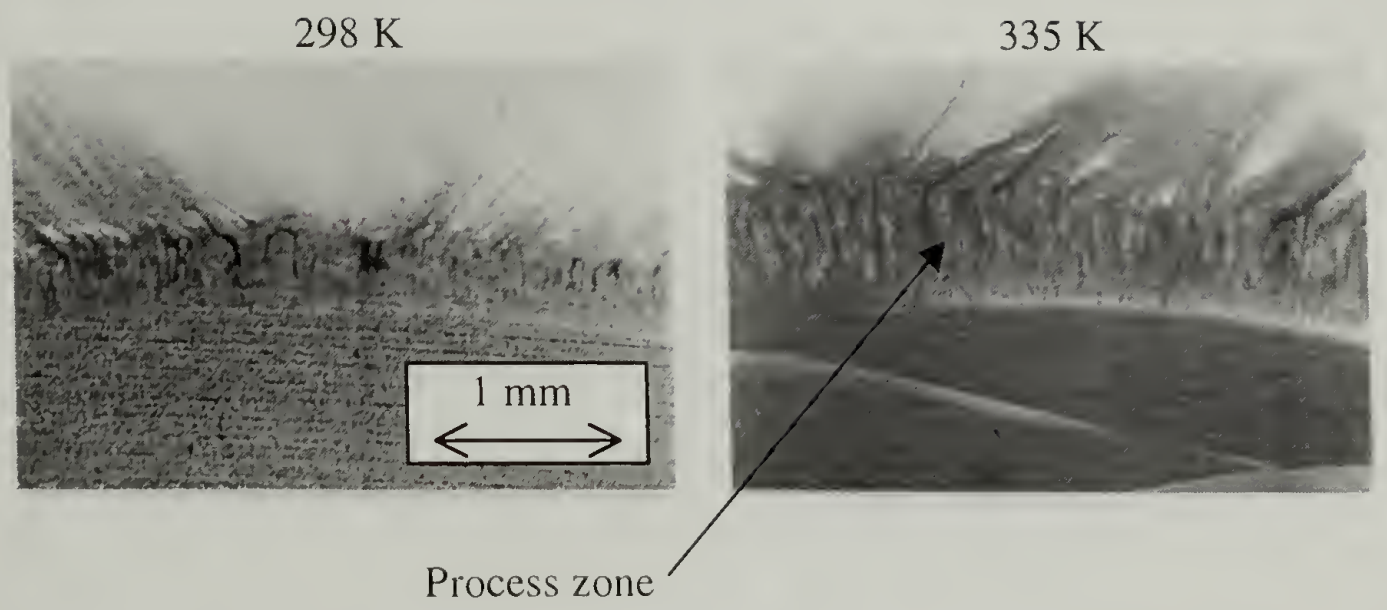

Figure 2.50: Top view of fracture specimen showing an increasing process zone size with increasing test temperature for a network constructed with Epon 828 and the aromatic curing agent system (M_c=0.9 kg/mol).

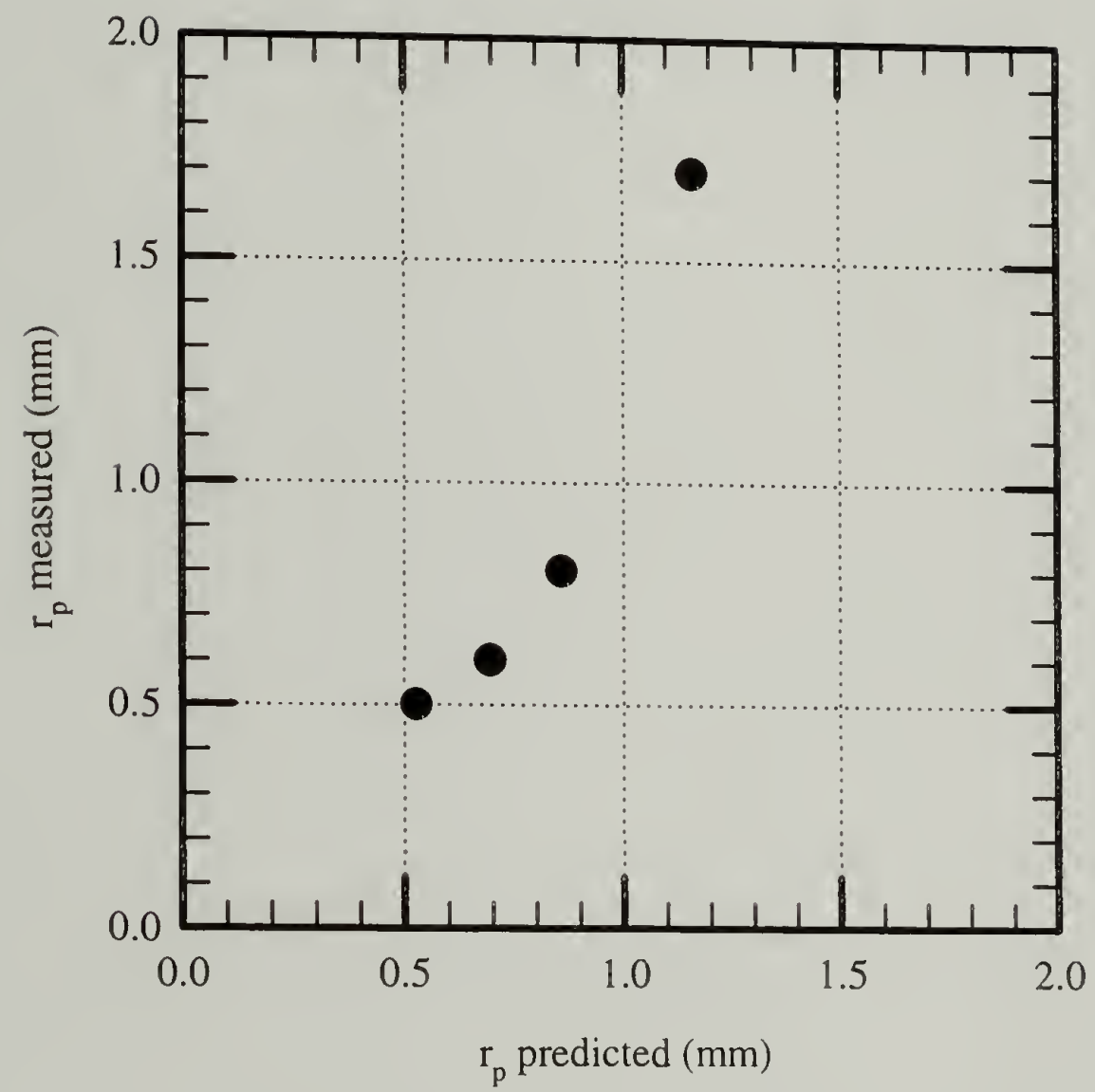

Figure 2.51: Predicted plastic zone size (equation 2.32) versus measured plastic zone size for a network constructed with Epon 828 and the aromatic curing agent system tested at various temperatures (M_c=0.9 kg/mol).

2.12 Instrumented Falling Weight Impact Test

2.12.1 Introduction

Instrumented impact testing of polymeric materials is used to assess a material's response at high loading rates. Despite its' prevalent use in the automotive and plastics industry, literature on instrumented impact testing is generally focused on Charpy or Izod test configurations,with the Gardner test or dropped dart test configuration receiving little attention.[62] Test geometry[63,64] and material[65,66] can influence both instrumented response and observed failure.

The Dynatup instrumented impact test consists of a clamped circular plate loaded transversely with a hemi-spherical dart or tup. This loading geometry results in "global" deformations and "local" deformations. The origin of "global" deformations can be associated with plate bending and the associated boundary conditions which affect it, while the origins of "local" deformation may be associated with biaxial necking and indentation and their associated boundary conditions. In order to understand these deformations, experiments are performed to evaluate the effect of dart radius. In addition, experiments investigating the combined effect of dart radius and epoxy cross-link density allow the relative importance of the "global" and "local" deformations upon failure mode and failure energy to be evaluated

2.12.2 Experimental Techniques

2.12.2.1 Instrumented Falling Weight Impact Tests

Instrumented falling weight impact tests were performed with a GRC Dynatup Model 8250 impact test machine. A 50 mm x 50 mm x 3.18 mm piece of material was placed into a pneumatic clamping fixture, GRC PNF Model 8250. The clamping fixture

had a 40 mm clamping diameter and was set to a 48 GPa clamping pressure. The material was then impacted with a 6.35 mm diameter hemi-spherical tup with a hammer mass of 3.26 kg from a height of 0.54 m. The response of the instrumented 3.5 kN high-strain gauge load cell tup was acquired at a data acquisition rate of 208 kHz. The displacement of the hammer (δ) was calculated by equation 2.39.[67]

$$\delta = v_o \tau - \frac{1}{M} \int_0^{\tau} \int_0^{\tau} F \, dt dt \qquad (2.39)$$

where: v_o impact velocity
τ time of interest
M mass of hammer
F force response of tup.

Five samples were impacted for each cross-linked material and the resulting force-displacement curves analyzed. The impacted samples were placed on black and white photographic print paper to make contact prints of the failure patterns.

2.12.2.2 Static Plate Bending Tests

A static plate bending fixture, modeled after the pneumatic clamping fixture for the impact work, was constructed for static plate bending tests be conducted with the Model 1123 Instron. The clamping fixture had a diameter of 40 mm, and clamping by a torque wrench ensured consistent boundary conditions at the clamping radius. Hemi-spherical carbon steel indenters were machined with radii of 1.59 mm, 2.38 mm, 3.18 mm, 3.97 mm, and 4.76 mm. Tests were performed at room temperature at a crosshead speed of 1 mm/min.

2.12.3 Impact Test Behavior

The instrumented falling weight impact tests provide additional information on the effect of M_c on material toughness. Figure 2.52 is a plot of the load deflection curves for the five networks with different M_c s constructed with Epon 825, ethylenediamine, and 3-methoxypropylamine. Ignoring dynamic effects, the initial response of all the networks can be modeled from simple rigid plate theory for a fixed end clamped circular plate under a concentrated load.[68]

$$K_p = \frac{P}{\delta} = \frac{4\pi E h^3}{3(1-\nu^2)R^2} \qquad (2.40)$$

where: K_p plate stiffness
P center line load
δ center line deflection
R radius of clamped plate (20 mm)
h plate thickness.

The simple rigid plate theory prediction is also plotted in Figure 2.52, using the average Young's modulus and average Poisson's ratio reported earlier. The simple rigid plate theory predicts the linear response of system, with a slight offset due to dynamic effects and with the deflection being an integrated response. The three most highly cross-linked samples failed in this first regime, while the lower two cross-linked samples exhibited another regime not predicted by plate theory. This additional deflection represents irreversible deformation as a result of local effects.

Integration of the load deflection response provides the energy required for failure (E_f). Figure 2.53 is a plot of E_f versus $1/M_c$. As M_c increases, the energy to failure increases. The energy required for failure displays the same trend with $1/M_c$ as the fracture energy (Figure 2.47). From dimensional analysis, the two measured properties are related by an area (A).

$$A = \frac{E_f}{R_{Ic}} \qquad (2.41)$$

Taking the slope of E_f versus fracture energy, shown in Figure 2.54, results in the best A value of 1500 mm^2, which would be dependent on the rate of the fracture testing and rate of the impact testing at a given temperature. However, it is interesting to note that the area of the clamped plate is 1300 mm^2. The type of failure mode displayed by the networks is also dependent on where the failure occurred in the load deflection tests, as shown in Figure 2.55. For the three highest cross-link density networks, the failure is dominated by radial cracks. The radial cracks arise as a result of surface flaws in combination with tensile bending stresses formed on the back side of the specimen. However, for M_c=1.04 kg/mol, a butterfly pattern was formed in addition to radial cracks and for M_c=2.14 kg/mol failure was achieved by penetration. Both "local" deformations and "global" deformations control the failures in the lightly cross-linked materials.

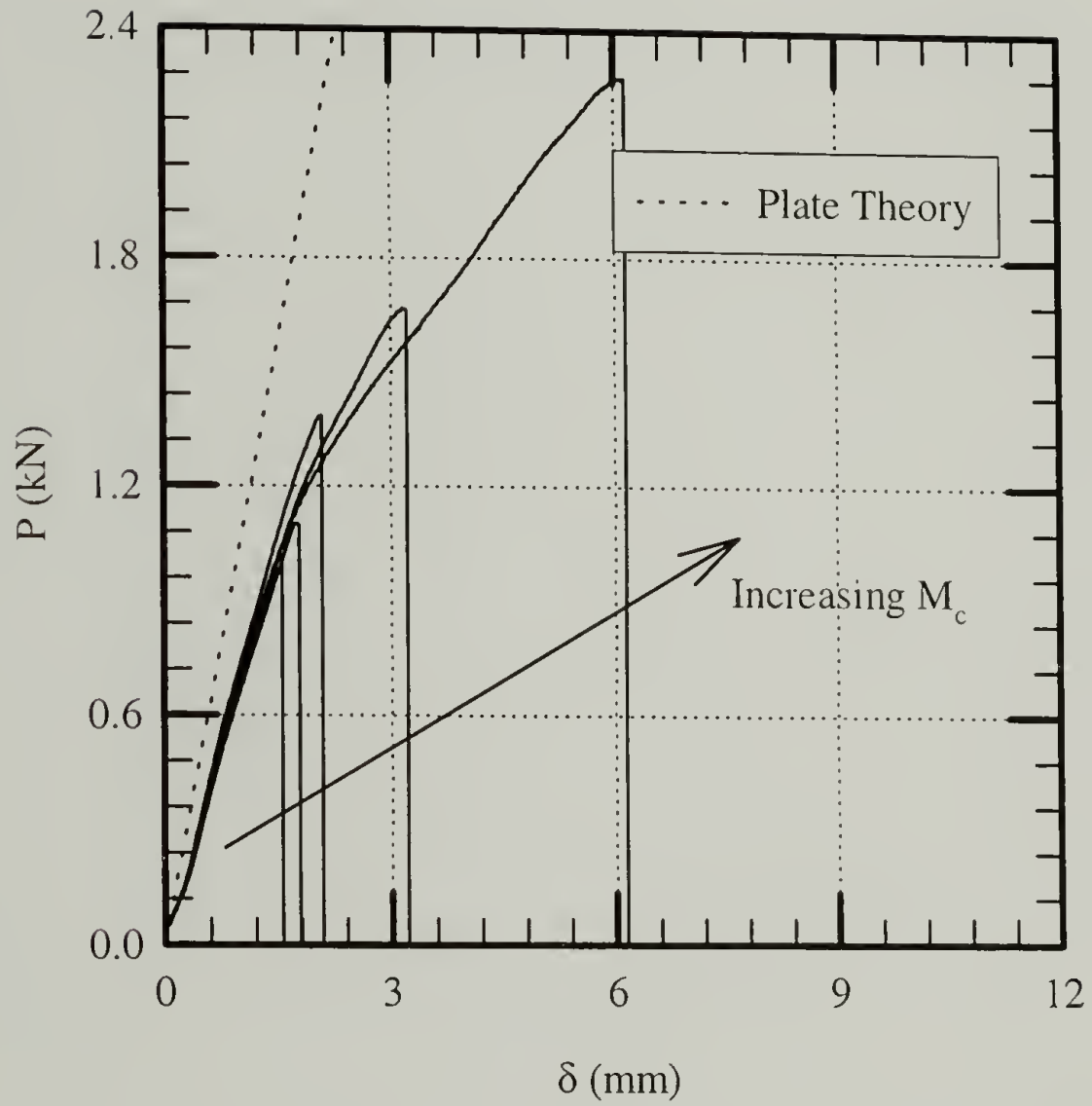

Figure 2.52: Instrumented impact test load deflection curves for networks constructed with Epon 825, ethylenediamine, and 3-methoxypropylamine (M_c=0.38, 0.49, 0.67, 1.04, 2.14 kg/mol).

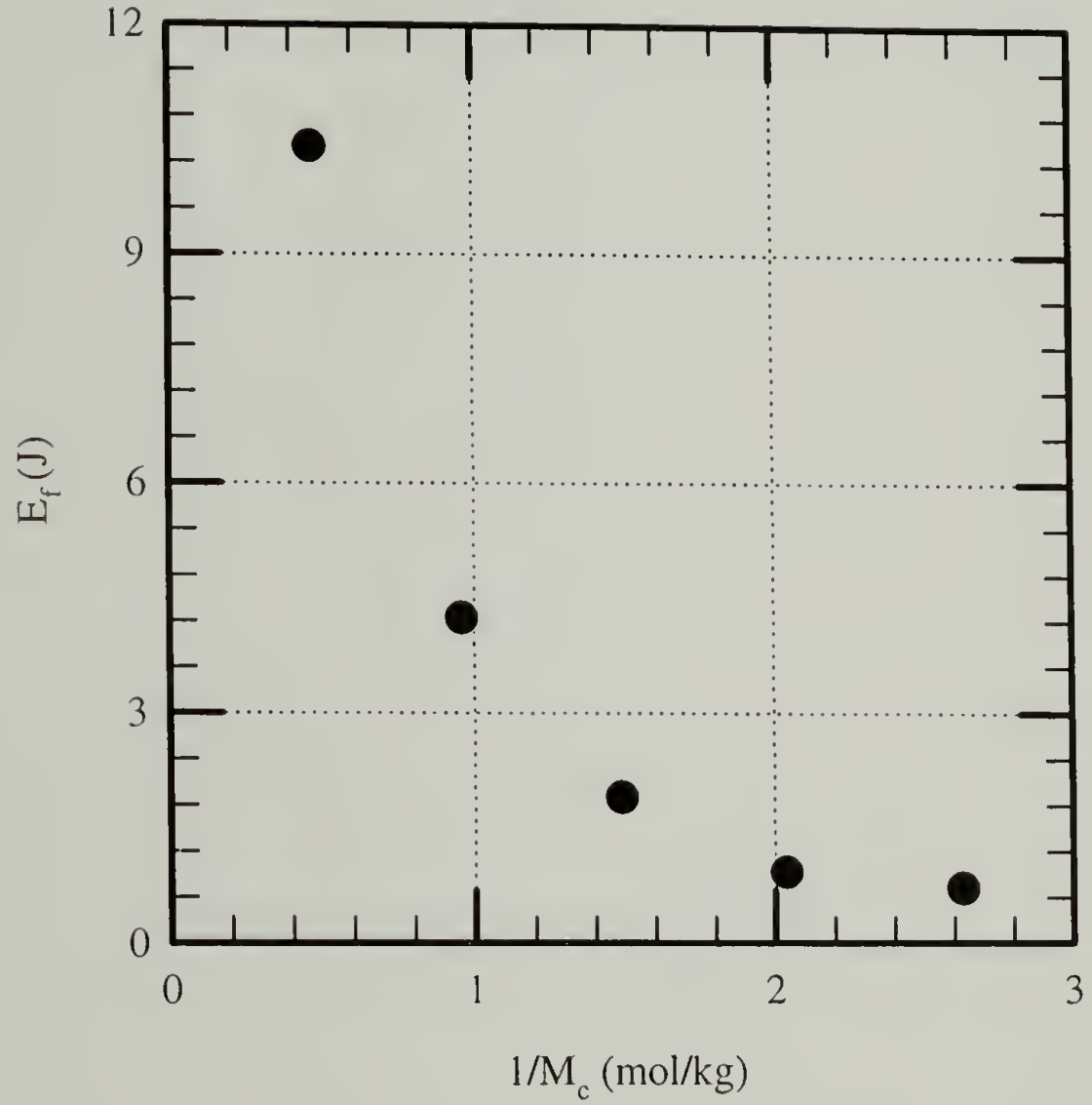

Figure 2.53: Instrumented impact failure energies for networks constructed with Epon 825, ethylenediamine, and 3-methoxypropylamine (M_c=0.38, 0.49, 0.67, 1.04, 2.14 kg/mol).

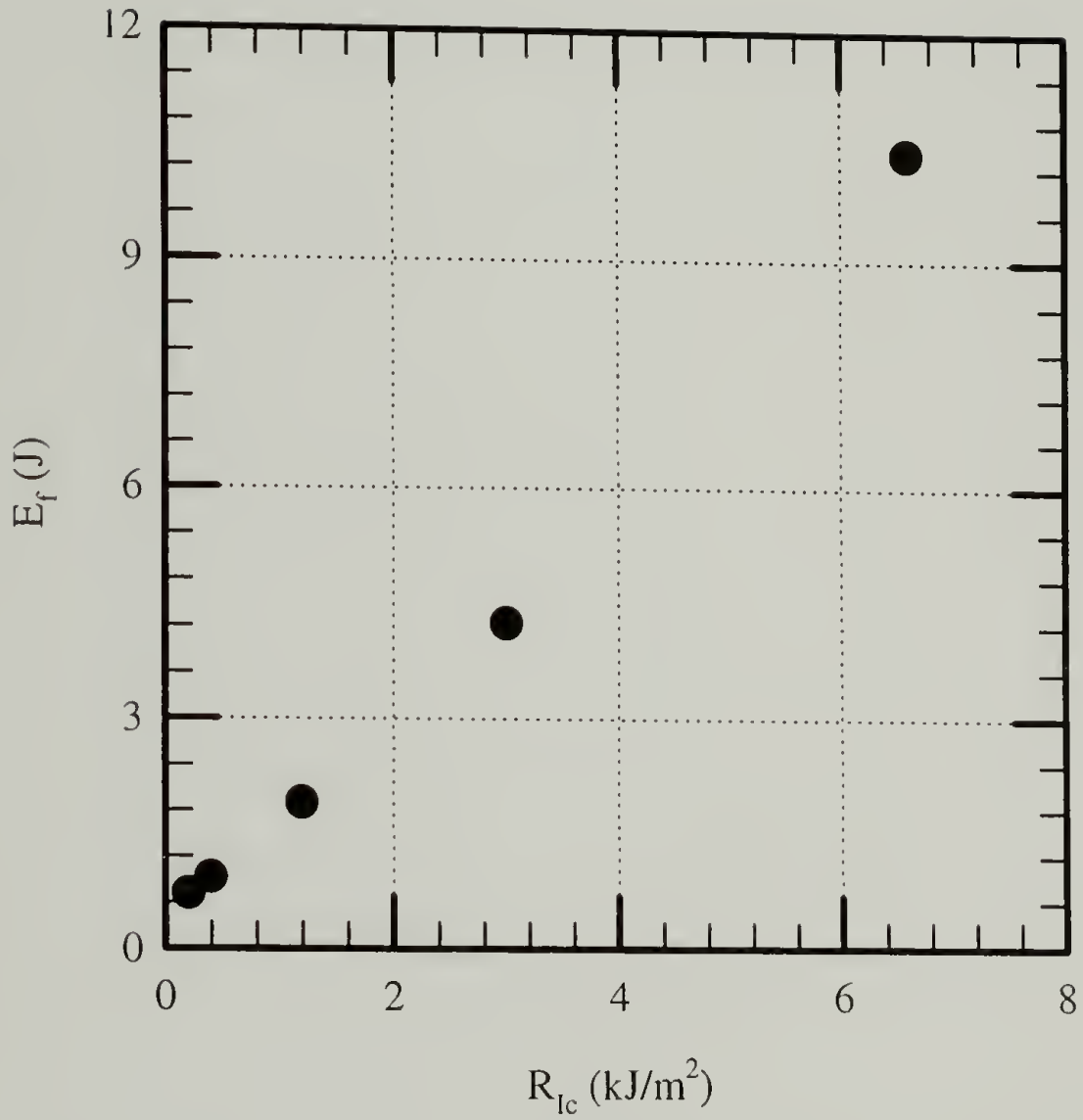

Figure 2.54: Instrumented impact failure energy versus fracture energy for networks constructed with Epon 825, ethylenediamine, and 3-methoxypropylamine (M_c=0.38, 0.49, 0.67, 1.04, 2.14 kg/mol).

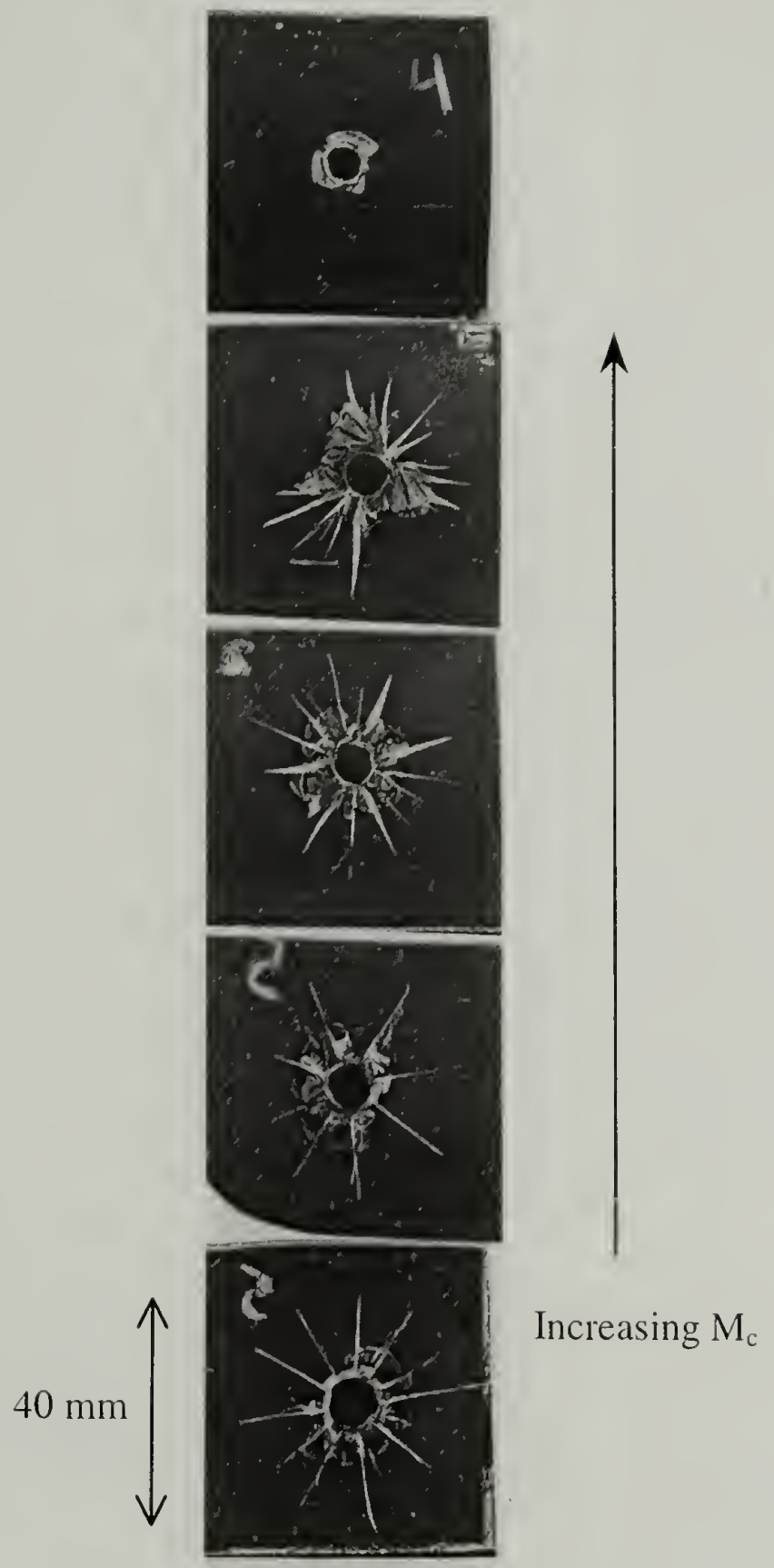

Figure 2.55: Instrumented impact failures ranging from brittle, low M_c, to ductile, high M_c, for networks constructed with Epon 825, ethylenediamine, and 3-methoxypropylamine (M_c=0.38, 0.49, 0.67, 1.04, 2.14 kg/mol).

2.12.4 Static Plate Bending Behavior

Static plate bending tests reveal the combined influence of network structure and testing geometry. Figure 2.56 shows the effect of tup radius on the response of a highly cross-linked network (M_c=0.49 kg/mol) constructed with Epon 825, ethylenediamine, and 3-methoxypropylamine. The deformation is comparable to the behavior seen in the instrumented impact test but with slightly higher deflections. The tup or indenter radius does not influence the first linear regime of the load deflection curve, yet an effect is noted in the response past the initial regime. The effect of tup radius on the response of a lightly cross-linked network (M_c=2.14) is shown in Figure 2.57. Again, the tup radius does not influence the initial linear regime. The influence of tup radius beyond the initial regime is more significant when compared with a highly cross-linked material. Increasing tup radius increases the deflection at failure in lightly cross-linked materials as well as the stiffness past the initial linear regime. Figure 2.58 shows the energy to failure as a function of tup radius and degree of cross-linking in networks constructed with Epon 825, ethylenediamine, and 3-methoxypropylamine. For highly cross-linked material, the effect of tup radius on E_f is negligible. This trend results from failure occurring in or near the initial linear regime of the load deflection response. As the cross-link density decreases, the effect of tup radius on E_f is more significant. The response is then dominated by local deformations such as drawing around the tup.

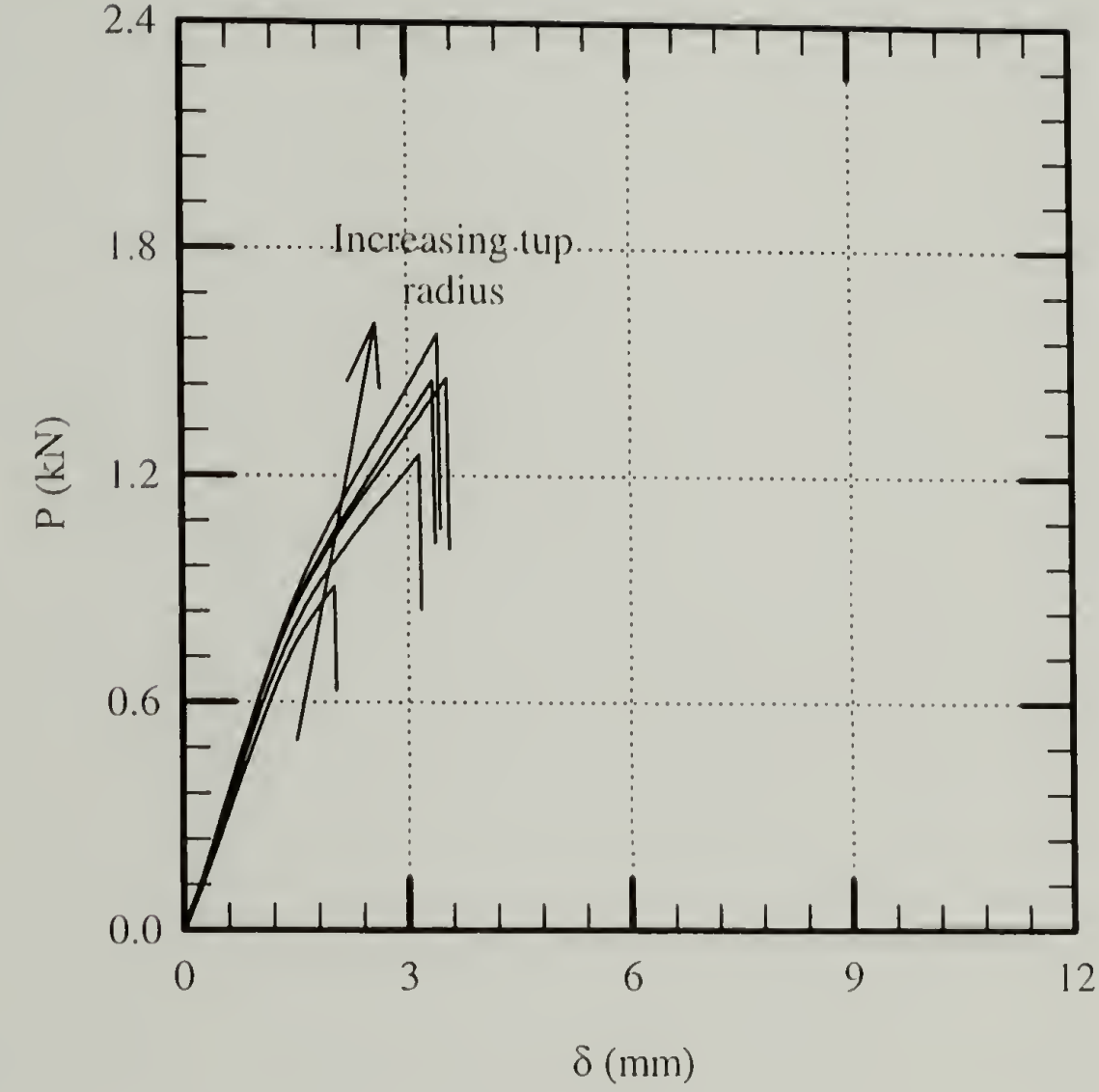

Figure 2.56: The effect of tup radius on the response of a highly cross-linked network (M_c=0.49 kg/mol) during a static plate bending test.

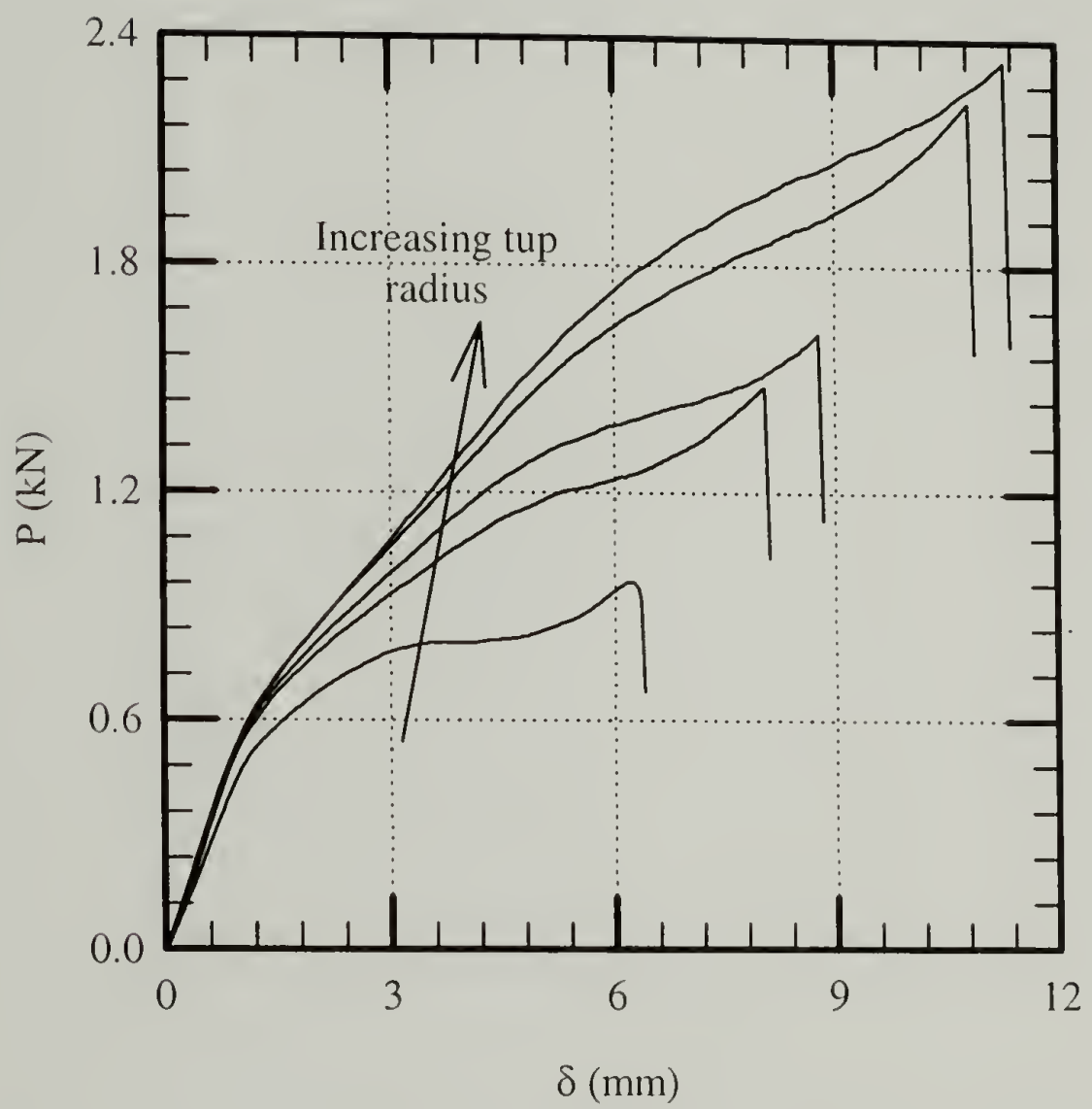

Figure 2.57: The effect of tup radius on the response of a highly cross-linked network (M_c=0.49 kg/mol) during a static plate bending test.

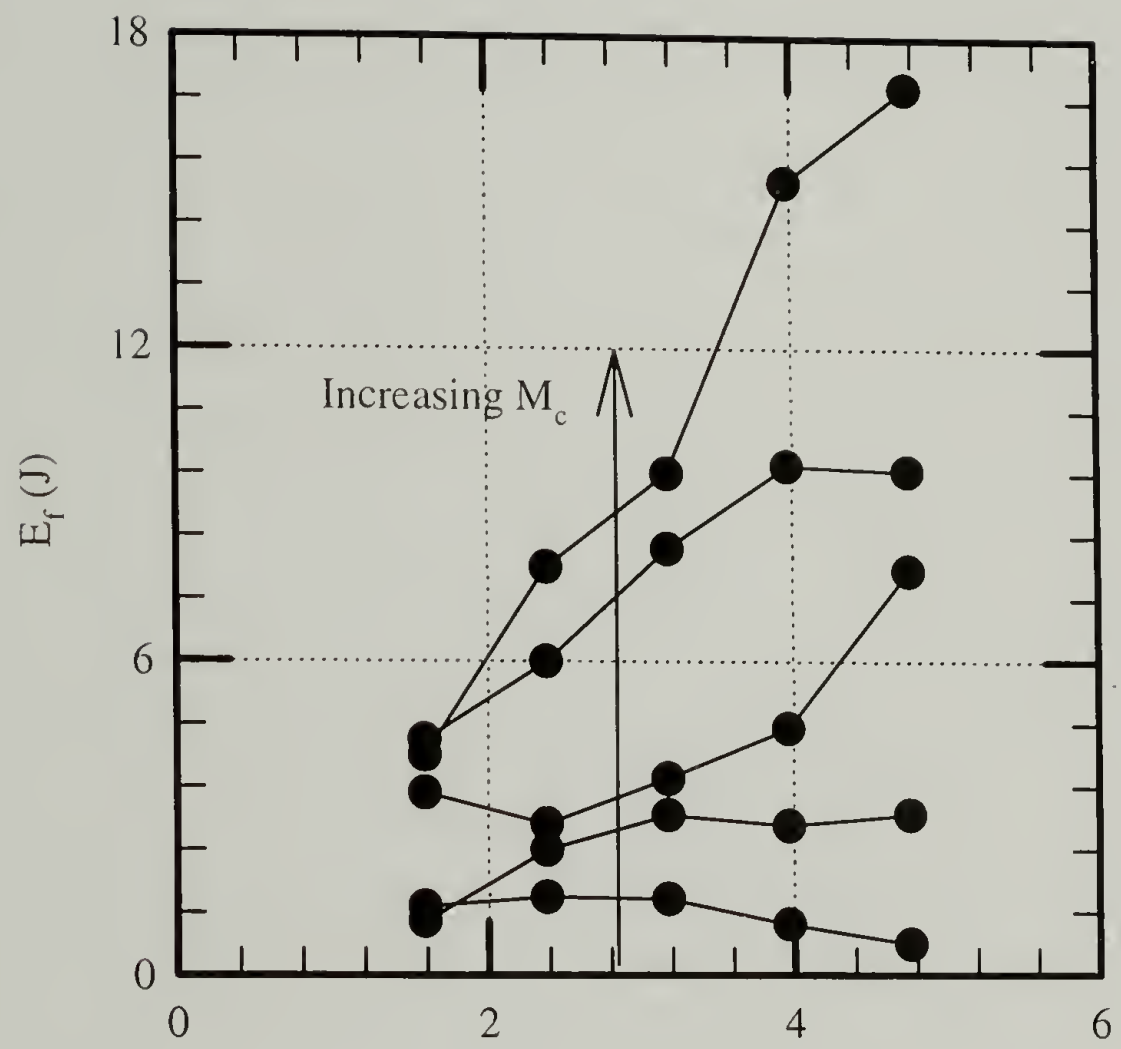

Figure 2.58: Combined effect of tup radius and M_c on the energy to failure during static plate bending tests.

2.13 Indentation Behavior

2.13.1 Introduction

Indentation tests were performed on the different cross-linked networks with carbon steel balls of various radii. The motivation of this portion of the study was to probe the "local" deformational characteristics of these materials. Characteristics of interest were the load deflection response and the network failure mechanisms under an indentation loading condition.

2.13.2 Measurement Techniques

Indentation tests were performed at room temperature on 50 mm x 50 mm x 3.18 mm plaques with carbon steel balls of different radii. The radii of the steel balls were 1.59 mm, 2.38 mm, 3.18 mm, 3.97 mm, and 4.76 mm. Plaques were placed on a compression platen and indented until failure with the various radii steel balls driven by a Model 1123 Instron operating at a crosshead speed of 1 mm/min at room temperature. The networks in this study were constructed from Epon 825, ethylenediamine, and 3-methoxypropylamine (M_c=0.38, 0.49, 0.67, 1.04, 2.14 kg/mol).

2.13.3 Theory

The load deflection response of a material under indentation can be divided into three regimes which are characterized by the mean contact pressure (p_m), the compressive yield strength (σ_{yc}), and the constraint factor (C).[69] The mean contact pressure is defined in equation 2.42.

$$p_m = \frac{P}{\pi a^2} \qquad (2.42)$$

where: P contact load
a contact area radius.

The constraint factor is defined as the ratio between the mean contact pressure and the compressive yield strength of the material. The three regimes of the load deflection curve are discussed below.

2.13.3.1 Regime 1 (Elastic): $p_m \leq \cong \sigma_{yc}$

Equations 2.43-2.45 describe the elastic response of an isotropic, linear elastic half space loaded normally with spherical ball of radius, r.[70]

$$\delta = \left(\frac{9}{16r}\right)^{1/3}\left(\frac{P}{E^*}\right)^{2/3} \qquad (2.43)$$

$$\frac{1}{E^*} = \frac{\left(1-\nu_m\right)}{E_m} + \frac{(1-\nu_i)}{E_i} \qquad (2.44)$$

$$a^2 = \delta\, r \qquad \text{for } \delta < r \qquad (2.45)$$

where: δ penetration depth
P contact load
E^* effective modulus of contact system
E_x Young's modulus of material (m) and indenter (i), respectively
ν_x Poisson's ratio of material (m) and indenter (i), respectively
a radius of contact area.

2.13.3.2 Regime 2 (Constrained Plastic Zone): $\sigma_{yc} \cong p_m \leq C\sigma_{yc}$

Plastic deformation occurs beneath the surface and the affected zone is encased by elastically strained material. The response of a material in this regime is quite complex due to the pressure dependent nature of the yield locus and the complex stress field underneath the spherical indenter. Recent studies by A. C. Fischer-Cripps[71] suggest the use of an empirical equation to fit the response of this regime.

2.13.3.3 Regime 3 (Unconstrained Plastic Zone): $p_m \geq C\sigma_{yc}$

Plastic flow is no longer constrained beneath the indenter. The radius of the circle increases, keeping p_m/σ_{yc} a constant. A residual depression is left in the material upon unloading, and the structure of the depression is related to the maximum load experienced. The critical load corresponding to full plastic flow (P_y) with a constraint factor of 3 can be deduced from equation 2.43-2.45.

$$P_y = \left(\frac{9}{16}\right)\left(\frac{r}{E^*}\right)^2 \left(3\pi\,\sigma_{yc}\right)^3 \qquad (2.46)$$

Modeling of the response in this regime is dependent on the shape of the indenter.[69] If the indenter is sharp (cone or pyramidal), a cutting mechanism occurs beneath the indenter along with material pile up at the point of indentation. With blunt spherical indenters, the plastic deformation is compressive, with the volume change of indentation taken up by the elastic strains in the sample. The expanding cavity model first suggested by Marsh[72] and latter expounded on by Johnson[73] has been used to model the behavior of this regime. The model itself is based on the work by Hill[74], which describes the expansion of a hydrostatically pressurized cavity in an elastic-plastic medium. This model gives insight but cannot be used quantitatively due to a violation of geometric similarity and effects of the platen. Also, polymeric materials are known to undergo densification plasticity during indentation[75], a feature which violates the model's assumption of an incompressible plastic region.

2.13.4 Network Responses

According to equation 2.46 the majority of the load deflection curve corresponds to regime 3 since the networks were taken to failure. Assuming the penetration is all plastic allows the radius of the contact area (a) to be calculated by geometry.

$$a = \sqrt{2r\delta - \delta^2} \qquad (2.47)$$

To take into account the elastic penetration, a cyclic loading procedure can be used to separate the total penetration into an elastic component and a plastic component; the procedure assumes unloading is completely elastic.[76,77] Only half of the elastic penetration results in an increase in the radius of contact as calculated from geometry. Therefore, equation 2.47 slightly overestimates the contact area. In order for p_{in}/σ_{yc} to be a constant, the load deflection curve should be described by equation 2.48.

$$P = C\sigma_{yc}\pi a^2 = \lambda \pi a^2 \qquad (2.48)$$

Using 5 different radii indenters, Figure 2.59 plots of P versus calculated contact area (equation 2.47) for a network constructed with Epon 825, ethylenediamine, and 3-methoxypropylamine (M_c=0.67 kg/mol). This approach collapses much of the data, until a critical area is reached and the load begins to rise until failure occurs. This phenomena, which results in non-linearity, may be an influence of the compression platen, since the epoxy plaques are relatively thin and train hardening. The critical area along with the critical load increases with an increase in the radius of the indenter. Linear regressions were performed on the initial regions (from 2 times the load value to 5 times the load value predicted by equation 2.46) of Figure 2.59 and the average slope (λ) recorded. This procedure was repeated for 5 different M_c networks constructed with Epon 825, ethylenediamine, and 3-methoxypropylamine. The slope (λ) of the regression

line is related to the compressive yield strength of the networks through equation 2.48. Figure 2.60 is the plot of the average slope (λ) for the networks versus their respective compressive yield strength. The slope of this plot represents the constraint factor and is equal to 2.3, which is relatively close to value of 3 reported for ductile metals.[69]

The failure mode or erack morphology of a material changes as the contact ehanges from an elastic contact to an elastic/plastic contact. In the case of an elastic contact failure, a eone craek forms just outside the radius of contact due to tensile stresses.[70] In the ease of an elastie/plastic contact, failures can occur by the formation of median, lateral, and radial craeks.[75] Failure in all the epoxy networks occurred via the formation of a median crack underneath the indenter. Figure 2.61 shows a typical cross-sectional view of the median craek formed as a result of indentation. The lowest cross-link density material exhibited a unique failure mode. A complex band of radiating micro-eraeks formed in addition to the median crack. This unique behavior is shown in Figure 2.62 with the indented materials viewed underneath cross-polars and compared with the behavior of the other networks. This micro-cracking could be a result of extensive shear band interactions leading to the formation of the micro-cracks. Quantitative analysis of indentation failure in the elastie-plastic regime is difficult. If the failure occurs by the formation of median and lateral cracks the problem is even more diffieult. Median and lateral cracks are generally nueleation limited as opposed to radial eracks that are eontrolled by preexisting surfaee flaws.[78] Figure 2.63 is a plot of the failure load versus indenter radius for the networks. A linear relationship exists between the critical load and the radius of the indenter. Higher failure loads are associated with higher yield strength materials, suggesting that plastic deformation is affecting the failure

response. The trends and failures observed during indentation are not consistent with the trends and failures observed in the instrumented impact test. The failures in the instrumented impact test are dominated by global deformations and local deformations arising from drawing around the tup.

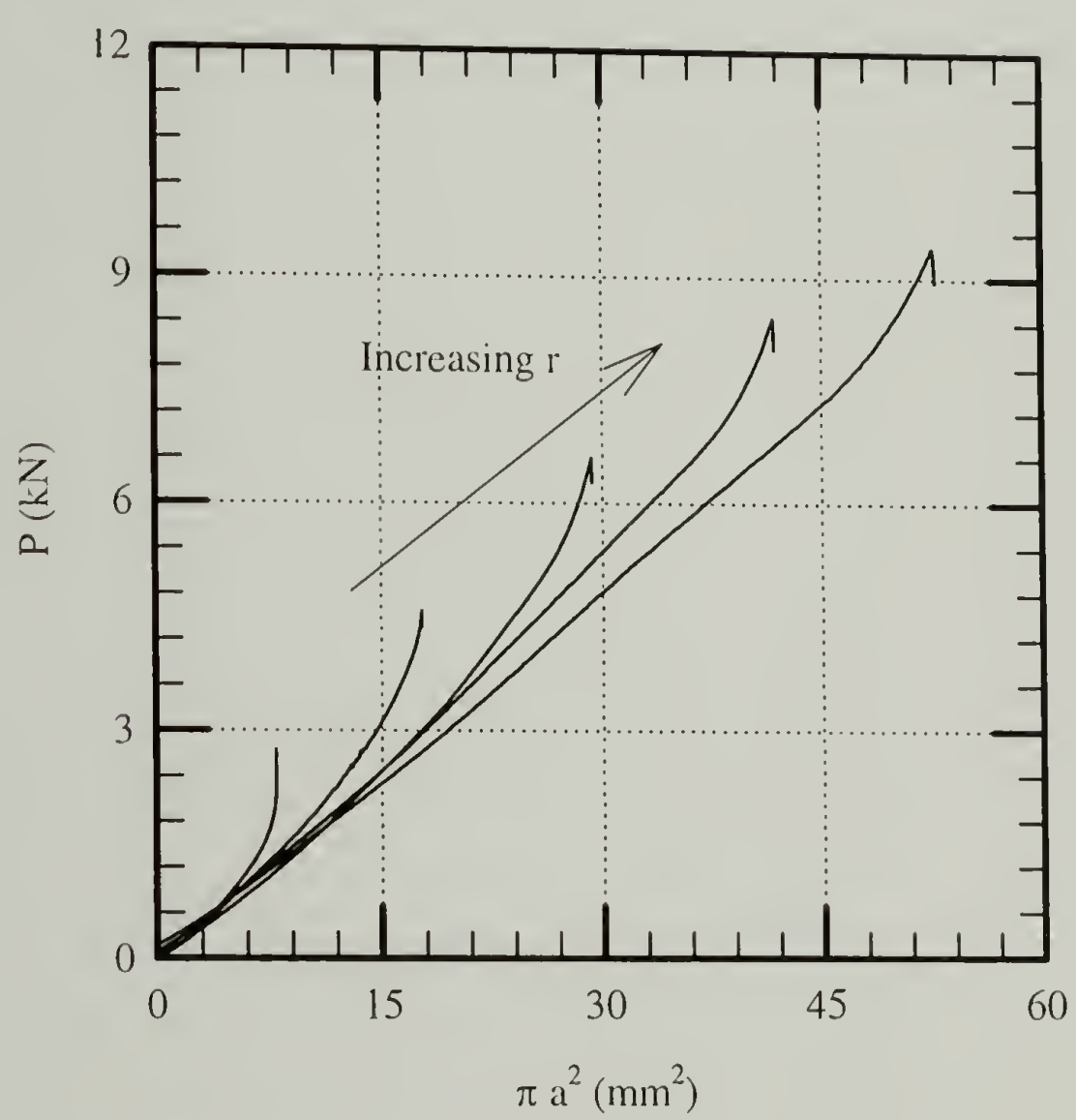

Figure 2.59: Load versus predicted contact area based on total plastic deformation for 5 different radii spherical indenters with M_c=0.69 kg/mol network.

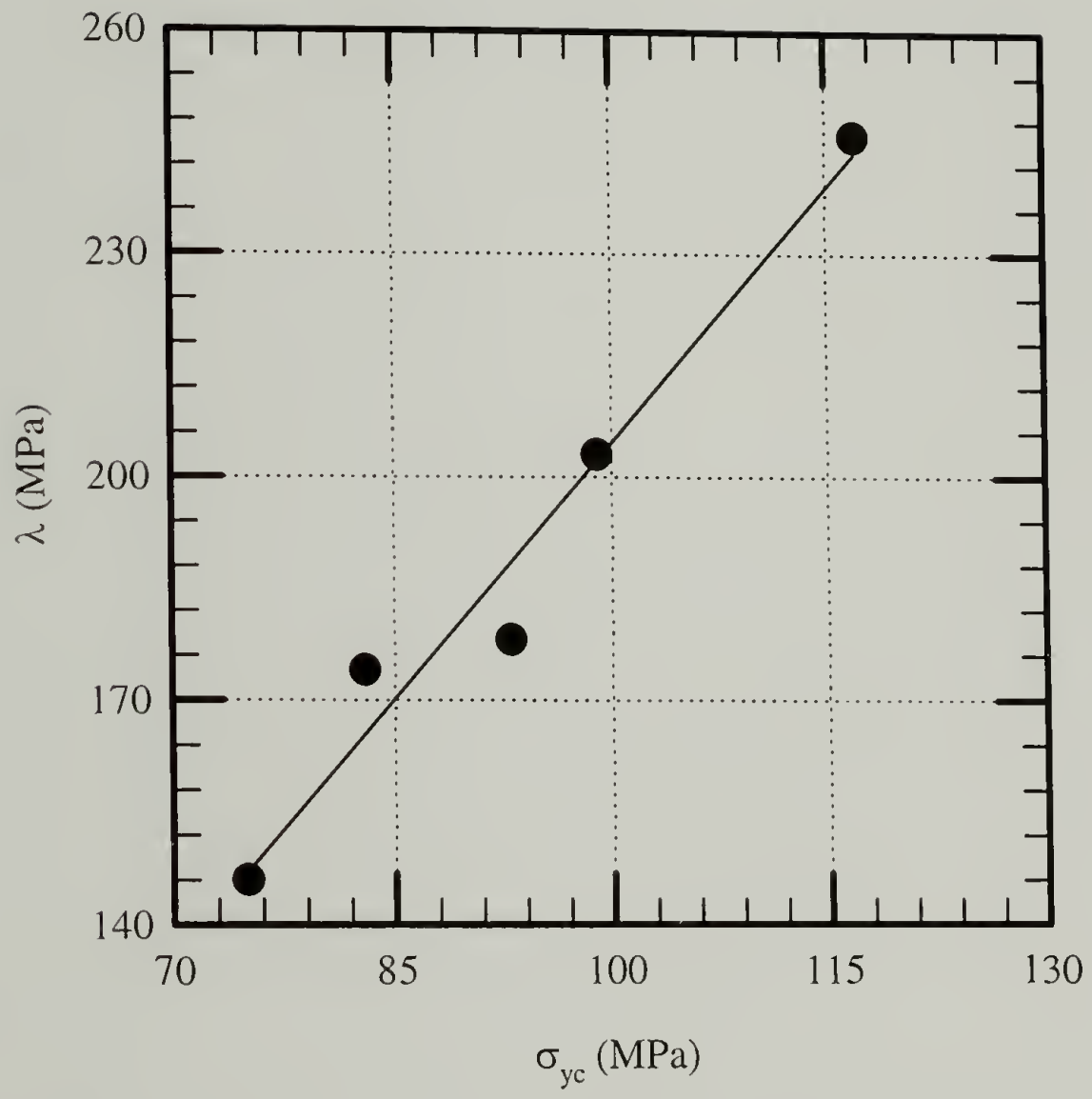

Figure 2.60: Indentation response, λ versus the compressive yield strengths of the networks.

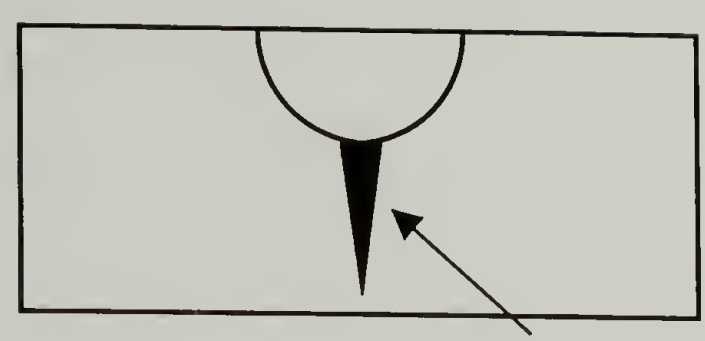

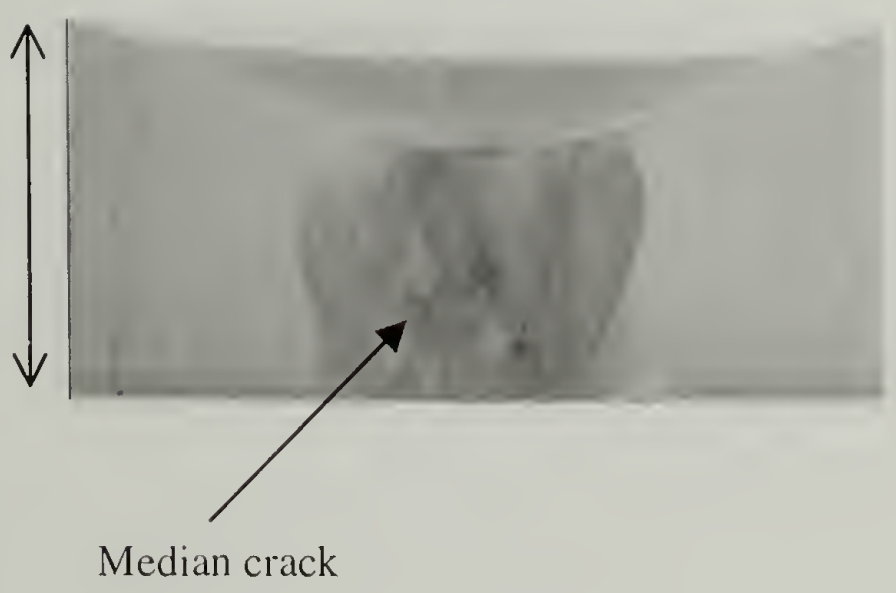

Figure 2.61: Median crack formed under indentation for M_c = 0.49 kg/mol and r = 3.97 mm.

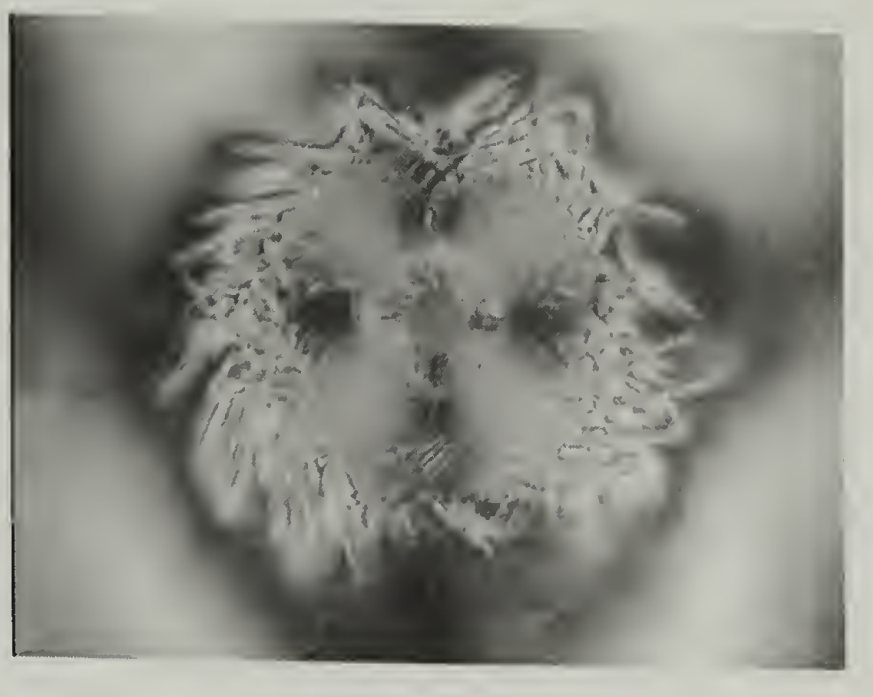

$M_c = 2.14$ kg/mol

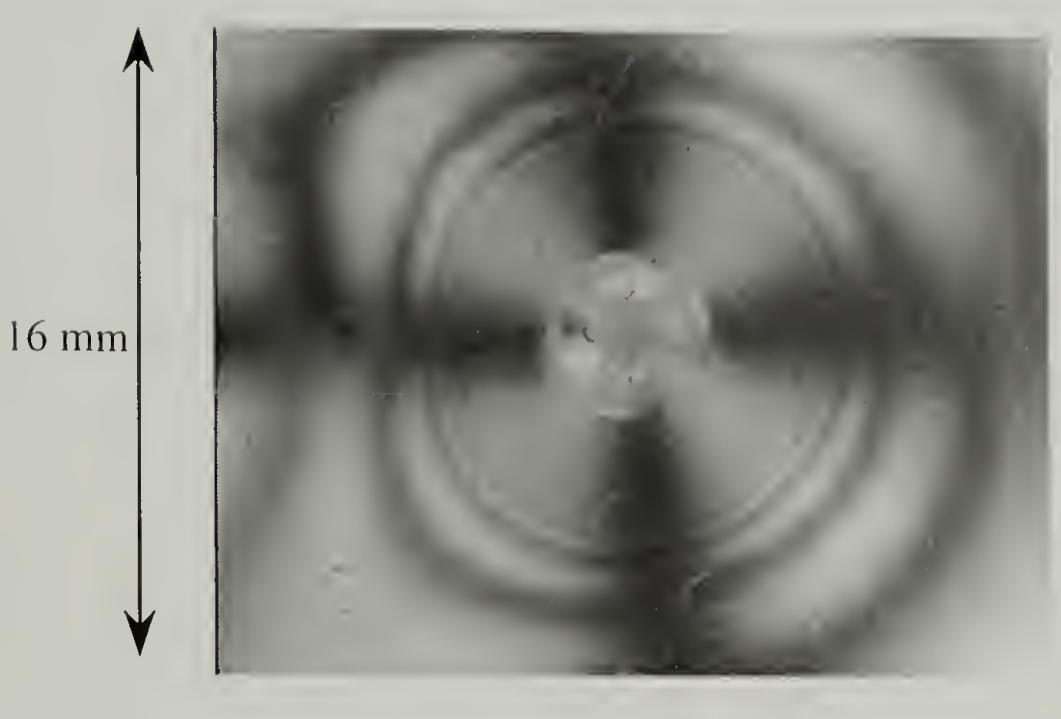

$M_c = 0.97$ kg/mol

Figure 2.62: Indentation failures for M_c=2.14 kg/mol and M_c=0.97 kg/mol with r=3.97 mm viewed under cross-polars.

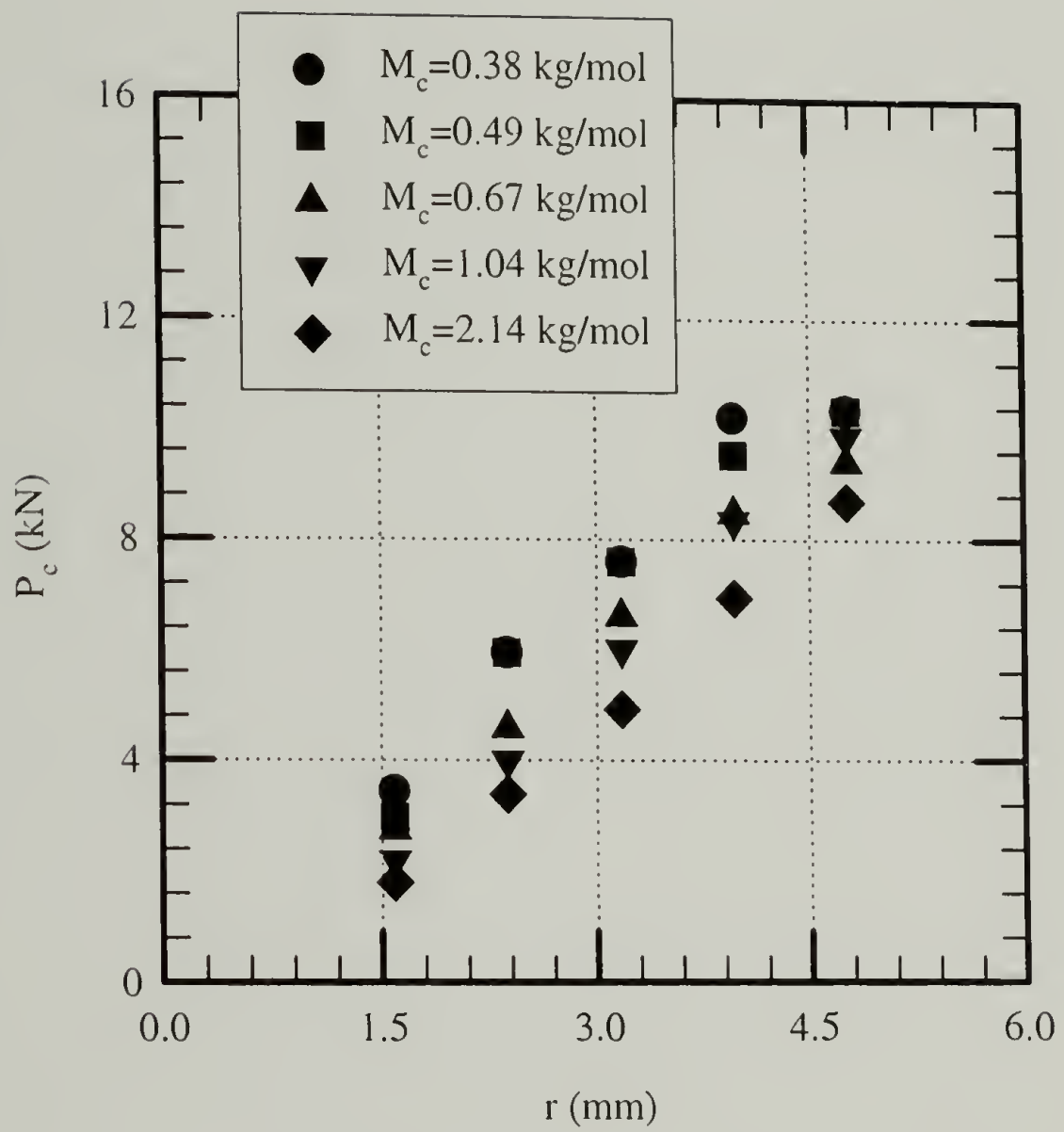

Figure 2.63: Indentation failure load versus ball radius for different networks.

CHAPTER 3

MICROSCOPIC SCALE INVESTIGATION

3.1 Introduction

The mechanical and thermal characteristics of amorphous polymeric materials are influenced by changes on the microscopic scale. Addition of soft rubber inclusions into glassy polymer matrices has been successfully employed to create tougher materials over the past five decades. Despite the wide use of rubber toughening agents in polymeric matrices, from polystyrene to polycarbonate, the relative importance and sequence of toughening mechanisms are not understood. The mechanisms of rubber toughening are dependent on the molecular nature of the matrix phase. Wu[79] showed that matrices with high entanglement densities deform by shear yielding (shear banding), while matrices with low entanglements densities deform by crazing. Rubbery inclusions provide additional mechanisms: stress intensification, cavitation (debonding), and inelastic void growth. Figure 3.1 shows the effect of particle size on toughening, and in particular the bounds of toughening effectiveness.

The lower bound of the toughening window has been attributed to rubber particle cavitation, while the upper bound of the toughening window has been attributed to yielding in between particles.[80] The work conducted in this investigation focuses on the lower bound of the toughening window with matrix materials having high entanglement densities. The objective of this investigation is to develop experimental methods to measure macroscopic mechanical responses and relate these responses to micro-mechanical toughening models. Studies in this investigation include the liquid rubber modification of epoxy networks, tensile dilatometry, the stress whitening behavior of a

rubber toughened polyvinylchloride, and the fracture and yield behavior of voided epoxy materials.

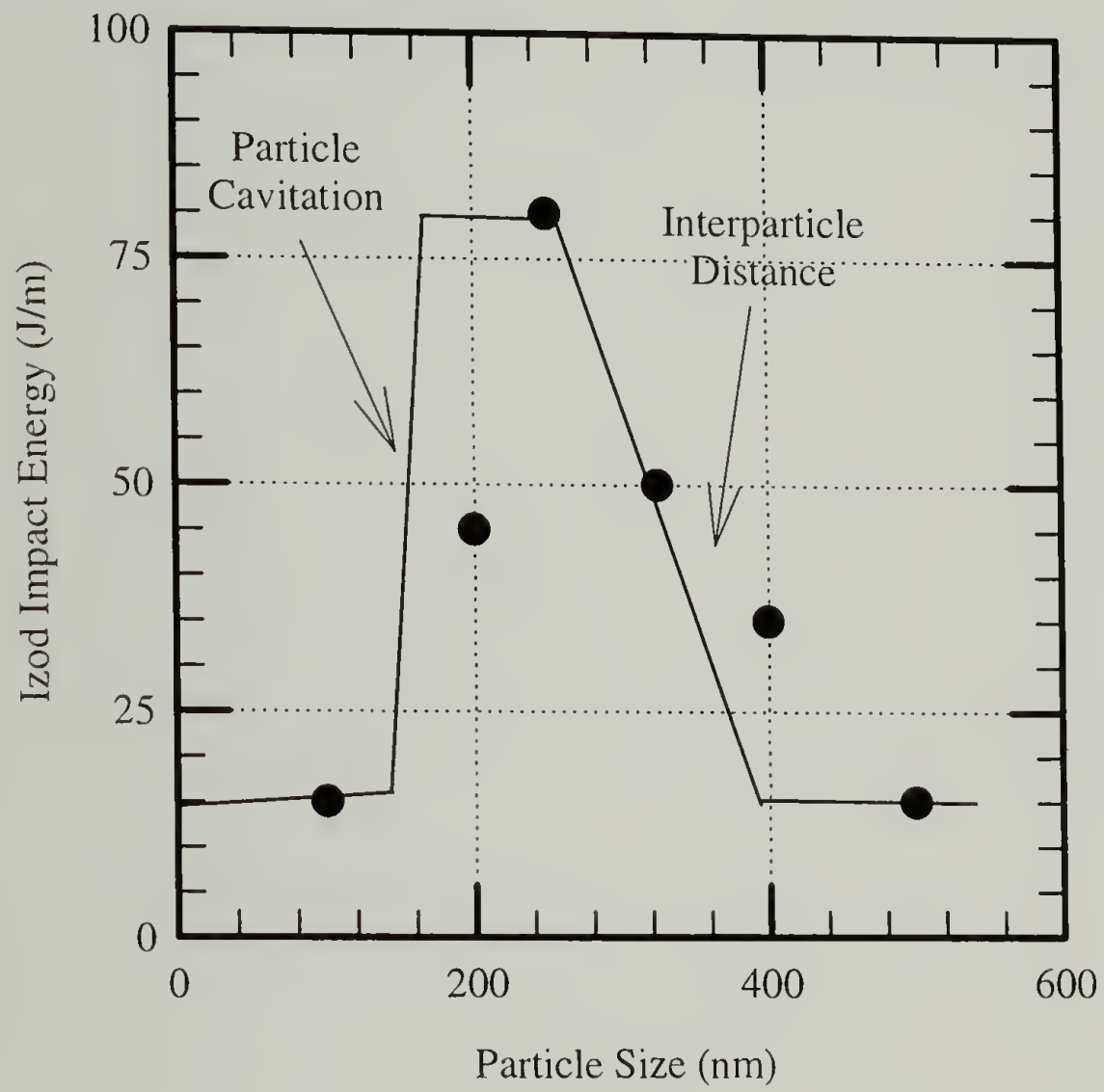

Figure 3.1: The upper and lower bounds of the toughening window.[80]

3.2 Liquid Rubber Modification of Epoxy Networks

3.2.1 Introduction

One of the critical performance properties of epoxy materials is fracture toughness. In order to improve fracture toughness, rubber modifiers were developed and added to epoxy formulations. Carboxyl terminated butadiene acrylonitrile (CTBN) liquid rubbers are the most widely used and studied rubber modifier for epoxy formulations.[81] Figure 3.2 shows the typical structure of a liquid CTBN rubber. Incorporation of these modifiers into epoxy networks results in the formation of liquid rubber domains on the order of 1 μm. Figure 3.3 shows a transmission electron micrograph of a CTBN modified epoxy stained with an osmium tetroxide solution.[82]

Control of the particle sizes in these systems is possible but difficult, since changing the temperature increases the solubility and rate of cure but decreases the viscosity at cloud point.[83,84] Once gelled, the morphology of the system is essentially locked.[83,84] With the morphology established, the effectiveness of the modifier is dependent on the nature of the cross-linked epoxy resin and testing conditions. This study will examine the use of these modifiers in combination with changes in the network structures described in Chapter 2.

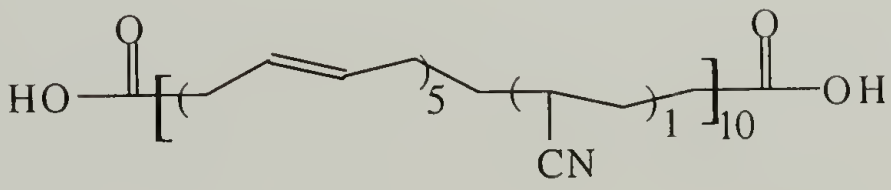

Figure 3.2: Typical structure of liquid CTBN rubber modifier.

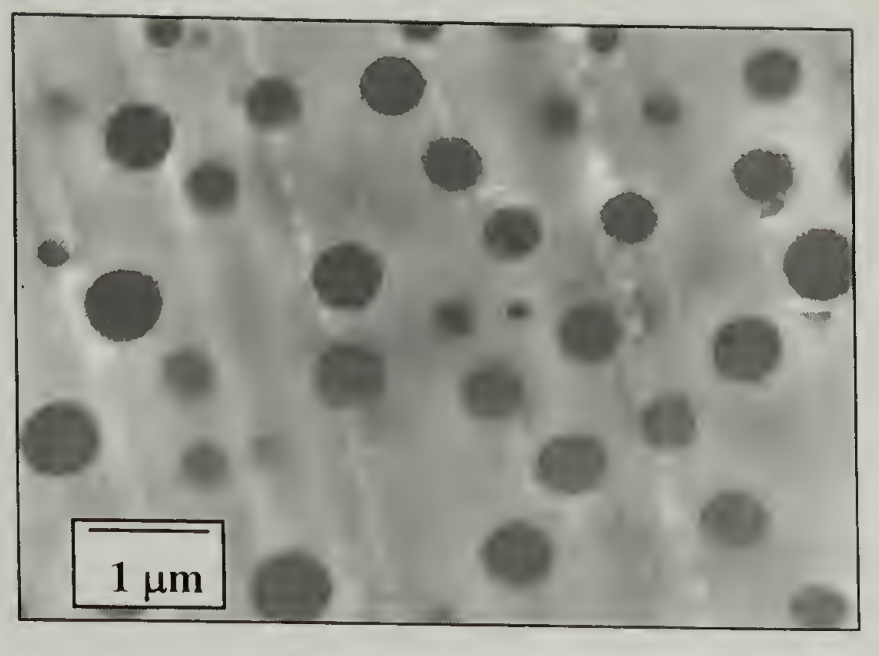

Figure 3.3: TEM micrograph of a CTBN liquid rubber modified cross-linked epoxy.

3.2.2 Experimental

3.2.2.1 Materials

The epoxy materials in this study are identical to those in Chapter 2. The chemical structures of the epoxy matrices are shown in Figures 2.1-2.4. B.F. Goodrich supplied Hycar 1300X8, a liquid CTBN rubber. The chemical structure of this modifier is shown in Figure 3.2. The CTBN rubbers were reacted with the epoxy resin at 160 °C for 3 hours prior to cross-linking to promote the formation of chemical ties between the rubber modifier and epoxy resin.[85]

B. F. Goodrich also supplied Hycar 1300X16, an amine terminated (ATBN) liquid rubber. The chemical structure of the ATBN rubber modifier is shown in Figure 3.4. Since the reaction kinetics between the ATBN modifier and epoxy resins are on the same order as the curing kinetics, pre-reaction is unnecessary.[86] However, ATBN modifiers typically contain free amines (3 wt% AEP) that can influence the cross-linking of the epoxy matrix phase.[86] The liquid rubbers were mixed with the epoxy resins and curing agent system. Initially, the mixture was homogenous and clear. Subsequent

curing resulted in the mixture becoming opaque as a result of the phase separation of liquid rubber domains. Both liquid rubber modifiers were added at various weight percentages to epoxy formulations and cured until the matrix phase reached its' maximum glass transition temperature.

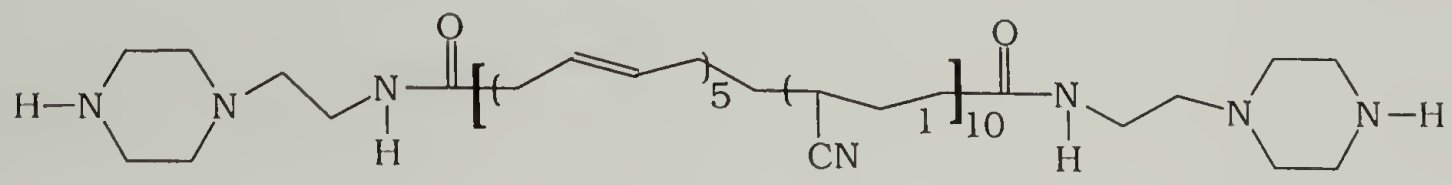

Figure 3.4: Structure of liquid ATBN rubber modifier.

3.2.2.2 Measurement Techniques

The materials in this study were characterized by a variety of techniques. The techniques include dynamic mechanical thermal analysis, tensile tests, compression tests, and fracture tests. The details of these experimental techniques were described previously in Chapter 2. In addition to previous techniques, microscopy was performed with a JEOL 35CF scanning electron microscope (SEM) and a JEOL JEM 100CX transmission electron microscope (TEM).

3.2.3 Results and Discussion

3.2.3.1 Glass Transition and Dynamic Mechanical Behavior

Incorporation of rubber modifiers into epoxy formulations and subsequent curing generally results in a two-phase morphology as indicated by Figure 3.3. If miscibility occurs between the rubbery phase and glassy phase, the glass transition temperature of the glassy (epoxy matrix) phase will be lowered. Figure 3.5 shows the effect of rubber concentration on the dynamic mechanical behavior of Epon 825 cured with AEP. The T_g of the polybutadiene rubbery phase is at 240 K, slightly lower than β relaxation

temperature of most cross-linked epoxies. The magnitude of the rubbery phase relaxation is proportional to the amount of modifier added. The addition of modifier lowers the glass transition temperature of the epoxy networks by 1-2 K, indicating that most of the rubber added has phase-separated. Even though phase separation is indicated, the resulting morphologies can be complicated, with epoxy inclusions in rubber domains. These morphological issues can affect mechanical performance.[8]

3.2.3.2 Elastic Properties

The use of rubber modifiers usually increases the fracture toughness of a material with the consequence that stiffness is lost. Table 3.1 shows the effect with wt% CTBN modification on Young's modulus at room temperature for networks constructed with Epon 825 and AEP. The trend displayed is typical of most rubber modified materials with decreasing modulus with increasing rubber content.

3.2.3.3 Yield Behavior

In addition to deleterious consequences for stiffness, incorporation of rubber modifiers also affects a material's strength. Table 3.2 shows the effect of wt% CTBN modification on the nominal tensile yield strength at room temperature for Epon 825 cured with AEP. Various theoretical and experimental models have been proposed to describe the effect of small rubbery domains on the yield behavior.[36,87,88] However, these models are basically indistinguishable for tensile and compression tests at practical levels (5-15%) of rubber modification.

The viscoelastic nature of the yield strength can be explained by modeling yield as a stress induced thermally activated process.[37,89] Equation 3.1 describes this process for a modified von Mises material in compression. The same viscoelastic model is also

used to describe the strain rate and temperature dependence of the yield strength for homogeneous polymeric systems (see section 2.10).

$$\frac{\sigma_{yc}}{T} = \frac{3}{\left(\sqrt{2}-\mu\right)}\left[\frac{\Delta E}{v^{*}T} + \frac{R}{v^{*}}\ln\left(\frac{2\dot{\gamma}_{oct}}{\Gamma}\right)\right] \qquad (3.1)$$

Figure 3.6 is a plot of the compressive yield strength as a function of temperature and strain rate for a 5 wt% CTBN modified epoxy network constructed with Epon 825 and AEP. Similar tests and plots were performed for materials with 0 wt% and 10 wt% CTBN modification. Table 3.3 shows that the activation volume (v^{*}) and activation energy (ΔE) are not strongly dependent on wt% of CTBN modification in the range of practical use. This finding is consistent with the results of Kinloch et al.[36]

3.2.3.4 Fracture Behavior

As stated in the introduction, the effectiveness of a modifier is dependent on the nature of the matrix phase. Glassy materials that behave in a brittle fashion in pure shear are not likely to be toughened by rubber modification. However, glassy materials that have the ability to yield under the influence of hydrostatic tension are more likely to be toughened by the addition of rubber. Rubber modifiers are believed to alleviate hydrostatic tension resulting in a stress state more favorable to matrix yielding.[90] In general, as the cross-link density of an epoxy resin increases it become more brittle. Figure 3.7 shows that rubber modification of a lightly cross-linked material (high M_c) is more effective than rubber modification of tightly cross-linked material (low M_c). Similar findings have also been reported with networks in which M_c s were not as well controlled.[1,58,91,92]

The effect of temperature on the fracture toughness of a CTBN modified and an unmodified epoxy network is shown in Figure 3.8. All K_{Ic} values were determined by a linear elastic fracture mechanics approach, since the load deflection curves were linear until failure in both the unmodified and modified materials. At low temperatures the fracture toughness is relatively low and constant. An increase in the fracture toughness occurs around 60 K below T_g. This behavior occurs for both modified and unmodified materials. Kinloch et al.[93] proposed a model to explain this upturn in fracture toughness, quantifying the contributions from rubber bridging, matrix shear yielding, and void growth after cavitation. Verification is extremely difficult due to experimental inaccessibility of the model's parameters. The rise in the fracture behavior is more likely the result of constraint effects, which were discussed in section 2.11.

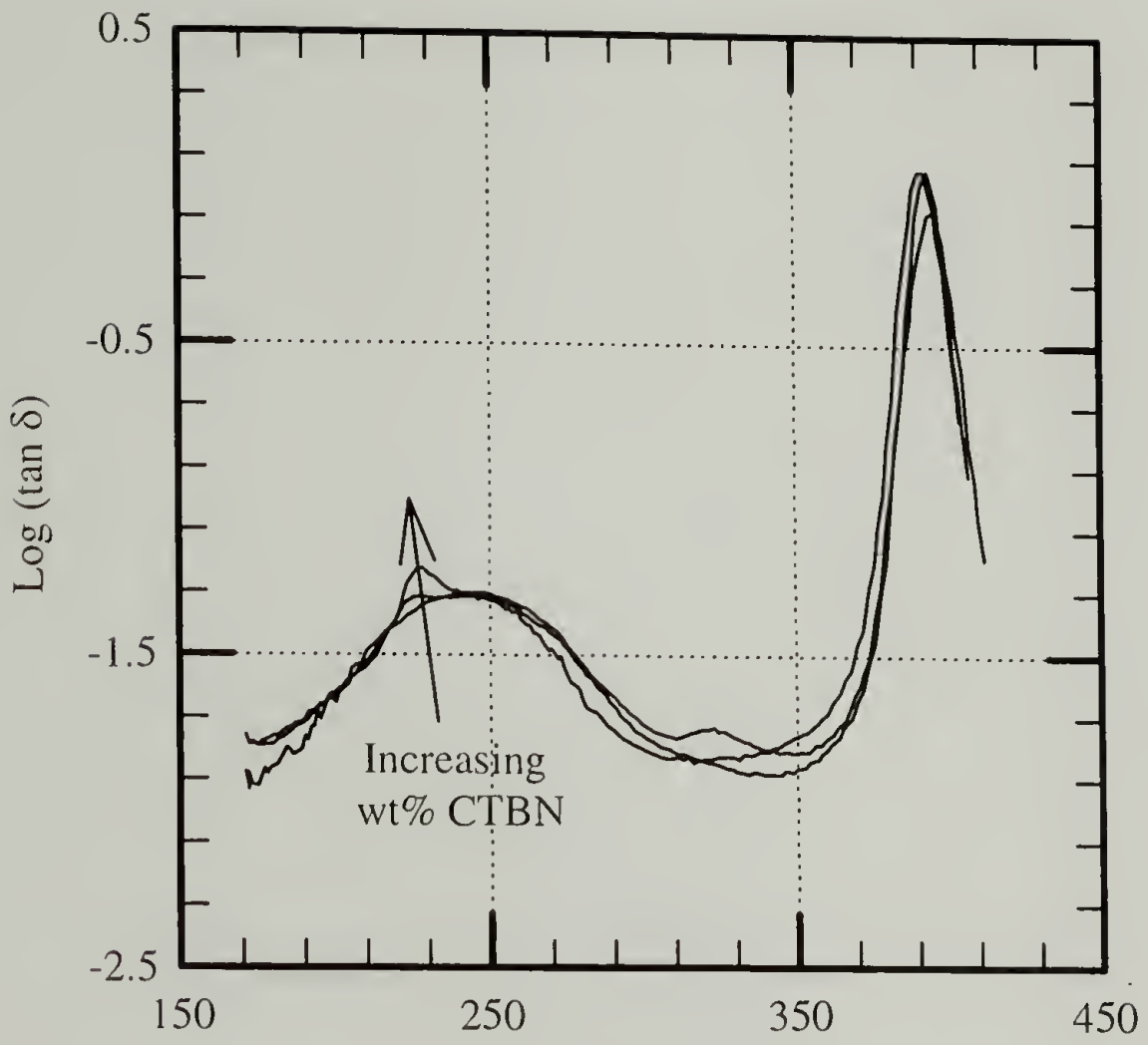

Figure 3.5: The effect of wt% CTBN on the dynamic mechanical behavior of an epoxy network constructed with Epon 825 and AEP.

Table 3.1: Young's moduli at room temperature as a function of wt% CTBN for network constructed with Epon 825 and AEP.

wt% CTBN	E (GPa)
0	2.7
5	2.4
10	1.9

Table 3.2: Tensile yield strength at room temperature as a function of wt% CTBN for network constructed with Epon 825 and AEP.

wt% CTBN	σ_{yt} (MPa)
0	71
5	66
10	57

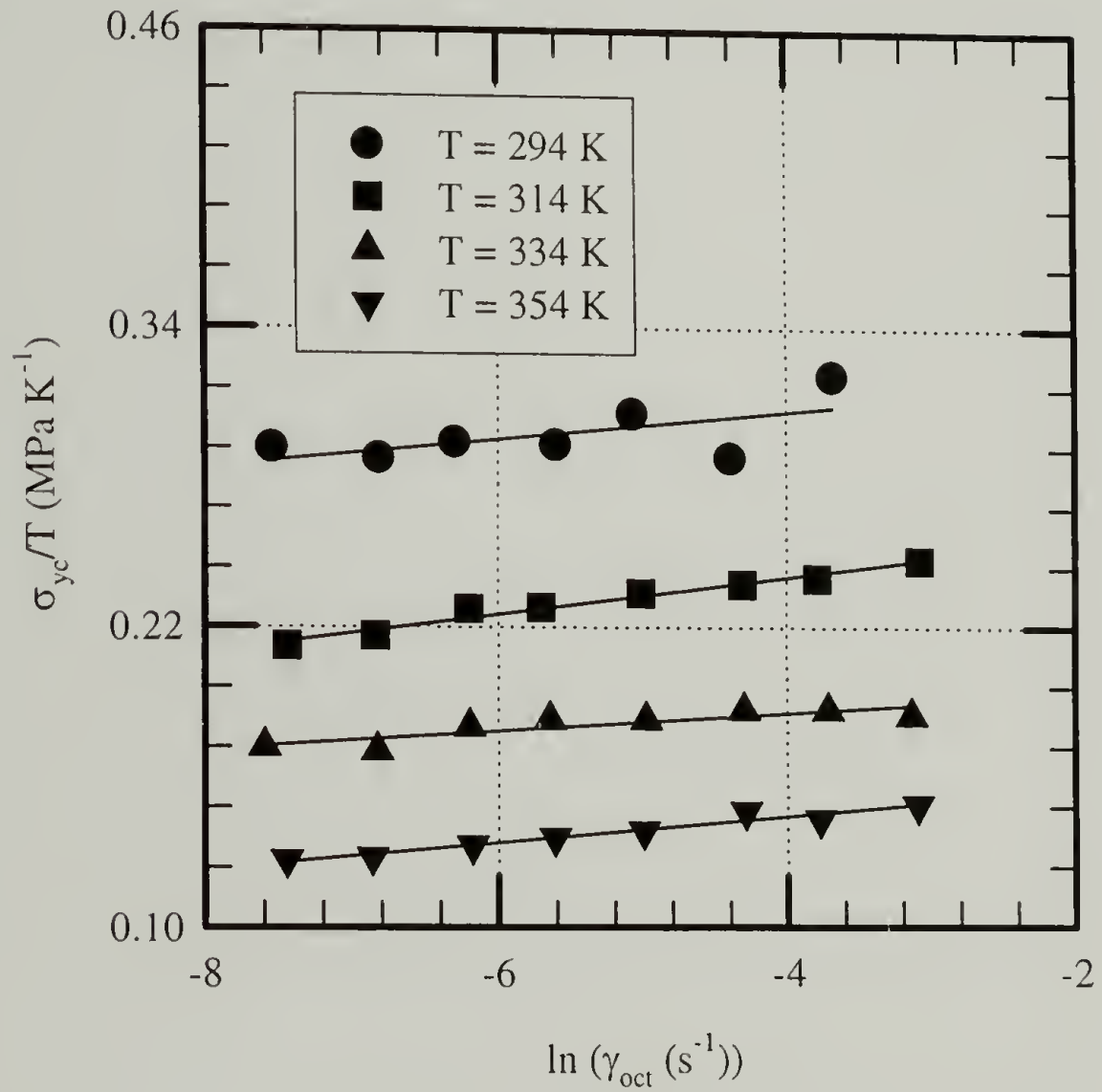

Figure 3.6: Compressive yield strength as a function of temperature and strain rate for Epon 825 cured with AEP and 5 wt% CTBN modification.

Table 3.3: Yield strength modeled as a stress induced thermally activated process as a function of wt% CTBN modification for epoxy networks constructed with Epon 825 and AEP.

wt% CTBN	ΔE (kJ/mol)	v^* (nm^3/molecule)
0	420	2.6
5	400	2.8
10	320	2.5

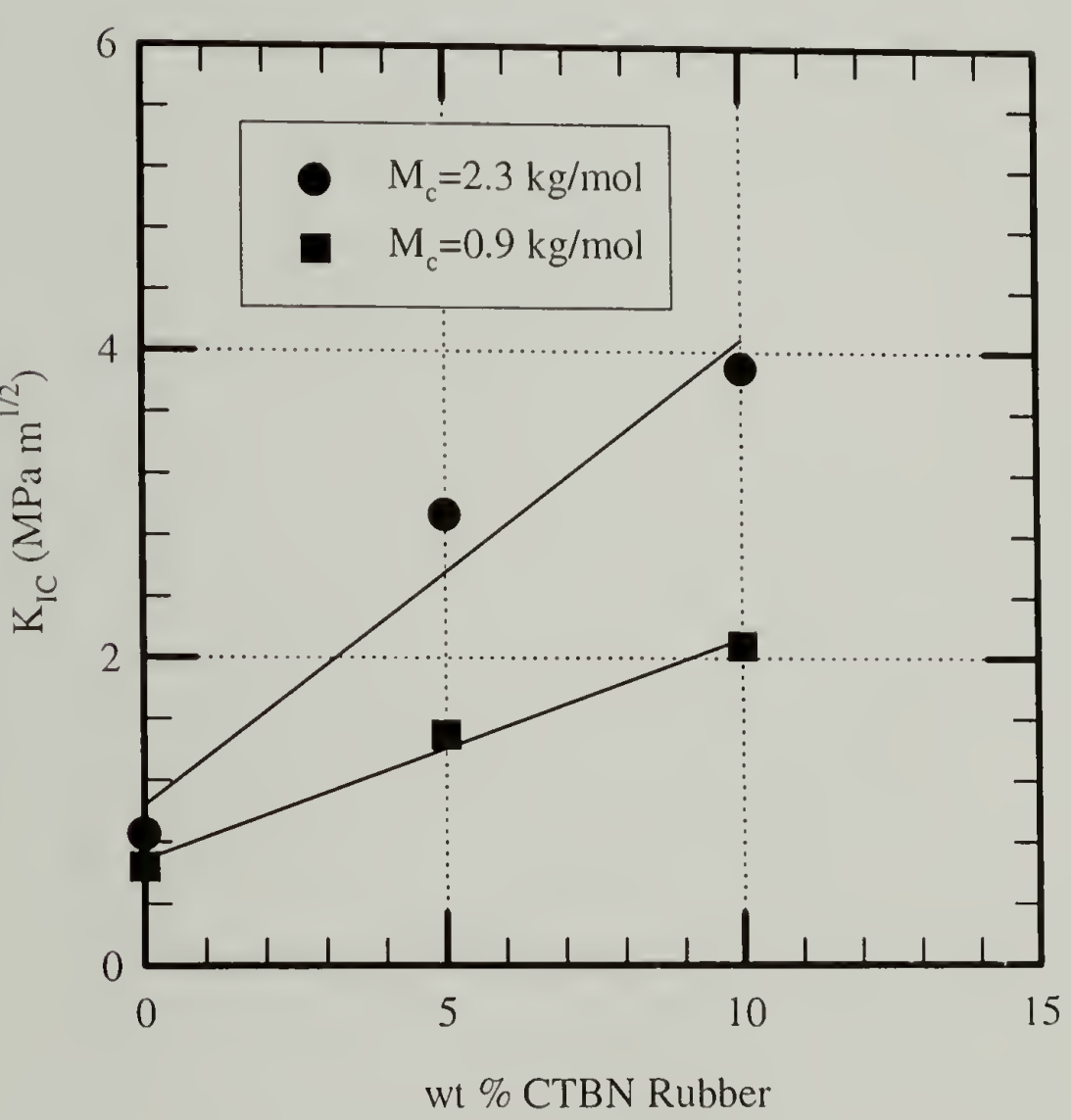

Figure 3.7: Synergistic toughening effect between wt% CTBN modification and M_c for networks constructed with Epon 828, 1,3-phenylenediamine, and aniline.

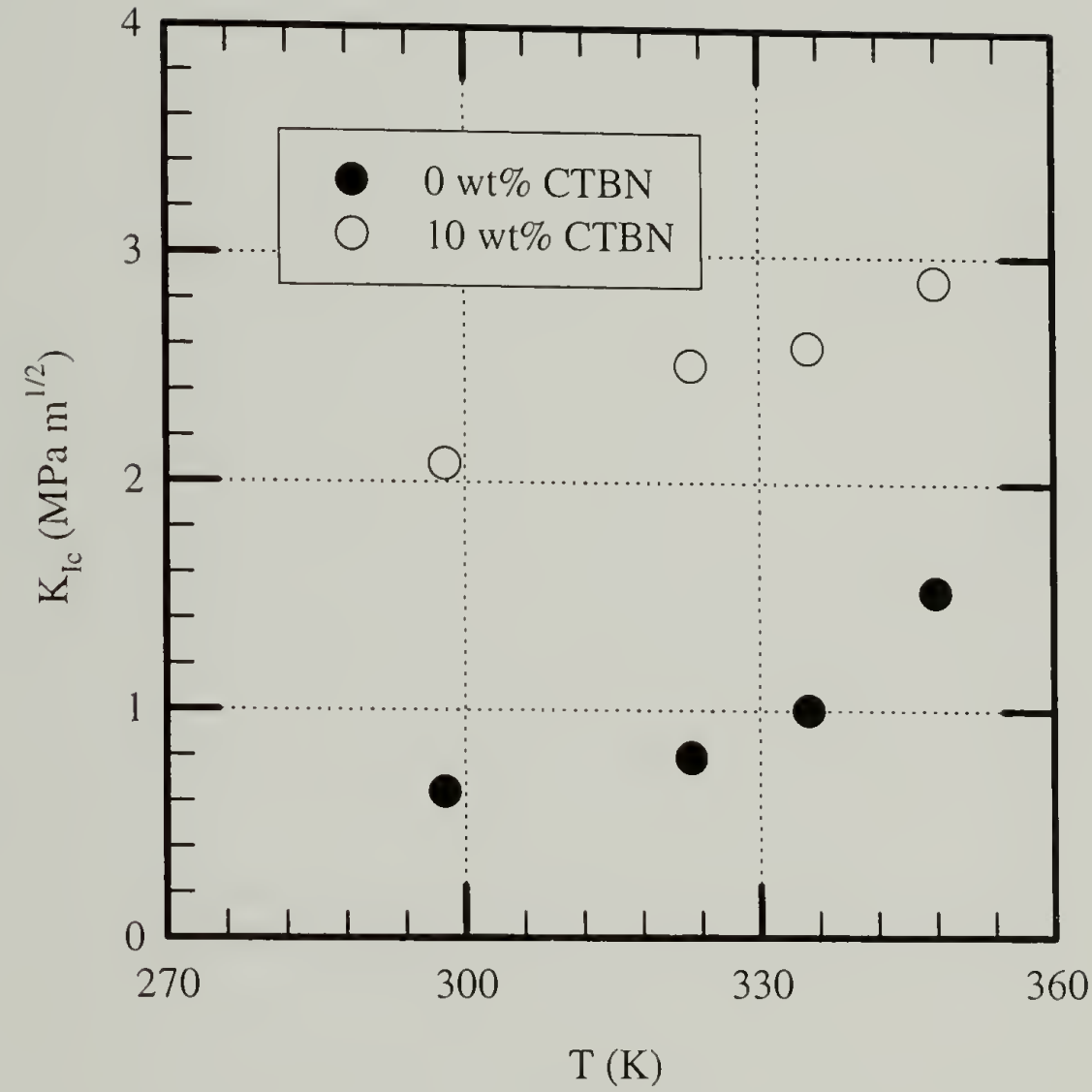

Figure 3.8: The effect of test temperature on the fracture toughness of a 10 wt% CTBN modified and unmodified epoxy network constructed with Epon 828, 1,3-phenylenediamine, and aniline (M_c=0.9 kg/mol, T_{gx}= 395 K)

3.3 Tensile Dilatometry

3.3.1 Introduction

Measuring a materials volume change with deformation (tensile dilatometry), therby evaluating the onset of cavitation and subsequent inelastic void growth, should in theory elucidate rubber toughening micro-mechanisms.[94] Figure 3.9 shows the typical response of volume strain (V_s), calculated by equation 3.2 assuming isotropy in the transverse contraction ratios, versus axial strain.

$$V_s = (1+\varepsilon_a)(1+\varepsilon_t)^2 - 1 \qquad (3.2)$$

where: ε_a axial strain
ε_t transverse strain.

In Figure 3.9, the dilational response of a material is the result of elastic deformation with a Poisson's ratio of 0.38. Additional volume change above this line represents a cavitational response. A constant volume strain with axial strain represents a deviatoric response, since shear yielding occurs under constant volume.

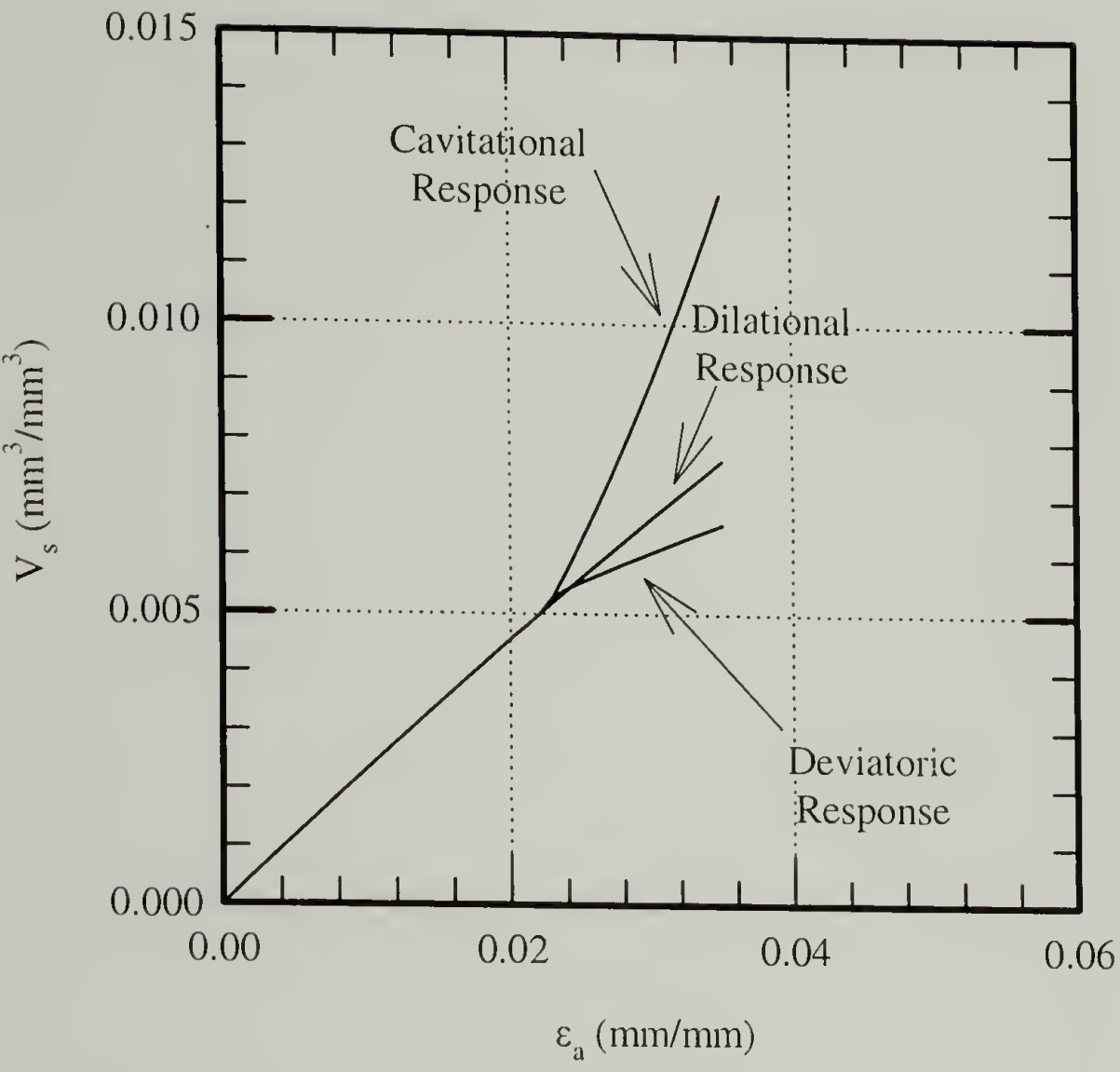

Figure 3.9: Possible tensile dilatometry responses.

3.3.2 Experimental

3.3.2.1 Materials

The materials used for this study included two rubber-modified cross-linked epoxy materials. One of these materials consisted of a CTBN modified epoxy network constructed with Epon 828, 1,3-phenylenediamine, and aniline (M_c=2.3 kg/mol). The other material consisted of an ATBN modified epoxy network constructed with Epon 825 and AEP. The materials were cast into 6 mm thick plaques and machined into ASTM D638 Type I tensile bars by a specially designed router. In addition, the ATBN modified materials were cast into 200 mm long test tubes (D=20 mm). The resulting rods were

machined into cylindrical specimens with the same cross-sectional area as the rectangular specimens.

3.3.2.2 Measurement Technique

Tests were performed at room temperature with a Model 1123 Instron equipped with a MTS axial extensometer and an Instron transverse extensometer. Tests were performed at a crosshead speed of 5 mm/min for the rectangular specimens and 3 mm/min for the cylindrical specimens. The rates were chosen to ensure an equivalent strain rate of testing (axial strain rate = 0.1 min^{-1}). Gripping of the cylindrical specimens was achieved by designed cylindrical grips. Figure 3.10 shows a picture of the experimental setup.

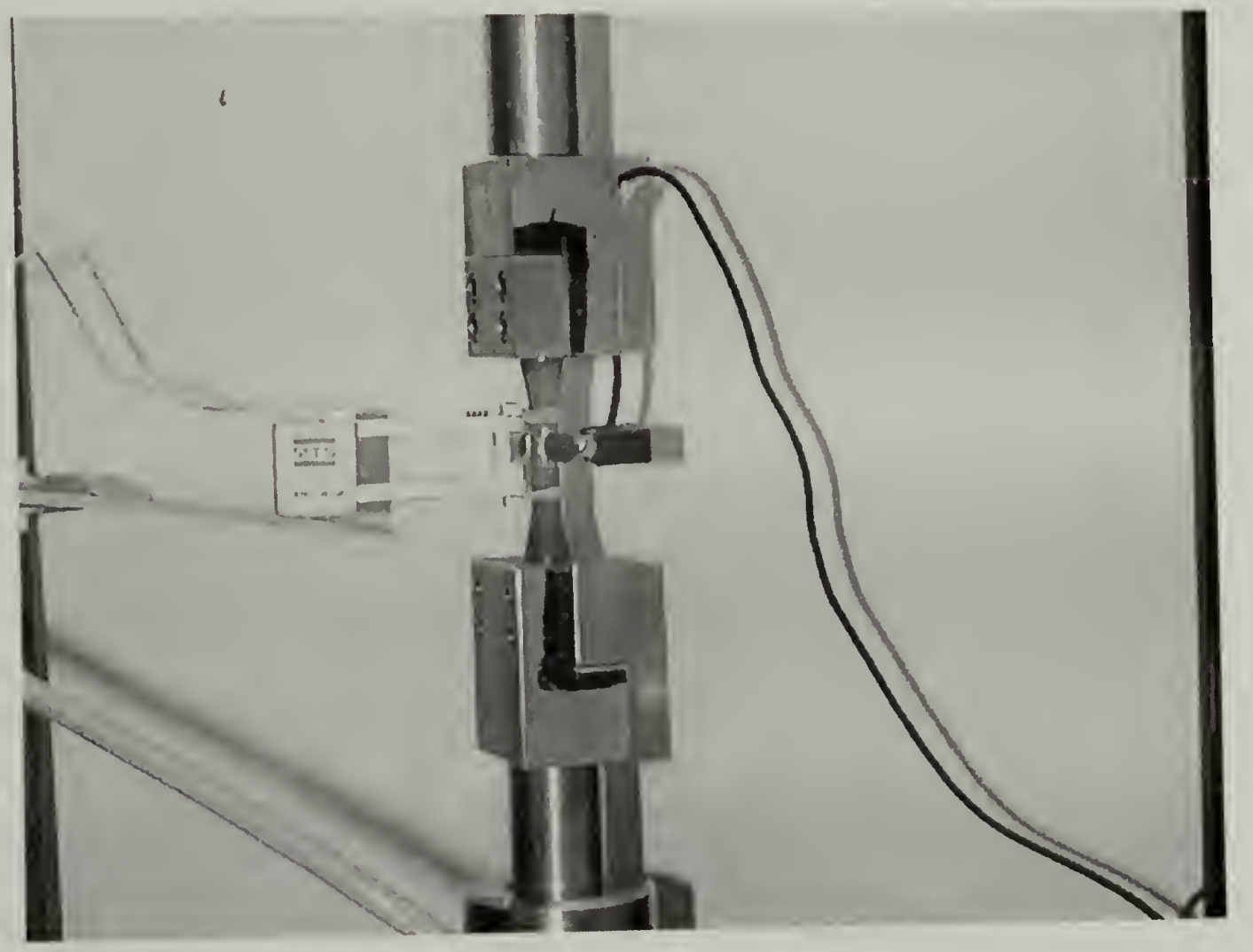

Figure 3.10: Experimental tensile dilatometry setup.

3.3.3 Results and Discussion

Figure 3.11 shows a plot of the volume strain versus ε_a for various CTBN modified epoxy materials. The responses of the materials are nearly identical in the region of small strain, ε_a between 0 and 0.04. Past ε_a of 0.04, the responses diverge to unreasonable values with no apparent trend. This chaotic divergence is the result of necking, which results in erroneous strain measurements until the necked region has propagated through both gauges. However, necking in these rectangular specimens is unstable as shown by a Conside're plot in Figure 3.12.[37]

Necking is a process based on a competition between area reduction (geometry) and strain hardening (material).[74] Neck stabilization can occur by changing the competition between geometry and strain hardening.[53] Stabilization allows dilatometry methods to be applied once the neck had developed through the gauge area. To test this idea, cylindrical specimens were made and tested. However, these attempts were unable to promote neck stabilization. The volume strain measurements are basically identical to the volume strain measurements of the rectangular specimens for the ATBN modified materials

In cases where the dominant mode of matrix plastic deformation is crazing, the use of tensile dilatometry in determining onset of cavitational processes has been effective.[95] However, tensile dilatometry results by Yee et al.[9,90,91,96] applied to modified matrices which predominately shear yield are ambiguous. The findings of this study support other the use of extreme caution in interpreting tensile dilatometry data.

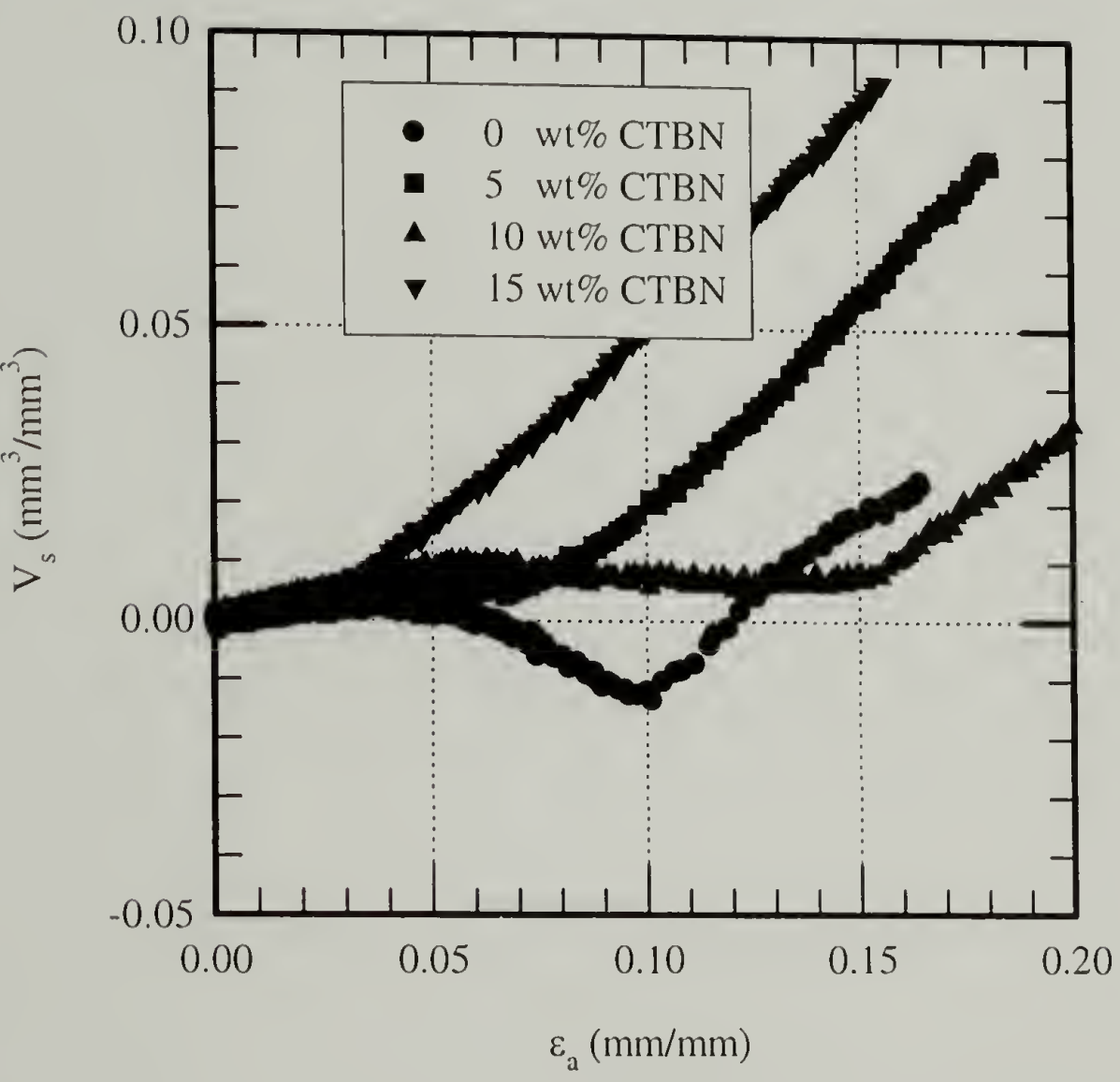

Figure 3.11: Volume strain versus axial strain for CTBN modified rectangular specimen (Epon 828 cured with 1,3-phenylenediamine and aniline, M_c=2.3 kg/mol).

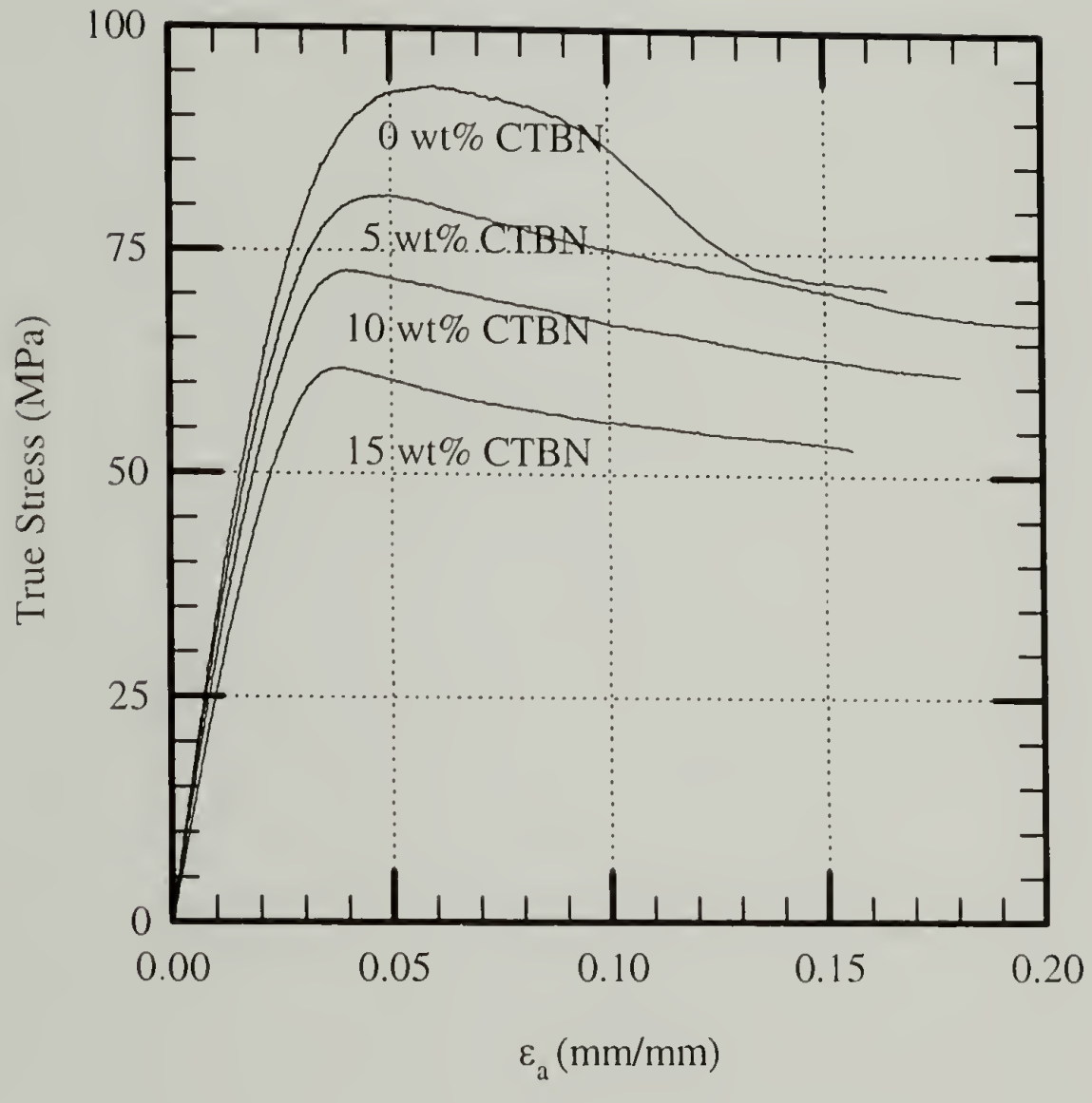

Figure 3.12: Conside're plots, true stress versus axial strain for a CTBN modified rectangular specimen. (Epon 828 cured with 1,3-phenylenediamine and aniline, M_c=2.3 kg/mol).

3.4 Stress Whitening of Modified PVC

3.4.1 Introduction

The addition of rubbery inclusions into a polymeric material is commonly employed to increase the toughness of polymeric materials.[8] Despite the frequent use, the mechanisms and sequence of mechanisms of this toughening are in debate. One opinion is that rubber particle cavitation occurs first to alleviate hydrostatic tension and promote a stress state favorable to shear yielding or shear band formation.[9,97,98] Another opinion is that rubber particle cavitation occurs after shear band formation.[99,100] Experimental studies investigating these issues are complicated by many factors. For instance, some studies draw conclusions based on post mortem analyse of fracture surfaces.[9,91] Such analyse reveals the presence of shear bands and cavitated rubber particles yet cannot effectively elucidate the sequence of mechanisms. Studies addressing the sequence of mechanisms often analyze the stress field ahead of a notch.[90,101,102] The assumptions of the stress field, the positional variation of the stress field, and the amount of constraint in the specimen limit the effectiveness of this approach. A clear experimental approach evaluating the mechanisms and sequence of mechanisms is needed.

Before describing the experimental approach, a brief review of the current thoughts on rubber particle cavitation and yielding in rubber toughened plastics is essential. Rubber particle cavitation, to alleviate hydrostatic tension, is often described from an energy balance approach.[88,97,103] This approach, ignoring some finer details, results in a surface energy term and a strain energy term as shown in equation 3.3.

$$E \approx \Gamma R^2 - K\Delta^2 R^3 \qquad (3.3)$$

where: E total energy
Γ surface energy
R rubber particle size
K bulk modulus
Δ volume strain.

Two important relationships arise from this energy balance. First, it is more favorable for larger particle to cavitate than smaller particles and that for a given particle size there is a critical volume strain associated with cavitation. For an isotropic elastic material, the critical volume strain is linearly related to a critical hydrostatic or mean stress (σ_m) through the bulk modulus. The shaded area in Figure 3.13 represents a hypothetical condition for rubber particle cavitation, with a narrow range of particle sizes, in a modified material. An alternative opinion to this criterion describes rubber particle cavitation initiating at the elastic/plastic boundary where plastic flow causes immediate debonding.[99,100]

The yield behavior or the elastic/plastic boundary of an isotropic homogenous polymeric material can be characterized by a modified von Mises criterion. For a given state of stress and selecting the octahedral plane, the resulting stress vector can be resolved into two components. The normal component on the octahedral plane is equal to the mean stress, which cause volume change. The parallel component on the octahedral plane is equal to the octahedral shear stress (τ^{oct}), which causes shape change. The critical octahedral shear strength ($\tau_y{}^{oct}$) required for yield in a homogeneous isotropic polymer has been found to be linearly dependent on the mean stress through the coefficient of internal friction (μ) as described by equation 3.4.

$$\tau_y{}^{oct} = \tau_{yo}{}^{oct} - \mu\sigma_m \qquad (3.4)$$

where $\tau_{yo}{}^{oct}$ is the octahedral shear yield strength in absence of a mean stress.

The solid line in Figure 3.13 with f=0.0 (void volume fraction) represents this yield criterion.

Recently, researchers[97,104] have proposed various yield loci for porous materials or cavitated polymeric systems based on a model by Gurson.[105] According to one of these criteria, proposed by Bucknall and Lazzeri[97], the introduction of voids (cavitated particles) results in a decrease in yield strength with the amount of decrease dependent on σ_m.

$$\left(\frac{\tau_y^{oct}}{\tau_{yo}^{oct}}\right)+\mu\frac{\sigma_m}{\tau_{yo}^{oct}}\left(2-\mu\frac{\sigma_m}{\tau_{yo}^{oct}}\right)+2f\cosh\left(\frac{3\sigma_m}{2\tau_{yo}^{oct}}\right)-f^2-1=0 \qquad (3.5)$$

This behavior is described by equation 3.5 and is represented by the solid lines for various void volume fractions (f) shown in Figure 3.13.

Effective evaluation of rubber particle cavitation and yielding in rubber toughened plastics demands materials with favorable properties and unique mechanical tests. The material in this study consists of a methacrylate-butadiene-styrene (MBS) core-shell modifier dispersed in polyvinylchloride (PVC). The material is initially clear but whitens during deformation as shown in Figure 3.14. The whitening in MBS modified PVC is attributed to rubber particle cavitation.[101,103,106] This material has favorable properties for studying rubber toughening, since it provides optical verification of rubber particle cavitation. The unique mechanical test in this study consists of a pressurized and loaded hollow cylinder.[39,107,108] This test allows a range of stress states, from uniaxial compression to equal biaxial tension (see Figure 3.13), to be interrogated with a single specimen geometry. Between the regions of uniaxial compression and equal biaxial tension, the mean stress (volume change) and the octahedral stress (shape change) can be

controlled independently. This stress state control coupled with in-situ light transmission measurements of the MBS modified PVC permits evaluation of the mechanisms and sequence of mechanisms in rubber toughened plastics.

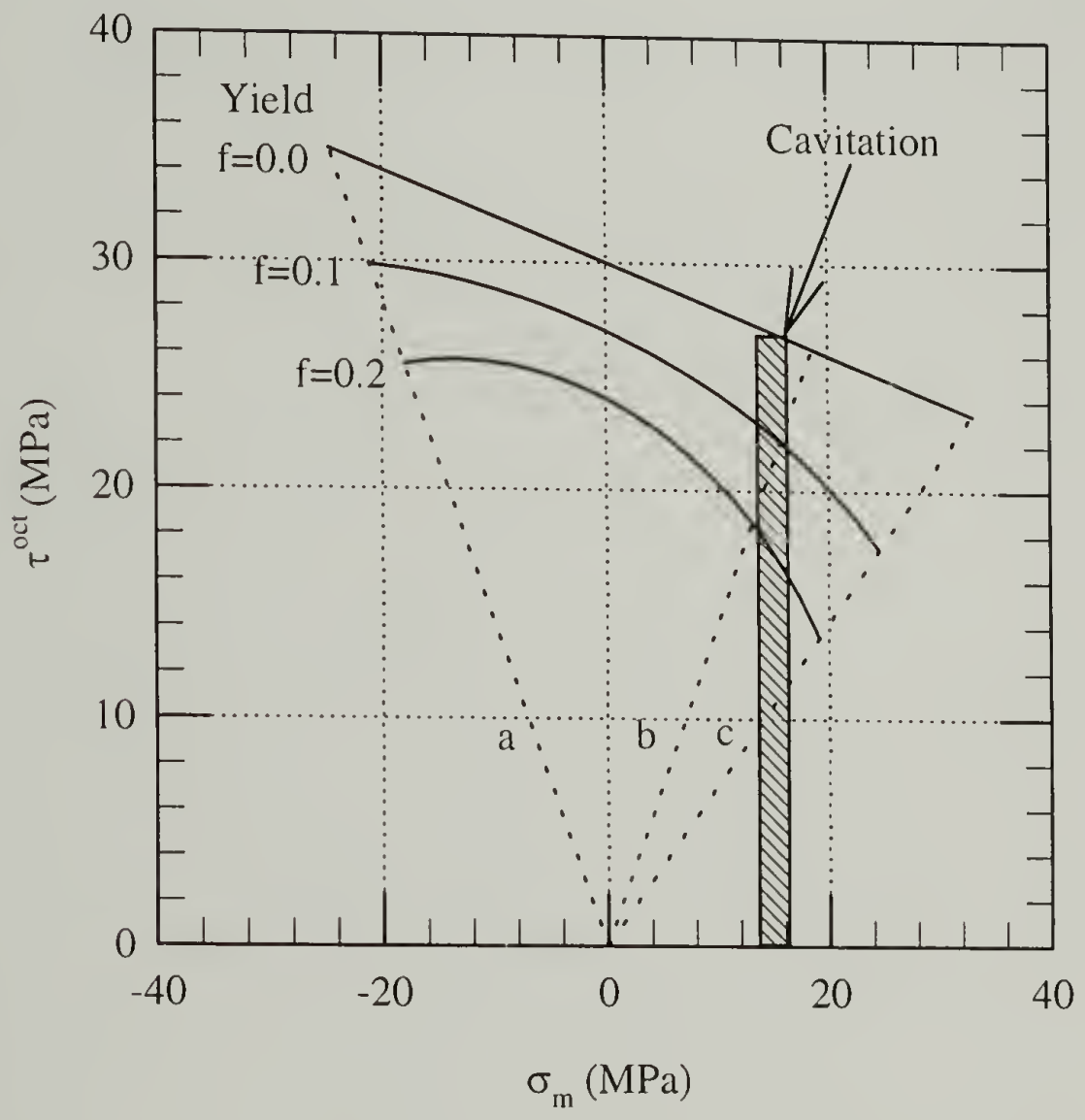

Figure 3.13: Yield behavior of cavitated polymeric systems at various void volume fractions. Boxed area represents prediction of rubber particle cavitation from energy balance theories. Dashed lines represent various loading conditions: a) uniaxial compression, b) uniaxial tension, and c) equal biaxial tension.

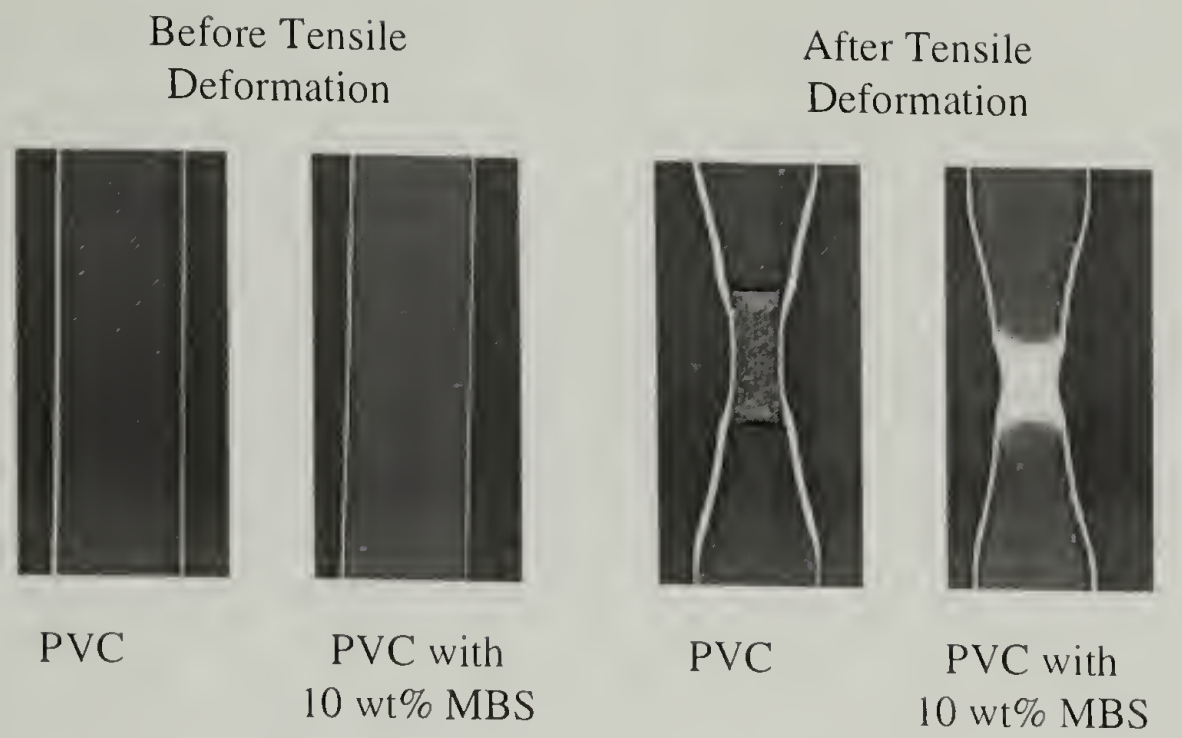

Figure 3.14: Contact prints showing the stress whitening behavior of MBS modified PVC with deformation.

3.4.2 Experimental

3.4.2.1 Material Fabrication

The material formulations used in this study consist of the following components.

Component	Product Name	Manufacturer
PVC (K=58)	Geon 334	The Geon Company
MBS modifier	Paraloid BTA 733	Rohm and Haas
Processing aid	Paraloid K120ND	Rohm and Haas
Heat Stabilizer	Advastab TM-181	Morton International, Inc.
Lubricant	Myverol 18-06	Quest International

The four material formulations were prepared by weight percentage for the various components shown in Table 3.4. The formulations were dry blended and compounded by roll-milling at 180°C for 10 minutes. The resulting sheets, approximately 0.2 mm thick, were then cut for compression molding of sheets and hollow cylinders.

The compression molding of 3 mm thick sheets was performed at 180°C for 10 minutes. The resulting sheet was machined into tensile specimens using a specially

designed router. The compression molding of hollow cylinders was achieved by a displacement mold shown in Figure 3.15.[109] The mold, lightly coated with a silicon mold release, was heated to 190° C in an oven. Fifteen grams of a compounded formulation was placed in the lower cavity surrounding the center. The top part of the displacement mold, the plunger, was placed into the lower part of the displacement mold, the cup. The entire mold was then placed into a hydraulic press and compressed, forcing the polymer into the annular region between the plunger and the center dowel. Complete filling of the hollow cylinder cavity was detected by the non-transient response of the pressure gauge on the hydraulic press upon compression. The mold was left under compression and allowed to cool to room temperature. After cooling, the hollow cylinder was removed from the mold and cut into two 75 mm long specimens. These specimens were then machined with a lathe to create a thin section as shown in Figure 3.16. This process ensures whitening will initiate in the area in which light transmission measurements will be made since the stress will be locally higher due to the reduction in cross-sectional area. Gripping of the hollow cylinder was achieved through the use of 15 mm Swagelok® compression fittings and metal inserts as shown in Figure 3.16.

3.4.2.2 Standard Material Characterization

Standard material characterization was performed on MBS modified PVC with a variety of techniques. These techniques include dynamic mechanical thermal analysis, transmission electron microscopy, ASTM D638 tensile tests, and fracture testing. The details of each of these techniques have been discussed in previous sections.

3.4.2.3 Pressurized and Loaded Hollow Cylinder Tests

Hollow cylinder tests were performed at room temperature with a Model 1321 Instron in combination with a Tescom ER3000 pressure regulator controlling the nitrogen pressure. The details of the experimental setup have been described by Kody and Lesser.[39] The stress state in the hollow cylinder, described by equations (3.6) and (3.7), is determined by the axial load and the internal pressure in the thin cylinder section.

$$\sigma_1 = \left(\frac{L}{\pi D t}\right) + \left(\frac{PD}{4t}\right) \qquad (3.6)$$

$$\sigma_2 = \left(\frac{PD}{2t}\right) \qquad (3.7)$$

where: σ_1 axial stress
σ_2 hoop stress
L axial load
P internal pressure
D mean cylinder diameter
t thickness.

In plane stress conditions (σ_3=0), which is achieved when D/t>10, the octahedral shear stress is described by equation 3.8 while the mean stress is described by equation 3.9.

$$\tau^{oct} = \frac{\sqrt{2}}{3}\sqrt{\sigma_1^2 - \sigma_1\sigma_2 + \sigma_2^2} \qquad (3.8)$$

$$\sigma_m = \frac{1}{3}(\sigma_1 + \sigma_2) \qquad (3.9)$$

For a homogenous isotropic material, the octahedral shear strain is related to the octahedral shear stress through the shear modulus. The shear modulus for each formulation was calculated from Young's modulus and Poisson's ratio values obtained from tensile tests. The octahedral shear strain rate was held constant at 0.01 min^{-1} for all

loading paths and formulations. On a particular loading path, the ratio of the octahedral shear stress to mean stress was held constant during the entire path. For instance, in uniaxial compression τ^{oct}/σ_m is equal to -1.41, in uniaxial tension τ^{oct}/σ_m is equal to 1.41, and in equal biaxial tension τ^{oct}/σ_m is equal to 0.71. These particular loading paths are displayed as dotted lines a, b, and c in Figure 3.13.

3.4.2.4 In-situ Light Transmission Measurements

In-situ light transmission measurements were made with a laser diode (λ=633 nm, beam dia.=3 mm) and a 100 mm^2 silicon detector. A linear response between the measured voltage of the detector circuitry and light intensity was verified through the use of optical density filters. The hollow cylinder specimens were lightly coated with silicon oil to prevent scattering arising from surface roughness. This setup allowed the onset of whitening, signified by a non-linear drop in light transmission to be measured as a function of mechanical deformation to be achieved. Figure 3.17 shows a plot of light transmission versus mean stress for a uniaxial tension tube test with the onset of whitening denoted. In-situ light transmission measurements were not performed with unmodified PVC, since the materials remain clear during the entire deformational process.

Table 3.4: MBS modified PVC formulations showing wt% of each component added.

MBS	PVC	Lubricant	Heat stabilizer	Processing aid
0	96	2	2	0
5	90	2	2	1
10	85	2	2	1
15	80	2	2	1

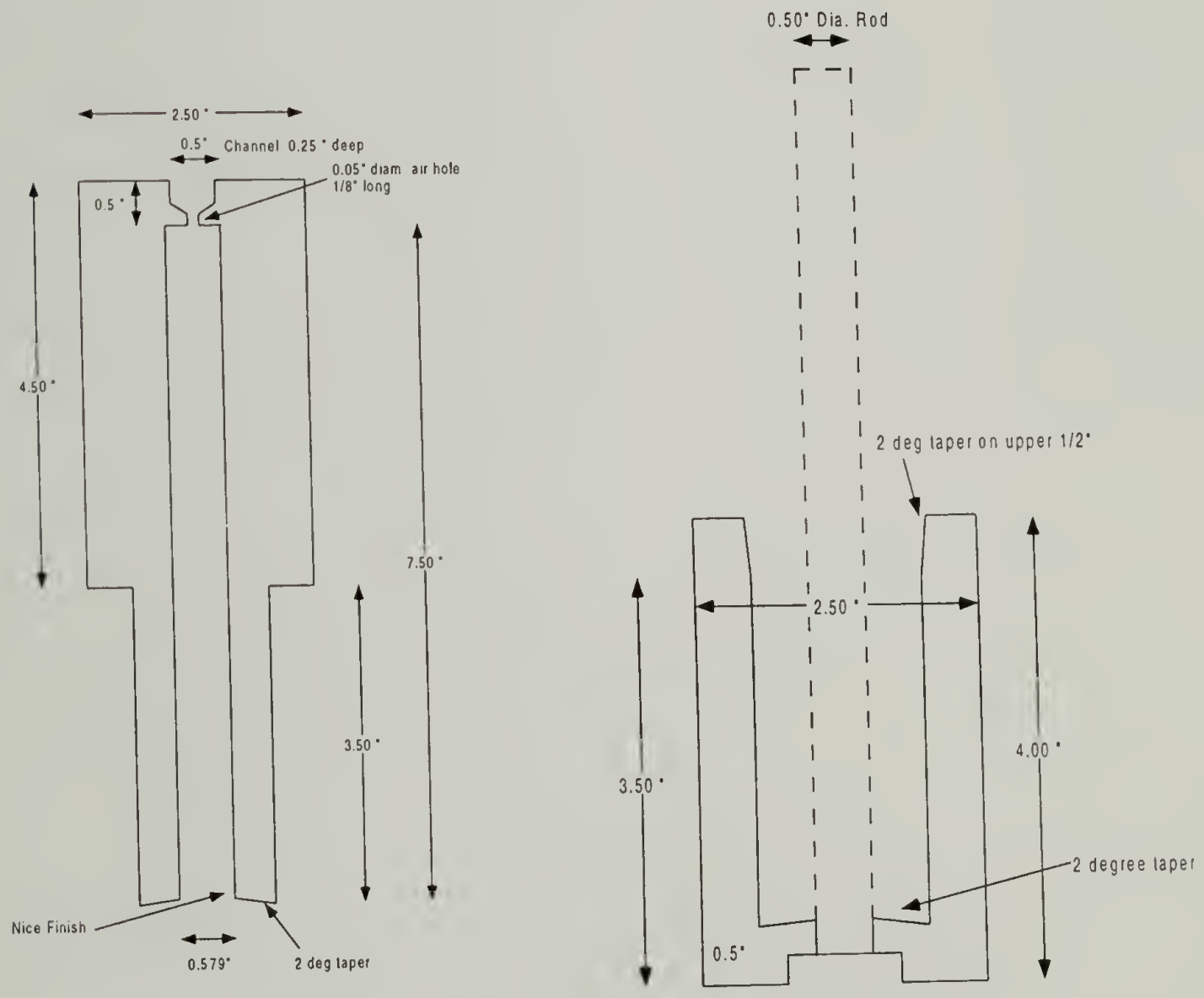

Figure 3.15: Displacement mold schematics; plunger (left) and pot (right).

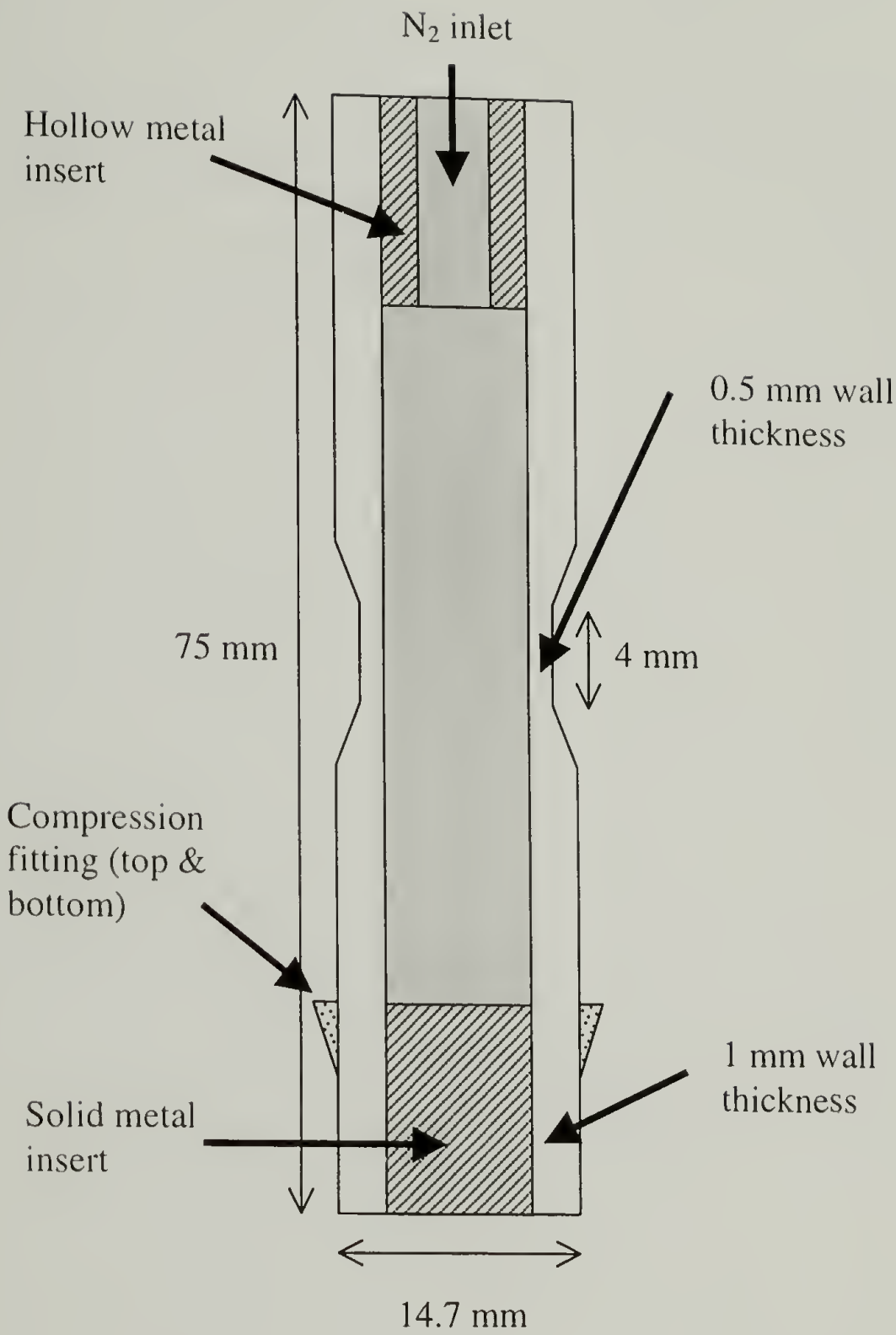

Figure 3.16: Hollow cylinder specimen showing thinned down section.

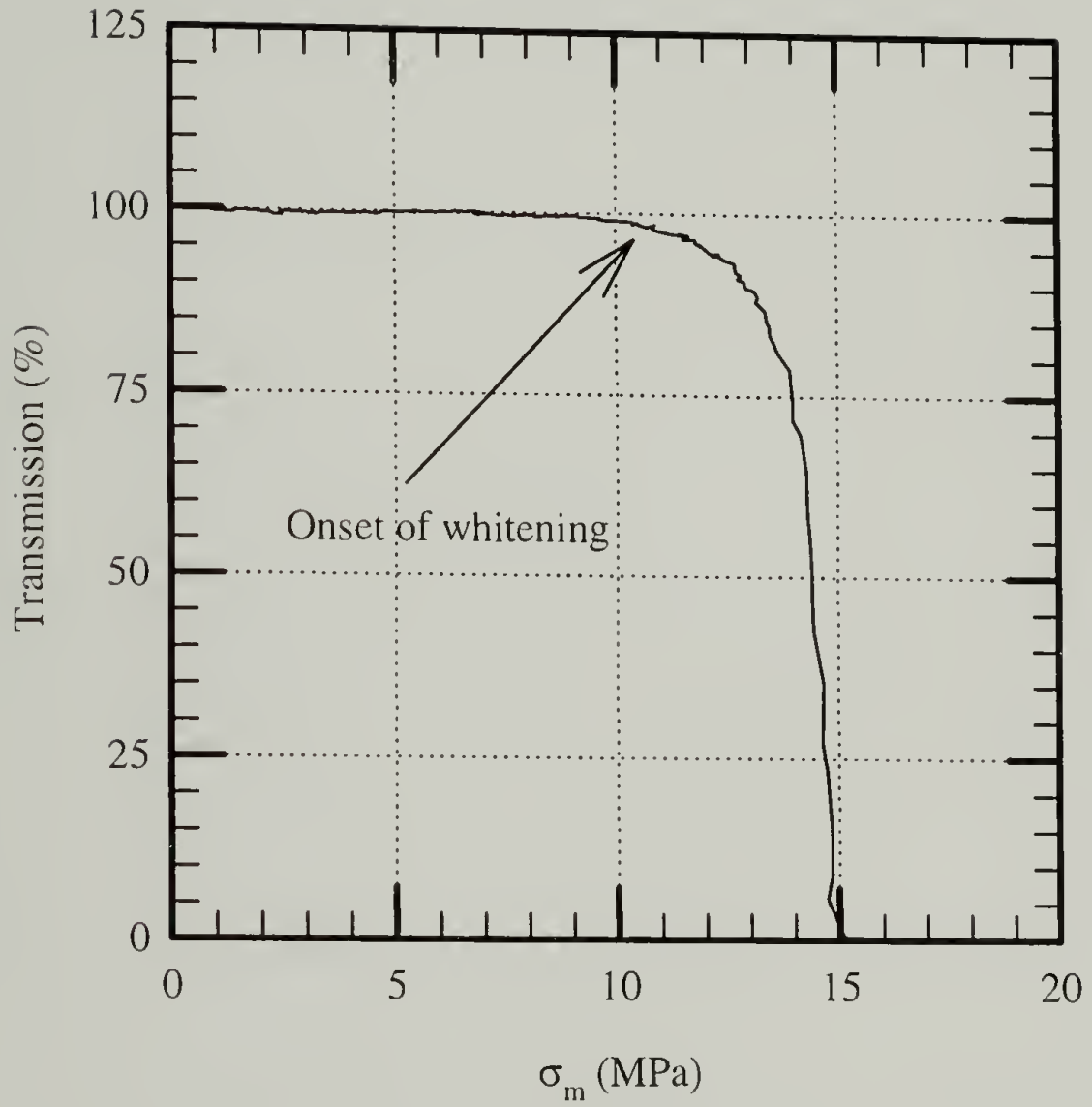

Figure 3.17: Light transmission versus mean stress for a uniaxial tension tube test showing the onset of whitening.

3.4.3 Standard Material Characterization Results

3.4.3.1 Dynamic Mechanical Behavior

A Dynamic mechanical thermal analysis performed on the MBS modified PVC, with results shown in Figure 3.18, indicates that the modifier does not influence the glass transition temperature of the PVC matrix (T_g=353 K). The MBS modifier displays an effect in the mechanical spectroscopy response at 240 K. The peak arises from the glass transition of the butadiene phase, with the height of the peak proportional to the wt% of MBS added. In addition, the unmodified PVC shows a β relaxation at 240 K. Studies report that the β relaxation in PVC cannot be attributed to any particular molecular motion.[110]

3.4.3.2 Microscopy

The phase separated system, indicated by DMTA, is further verified by the transmission electron micrograph in Figure 3.19. The rubbery domains, indicated by the black in Figure 3.19 from the osmium tetroxide stain, are on the order of 300 nm. The microscopy indicates that the processing results in an even dispersion of the MBS modifier in the PVC matrix.

3.4.3.3 Elastic Properties

The elastic properties for the different formulations are shown in Table 3.5. With increasing wt% MBS, there is a decrease in Young's modulus (E) and no change in Poisson's ratio (ν). The shear moduli (G) reported in Table 3.5 and used in the hollow cylinder test to maintain a constant octahedral shear strain rate are calculated using equation 3.10, a formula valid for an isotropic homogenous material.

$$G = \frac{E}{2(1+\nu)} \qquad (3.10)$$

The elastic properties and trends with weight percent MBS modification are consistent with the findings of others.[101] In the rubber modification of many polymeric systems, the gain in toughening outweighs the loss in stiffness and strength.[8]

3.4.3.4 Fracture Behavior

The gain in fracture toughness (R_{Ic} -energy release rate criteria) upon the addition of MBS modifier is shown in Table 3.6. A linear elastic fracture mechanics approach was used to determine the fracture toughness of the unmodified PVC, while an elastic plastic fracture mechanics approach was used to determine the fracture toughness of the MBS modified PVC. The details of these approaches were discussed in section 2.11. The different approaches were necessitated by the brittle behavior in the PVC fracture differing significantly from the ductile behavior in the MBS modified PVC fracture specimen. The ductile behavior in the modified PVC can be seen in Figure 3.20, which shows the elastic plastic fracture toughness analysis along with a contact print showing the stress whitening zone ahead of the crack tip during crack growth (Δa). There is a significant increase in the fracture toughness from 0 wt% MBS to 5 wt% MBS but no further increase in the fracture toughness with 10 wt% or 15 wt% MBS. In addition, the slope of the elastic plastic fracture analysis (dJ/da), which relates to the non-essential work of fracture, is relatively unaffected by wt% MBS.

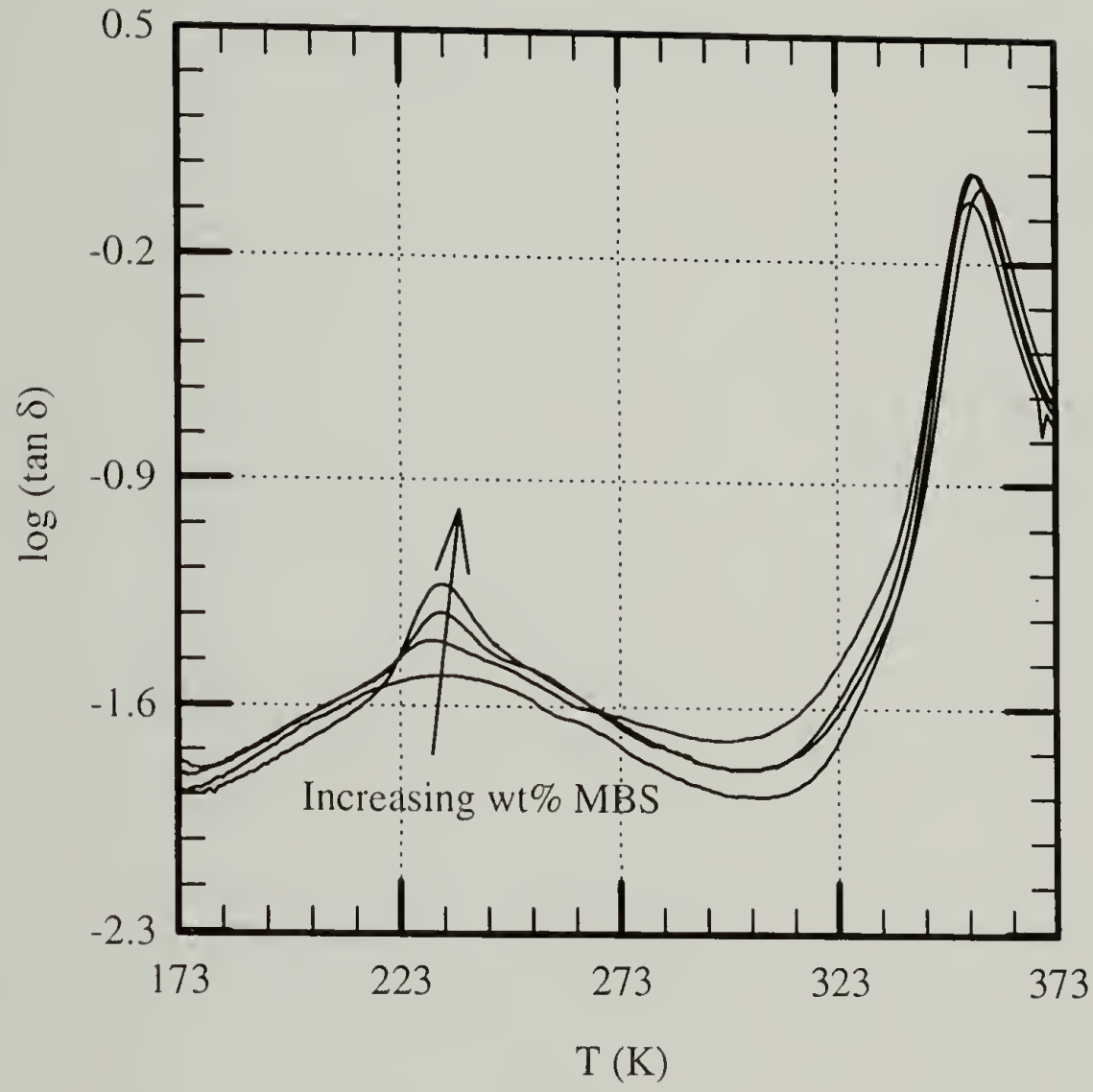

Figure 3.18: Dynamic mechanical thermal analysis of MBS modified PVC formulations (0, 5, 10, 15 wt% MBS).

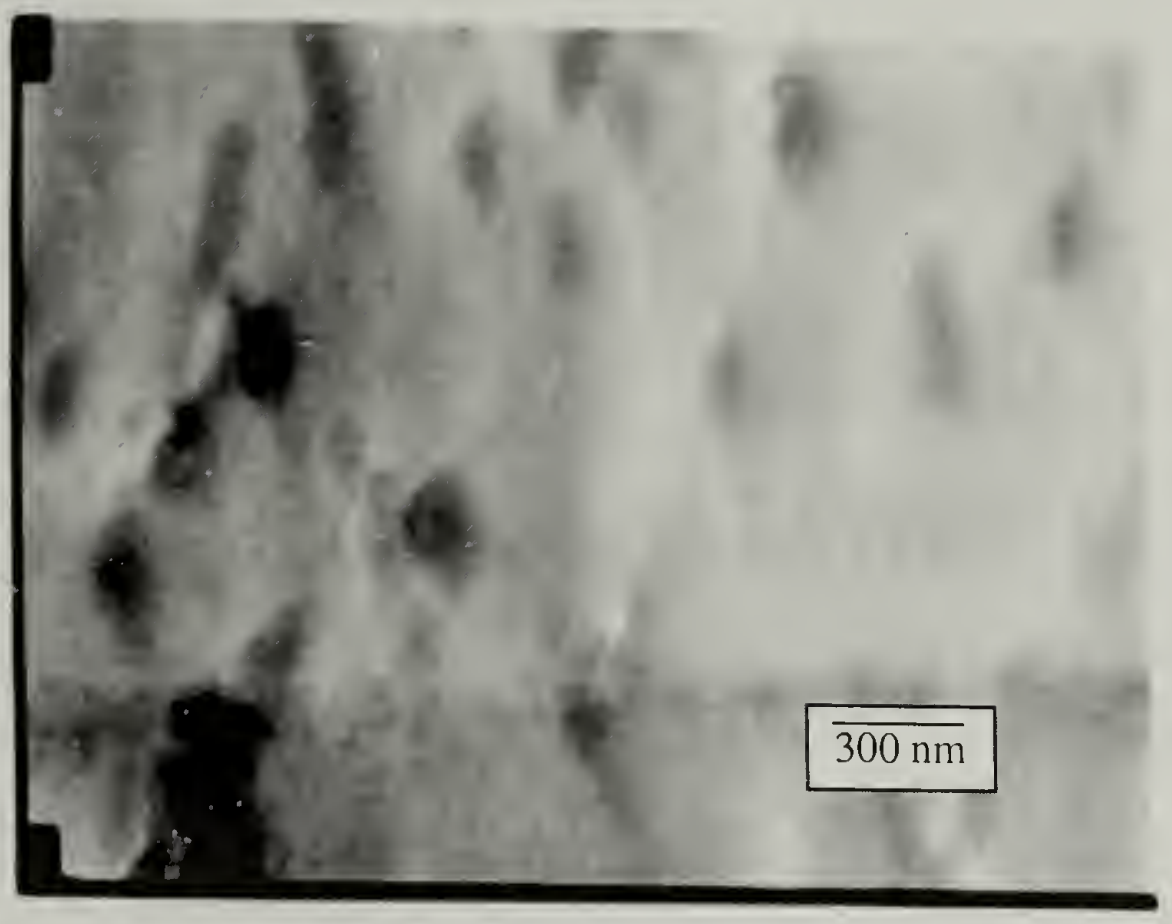

Figure 3.19: Transmission electron micrograph of 10 wt% MBS modified PVC.

Table 3.5: Elastic properties of MBS modified PVC at room temperature.

wt% MBS	E (GPa)	ν	G (GPa)
0	3.27	0.38	1.18
5	2.92	0.38	1.06
10	2.47	0.38	0.89
15	2.04	0.38	0.74

Table 3.6: Fracture toughness of MBS modified PVC at room temperature.

wt% MBS	R_{Ic} (kJ/m^2)	dJ/da (MPa)
0	0.78	-
5	5.5	27.3
10	5.5	23.1
15	4.8	24.2

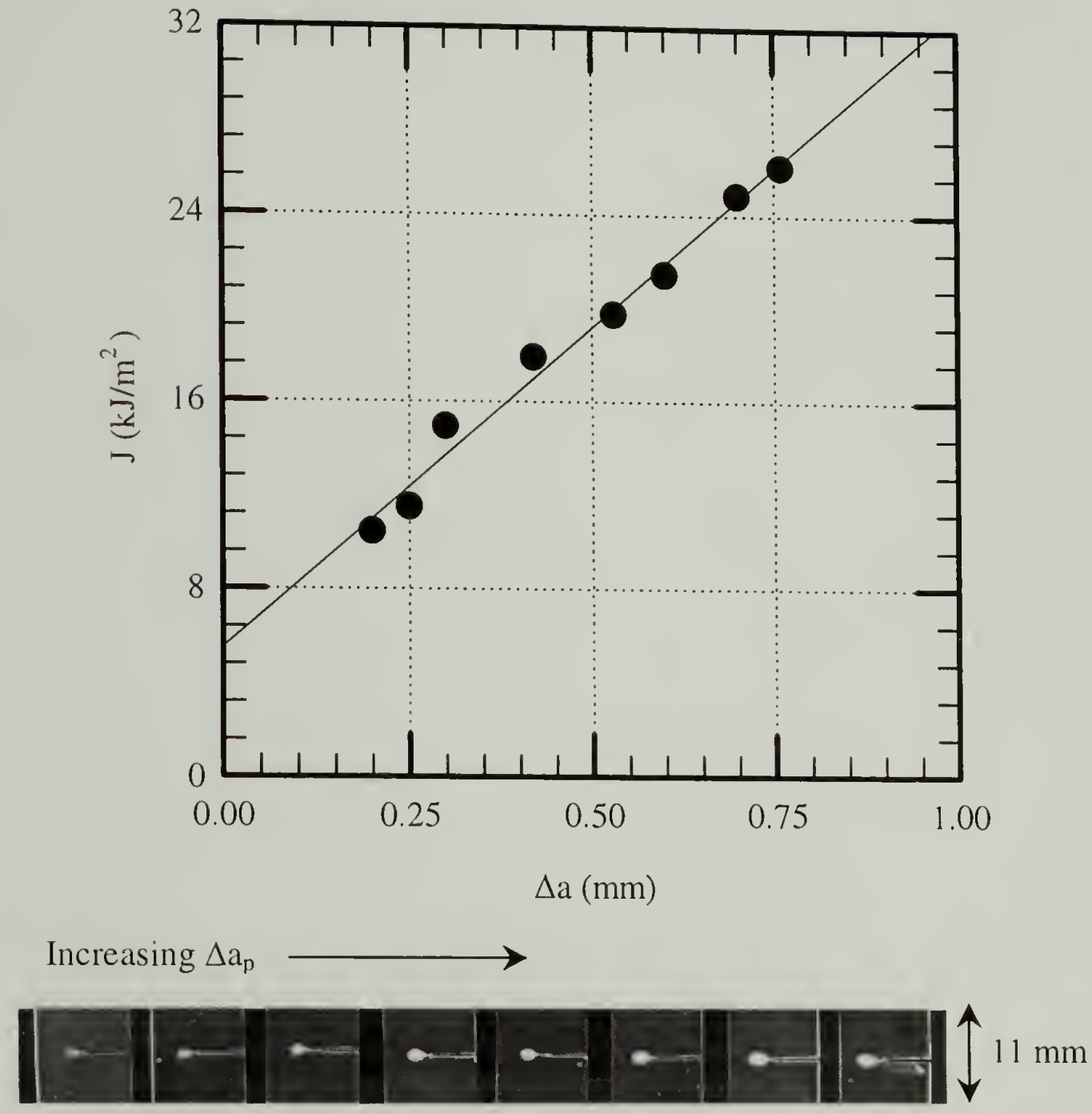

Figure 3.20: Elastic plastic fracture toughness analysis of 5 wt% MBS modified PVC and contact prints of the stress whitening zone of ahead of advancing crack tip.

3.4.4 Yield and Whitening Behavior in Multi-Axial Stress States

The loaded and pressurized hollow cylinder tests coupled with light transmission measurements revealed the yield behavior and whitening behavior of the MBS modified PVC. The unmodified PVC, shown in Figure 3.21, shows a modified von Mises yield behavior with τ_{yo}^{oct}=30.1 MPa and μ=0.18. This coefficient of internal friction is similar to other polymeric materials.[39] Figure 3.22 shows the yield behavior and onset of whitening behavior for 5 wt% MBS modified PVC. The yield behavior again follows a modified von Mises yield behavior with τ_{yo}^{oct}=27.6 MPa and μ=0.21. The onset of whitening appears to occur at a relatively constant octahedral shear stress of 15-16 MPa in the positive σ_m half. Whitening did not occur at negative σ_m until yield was reached, resulting in sample buckling and subsequent whitening. The 10 wt% and 15 wt% MBS modified PVC display a similar behavior as shown in Figures 3.23 and 3.24. The yield behavior can be described by a modified von Mises criteria with τ_{yo}^{oct}=26.2 MPa and μ=0.21 for the 10 wt% MBS modified PVC and with τ_{yo}^{oct}=24.0 MPa and μ=0.24 for the 15 wt% MBS modified PVC. The onset of whitening in the 10 wt% MBS modified PVC occurs at a octahedral shear stress of 14-15 MPa at positive σ_m, while the onset of whitening occurs at 15-16 MPa at positive σ_m half for the 15 wt% MBS modified PVC.

Figure 3.25 shows a linear relationship between wt% MBS on the octahedral shear strength in pure shear (τ_{yo}^{oct}). This trend is consistent with equation 3.10, since the incorporation of voids should result in a linear decrease in the τ_{yo}^{oct}.

$$\tau_{yo}^{oct}(f) = \tau_{yo}^{oct}(0)(1-f) \qquad (3.10)$$

where $\tau_{yo}^{oct}(0)$ is the unmodified octahedral yield strength in pure shear.

It would be difficult to attribute any non-linearity in the yield locus of the modified systems to the inelastic void growth described by equation 3.5. Non-linearity could also arise from slight orientation effects resulting from processing.

The onset of whitening appears to be relatively unaffected by wt% MBS and occurs at a relatively constant octahedral shear stress at positive σ_m. This results is in disagreement with energy balance cavitation theories (equation 3.3) that describe cavitation (onset of whitening) occurring at a constant positive σ_m. The results indicate that the whitening behavior, which arises from particle cavitation or particle debonding, is a shear-dominated process at positive σ_m.

There are several reports in the literature which support these findings. Bensason et al.[101] suggested that the shear yielding precedes particle cavitation at temperatures greater than –20 °C in MBS modified PVC. The stress whitening studies by H. Breuer et al.[106] on MBS modified PVC revealed that ruptured rubber particles occur in bands. These bands of cavitated particles are called dilatational bands and occur in many rubber-toughened materials.[97] These bands correspond to shear bands of the matrix material. Since the onset of whitening is shear dominated, it seems likely that cavitation occurs by debonding during shear. The stress concentration of an isolated void in a matrix is on the order of 1.5-2, which given the yield strength of the unmodified PVC further supports the onset of whitening trends by a shear process. Positive σ_m is only required to open the sheared particle to create a void and scatter light.

Some literature results disagree with the behavior observed in this study. Dompas and Groeninckx[103] used an energy balance approach (constant mean stress criteria) to describe the particle size dependence of the whitening behavior of MBS modified PVC.

However, objections can be raised about the experimental procedure used by Dompas and Groeninckx[80] to determine the onset of whitening. Researchers in the field have consistently described fracture behavior and microscopy as arising first from particle cavitation and subsequent shear yielding. The findings of this study do not support this popular opinion. However, the experimental techniques used in this study provide excellent control of the state of stress, allowing separation of shear and volume deformations. In addition, the materials used in this study provide favorable properties for determining cavitation or debonding processes. This combination allows for an effective study of the mechanics of rubber toughened polymeric systems.

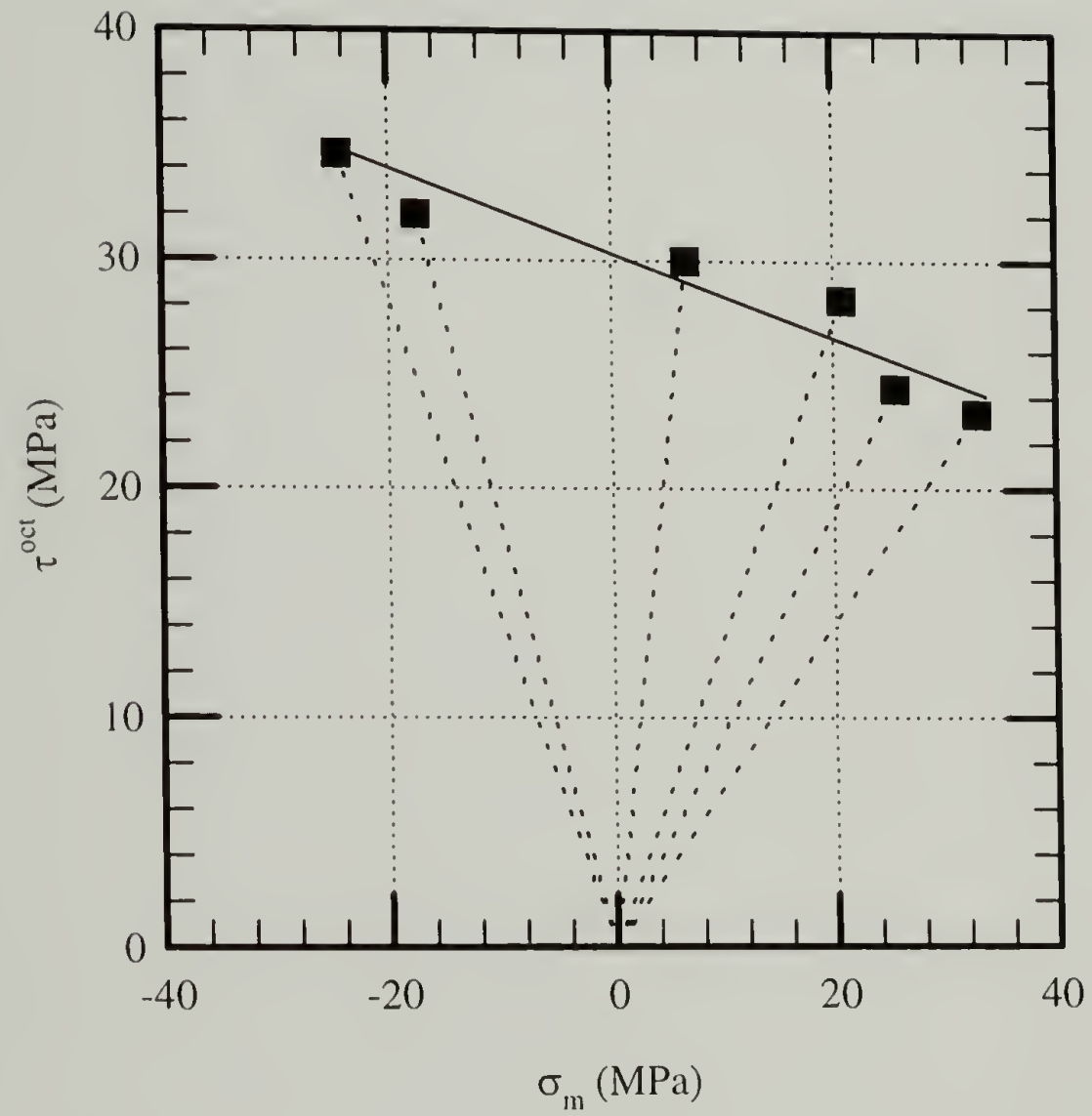

Figure 3.21: Yield locus of 0 wt% MBS modified PVC.

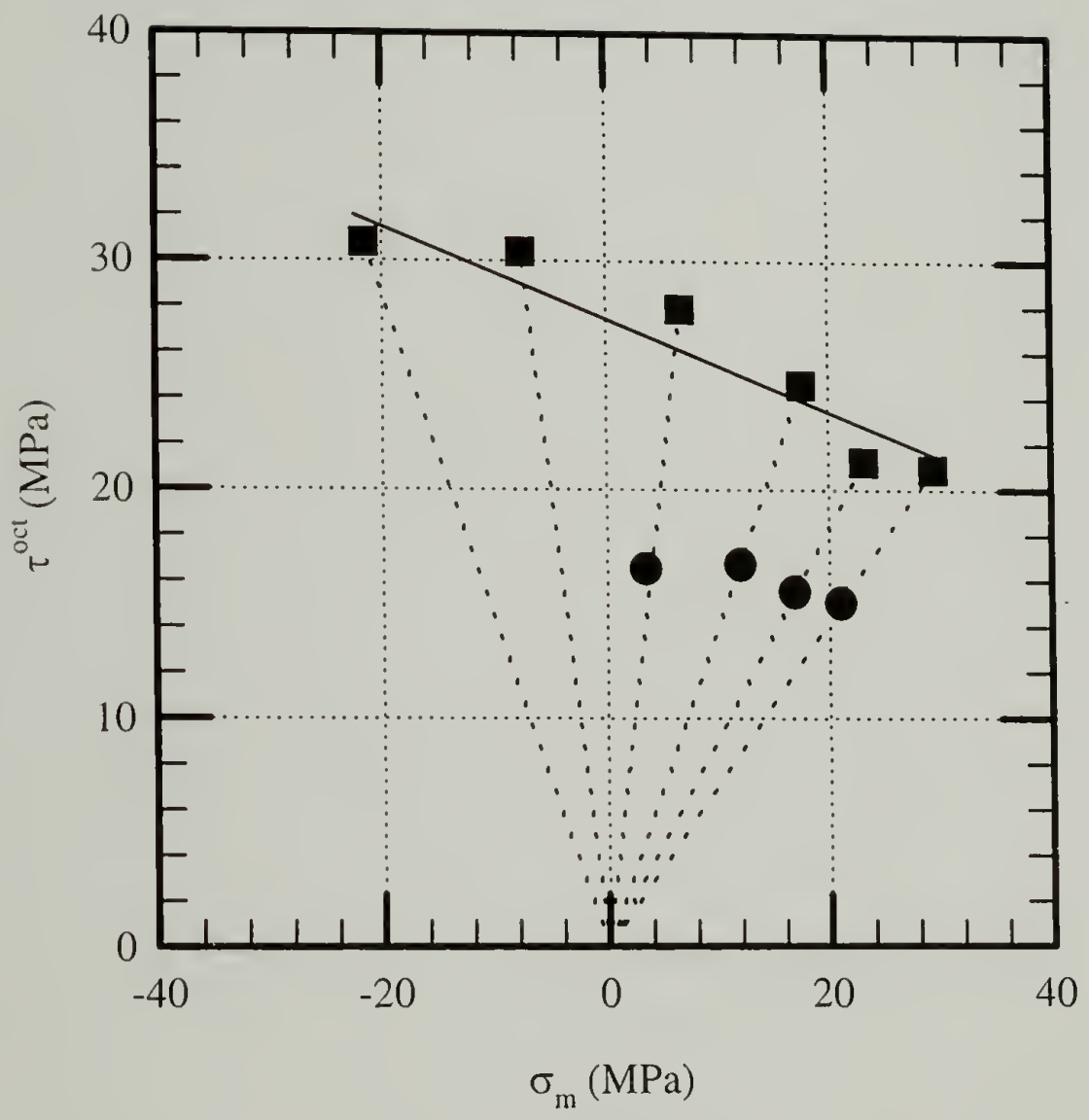

Figure 3.22: Yield locus (squares and solid line) and whitening onset (circles) for 5 wt% MBS modified PVC.

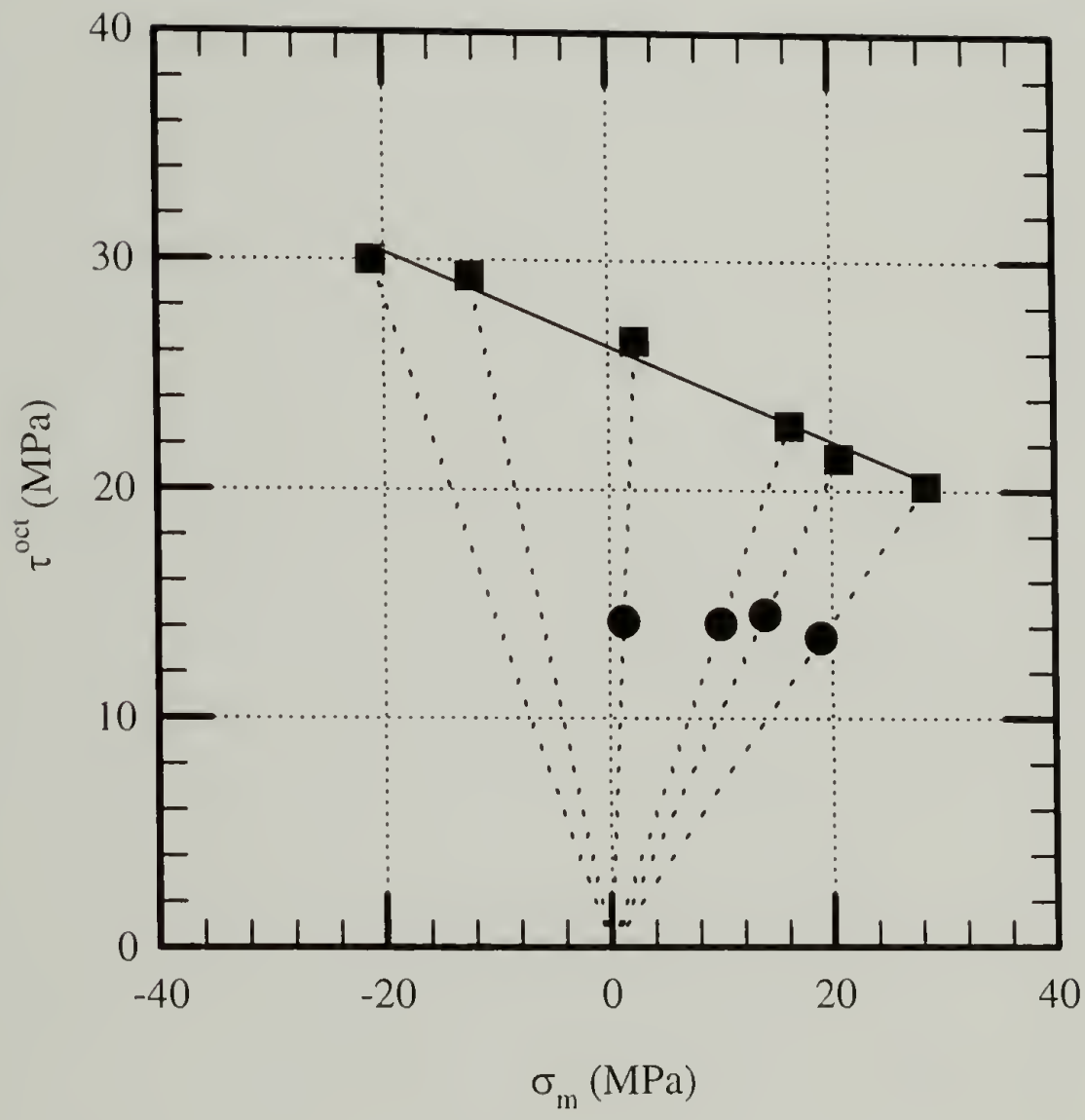

Figure 3.23: Yield locus (squares and solid line) and whitening onset (circles) for 10 wt% MBS modified PVC.

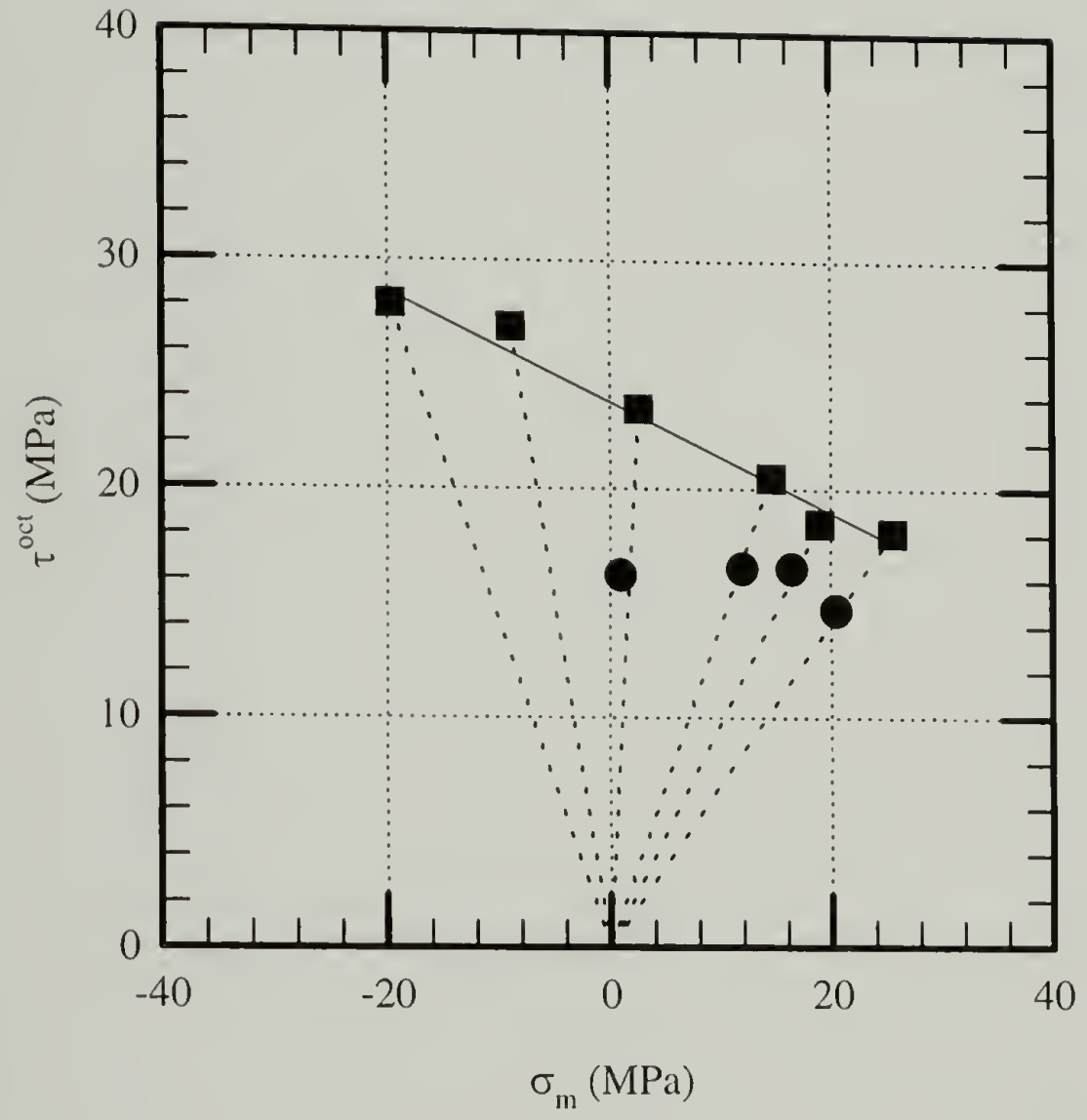

Figure 3.24: Yield locus (squares and solid line) and whitening onset (circles) for 15 wt% MBS modified PVC.

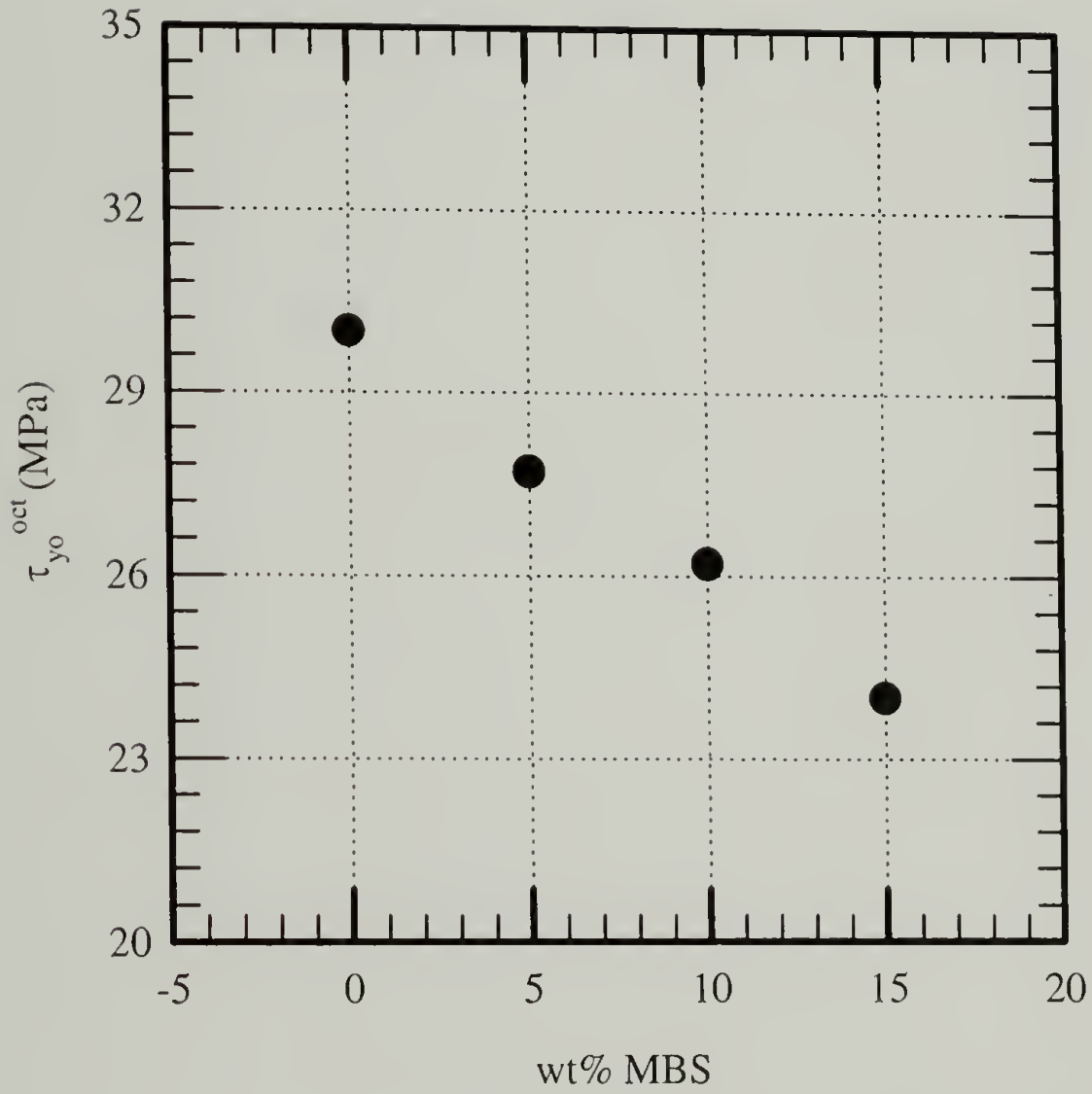

Figure 3.25: Octahedral shear strength at σ_m=0 as a function of wt% CTBN.

3.5 Voided Epoxy Materials

3.5.1 Introduction

Much of the literature on rubber toughening has recently been focused on particle cavitation. In particular, Dompas[103] and Bucknall[97] have developed models describing rubber particle cavitiation energetics. After cavitation, the local release of hydrostatic stress results in a state of stress promoting flow or yielding. The cavitational energy has been shown to be quite small compared with the subsequent matrix yielding process.[88] Since the energy associated with particle cavitation is insignificant, creating a material with pre-cavitated particles or voids should also provide significant levels of toughening. Finite element studies performed by Guild and Young[111] reveal identical stress states for voids and rubber particles. However, Guild and Young[111] state that "epoxy resin containing holes is known to be a very poor material".

In addition to testing these ideas, the creation of voided materials will allows matrix effects to be isolated from rubbery phase influences. Several attempts at creating voided epoxy materials include non-reactive liquid rubber[112] and hollow latex spheres.[87,113] However, non-reactive liquid rubbers maintain interfacial adhesion and interfacial tension, while dispersion problems are associated with the use of hollow latex spheres.

In addition to isolating cavitational effects, a yield model has recently been proposed by Bucknall[97,105] to describe the effect of void concentration. This model, described by equation 3.11 and shown by the solid lines in Figure 3.26, represents a lower bound of a pressure dependent yield locus for a rubber modified material.

$$\left(\frac{\tau_y^{oct}}{\tau_{yo}^{oct}}\right)+\mu\frac{\sigma_m}{\tau_{yo}^{oct}}\left(2-\mu\frac{\sigma_m}{\tau_{yo}^{oct}}\right)+2f\cosh\left(\frac{3\sigma_m}{2\tau_{yo}^{oct}}\right)-f^2-1=0 \qquad (3.11)$$

The introduction of voids lowers the yield strength, with the amount dependent on the mean stress.

In this study, voided materials are fabricated with a method recently reported by Hilborn et al.[114], which involves a chemically induced phase separation between a low molecular weight solvent and epoxy formulation. The fracture and yield behavior of these materials is determined with a variety of techniques including a multi-axial stress state test which for a single specimen geometry allows independent control of the octahedral shear stress and mean stress in the regions between uniaxial compression and equal biaxial tension.

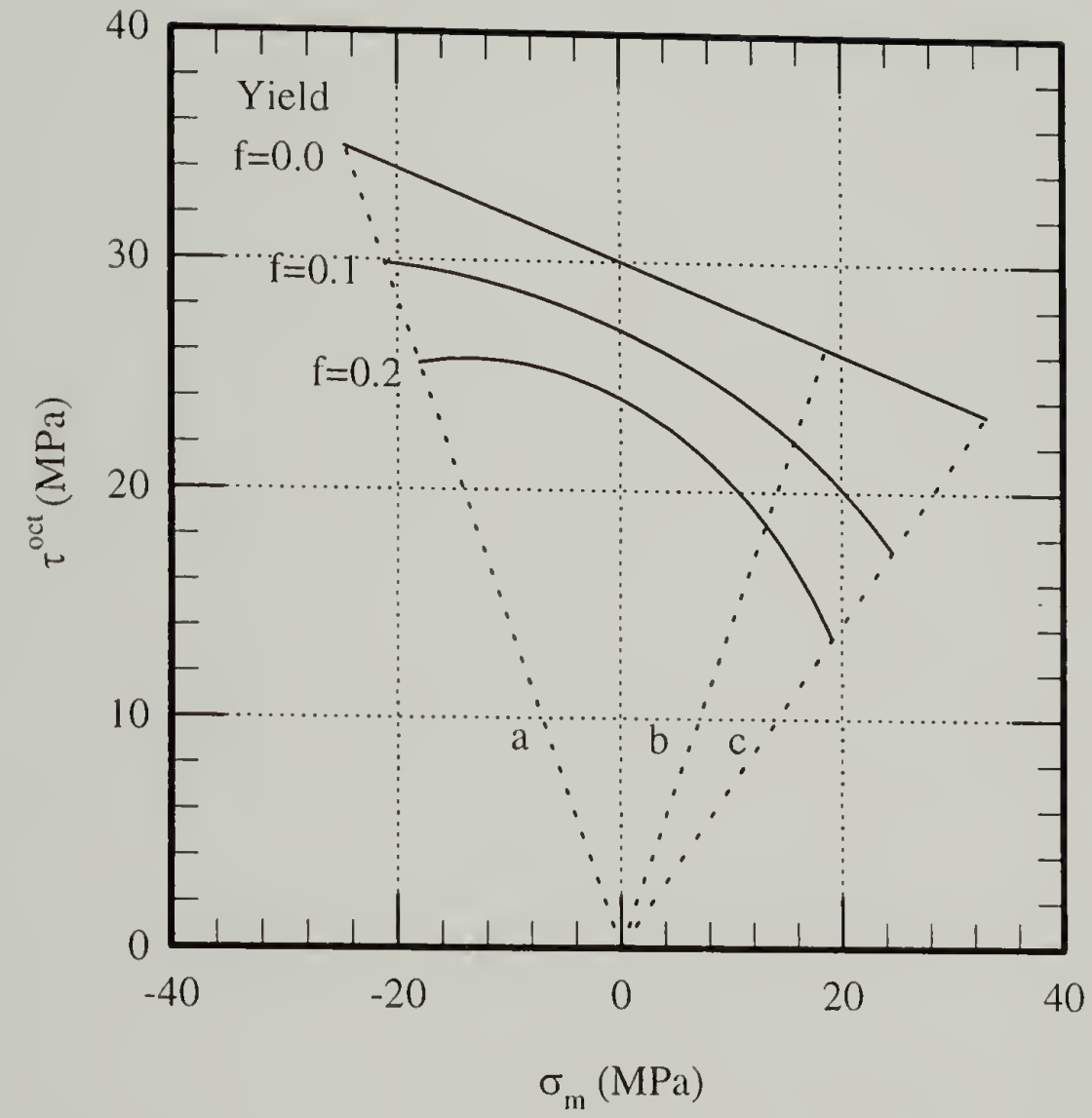

Figure 3.26: Yield behavior of a voided polymeric systems at various void volume fractions. Dashed lines represent various loading conditions: a) uniaxial compression, b) uniaxial tension, and c) equal biaxial tension.

3.5.2 Experimental

3.5.2.1 Materials

Fifty grams of Epon 825, 12.4 grams of AEP, and various amounts of hexane were mixed with a stir plate for 5 minutes at room temperature. After mixing, an emulsion was produced with the higher density phase consisting of epoxy, AEP, and soluble hexane, and a lower density phase consisting primarily of hexane. This mixture was poured into molds and allowed to gel for 8 hours at room temperature. After gelation, the materials were cured at 60 °C for 3 hrs. and then curing at 150 °C for an additional 3 hrs.. Unmodified materials were made with the same procedure without the addition of hexane. In addition, other solvents (cyclohexane, n-propylbenzene) were used in the fabrication of voided epoxy materials. In the case of multi axial stress state test, hollow cylinder specimens were produced by spin casting the mixture until cured. Grips were then molded onto the sample as described by Kody.[39]

3.5.2.2 Material Characterization

DSC, compression tests, fracture tests, and SEM techniques were used to characterize the materials. In addition to these tests, the details of which have been described previously, Robert Kody performed multi-axial stress state tests, which were discussed in section 3.4, on the voided materials. The multi-axial stress state test employs a pressurized and uniaxially loaded hollow cylinder. This test allows a range of stress states, from uniaxial compression to equal biaxial tension, to be achieved in a single specimen geometry. Details of the experimental setup have been reported by Kody and Lesser.[39] The tests were run at a constant octahedral shear strain rate of 0.1 min^{-1}.

3.5.3 Results and Discussion

Scanning electron microscopy performed on a cryogenically fast fractured sample is shown in Figure 3.27. Stereological analysis reveals an average void size of 6 μm with an estimated void volume fraction (f) of 0.07. Higher void volume fractions, near 0.12, were achieved with the use of cyclohexane and even higher void volume with the use of n-propylbenzene. Figure 3.28 shows a SEM micrograph of a porous epoxy, possesing a void volume fraction of 0.28, formed with n-propylbenzene. The void sizes in Figures 3.27 and 3.28 are slightly larger than those typically found in most rubber modified epoxies, which are around 1 μm. However, the yielding behavior described by equation 3.11 does not describe void size dependence.

The thermal and mechanical characteristics of the hexane modified epoxy network are shown in Table 3.7. The drop in T_g suggests solubility of hexane in the cross-linked epoxy network. This view is consistent with the stereological results and fabrication process. The drop in compressive yield strength and increase in fracture toughness may be attributed to both the presence of voids and plasticization. If plasticization is modeled as a function of $(T-T_g)$, the increase in fracture toughness for the hexane modified materials as a result of the inelastic void growth appears to be small. This analysis is shown in Figure 3.29.

Multi-axial stress state tests, performed by Robert Kody, do not reveal any distinguishable non-linearity in the yield locus of these materials with increasing hydrostatic stress, as would be predicted by equation 3.11. Figure 3.30 shows the octahedral shear yield strength as a function of mean stress for a hexane modified network with a void volume fraction of 0.07. Increasing the void volume fraction to 0.28

by changing the solvent to n-propylbenzene did not induce any noticeable non-linearity in the octahedral shear yield strength versus mean stress. This behavior is shown in Figure 3.31. Discrepancies with theory could be the result of kinematic limits of plasticity due to cross-linking and residual solvent in the epoxy matrix creating an internal hydrostatic tension. However, it is plausible that the yield behavior described by equation 3.11 is incorrect due to errors associated with the assumed superposition of hydrostatic effects and shear effects in polymers.

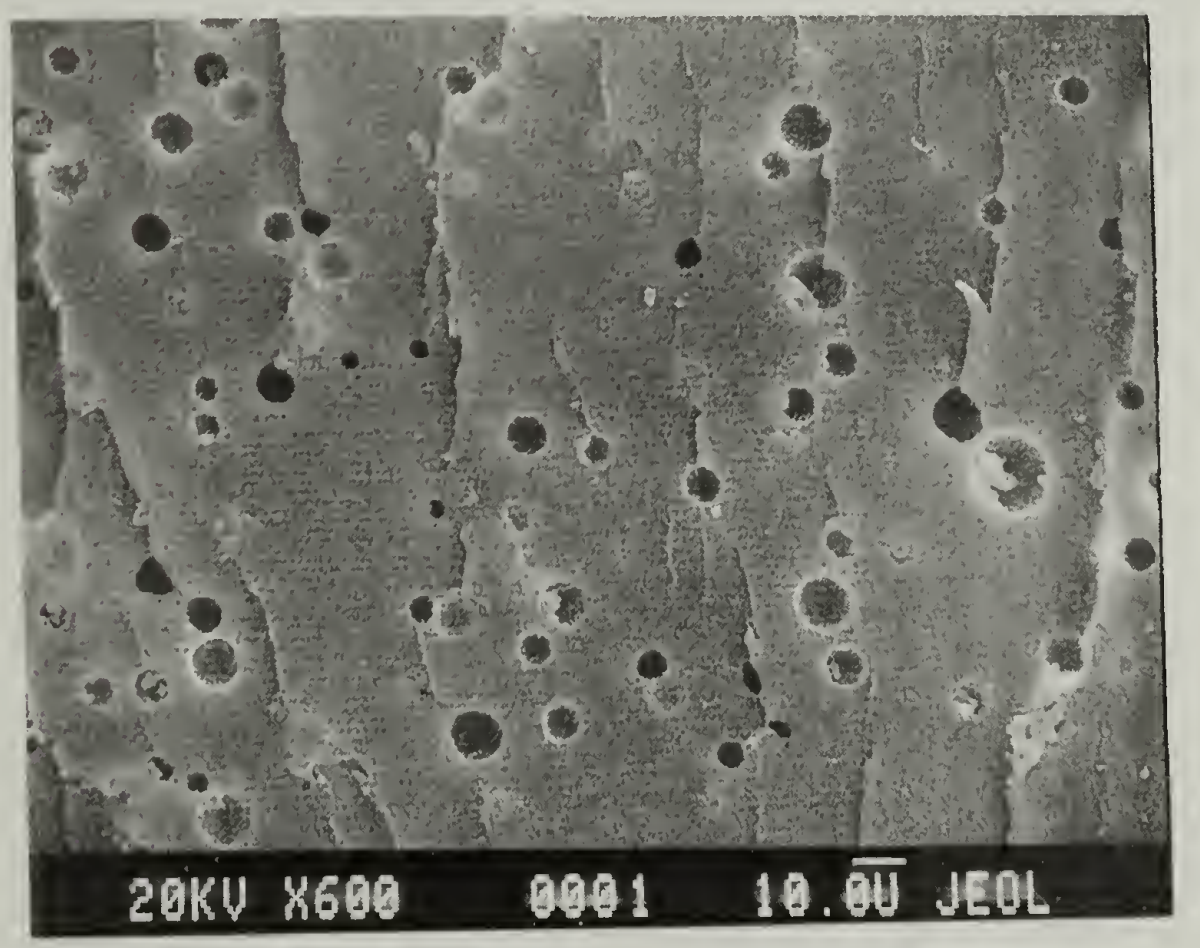

Figure 3.27: Scanning electron micrograph of a hexane modified epoxy network.

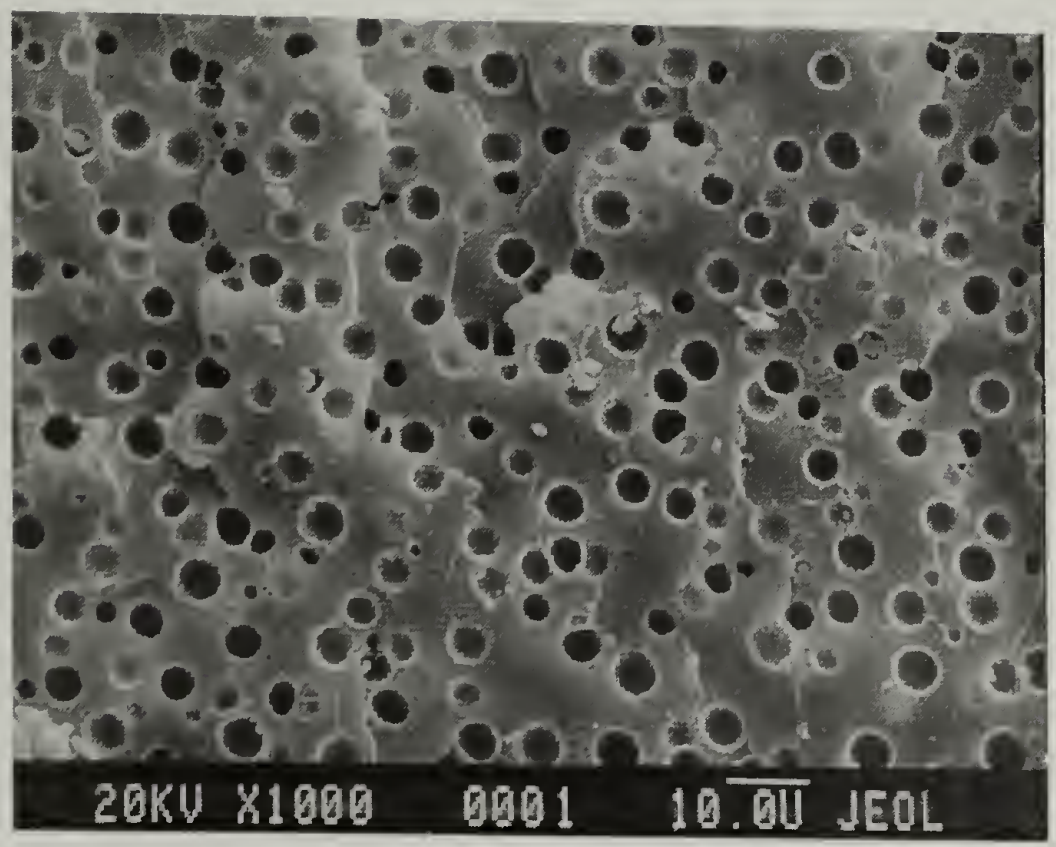

Figure 3.28: Scanning electron micrograph of a n-propylbenzene modified epoxy network.

Table 3.7: Mechanical and thermal characteristics of unmodified and hexane modified epoxy network.

	T_g (°C)	E (GPa)	σ_{yc} (MPa)	K_{Ic} (MPa $m^{1/2}$)
Unmodified	126	2.8	90	1.5
Hexane modified	93	2.3	76	1.7

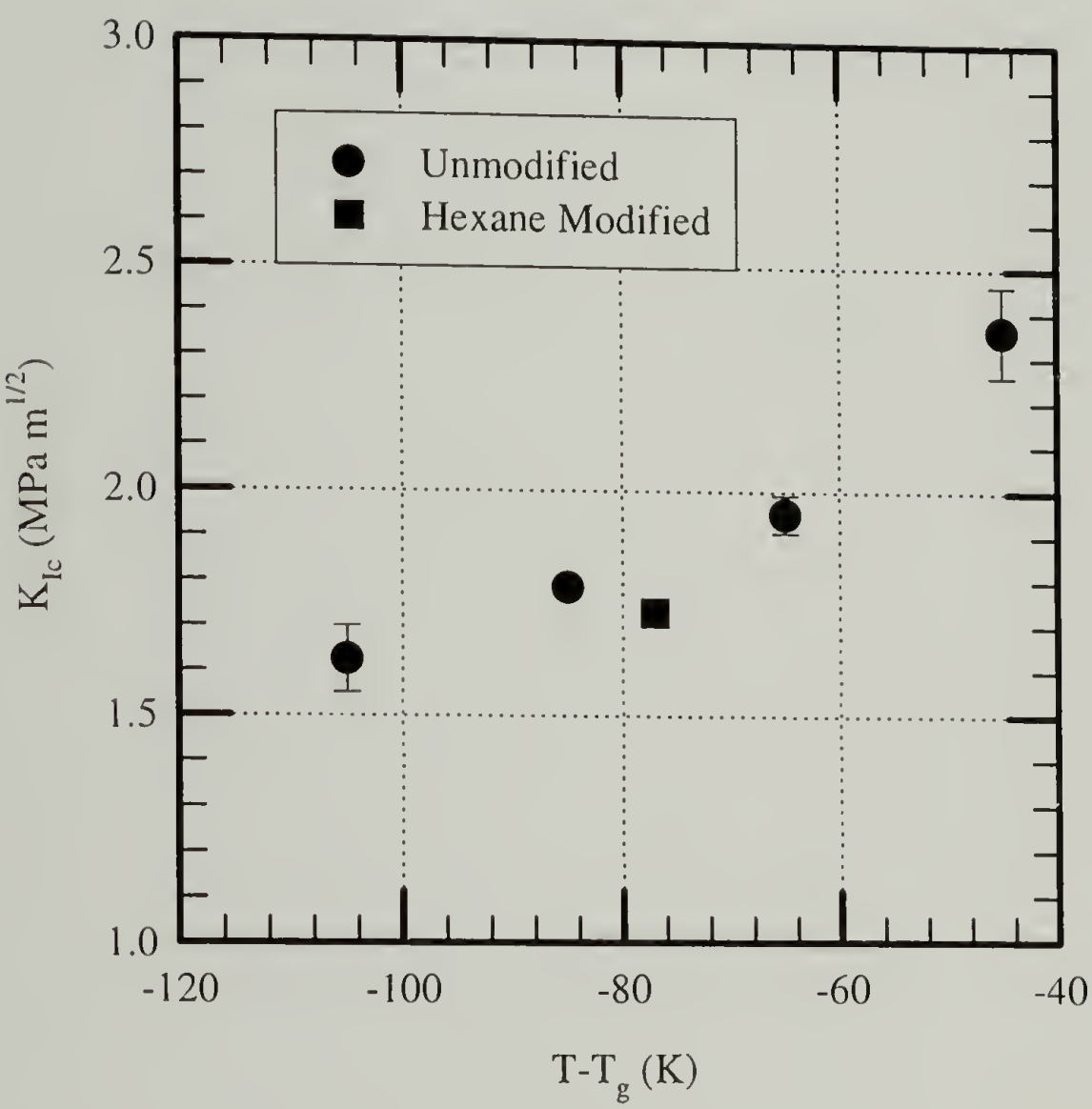

Figure 3.29: Fracture toughness collapsed as a function of ($T-T_g$) for hexane modified and unmodified materials.

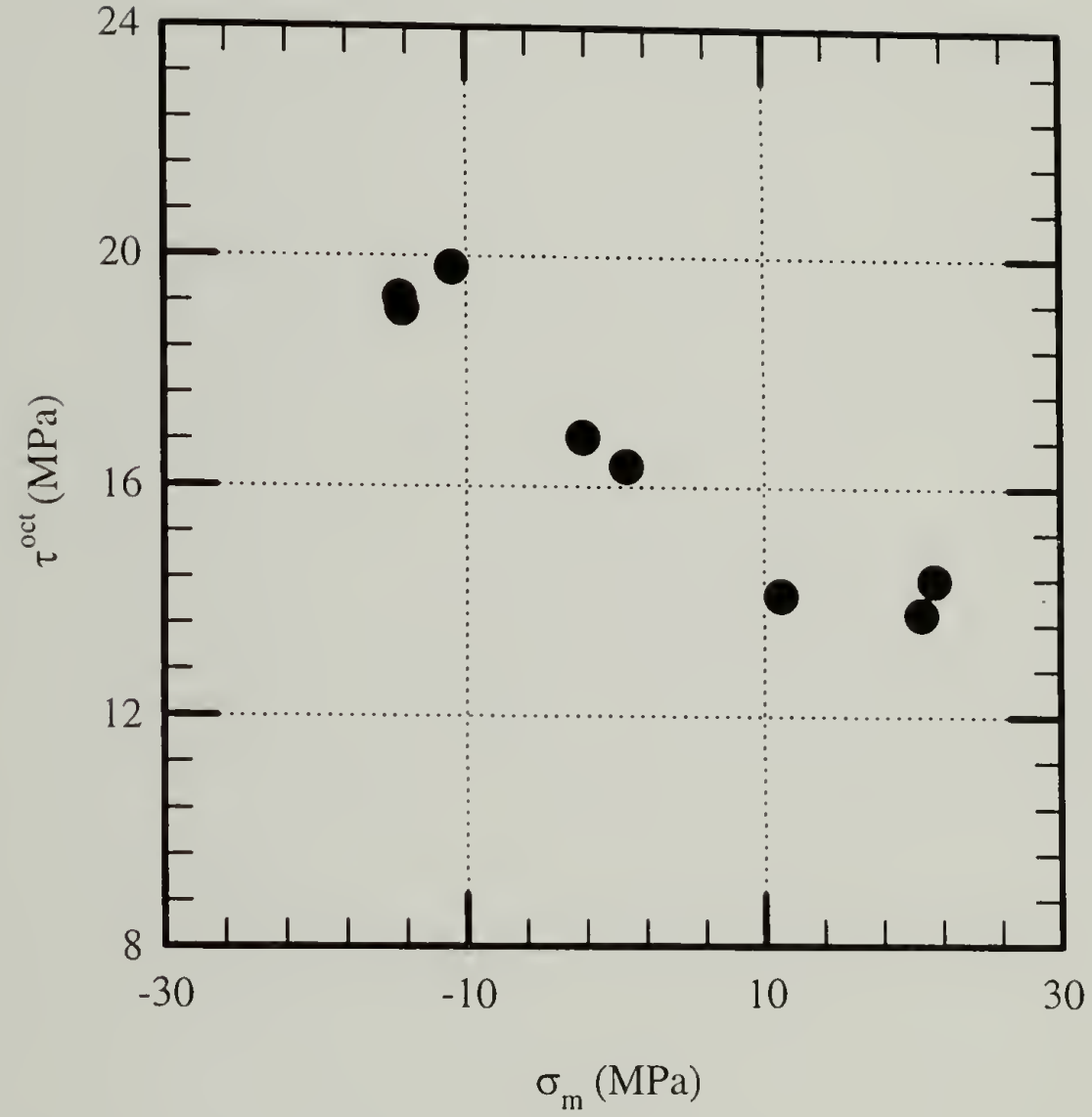

Figure 3.30: Yield locus of hexane modified epoxy network with f=0.07.

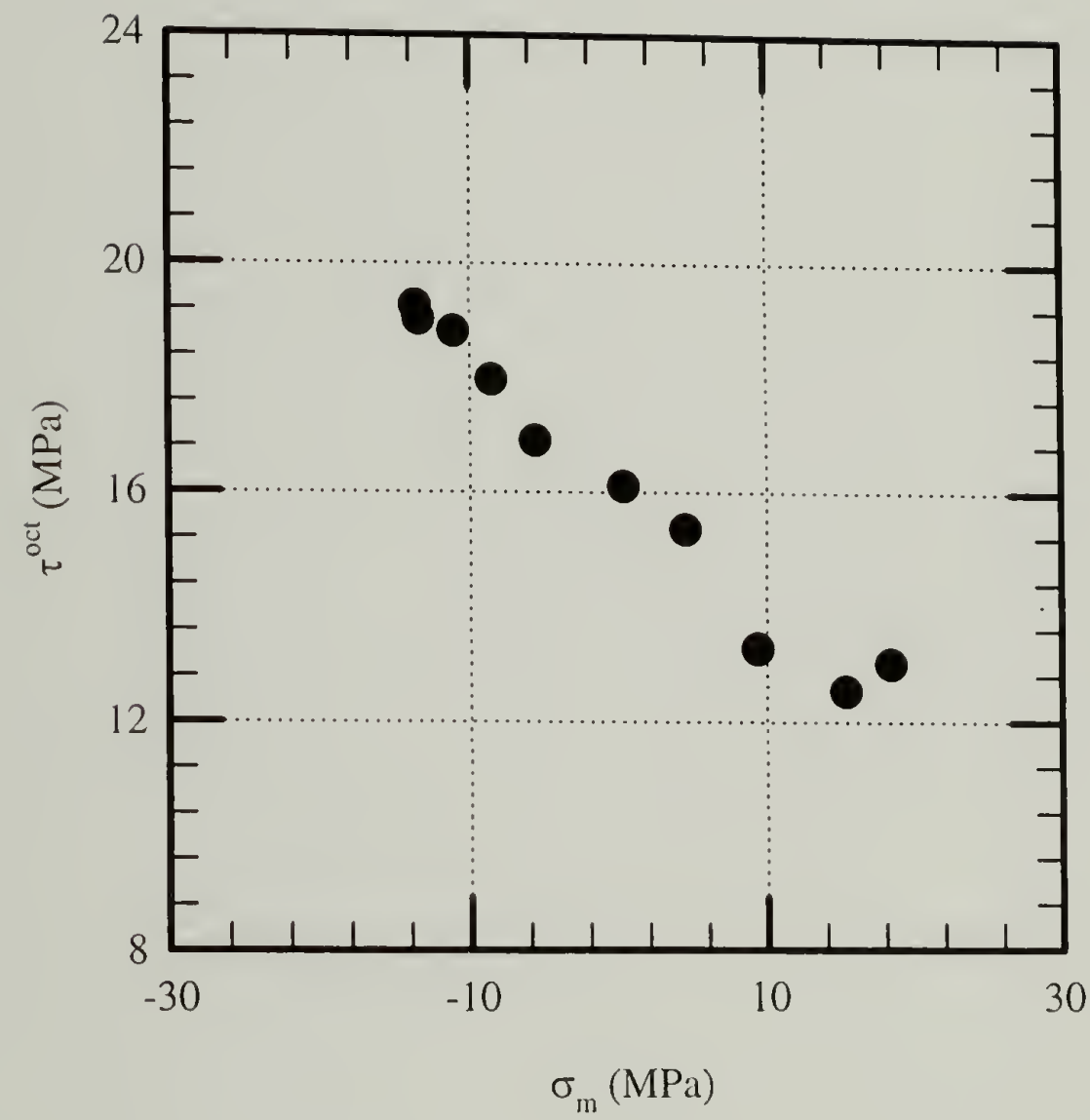

Figure 3.31: Yield locus of n-propylbenzene modified epoxy with f=0.28.

BIBLIOGRAPHY

1. Bradley, W. L., Schultz, W., Carleto, C. and Kotmatsu, S. in *Toughenend Plastics I: Science and Engineering*, p. 317, Riew, C. K. and Kinloch, A. J., Ed., American Chemical Society, Washington D.C. (1993).

2. Fischer, M., *Adv. Polym. Sci.*, **100**, 313 (1992).

3. Banks, L. and Ellis, B., *Polymer*, **23**, 1466 (1982).

4. Vakil, U. M. and Martin, G. C., *J. Appl. Polym. Sci.*, **46**, 2089 (1992).

5. Graessley, W. W., *Macromolecules*, **8**, 186 (1975).

6. Flory, P. J., *Polymer*, **20**, 1317 (1979).

7. Duiser, J. A. and Staverman, A. J. in *Physics of Non-Crystalline Solids*, p. 376, Prins, J. A., Ed., North-Holland Publishing Co., Amsterdam (1965).

8. Bucknall, C. B. in *The Physics of Glassy Polymers*, p. 363, 2 ed., Haward, R. N. and Young, R. J., Ed., Chapman & Hall, London (1997).

9. Yee, A. F. and Pearson, R. A., *J. Mater. Sci.*, **21**, 2462 (1986).

10. Ashcroft, W. R. in *Chemistry and Technology of Epoxy Resins*, p. 37, Ellis, B., Ed., Blackie Academic & Professional, Glasgow (1993).

11. Bell, J. P., *J. Appl. Polym. Sci.*, **14**, 1901 (1970).

12. Oleinik, E. F., *Adv. Polym. Sci.*, **80**, 1901 (1986).

13. Riccardi, C. C. and Adabbo, H. E., *J. Appl. Polym. Sci.*, **29**, 2481 (1984).

14. Ellis, B. in *Chemistry and Technology of Epoxy Resins*, p. 72, Ellis, B., Ed., Blackie Academic & Professional, Glasgow (1993).

15. Wisanrakkit, G. and Gillham, J. K., *J. Appl. Polym. Sci.*, **41**, 2885 (1990).

16. Horie, K., Hiura, H., Sawada, M., Mita, I. and Kambe, H., *J. Polym. Sci., Part A: Polym. Chem.*, **8**, 1357 (1970).

17. Charlesworth, J. M., *Polym. Eng. Sci.*, **28**, 221 (1988).

18. Blokland, R., *Elasticity and Structure of Polyurethane Networks*, Rotterdam University Press, Rotterdam (1968).

19. Nielsen, L., *J. Macromol. Sci. Rev. Macromol. Chem.*, **C3**, 69 (1969).

20. Charlesworth, J. M., *Polym. Eng. Sci.*, **28**, 230 (1988).

21. LeMay, J. D. and Kelley, F. N., *Adv. Polym. Sci.*, **78**, 115 (1986).

22. Miller, D. R. and Macosko, C., *Macromolecules*, **9**, 207 (1976).

23. Ilavsky, M., Bodanova, L. and Dusek, K., *J. Polym. Sci., Part B: Polym. Phys.*, **22**, 265 (1984).

24. Fox, T. G. and Loshaek, S., *J. Polym. Sci.*, **15**, 371 (1955).

25. DiBenedetto, A. T., *J. Polym. Sci., Part B: Polym. Phys.*, **25**, 1949 (1987).

26. Stutz, H., Illers, K. and Mertes, J., *J. Polym. Sci.: Part B: Polym. Phys.*, **28**, 1483 (1990).

27. DiMarzio, E. A., *J. Res. Nat. Bur. Stand.*, **68A**, 611 (1964).

28. Urabaczewski-Espuche, E., Galy, J., Gerard, J., Pascault, J. and Sautereau, H., *Polym. Eng. Sci.*, **31**, 1572 (1991).

29. Williams, J. G., *J. Appl. Polym. Sci.*, **23**, 3433 (1979).

30. Delatycki, O., Shaw, J. and Williams, J. G., *J. Polym. Sci., Part A2: Polym. Phys.*, **7**, 753 (1969).

31. Pogany, G. A., *Polymer*, **11**, 66 (1970).

32. Shi, J. F., Inglefield, P. T., Jones, A. A. and Meadows, M. D., *Macromolecules*, **29**, 605 (1996).

33. Wang, X. and Gillham, J. K., *J. Coatings Tech.*, **64**, 37 (1992).

34. Sindt, O., Perez, J. and Gerard, J. F., *Polymer*, **37**, 2989 (1996).

35. Crawford, E. and Lesser, A. J., *J. Polym. Sci., Part B: Polym. Phys*, **36**, 1371 (1998).

36. Kinloch, A. J., Shaw, S. J. and Hunston, D. L., *Polymer*, **24**, 1355 (1983).

37. Ward, I. M., *Mechanical Properties of Solid Polymers*, 2 ed., John Wiley & Sons, Chichester (1983).

38. Lesser, A. J. and Kody, R. S., *J. Polym. Sci., Part B: Polym. Phys.*, **35**, 1611 (1997).

39. Kody, R. S. and Lesser, A. J., *J. Mater. Sci.*, **32**, 5637 (1997).

40. Broek, D., *The Practical Use of Fracture Mechanics*, Kluwer Academic Publishers, Dordrecht (1989).

41. *1994 Annual Book of ASTM Standards*, **03.01**, 407 (1994).

42. *1994 Annual Book of ASTM Standards*, **08.01**, 310 (1994).

43. *1988 Annual Book of ASTM Standards*, **03.01**, 698 (1988).

44. Garg, A. and Mai, Y., *Compos. Sci. and Technol.*, **31**, 225 (1988).

45. Kinloch, A. J. and Williams, J. G., *J. Mater. Sci.*, **15**, 987 (1980).

46. Lesser, A. J. and Crawford, E., *J. Appl. Polym. Sci.*, **66**, 387 (1997).

47. Parvin, M. and Williams, J. G., *Int. J. Fracture.*, **11**, 963 (1975).

48. Cantwell, W. J. and Kausch, H. H. in *Chemistry and Technology of Epoxy Resins*, p. 144, Ellis, B., Ed., Blackie Academic & Professional, Glasgow (1993).

49. Hashemi, S. and Williams, J. G., *J. Mater. Sci.*, **19**, 3746 (1984).

50. Mai, Y. and Powell, P., *J. Polym. Sci., Part B: Polym. Phys.*, **29**, 785 (1991).

51. Narisawa, I. and Takemori, M. T., *Polym. Eng. Sci.*, **29**, 671 (1989).

52. Anderson, T. L. and Dodds, R. H., *Journal of Testing and Evaluation*, **19**, 123 (1991).

53. Hertzberg, R., *Deformation and Fracture Mechanics of Engineering Materials*, 3 ed., John Wiley & Sons, New York (1989).

54. Cotterell, B. and Reddel, J., *Int. J. Fract.*, **13**, 267 (1977).

55. Levita, G., Parisi, L. and McLoughlin, S., *J. Mater. Sci.*, **31**, 1545 (1996).

56. Link, R. and Joyce, J. in Constraint Effects in Fracture, p. 286, Link, R. and Joyce, J., Ed., ASTM, Philadelphia (1995).

57. Kinloch, A. J., *Adv. Polym. Sci.*, **72**, 45 (1985).

58. Levita, G., Petris, S. D., Marchetti, A. and Lazzeri, A., *J. Mater. Sci.*, **26**, 2348 (1991).

59. Yap, O. F., Mai, Y. W. and Cotterell, B., *J. Mater. Sci.*, **18**, 657 (1983).

60. Irwin, G. R., *J. Basic Eng.*, **84**, 417 (1960).

61. Irwin, G. R., *Appl. Mater. Res.*, **3**, 65 (1964).

62. Bucknall, C. B., *Plast. Rubb. Proc. Appl.*, **17**, 141 (1992).

63. Turner, S., Reed, P. E. and Money, M., *Plast. Rubb. Proc. Appl.*, **4**, 369 (1984).

64. Tryson, G. R., Takemori, M. T., Yee A. F., *SPE ANTEC Tech. Papers*, **37**, 638 (1979).

65. Liu, T. M. and Bui, V. T., *J. Appl. Polym. Sci.*, **56**, 345 (1995).

66. Fowler, M. W. and Baker, W. E., *Polym. Eng. Sci.*, **28**, 1427 (1988).

67. Savadori, A., *Polymer Testing*, **5**, 209 (1985).

68. Roark, R. J., *Formulas for Stress and Strain*, McGraw-Hill, New York (1954).

69. Johnson, K. L., *Contact Mechanics*, Cambridge University Press, Cambridge (1985).

70. Lawn, B. and Wilshaw, R., *J. Mater. Sci.*, **10**, 1049 (1975).

71. Fischer-Cripps, A. C., *J. Mater. Sci.*, **32**, 727 (1997).

72. Marsh, D. M., *Proc. R. Soc. A*, **279**, 420 (1964).

73. Johnson, K. L., *J. Mech. Phys. Solids*, **18**, 115 (1970).

74. Hill, R., *The Mathematical Theory of Plasticity*, Oxford University Press, Oxford (1983).

75. Chiang, S. S., Marshall, D. B. and Evans, A. G., *J. Mater. Sci.*, **53**, 298 (1982).

76. Kourtesis, G., Renwick, G. M., Fischer-Cripps, A. C. and Swain, M. V., *J. Mater. Sci.*, **33**, 4493 (1997).

77. Field, J. S. and Swain, M. V., *J. Mater. Res.*, **8**, 297 (1983).

78. Chiang, S. S., Marshall, D. B. and Evans, A. G., *J. Appl. Phys.*, **53**, 312 (1982).

79. Wu, S., *Polym. Int.*, **29**, 229 (1992).

80. Dompas, D. and Groeninckx, G., *Polymer*, **33**, 4750 (1994).

81. Shaw, S. J. in *Chemistry and Technology of Epoxy Resins*, p. 117, Ellis, B., Ed., Chapman & Hall, London (1993).

82. Riew, C. K. and Smith, R. W., *J. Polym. Sci., Part A1: Polym. Chem.*, **9**, 2739 (1971).

83. Ruseckaite, R. and Williams, R. J., *Polym. Int.*, **30**, 11 (1993).

84. Ruseckaite, R., Hu, L., Riccardi, C. C. and Williams, R. J., *Polym. Int.*, **30**, 287 (1993).

85. Drake, R. and Siebert, A., *SAMPE Quarterly*, 11 (1975).

86. Riew, C. K., *Rub. Chem. Tech.*, **54**, 374 (1980).

87. Bagheri, R. and Pearson, R., *Polymer*, **37**, 4529 (1996).

88. Bucknall, C. B., Karpodinis, A. and Chang, X. C., *J. Mater. Sci.*, **29**, 3377 (1994).

89. Duckett, R. A., *Brit. Polym. J.*, **10**, 11 (1978).

90. Parker, D. S., Sue, H.-J., Huang, J. and Yee, A., *Polymer*, **31**, 2267 (1989).

91. Pearson, R. A. and Yee, A. F., *J. Mater. Sci.*, **24**, 2571 (1989).

92. Kinloch, A. J., *Polym. Commun.*, **28**, 322 (1987).

93. Huang, Y. and Kinloch, A. J., *J. Mater. Sci.*, **27**, 2763 (1992).

94. Naqui, S. I. and Robinson, I. M., *J. Mater. Sci.*, **28**, 1421 (1993).

95. Bucknall, C. B., *Toughened Plastics*, Applied Science, London (1977).

96. Pearson, R. A. and Yee, A. F., *J. Mater. Sci.*, **26**, 3828 (1991).

97. Lazzeri, A. and Bucknall, C. B., *J. Mater. Sci.*, **28**, 6799 (1993).

98. Lu, F., Cantwell, W. J. and Kausch, H. H., *J. Mater. Sci.*, **32**, 3059 (1997).

99. Evans, A. G., Ahmad, Z. B., Gilbert, D. G. and Beaumont, P. W., *Acta Metall*, **34**, 79 (1986).

100. Dekkers, M. E., Hobbs, S. Y. and Watkins, V. H., *J. Mater. Sci.*, **23**, 1225 (1988).

101. Bensason, S., Hiltner, A. and Baer, E., *J. Appl. Poly. Sci.*, **63**, 715 (1997).

102. Tse, A., Shin, E., Hiltner, A. and Baer, E., *J. Mater. Sci.*, **26**, 5374 (1991).

103. Dompas, D. and Groeninckx, G., *Polymer*, **35**, 4743 (1994).

104. Steenbrink, A. C., Giessen, V. D. and Wu, E., *J. Mech. Phys. Solids*, **45**, 405 (1997).

105. Gurson, A. L., *J. Eng. Mater. Technol., Trans. ASME*, **99**, 2 (1977).

106. Breuer, H., Haaf, F. and Stavenow, J., *J. Macromol. Sci., Phys.*, **14**, 387 (1977).

107. Sultan, J. and McGarry, F. J., *Poly. Eng. Sci.*, **13**, 29 (1972).

108. Tuttle, M. E., Semeliss, M. and Wong, R., *Exp. Mech.*, **32**, 1 (1992).

109. Butler, J., *Compression and Transfer Molding*, Interscience Publshers Inc., New York (1959).

110. Havriliak, S., *J. Polym. Sci., Part B: Polym. Phys.*, **28**, 1987 (1990).

111. Guild, F. J. and Young, R. J., *J. Mater. Sci.*, **24**, 2454 (1989).

112. Huang, Y. and Kinloch, A. J., *Polymer*, **33**, 1330 (1992).

113. Bagheri, R. and Pearson, R., *Polymer*, **36**, 4883 (1995).

114. Kiefer, J. and Hilborn, J. G., *Polymer*, **37**, 5715 (1996).